Global optimization of material properties: clusters, solar cells and metal surfaces

Dissertation
zur Erlangung des Grades
des Doktors der Naturwissenschaften
der Naturwissenschaftlich-Technischen Fakultät
der Universität des Saarlandes

von

Kai Udo Huwig

Saarbrücken
2020

Tag des Kolloquiums: 24. Februar 2021
Dekan: Prof. Dr. Jörn Erik Walter
Berichterstatter: Prof. Dr. Michael Springborg
Prof. Dr. Kaspar Hegetschweiler

Vorsitz: Prof. Dr. Uli Kazmaier
Akad. Mitarbeiter: Dr. Bernd Morgenstern

„Aus bloßer Vernunft kömmt keine Philosophie, denn Philosophie ist mehr,
denn blinde Forderung eines nie zu endigenden Fortschritts
in Vereinigung und Unterscheidung eines möglichen Stoffs.“

Friedrich Hölderlin (Hyperion)

Contents

List of Figures

List of Tables

1 Acknowledgements

Only with the support of several people this work could be realized successfully. I would like to express my deepest appreciation to my supervisor Prof. Dr. Michael Springborg. All the fruitful discussions with him and the many useful advices he gave me helped me to accomplish my different projects within my thesis. His support, may it be professional or personal, can not be overestimated. He also gave me a lot of freedom to develop and implement my own ideas and concepts.

Furthermore, I would like to express my special gratitude to Dr. Valeri Grigoryan. I greatly value his experience and his valuable assistance in so many special issues concerning clusters and computational details. I highly appreciate his support in non-scientific issues as well as always having an open door in case of any problems.

I also want to thank Dr. Mohammad Molayem for providing assistance and advice in so many different fields of work. It was a pleasure to work with him. And I want to thank my office mates Meijuan Zhou and XU Hao for creating a relaxed and pleasent working atmosphere and I remember with pleasure the one or other funny situation. Furthermore, I want to thank Chencheng Fan. It was a pleasure to work with her and to learn from her about the theoretical background of solar-energy harvesting.

Special thanks go to Nicolas Louis for providing assistance in all kinds of technical issues, may it be the use of computational ressources or any kind of technical problems. Moreover, I want to thank Silvia Nagel for helping me with organizational and administrative issues of all sorts and also for some discussions not related to work. Another thank you goes to my colleagues Phillip Thiel, Dr. Jihene Jerbi and Dr. Hilke Bahmann for a pleasant working atmosphere.

There are still some persons left: special thanks also go to Dr. Stephan Kohaut for many interesting and fruitful discussions and for teaching me some useful concepts of the Python programming language at the beginning of my PhD thesis. Furthermore I want to thank: Dr. Abdullah Saleem Khazaal, Dr. Sahar Abdallah, Aaruni Mahendra, Stephan Muth, Julian Beckmann and Moritz Wolfer.

I want to express my deepest appreciation to my family. I want to thank my mother, my father and my grandmother for their endless support and encouragement over all the years. I also want to thank my parents-in-law for their support. My deepest gratitude goes to my wonderful wife Lisa. Particularly during more difficult times her endless and loving support can not be overestimated. I will always love you and our two wonderful children Felix and Amalia, who are the whitnesses of our happiness.

2 Kurzzusammenfassung

In dieser Arbeit werden verschiedene globale Optimierungsprobleme behandelt. Unter Verwendung einer analytisch modifizierten Embedded-Atom-Methode (MEAM), wurden strukturell-energetische globale Optimierungen von Lithium- und Natriumclustern durchgeführt. Für jede Clustergröße N im Bereich $2 \leq N \leq 150$ identifizierten wir mittels des *Aufbau-Abbau*-Verfahrens bis zu sechs der stabilsten Isomere, woran sich eine detaillierte energetische und strukturelle Analysen der erhaltenen Li- und Na-Isomere anschloss. Für $N \leq 5$ liefert die MEAM zum Teil, für Modellpotentiale, untypische Ergebnisse, wie flache oder lineare Clustergeometrien. Neben der strukturellen Optimierung von Clustern innerhalb kontinuierlicher Suchräume, wurden auch globale Optimierungen von Materialeigenschaften in diskreten Suchräumen durchgeführt. Unter Verwendung eines genetischen Algorithmus, ein Bestandteil unseres Inverse-Design-Konzeptes, optimierten wir organische Moleküle hinsichtlich ihres Einsatzes in Solarzellen. Chemische Intuition kann vereinzelt hilfreich sein, die für die Nutzung von Sonnenenergie vorteilhaften Substitutionsmuster der Moleküle vorherzusagen und zu verstehen. Zudem erweiterten wir unseren Inverse-Design-Ansatz um die Optimierung der Adsorptionseigenschaften von Metalloberflächen. Die Umsetzung dieses Vorhabens war herausfordernd und mit einigen Problemen verbunden. Jedoch konnten auch hier interessante Ergebnisse erhalten werden, die als Basis weiterer Studien dienen können.

3 Abstract

Different global optimization tasks have been treated within this thesis. Using an analytic modified embedded atom method (MEAM), a structural-energetic global optimization of lithium and sodium clusters has been performed. With the *Aufbau-Abbau* procedure we identified up to six most stable isomers for each cluster size N within the size range $2 \leq N \leq 150$, which was followed by a detailed energetic and structural analysis of the obtained Li and Na isomers. For $N \leq 5$ the MEAM partly yields results which are unusual for model potentials, such as planar or linear cluster geometries. Besides the structural optimization of clusters within continuous search spaces, also global property optimizations within discrete search spaces have been performed. Employing a genetic algorithm, a part of our inverse design concept, we optimized organic molecules with respect to their usage within solar cells. Occasionally chemical intuition may help to predict and to understand the substution patterns of the molecules that may be beneficial for solar energy harvesting. Moreover, we extended our inverse design approach to the optimization of the adsorption properties of metal surfaces. The implementation of this project was challenging and associated with several problems. However, also here interesting results could be obtained, which can serve as starting point for further investigations.

4 Preface

A part of the work in this thesis, i.e. the global optimization of alkali clusters (part II) and the optimization of the solar harvesting properties (part III, chapter 12), was published in two articles. No results for the investigation of the adsorption properties of transition metal surfaces (part III, chapter 13) have been published until now.
The Fortran codes used for the global optimization of the clusters are based on already existing programs written by V. G. Grigoryan. These codes were rewritten and adjusted to the problems under study by K. Huwig. The energetic and structural analysis of the clusters was performed with a code provided by M. Springborg.
The genetic algorithm for the global optimization of the solar energy harvesting properties is based on a program also provided by M. Springborg. This program was rewritten by C. Fan and K. Huwig in parts and adjusted to the treatment of organic molecules.
The genetic algorithm for optimizing the adsorption properties of transition metal surfaces was implemented in Python by K. Huwig and combined with the Atomic Simulation Environment (ASE) [1, 2]. Multiprocessing [3] was employed to parallelize this genetic algorithm.
The Slater-Koster files, including the parametrizations for the DFTB method, were taken from dftb.org [4] and the potential files for DFT calculations were taken from the *Virtual Vault for Pseudopotentials.* [5]
The invesigations concerning the alkali clusters and the dye solar cells and have been published in the following articles:

1. **Structural-energetic GO of Li and Na clusters** (part II in this thesis)
   K. Huwig, V. G. Grigoryan and M. Springborg, Global Optimization of Li and Na Clusters: Application of a Modified Embedded Atom Method. *J. Clust. Sci.*, 31(4):769-790, 2020.

2. **Solar energy harvesting** (part III, chapter 12 in this thesis)
   K. Huwig, C. Fan and M. Springborg, From properties to materials: An efficient and simple approach. *J. Chem. Phys.*, 147(23):234105, 2017.

Moreover, in my bachelor thesis I already did some preliminary work on the global optimization of sodium clusters. However, smaller, not fundamental errors within the source codes have been removed for the work done in the present thesis. Furthermore, the limited period of time during the bachelor project prohibited the extensive studies in this thesis. Therefore, with this improved source code, also a much more extended and thorough search for the clusters' global minimum structures could be performed now. Within the Bachelor thesis, only sodium clusters Na_N with $2 \leq N \leq 60$ and up to three isomers for each cluster size have been considered. Here, we took up to six isomers for each cluster size and Li_N and Na_N clusters with $2 \leq N \leq 150$ into account. A much more extensive global optimization procedure and a much more detailed energetic and structural analysis has been performed. Moreover, it has to be stressed that none of the preliminary results included within my bachelor thesis have been used for the present work.

5 Introduction

Synthesized or isolated chemical compounds have been documented since the beginning of the 19th century and until the year 2015 an exponential increase in the number of new chemical compounds can be observed [6]. In this connection nowadays total chemical space, consisting of all thermodynamic stable structures, is indiscribable large. In the search for drug-like compounds with up to 30 atoms, consisting only of carbon, oxygen, nitrogen and sulfur, in total 10^{60} different organic molecules would have to be examined [7]. Another example would be the theoretical investigation of a pseudo-binary alloy of the general composition $A_{0.25}B_{0.75}C$ with 128 lattice sites, with the cationic sites occupied either with element A or B. Roughly 10^{14} different alloys with potentially different electronic properties are possible [8]. Hence, regardless of whether doing experimental or theoretical work, in the field of materials design scientists face the big challenge of huge search spaces.

Exploring these chemical spaces using heuristical trial-and-error approaches of classical science is time-consuming, expensive and inefficient. With the rise of more advanced technologies combinatorial chemistry and high-throughput-screening methods came up, which are applied mainly in heterogeneous catalysis [9, 10] and drug design [11, 12], but also in other fields of materials science [13]. The automatized, experimental combinatorial and high-throughput techniques involve the parallelized generation of an enormous number of chemical compounds and their subsequent parallelized screening for desired properties. Despite the increase in efficiency [10] and the quantitative miniaturization of single reactions [14, 15], the problem of high financial expenditure, resource and time consumption still prevails for these experimental methods. Moreover, combinatorial and high-throughput techniques are not suitable for every area of materials science and often trial-and-error methods are still predominant.

With the advent of increasingly improved computer technologies computational, theoretical investigations became more and more important for the assistance of experimental research. Not only within the aforementioned high-throughput approaches computational methods became a valuable tool [13, 16, 17], now theoretical calculations are an integral part of many fields of modern science [18, 19, 20, 21, 22].

Particularly in the case of the chemical space problem the use of computers plays an important role in science [23, 24]. Due to the huge search spaces met in materials design, an exclusively experimental strategy is often not appropriate. The prescreening of these chemical spaces using computational methods is time and cost saving and enables a sub-

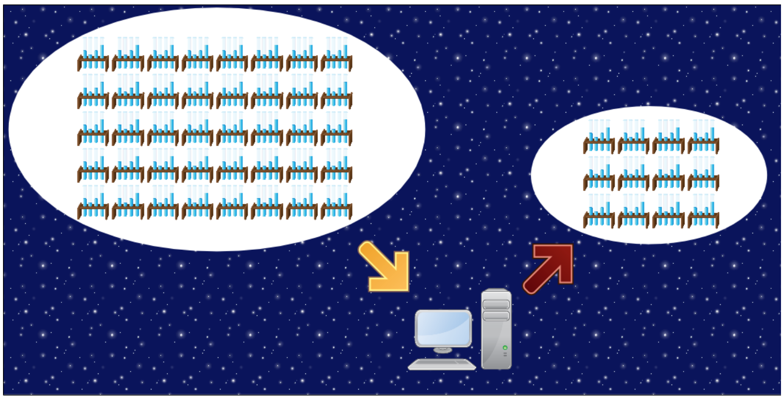

Figure 5.1: Illustration of the chemical space problem and a possible solution: a huge search space with a large number of different chemical structures, represented via the test tubes, is reduced to a smaller space via computational tools. For instance, the computational tool may be some global optimization procedure, which is used to identify certain promising candidate structures. In doing so, the large search space does not have to be investigated via experimental methods, but instead the smaller search space can be examined experimentally.

sequent, more targeted utilization of experimental studies. A generalized chemical space problem and its solution is depicted in figure 5.1. Here, a large search space including a vast number of chemical compounds (represented by the test tubes) is reduced to a much smaller space using computers. The remaining systems after the computational screening are promising candidate structures that may exhibit the desired properties. Subsequent experimental investigations of the drastically reduced space may be much more effective than on the initial one.

One opportunity to handle the large amount of chemical and biological information is big data analysis [25, 26, 27]. A different approach that is used for exploring search spaces is based on physical and/or quantum-mechanical principles. Using quantum theory some approximation to the Schrödinger equation describes the electronic structure(s) of the system(s) of interest. The calculated electronic properties are the basis for the search for a chemical structure with the desired properties within the corresponding chemical space. Some algorithm is used to identify that/these structure(s) with the optimal properties among a wide range of possible compounds. Such (unbiased) global optimizations are standard problems within theoretical and computational materials design and a lot of effort has been put into the development of efficient global optimization (GO) procedures [28, 29, 30, 31, 32].

One of the most evident physical-chemical issues is that of identifying the most stable geometrical structure of a certain chemical system. Here, the property of interest is the total energy of the system and the purpose is to find the structure with the lowest total energy within the search space. This kind of optimization can be referred to as a global energy optimization (GEO). Special attention has always been paid to the GEO of clusters [33, 34]. Clusters are nanosized particles, consisting of $2 - 10^7$ atoms or molecules and they can be homo- or heteroatomic [35]. Moreover, different types of clusters exist, e.g. metal, rare gase or molecular clusters [35]. The clusters' properties are particularly influenced by their large proportion of surface atoms and these properties vary strongly with the number of particles they consist of. Especially metal clusters have been the subject of intensive research [36, 37, 38]. For instance, the abundance spectra of metal clusters revealed that certain cluster sizes appear more frequently than others, which is in connection with a higher stability of these sizes [37]. To understand these phenomena as well as the growth patterns and other properties of the clusters, the identification of the most stable structures (and the metastable isomers) for each cluster size is very important [34, 39, 40]. Since the experimental investigation of clusters is cost- and time-intensive the computational determination of the global energy minima (GEM) of clusters is a central issue in cluster science.

But the total energy is just one of the many possible properties that can be optimized. In this connection the concept of Inverse Design (ID) comes into play. The structural-energetic global optimization of a system, introduced above, can also be considered as a first step in the calculation of properties different from the total energy. After the GO and the identification of the lowest-energy structures and the metastable isomers, in a second step in principle any desired property of the GEM (and their isomers) can be calculated. This means that initially chemical structures are sought and then the properties of these systems are calculated [41]. This "direct" approach used for exploring chemical-space can not guarentee to find the structures with the best properties since the GEM (and the metastable isomers) do not necessarily exhibit the optimal values concerning another property. The ID strategy, mentioned above, tries to overcome these drawbacks of the "direct" approach by taking the inverse route to materials design: a desired property is defined at the beginning of the procedure and subsequently the structures with the optimal property values are indentified using an optimization algorithm [41]. Within this global property optimization (GPO) the two-step direct procedure is replaced via a more targeted and efficient one-step method that does not require the GEM. This does not, however, mean that the "direct" method or the GEO is redundant and it can always be substituted via an ID approach. In many other fields of science and, as stressed before, especially in cluster science, the determination of the lowest-energy structures is essential.

In principle there are no limits for ID concerning the system and property to investigate. The application of ID methods ranges from the design of photonic crystals with optimal properties [42, 43] to the study of green catalysts for the conversion of biomass [44] and the optimization of the acidity of naphtol derivatives [45]. Due to the steadily increasing demand for environmentally friendly and resource saving energy supply, there is an ongoing research on different types for solar cells [46, 47, 48, 49], also via ID [50, 51, 52]. Also the adsorption properties of various systems are scientific problems that can be treated via property optimization using ID or ID related methods. As examples can be mentioned the adsorption of methane by zeolites [53] or the adsorption performance of bimetallic nanoalloys concerning molecular species that occur within catalytic processes [54].

Regardless of which properties are sought or which chemical systems have to be investigated, theoretical GO procedures are an important tool in science. It has to be re-emphasized that without these computational studies, research in many fields of science would be much less effective and targeted. Therefore working on and with GO techniques, whether the development of algorithms or their application to various search spaces, is of fundamental importance and a frequently occuring challenge.

In general there are two different types of GO algorithms. A GO is termed biased, if some prior information on the system to investigate is used. This can be structural information about the bonding situation within the system or constraints about the positions of certain molecular fragments. This can enhance the optimization procedure, but may also lead to an exclusion of possible structures due to the use of these constraints. In contrast a strictly unbiased GO is performed, if there is no prior information on the system at all. In practice this exact classification is usually not possible and some prior knowledge is always involved in a GO process. Hence, it is possible to speak of GO algorithms that are more or less unbiased. This designation is also related to the kind as well as the amount of information that is used and this may also differ from case to case.

In this work theoretical unbiased global optimizations are performed within different search spaces. Although some prior information on the systems of interests is used, in order to enhance the optimization procedure and to explore the corresponding chemical spaces more efficiently, the applied algorithms can be referred to as unbiased optimization approaches. An unbiased GEO of alkali clusters is performed as well as an unbiased GPO concerning solar energy harvesting. Finally, the latter inverse design concept is expanded to the treatment of adsorption properties of transition metal surfaces.

This thesis is organized as follows: Within Part I fundamental aspects concerning the theoretical unbiased global optimizations are discussed. These include basics about quantum chemical calculations, i.e. foundations of quantum theory, as well as general considerations concerning GEOs and the GPOs, e.g. potential energy and property hypersurfaces. The presented basic principles underly the theoretical investigations presented in part II and III.

Part II deals with an unbiased GEO of Li and Na clusters, consisting of up to 150 atoms. Up to six different isomers are considered for each cluster size. A fast and efficient semiempirical modified embedded atom method (MEAM), which was initially developed for bulk alkali metals, is used for this global optimization task. In combination with the *Aufbau-Abbau* method, an effective GO algorithm, the simple analytic formulae of the MEAM enable an extensive investigation of the continuous search spaces of the clusters. Despite their ideal suitability for such an unbiased optimization, there is a lack of investigations of alkali metal clusters using embedded atom potentials. Cluster structures for Li and Na are obtained that are dictated by packing effects and which are common for a model potential like the MEAM. But there are also cluster geometries that rather would be expected for higher-level theory than for an embedded atom method, e.g. linear or planar structures. A detailed structural and energetic analysis for the alkali clusters is performed, including growth patterns of the clusters and structural similarities between the Li and Na clusters.

Unbiased GPOs are the subject of the third part of this thesis and here, discrete property search spaces are investigated. Two different studies are presented. A simple and efficient approach, called PooMa (Poor Man's Material Optimization), is used to optimize organic molecules with respect to solar energy harvesting properties. As test system we use benzene derivatives with a pool of 18 different substituents, which can be attached as functional groups. First, a detailed description of the technical details of this approach is given, involving a genetic algorithm as global optimization procedure, the chosen performance functions and the used theoretical electronic-structure method, the density functional tight-binding (DFTB) approach. Several properties are investigated, e.g. the capability for sunlight absorption or the spatial arrangement of the orbitals within the organic molecules. A few trends can be identified, where some molecular fragments or functional groups seem to be beneficial for a certain property. But some molecules' substitution patterns are not self-explanatory using chemical intuition and are not easy to understand. The subsequent chapter describes the extension of the PooMa approach to the adsorption properties of transition metal surfaces. We present the further development of our ID method and the associated opportunities, includind the increased flexibility and the parallelization of the corresponding source code. The investigated adsorbent-adsorbate systems are Ni(111)/CO and Ti(0001)/H_2. Difficulties concerning the optimization of the system Ni(111)/CO are discussed as well as first test calculations with Ti(0001)/H_2 are performed. A surface is represented by a slab consisting of several atomic layers. The positions within the top layer of a slab can either be occupied by a transition metal atom or a vacancy. Our PooMa approach is used to determine automatically that arrangements of slab atoms/vacancies within the uppermost layer of the slab, which yield the optimal adsorption energies. Interesting results for the dissociative adsorption of H_2 on the Ti(0001) surface are obtained, with vacancies enhancing the adsorption properties of the surfaces. These initial studies are a good basis for further investigations on the adsorption properties of surfaces with PooMa.

Part I

Global optimization in quantum chemistry

The GO tasks that are treated within this thesis, include several indispensable components. For instance, a computational method has to be chosen that describes the electronic structure of the systems of interest and/or the interaction between the constituting atoms. The choice of the method is governed by the type of chemical structures that have to be investigated, as well as the required accuracy for a reliable description of the sought properties of these structures. Furthermore, the computational effort of the chosen theoretical approach is of particular importance. Especially in case of an unbiased GO within large search spaces, where a large number of structures has to be optimized to locate that one with the desired properties, too time-consuming methods are impractical. But, in many cases, a less computationally expensive method exhibits a lower accuracy. Thus, the reliability of the calculated properties should not suffer from the simplifications or approximations of the corresponding method. Therefore, often not an easy task to perform, one has to make compromises concerning the accuracy and the effort of a given method. In chapter 6 basics in quantum-mechanics are discussed, which are neccesary to understand the significance of approximations and models that are used within the computational methods within this work.

The electronic and geometrical structure of the considered system is determined by the computational method. The electronic and geometrical structure in turn determines the property of interest. Hence, the desired property depends on the chosen method. Upon variation of certain parameters of the system, e.g. nuclear position-space coordinates or composition, a variety of different electronic and geometrical structures and therefore different properties is created. These many different structures span a huge space, a hypersurface, consisting of different property values as a function of the varied parameters. Now some procedure has to be chosen to locate the system with the lowest total energy or optimal property on this hypersurface (or within this search space). In this connection a GO algorithm determines the way of generating the structures and how effective the search space is explored during the optimization procedure [39]. In chapter 7 some basic principles and algorithms concerning GEOs and GPOs are briefly being discussed.

6 Electronic structure calculations: Quantum theory

Initially some introductory remarks on quantum theoretical foundations will be made. A short overview over fundamental approximations within quantum mechanics is followed by a brief description of wavefunction-based methods. Subsequently the density-functional theory (DFT), which forms the basis for the theoretical methods used in this thesis, will be discussed.

6.1 Foundations: The Schrödinger equation

According to the first postulate of quantum mechanics some wavefunction

$$\Psi(\vec{q}, \vec{Q}, t) \tag{6.1}$$

completely determines the state of a quantum mechanical system consisting of N electrons and M nuclei and it is a solution to the time-dependent Schrödinger equation. Here $\vec{q} = (\vec{r}_1, \sigma_1, ..., \vec{r}_N, \sigma_N)$ comprises the position-space coordinates $\vec{r}_i$ and the spin coordinates σ_i of the electrons, $\vec{Q} = (\vec{R}_1, \Sigma_1, ..., \vec{R}_M, \Sigma_M)$ the corresponding nuclear coordinates for position $\vec{R}_i$ and spin Σ_i and t represents the time. Since we are only interested in stationary states, we factorize $\Psi(\vec{q}, \vec{Q}, t)$, and a product of two functions $\Psi(\vec{q}, \vec{Q}) \cdot A(t)$ is obtained. Using this factorization procedure, the time-dependent Schrödinger equation can be transformed into the corresponding time-independent form. Only the function $\Psi(\vec{q}, \vec{Q})$, depending on the position-space and spin coordinates, is of importance for the further explanations in this thesis. Knowing $\Psi(\vec{q}, \vec{Q})$ for a particular state allows for the description of the whole system and therefore in principle any property of the system in this state is accessible. The state function $\Psi(\vec{q}, \vec{Q})$ itself can be obtained by solving the aforementioned time-independent Schrödinger equation:

$$\hat{H} \cdot \Psi(\vec{q}, \vec{Q}) = E \cdot \Psi(\vec{q}, \vec{Q}). \tag{6.2}$$

The Schrödinger equation is an eigenvalue problem, with $\hat{H}$ being the Hamiltonian, the total-energy operator, and E being the energy of the considered system. The problem, though, is that, except for a few model systems (e.g. the particle in a box, the quantum harmonic oscillator) the Schrödinger equation can not be solved analytically. Beyond such simple model systems approximations have to be made. Rewriting the hamiltonian $\hat{H}$ in equation 6.2 as a sum of its parts leads to

$$(\hat{T}_e + \hat{T}_n + \hat{V}_{e-e} + \hat{V}_{n-n} + \hat{V}_{e-n}) \cdot \Psi(\vec{q}, \vec{Q}) = E \cdot \Psi(\vec{q}, \vec{Q}). \tag{6.3}$$

$\hat{T}_e$, $\hat{T}_n$, $\hat{V}_{e-e}$, $\hat{V}_{n-n}$, $\hat{V}_{e-n}$ represent the operators for the kinetic energy of the electrons, the kinetic energy of the nuclei, the potential energy of the electron-electron interaction, the potential energy of the nucleus-nucleus interaction and the potential energy of the electron-nucleus interaction, respectively.

Due to the huge difference in mass between the electrons and the nuclei, the much heavier nuclei are treated as fixed particles: the electrons move very fast when compared to the movement nuclei and they are able to react immediately to any change in the positions of the nuclei. So the electrons adjust directly to a new arrangement of the nuclei and it seems as if the latter did not move at all. The above-mentioned assumptions are called the Born-Oppenheimer (BO) approximation [55]. Applying this approximation to equation 6.3 leads to the electronic Schrödinger equation

$$\hat{H}_e \cdot \Psi_e(\vec{q}, \vec{Q}) = (\hat{T}_e + \hat{V}_{n-e} + \hat{V}_{e-e}) \cdot \Psi_e(\vec{q}, \vec{Q}) = E_e(\vec{Q}) \cdot \Psi_e(\vec{q}, \vec{Q}), \tag{6.4}$$

with $E_e(\vec{Q}) = E - \hat{V}_{n-n}$ and $\Psi_e(\vec{q}, \vec{Q})$ being the electronic energy and the electronic wavefunction, respectively. Since the nuclei are assumed to be fixed the kinetic energy of the nuclei $\hat{T}_n$ is neglected. Both, $E_e(\vec{Q})$ as well as $\Psi_e(\vec{q}, \vec{Q})$, depend parametrically on the nuclear coordinates $\vec{Q}$. This dependence means that solving equation 6.4 for a certain set of atomic positions $\vec{Q}_1$ will give a electronic wavefunction $\Psi_e(\vec{q}_1, \vec{Q}_1)$ and an electronic energy $E_e(\vec{Q}_1)$. Another set of nuclear coordinates leads to another wavefunction $\Psi_e(\vec{q}_2, \vec{Q}_2)$ and energy $E_e(\vec{Q}_2)$. In order to obtain the total energy of the system, the corresponding potential energy of the nuclear repulsion, a classical Coulomb interaction, is added to the electronic energy E_e.

Within the BO approximation the nuclei are treated as classical particles that create an electrostatic potential in which the electrons move. The quantum efffects of the nuclei are neglected. Except for some cases [56, 57, 58], for the vast majority of systems treated in quantum chemistry, especially their ground-state configurations, the above-mentioned assumptions are valid.

6.2 Wavefunction-based methods

Central issue of wavefunction-based (*ab initio*) methods is the optimization of the electronic wavefunction $\Psi_e(\vec{q}, \vec{Q})$ that minimizes the total energy of the system. Since electrons are fermions, they are indistinguishable and $\Psi_e(\vec{q}, \vec{Q})$ has to be antisymmetric concerning the exchange of two electrons. In order to take this into account, the wavefunction is written as a so-called Slater determinant [59]. For a N-electron system it takes the form:

$$\Psi_e = \frac{1}{\sqrt{N!}} \begin{vmatrix} \psi_1(1) & \psi_1(2) & \dots & \psi_1(N) \\ \psi_2(1) & \psi_2(2) & \dots & \psi_2(N) \\ \vdots & \vdots & \ddots & \vdots \\ \psi_N(1) & \psi_N(2) & \dots & \psi_N(N) \end{vmatrix} \tag{6.5}$$

Here $\Psi_e = \Psi_e(\vec{q}, \vec{Q})$ and $\frac{1}{\sqrt{N!}}$ ensures that Ψ_e is normalized. $\psi_i(i)$ represents the ith spin orbital, occupied by the ith electron. Here, the the short notation i for the position-space coordinate $\vec{r_i}$ and the corresponding spin coordinates σ_i is used. The mathematical formulation of the wavefunction in equation 6.5 is the so-called Hartree-Fock approximation and it is is based on the orbital picture. According to the orbital picture, each orbital $\psi_i(i)$ is occupied by one single electron i.

6.2.1 The Hartree-Fock method

Due to the unsolvability of the Schrödinger equation for multielectron systems, an approximation is introduced: the independent-particle model (IPM). The Hartree-Fock approach [60, 61, 62, 63, 64] includes the IPM and according to that each electron moves in an effective potential, an averaged field that is caused by all the other electrons. Apart from that, their movement is not correlated. Each electron moves independently from the position-space coordinates of the other electrons.

The following descriptions in section 6.2.1 are related to atomic systems. Equation 6.4 can be rewritten as

$$\hat{H}_e \cdot \Psi_e = (\hat{H}_1 + \hat{H}_2) \cdot \Psi_e = E_e \cdot \Psi_e, \tag{6.6}$$

where $\hat{H}_1 = \hat{T}_e + \hat{V}_{n-e}$ and $\hat{H}_2 = \hat{V}_{e-e}$ are a one- and a two-electron operator, respectively, and $E_e = E_e(\vec{Q})$. Due to the IPM, $\hat{H}_2$ can be replaced with a simpler one-electron operator $\hat{H}_{2,eff}$, describing the above-mentioned effective potential in which each electron moves. According to that equation 6.6 then reads:

$$(\hat{H}_1 + \hat{H}_{2,eff}) \cdot \Psi_e = E_e \cdot \Psi_e. \tag{6.7}$$

The objective is now to find that set of spin orbitals $\psi_i(i)$, leading to a Slater determinant Ψ_e, which minimizes the energy E_e of the system under consideration. For this purpose the method of Lagrange multipliers is used, where extreme values are determined with simultaneous consideration of constraints. A functional L is minimized according to

$$\delta L = \delta[\langle \Psi_e | \hat{H}_e | \Psi_e \rangle - \sum_{k=1}^{N} \sum_{l=1}^{N} \epsilon_{kl} (\langle \psi_k(i) | \psi_l(i) \rangle - \delta_{k,l})] = 0, \tag{6.8}$$

with δ, $\langle \Psi_e | \hat{H}_e | \Psi_e \rangle$ and $\delta_{k,l}$ denoting the variation, the expectation value of $\hat{H}_e$ (the average energy value of the system) and the Kronecker delta, respectively. The second term in equation 6.8 represents the constraint that the spin orbitals $\psi_k(i)$ have to be orthonormal, with the ϵ_{kl} being the Lagrange multipliers. Solving equation 6.8 leads to N solutions of the form

$$\hat{f} \cdot \psi_k(i) = \epsilon_k \cdot \psi_k(i), \tag{6.9}$$

which are the so-called Hartree-Fock (HF) equation. In contrast to the Schrödinger equation (equation 6.7) the Hartree-Fock equations are single-particle equations that determine the one-electron functions (spin orbitals) $\psi_k(i)$ and their eigenvalues ϵ_k. This is another consequence of the application of the IPM. $\hat{f}$ is the Fock operator and unlike the Hamiltonian a single-particle operator, that takes the following form:

$$\hat{f} = \hat{h}_1(i) + \sum_{l=1}^{N} [\hat{J}_l(i) - \hat{K}_l(i)]. \tag{6.10}$$

$\hat{h}_1(i)$ is the operator for the kinetic energy of electron i, which moves in an electrostatic field caused by the nucleus. $\hat{J}_l(i)$ represents the Coulomb operator and $\hat{K}_l(i)$ is the so-called exchange operator. $\hat{h}_1(i)$ is defined as follows:

$$\hat{h}_1(i) = T_e(i) + V_{n-e}(i) = -\frac{\hbar^2}{2m_e} \Delta_i - \sum_{\alpha} \frac{Z_\alpha e^2}{4\pi\epsilon_0 r_{i,\alpha}}, \tag{6.11}$$

with the first term being the kinetic energy of the ith electron and the second term being the classical Coulomb interaction between electron i and a nucleus α with charge Z_α. $r_{i,\alpha}$ is the distance between the electron i and the nucleus α.

The quantity $\hat{J}_l(i)$ in equation 6.10 describes the interaction between two electrons i and

j and can be understood as the quantum mechanical analogue to a classical Coulomb interaction between charges. It is defined as an integral over four coordinates, i.e. three spatial coordinates $\vec{r}_j$ and one spin coordinate σ_j:

$$\hat{J}_l(i)\psi_k(i) = \left[\int \frac{e^2\psi_l^*(j)\psi_l(j)}{4\pi\epsilon_0 r_{ij}} d\vec{r}_j d\sigma_j\right] \psi_k(i). \tag{6.12}$$

$\psi_l(j)$ describes the jth electron in spin orbital l and $\psi_l^*(j)$ the corresponding complex conjugate, whereas $\psi_k(i)$ is the wavefunction describing the ith electron in the spin orbital k. r_{ij} is the distance between the electrons i and j. The expression $\psi_l^*(j)\psi_l(j)$ is the charge density of electron j acting on electron i.

The third term in equation 6.10, the exchange operator $\hat{K}_l(i)$, has no corresponding quantity in classical physics and results from a pure quantum mechanical effect. It arises from the fact that fermions like electrons are not distinguishable. As in the case of the Coulomb operator $\hat{J}_l(i)$, $\hat{K}_l(i)$ is an integral operator over four coordinates:

$$\hat{K}_l(i)\psi_k(i) = \left[\int \frac{e^2\psi_l^*(j)\psi_k(j)}{4\pi\epsilon_0 r_{ij}} d\vec{r}_j d\sigma_j\right] \psi_l(i). \tag{6.13}$$

The HF equations 6.9 are used to determine the spin orbitals $\psi_k(i)$. Since the Coulomb operator $\hat{J}_l(i)$ (equation 6.12) as well as the exchange operator $\hat{K}_l(i)$ (equation 6.13) depend on these orbitals, equations 6.9 can only be solved iteratively, self-consistently [64]. The Hartree-Fock equations, seperated into the different energetic terms is

$$\left[-\frac{\hbar^2}{2m_e}\Delta_i + V_{n-e}(i) + \sum_{\substack{l=1 \\ l\neq k}}^{N} J_l(i)\right] \psi_k(i) - \left[\sum_{\substack{l=1 \\ l\neq k}}^{N} K_l(i)\right] \psi_l(i) = \epsilon_k\psi_k(i), \tag{6.14}$$

6.2.2 The Hartree-Fock-Roothaan method

For practical applications, further simplifications have to be introduced into the Hartree-Fock formalism. The HF equations are complex integro-differential equations and have to be solved iteratively. Furthermore within atoms, only one nucleus exists and since the electron movement is not correlated, the effective potential acting on each electron just depends on the distance to that single nucleus. A central field exists, which makes the solution of the Hartree-Fock equations easier. This is different for molecules. The treatment of molecular systems, however, increases complexity, since molecules posses several nuclear centers and the central-field approximation is no longer valid [65]. This complicates the solvability of the HF equations.

Within the Roothaan approximation [65, 66] the spin orbitals are expanded in a set of basic functions. Each molecular one-electron wavefunction $\psi_k(i)$ is written as a linear combination of a finite number P of predefined atomic orbitals $\chi_\mu(i)$:

$$\psi_k(i) = \sum_{\mu=1}^{P} c_{\mu k}\chi_\mu(i) \tag{6.15}$$

Using the LCAO (linear combination of atomic orbitals) approach one restricts the variational procedure to determine the Slater determinant that minimizes the energy of the system to the variation of the linear combination coefficients $c_{\mu k}$. The basis functions χ_μ are kept fixed. In order not to go beyond the scope of this work, just a brief comment on basis functions. Their analytical form is known and for instance either Slater-type or Gauss-type orbitals can be used to describe them. Concerning practical applications the use of Gaussians has been shown to be advantageous [67]. Various sets and sizes of basic functions are available. The selection depends on the kind of system to investigate as well as on the compromise between accuracy and computational costs.
Using the method of the Lagrange multipliers under consideration of the Roothaan approximation 6.15, i.e. by varying the coefficients $c_{\mu k}$, leads to secular eigenvalue equations, the Roothaan-Hall equations [65, 66], of the form:

$$(\mathbf{F} - \mathbf{E}\mathbf{S})\mathbf{C} = 0, \tag{6.16}$$

with $\mathbf{F}$ and $\mathbf{S}$ being the Fock and overlap matrix, respectively. The matrix $\mathbf{C}$ contains the sought coefficients $c_{\mu k}$ to the atomic basic functions $\chi_\mu(i)$, that constitute the molecular spin orbitals $\psi_k(i)$ according to equation 6.15. $\mathbf{E}$ is a diagonal matrix with the eigenvalues ϵ_k of the molecular spin orbitals $\psi_k(i)$. The application of the Roothaan approximation transforms the complicated integro-differential Hartree-Fock equations 6.9, into a secular matrix eigenvalue problem 6.16, that is much easier to solve [65, 66]. In doing so the coefficients $c_{\mu k}$ as well as the orbital energies ϵ_k can be determined. The Fock matrix $\mathbf{F}$ is an approximation to the Fock operator $\hat{f}$ (equation 6.10), with the matrix elements

$$F_{\mu\nu} = \langle\chi_\mu|\hat{h}_1|\chi_\nu\rangle + \sum_{i=1}^{N}\sum_{\rho,\sigma=1}^{P} c^*_{\rho i}c_{\sigma i}\left[\langle\chi_\mu\chi_\rho|\hat{h}_2|\chi_\nu\chi_\sigma\rangle - \langle\chi_\rho\chi_\mu|\hat{h}_2|\chi_\nu\chi_\sigma\rangle\right]. \tag{6.17}$$

This matrix elements consist of contributions from the electronic kinetic energy and the electron-nuclear attraction (first term in equation 6.17), the electronic Coulomb (second term) and the exchange interaction (third term). The elements $S_{\mu\nu}$ of the overlap matrix

S describe the extent of the spatial overlap of the atomic basic functions χ_μ and χ_ν:

$$S_{\mu\nu} = \langle \chi_\mu | \chi_\nu \rangle. \tag{6.18}$$

However, solving equation 6.16 still has to be done iteratively, because through the elements $F_{\mu\nu}$ of the Fock matrix **F** (see equation 6.17) the Roothaan-Hall equations depend on the sought coefficients $c_{\mu k}$. Also here a self-consistent procedure is applied [65].

6.2.3 Limits of the Hartree-Fock approximation

The limits of the HF method emerge from the neglection of explicit electron correlation [68]. Being sufficient for the ground state of numerous systems, the IPM fails in describing others with adequate accuracy. Hence, the energy calculated within the HF approach E_{HF} is an upper limit to the exact energy E_{exact} of a system and the difference between these two quantities is the correlation energy E_{corr}:

$$E_{\mathrm{corr}} = E_{\mathrm{exact}} - E_{\mathrm{HF}}. \tag{6.19}$$

These correlation effects are reflected in the difference between the exact wavefunction of the system and the approximated Slater determinant of equation 6.5. Beyond HF many attempts have been made to develop methods that somehow consider a correlated electron movement.

6.2.4 Beyond Hartree-Fock methods

One possibility to consider correlation effects is to use several Slater determinants instead of one to describe the system of interest. In doing so, the exact wavefunction is approximated as a linear combination of Slater determinants, each with a different configuration [69]. These configurations refer to the occupation of different spin orbitals. Besides the ground-state electron configuration Φ_0 there are singly excited configurations Φ_i^a, where an electron in an occupied spin orbital i has been excited to an virtual spin orbital a. Similar definitions for multiply excited configurations are used, e.g. Φ_{ij}^{ab} for a doubly excited configuration, where electrons from two occupied orbitals i and j are excited into two virtual orbitals a and b. This can be expanded to even more configurations and with this the wavefunction Ψ_e reads:

$$\Psi_e = C_0\Phi_0 + \sum_i \sum_a C_i^a \Phi_i^a + \sum_{ij} \sum_{ab} C_{ij}^{ab} \Phi_{ij}^{ab} + \sum_{ijk} \sum_{abc} C_{ijk}^{abc} \Phi_{ijk}^{abc} + \cdots . \tag{6.20}$$

C_0, C_i^a, C_{ij}^{ab} and C_{ijk}^{abc} are the linear combination coefficients of this series expansion and Φ_{ijk}^{abc} represents triply excited configurations. The sums in equation 6.20 include all possible combinations of excitations from occupied orbitals (i, j, k) to virtual ones (a, b, c). This approach is called configuration interaction and has become quite popular within computational chemistry/physics [70, 71, 72]. But only configuration interaction methods with a restricted number of determinants and excited electrons are of practical importance [69], e.g. CISD (configuration interaction with single and double excitations). But this truncation of the linear combination brings forth another problem: the size-inconsistency [72]. It means that for truncated CI methods the summed up energy of two single particles is not the same as the energy of a system, consisting of both particles, located at infinite distance from each other. CI methods, which remove the size-inconsistency problem include the Coupled Cluster (CC) approaches [72]. These shall not be explained here in detail.

Another option of considering electron correlation is a perturbative treatment. Within the Møller-Plesset perturbation theory [73] it is assumed that the Hamiltonian $\hat{H}_e$ can be expressed in terms of an unperturbed operator $\hat{H}_0$ and a perturbation operator $\hat{P}$ [74]:

$$\hat{H}_e = \hat{H}_0 + \lambda \hat{P}, \tag{6.21}$$

with λ being a control parameter for the size of the perturbation. The exact energy of the ground state E_e is calculated using a series expansion [74]:

$$E_e = E^{(0)} + \lambda E^{(1)} + \lambda^2 E^{(2)} + \lambda^3 E^{(3)} + \cdots , \tag{6.22}$$

with $E^{(0)}$, $E^{(1)}$, $E^{(2)}$ and $E^{(3)}$ representing the zeroth, first, second and third order perturbation energy, respectively. Perturbative energy contributions of higher order are defined accordingly. Furthermore, $E^{(0)} + E^{(1)}$ is the HF energy E_{HF}.

Also the wavefunction Ψ_e of the system is written as a power series [74]:

$$\Psi_e = \Phi^{(0)} + \lambda \Phi^{(1)} + \lambda^2 \Phi^{(2)} + \lambda^3 \Phi^{(3)} + \cdots . \tag{6.23}$$

For practical purposes the series have to truncated at a certain term. Consideration of perturbative contributions to second, third and fourth order gives the MP2, MP3 and MP4 method, respectively. However, the computational costs increase with the number of terms that are considered.

6.3 Density functional theory

Until the rise of density functional theory (DFT) [75] *ab initio* methods have been the method of choice for computational chemists. Although there exist some similarities between DFT methods and the wavefunction-based ones that will be discussed later, the fundamental assumptions both methods are based on are quite different.

6.3.1 Foundations of density-based methods

Refering to the Thomas-Fermi model [76, 77] Hohenberg and Kohn developed two theorems in 1964 [78]. In accordance with the first theorem, there is a one-to-one relationship between the ground-state wavefunction $\Psi_e(\vec{r}_1, ..., \vec{r}_N)$ and the ground-state electron density $\rho(\vec{r})$ of a quantum-mechanical system:

$$\Psi_e(\vec{r}_1, ..., \vec{r}_N) \longleftrightarrow \rho(\vec{r}) \tag{6.24}$$

The form $\Psi_e(\vec{r}_1, ..., \vec{r}_N)$ is used for simplification, neglecting the wavefunction's parametrical dependence on the nuclear position-space and spin coordinates $\vec{Q}_i$ and the dependence on the electronic spin coordinates σ_i. By analogy with the above-mentioned first postulate of quantum mechanics (see section 6.1), the knowledge of the density $\rho(\vec{r})$ is sufficient to determine the state of a quantum system and basically all electronic properties of that system can be calculated [75]. The electron density $\rho(\vec{r})$ of a system can be used to determine the electronic energy E_e of that system, i.e. the electronic energy E_e is a functional of the electron density: $E_e = E[\rho(\vec{r})]$.

The second theorem states that, by applying the variational procedure it is possible to obtain an electron density that minimizes the energy functional $E[\rho(\vec{r})]$. According to the first theorem (see equation 6.24) the minimization of $E[\rho(\vec{r})]$ with respect to the variation of the electron density $\rho(\vec{r})$ gives the same minimum energy E_0 (ground state energy) as it is obtained from the variation of the expectation value $\langle\Psi_e|\hat{H}|\Psi_e\rangle$. The relationship between the minimized energy $\tilde{E}[\tilde{\rho}(\vec{r})]$ obtained upon variation of some electron density $\tilde{\rho}(\vec{r})$ and the energy value for the "true" electron density $E_0[\rho_0(\vec{r})]$ is given by:

$$\tilde{E}[\tilde{\rho}(\vec{r})] \geq E_0[\rho_0(\vec{r})]. \tag{6.25}$$

Equation 6.25 is also denoted the "variational theorem". As mentioned above, it is a direct consequence of the so-called "existence theorem" of equation 6.24.

6.3.2 The Kohn-Sham-DFT

A basic challenge is how to express the energy E_e of a quantum-mechanical system in terms of its electron density $\rho(\vec{r})$. The theorems of Hohenberg and Kohn [78] do not include practical instructions for this task. An expression for E_e with regard to the electron density $\rho(\vec{r})$ and as a sum of single energy contributions may be

$$E_e = T[\rho] + V_{e-n}[\rho] + V_{e-e}[\rho] = T[\rho] + V_{e-n}[\rho] + J[\rho] + E_{xc}[\rho], \tag{6.26}$$

with $\rho = \rho(\vec{r})$. $T[\rho]$, $V_{e-n}[\rho]$ and $V_{e-e}[\rho]$ are the kinetic energy of the electrons, the energy of the electron-nuclei interaction and energy of the electron-electron interaction, respectively. $V_{e-e}(\rho)$ is a sum of the Coulomb $J[\rho]$ and exchange-correlation energy $E_{xc}[\rho]$. Simple analytical formulas, derived from classical physics, can be found for $V_{e-n}[\rho]$ and $J[\rho]$, but not for the quantum-mechanical quantity $E_{xc}[\rho]$ [75]. Also for the kinetic energy of the electrons $T[\rho]$ a suitable expression for an inhomogeneous charge distribution, as in molecules or atoms, can not be found. The Thomas-Fermi method [76, 77] provides an expression for the kinetic energy, but solely for a homogeneous electron gas.

The idea within the Kohn-Sham (KS) method [79] is to assume the existence of a model system of uncharged, non-interacting quasiparticles, which move in an external potential. This model system has the same number of particles N and the same ground-state density/energy as the corresponding real system [75, 79]. The latter consists of charged, interacting electrons and nuclei. As in the case of the HF approach, the ground-state of the model system can be described with a single Slater determinant (see equation 6.5). Here, the determinant includes the one-electron wavefunctions $\psi_k^{\mathrm{KS}}(\vec{r})$. They are called Kohn-Sham orbitals [75] and are different from the single-particle functions of the Hartree-Fock method [80]. The model system's ground-state density [79] can be expressed as

$$\rho(\vec{r}) = \sum_{k=1}^{N} e \left| \psi_k^{\mathrm{KS}}(\vec{r}) \right|^2. \tag{6.27}$$

The introduction of the orbital picture into the density-based methods makes it more convenient to set up suitable expressions for the different energetic contributions of equation 6.26. The kinetic energy for example reads:

$$T_{qp}[\rho] = \sum_{k=1}^{N} \left\langle \psi_k^{\mathrm{KS}} \right| - \frac{\hbar^2}{2m_e} \Delta \left| \psi_k^{\mathrm{KS}} \right\rangle, \tag{6.28}$$

with the index *qp* denoting that the kinetic energy term in equation 6.28 refers to non-interacting, uncharged quasiparticles. The difference to the kinetic energy of the real system $T[\rho]$ (equation 6.26) due to the interaction between the electrons is included in another term and will be discussed below. Similar to HF the Coulomb energy $J[\rho]$ within the KS approximation is [81]:

$$J[\rho] = \frac{1}{2} \sum_{k=1}^{N} \sum_{\substack{l=1 \\ l \neq k}}^{N} \left\langle \psi_k^{\mathrm{KS}} \psi_l^{\mathrm{KS}} \right| \frac{e^2}{4\pi\epsilon_0 r_{ij}} \left| \psi_k^{\mathrm{KS}} \psi_l^{\mathrm{KS}} \right\rangle. \tag{6.29}$$

The functional $E_{xc}[\rho]$ that describes the energetic contributions arising from the exchange and correlation interaction between the electrons can be written as [81]

$$E_{xc}[\rho] = (T[\rho] - T_{qp}[\rho]) + (V_{e-e}[\rho] - J[\rho]), \tag{6.30}$$

with $T[\rho] - T_{qp}[\rho]$ describing the difference in the kinetic energy, when comparing the real system to the model system of quasiparticles. The second difference term, $V_{e-e}[\rho] - J[\rho]$, represents all the electron-electron interactions that are not taken into account by the Coulomb energy $J[\rho]$. Remembering that there are no interactions between the particles of the KS model system, but instead the existence of an external potential is assumed, the total energy is [81]

$$E_e[\rho] = T_{qp}[\rho] + J[\rho] + E_{xc}[\rho] + \int V_{ext}(\rho(\vec{r}))\rho(\vec{r})d\vec{r}, \tag{6.31}$$

with the external potential $V_{ext}(\rho(\vec{r}))$ acting on the system of quasiparticles. The aim is now to define this potential in such a way that the orbitals $\psi_k^{\mathrm{KS}}(\vec{r})$ minimize the energy functional $E_e[\rho]$ under the constraint that the correct density and energy are obtained. This can be achieved by applying the variational principle to $E_e[\rho]$ in consideration of the orthonormality of the KS orbitals [75]. This gives the KS equations

$$\hat{h}_{eff} \psi_k^{KS}(\vec{r}_i) = \epsilon_k^{\mathrm{KS}} \psi_k^{\mathrm{KS}}(\vec{r}_i), \tag{6.32}$$

by which the KS orbitals $\psi_k^{\mathrm{KS}}(\vec{r}_i)$ and their energies ϵ_k^{KS} are determined. Hence, the electron density that minimizes $E_e[\rho]$, is determined, too. The effective single-particle operator $\hat{h}_{eff}$ of equation 6.32 takes the following form [75]

$$\hat{h}_{eff} = -\frac{\hbar^2}{2m_e}\Delta_i + V_{eff}(\vec{r_i}), \tag{6.33}$$

where the first term represents the kinetic energy operator and the second term is an effective potential. $V_{eff}(\vec{r_i})$ can be further separated into [75]

$$\begin{aligned} V_{eff}(\vec{r_i}) &= V_{ext}(\vec{r_i}) + V_c(\vec{r_i}) + V_{xc}(\vec{r_i}) \\ &= -\sum_{\alpha=1}^{M} \frac{Z_\alpha e}{4\pi\epsilon_0 r_i} + \sum_{\substack{l=1 \\ l\neq k}}^{N} \left\langle \psi_l^{\mathrm{KS}} \middle| \frac{e^2}{4\pi\epsilon_0 r_{ij}} \middle| \psi_l^{\mathrm{KS}} \right\rangle + V_{xc}(\vec{r_i}) \end{aligned} \tag{6.34}$$

with $V_{ext}(\vec{r_i})$, $V_c(\vec{r_i})$ and $V_{xc}(\vec{r_i})$ being the external, the Coulomb and the exchange-correlation potential, respectively. Here it is assumed that $V_{ext}(\vec{r_i})$ originates solely from the electrostatic field of the nuclei. The form of the exchange-correlation potential $V_{xc}(\vec{r_i})$ is not known [81] and for practical applications approximations are used. In most cases this is sufficient, due to the comparatively small size of the exchange-correlation effects.

Writing down the KS equations in detail

$$\left[-\frac{\hbar^2}{2m_e}\Delta_i + V_{ext}(\vec{r_i}) + V_c(\vec{r_i}) + V_{xc}(\vec{r_i})\right]\psi_k^{\mathrm{KS}}(\vec{r_i}) = \epsilon_k^{\mathrm{KS}}\psi_k^{\mathrm{KS}}(\vec{r_i}) \tag{6.35}$$

and also recapitulating the HF equations of equation 6.14

$$\left[-\frac{\hbar^2}{2m_e}\Delta_i + V_{n-e}(i) + \sum_{\substack{l=1 \\ l\neq k}}^{N} J_l(i)\right]\psi_k(i) - \left[\sum_{\substack{l=1 \\ l\neq k}}^{N} K_l(i)\right]\psi_l(i) = \epsilon_k\psi_k(i), \tag{6.36}$$

similarities and differences between the two methods can be noticed. While the Coulomb potential $V_c(\vec{r_i})$ in equation 6.35 corresponds to the sum of of the Coulomb operators $\hat{J}_l$ of the HF equations 6.36, the difference lies in the treatment of the exchange-correlation interactions. Within the KS approach these effects are included in the unknown potential $V_{xc}(\vec{r_i})$ (fourth term in equation 6.35). The HF method neglects the correlation effects, but an explicit formula for the exchange operator $\hat{K}_l(i)$ is available (fourth term in equation 6.36).

One of the biggest challenges within DFT is to find suitable approximations for the exchange-correlation potential $V_{xc}(\vec{r_i})$. Besides the local density approximations (LDA), where $V_{xc}(\vec{r_i})$ is just a function of the electron density $\rho(\vec{r_i})$ at point r_i in position-space, more advanced gradient-corrected approaches have been developed [81]. These methods take into account that the electron density $\rho(\vec{r_i})$ varies spatially and therefore the exchange-correlation potential also depends on the gradient of the electron density.
As for $\hat{J}_l$ in the HF equations 6.36, the Coulomb potential $V_c(\vec{r_i})$ of equation 6.35 depends on the sought solutions $\psi_k^{\mathrm{KS}}(\vec{r_i})$ (see equation 6.34). Therefore an iterative, self-consistent procedure is applied to solve the KS equation 6.35 [79]. Furthermore the KS orbitals are expanded into sets of basic functions. Thereby the KS equations are transformed into secular eigenvalue equations that are solved iteratively to determine the linear combination coefficients. Despite the fundamental differences of the theoretical methods, recurring principles and practical applications are met throughout quantum chemistry.
At the end of an iteration step, the total energy $\mathrm{E_{tot}}$ of a system for a certain nuclear arrangement can be calculated according to the following expression,

$$E_{\mathrm{tot}}[\rho] = \sum_{\substack{\alpha\beta \\ \beta>\alpha}} \frac{Z_\alpha Z_\beta e^2}{4\pi\epsilon_0 R_{\alpha\beta}} + \sum_k n_k \left\langle \psi_k \middle| -\frac{\hbar^2}{2m_e}\Delta_i + v_{ext}(\vec{r_i}) + \frac{1}{2}\int \frac{e^2\rho(\vec{r_j})}{4\pi\epsilon_0 r_{ij}} dr_j \middle| \psi_k \right\rangle + E_{xc}[\rho], \tag{6.37}$$

where the first term is the repulsive potential between the nuclei α and β of the system, with Z_α, Z_β, and $R_{\alpha\beta}$ being the charge of nucleus α, the charge of nucleus β and the internuclear distance, respectively. The quantity n_k is the occupation number of the kth KS orbital. The remaining terms represent the electronic energy according to the KS approach.

7 Global optimization: basic principles and problems

7.1 Global energy optimization: the potential energy surface

The structural-energetic GO usually refers to the search for the geometric global energy minimum of a system, e.g. the energy minima of alkali clusters within this thesis, whose size and/or composition is predefined [82]. The central question is, which arrangements of atoms gives the lowest total energy? In this context some basic principles of energy minimization have to be discussed.

Within the BO approximation (section 6.1) the nuclei of a quantum mechanical N-electron system are treated as fixed, classical particles [55]. The electronic energy $E_e(\vec{R})$ of this system can be obtained by solving the resulting electronic Schrödinger equation via one of the aforementioned approximated methods (section 6). Thereby $E_e(\vec{R})$ exhibits a parametrical dependence on the nuclear position-space coordinates $\vec{R}$: for different nuclear arrangements different electronic energies result. The total energy of a system, consisting of M nuclei, is

$$E_{\text{tot}}(\vec{R}) = E_e(\vec{R}) + \sum_{\alpha=1}^{M} \sum_{\substack{\beta=1 \\ \beta>\alpha}}^{M} \frac{Z_\alpha Z_\beta e^2}{4\pi\epsilon_0 R_{\alpha\beta}}. \tag{7.1}$$

E_{tot} as function of the nuclear coordinates $\vec{R}$ gives the so-called potential energy surface (PES) or potential energy hypersurface, the chemical search space that has to be investigated. Here, the energy can be imagined as a continuous function of the nuclear position-space coordinates. In principle, the coordinates $\vec{R}$ are able to adopt any value and therefore the PES is a continuous search space. A visualization of a section of some PES is depicted in figure 7.1.

The mountains on this surface represent atomic arrangements of higher energy values and are highlighted in red via a colour gradient. Structural-energetic minima correspond to valleys on the surface and are coloured blue. The position-space coordinates of the atoms that constitute the system under consideration can in principle adopt any value on this surface, leading to a continuous optimization problem. An infinitesimal or small shift of the nuclear coordinates basically may lead to “another” structure, although in

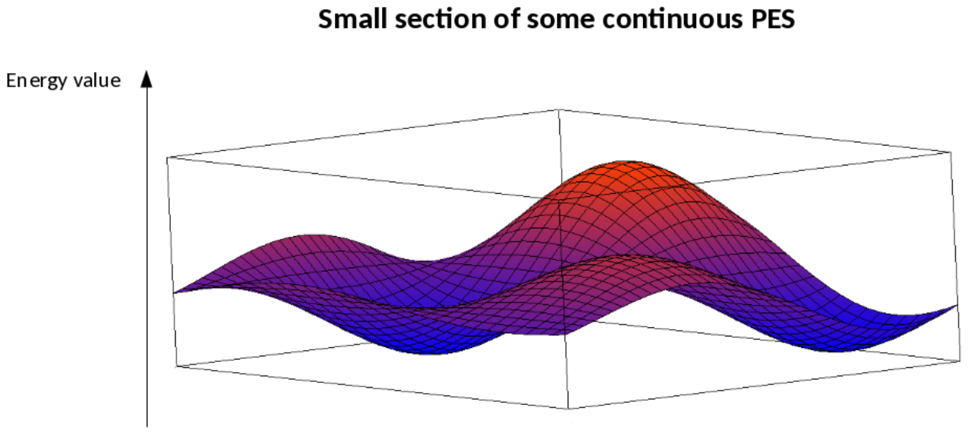

Figure 7.1: Section of some continuous search space, as it exists within the structural-energetic optimization of clusters with the atomic position-space coordinates as continuous variables. Mountains and valleys on the surface represent energetic maxima and minima, respectively. The colour gradient used, ranges from low energy values (blue) to large energy values (red).

many cases very small changes within the atomic arrangement do not affect the electronic structure of the system. Nevertheless, these slightly different position-space coordinates could be adopted. The GO of the Li and Na clusters, described in part II of this thesis, is such a continuous optimization task.

The principle of the PES dates back to the 1930s, where Eyring and Polanyi used it to describe reactions between gases [83]. In this connection they calculated the energy resulting from the interaction between the reactands with respect to the distances among the participating chemical species, e.g. for the reaction of H with Br_2. Apart from the identification of transitions states and reaction pathways by using the PES, the question within structural energy minimization is: which atomic arrangement leads to the lowest total energy and to a minimization of the forces acting on the atoms of the structure? That structure with the lowest total energy represents the ground-state global minimum structure of that system on the ground-state hypersurface. Furthermore the excited states of a system are described with an excited-state energy surface.

As mentioned above a PES is a multidimensional object. A non-linear system with M nuclei gives a $(3M-6)$- and a linear one a $(3M-5)$-dimensional PES. Due to the high dimensionality even for medium-sized systems, a crucial issue in computational chemistry, is the so-called NP-hard problem. There is no underlying polynomial growth [84, 85]: the increase in the number of possible non-equivalent energy minima on the

PES with increasing system size is exponential. Therefore locating the overall lowest energy minimum, i.e. carry out a global optimization, is a huge challenge. For instance, using the simple Lennard-Jones (LJ) potential to describe the interatomic interactions, there are not less than 10^{10} different minimum structures for a 55-atom cluster [82]. This is a huge amount of possible geometrical arrangements of lower energy. But, however, the properties of the PES, i.e. its shape or topography, play a pivotale role in identifying the global minimum structures [82]. For example, the existence of many "convergent pathways" [86] towards the global minimum on a PES faciliates the identification of the GEM. In contrast, one may easily be trapped in a local minimum, if there are several pathways that are divergent, i.e. that lead to different minima on the PES [86]. In spite of the large number of minima for the LJ-cluster with 55 atoms, determining the GEM is quite easy for this cluster size [82]. But this is not the case for many other cluster sizes, where the structure of the PES complicates the identification of the GEM and therefore efficient GO algorithms are essential [82]. In order to solve the global optimization problems such algorithms are used to investigate a PES. Scanning the entire hypersurface is not feasible, even for smaller systems. To prevent a random, time-consuming screening of the whole hypersurface, these algorithms use information of the characteristics of the surface and by which means a more targeted study on certain interesting areas of the PES can be performed, i.e. the stationary points, the minima and maxima of the function to investigate. Of particular interest are the minima on the PES and according to the mathematical expression for the optimization principle of reference [87] a corresponding formulation for an energy minimization operation f_{ener} would be

$$f_{\mathrm{ener}} = \min_{\vec{R}_1,\vec{R}_2,\cdots} \{\hat{E}[\hat{\mathbf{H}}[\vec{R}_1,\vec{R}_2,...,\vec{R}_M]]\}, \tag{7.2}$$

where the Hamiltonian $\hat{H}$ is a functional of the nuclear coordinates $\vec{R}_\alpha$. The observable $\hat{E}$, representing the energy of the molecule, is a functional of $\hat{H}$ and *min* is an operation, denoting a minimization procedure. Here, we search for that atomic arrangement, i.e. that set of atomic coordinates $\vec{R}_\alpha$, which gives the lowest energy for a system with M nuclei (atoms).

7.2 Global property optimization: the property hypersurface

A specific issue within GO is the optimization of materials' properties different from the energy, e.g. the HOMO-LUMO gap and visible light absorption of solar cell materials or the adsorption properties of surfaces. Hereafter the theoretical background regarding the GPO is described.

Similar as in the case of the PES within the energetic optimization, one tries to find structures with optimal property values on a property hypersurface. Here the hypersurface represents "property-structure relationships" [87] and in analogy to the energy minimization problem discussed in section 7.1 the property optimization task [87] could be defined as

$$f_{prop} = \min_{\lambda_1,\lambda_2,\cdots} \{\hat{P}[\hat{\mathbf{H}}[\lambda_1, \lambda_2, ..., \lambda_n]]\} \tag{7.3}$$

and

$$f_{prop} = \max_{\lambda_1,\lambda_2,\cdots} \{\hat{P}[\hat{\mathbf{H}}[\lambda_1, \lambda_2, ..., \lambda_n]]\}. \tag{7.4}$$

Eqs. 7.3 and 7.4 denote a property minimization and a property maximization, respectively. $\hat{P}$ is an observable that describes the sought property. It is functional of the Hamilton operator $\hat{H}$, which in turn is a functional of the parameters λ_i. The goal is to vary the parameters λ_i and to yield a Hamiltonian $\hat{H}$, which optimizes the property $\hat{P}$. Equation 7.3 is a general representation of a property minimization, e.g. the search for a HOMO-LUMO gap, which is as small as possible. On contrast equation 7.4 describes a maximization procedure, such as finding a maximum value for sunlight absorption of solar cells. Within property optimization the parameters λ_i often are indices describing the composition of the investigated system. The indices can represent atom types, molecular fragments but also defects within the system. In this case the variable parameters often are not continuous like the positions-space coordinates as within the structural energetic minimization problem discussed in section 7.1. Instead they adopt discrete values and the property optimization issue is a discrete problem of the order T^s, i.e. T^s different structures exist for that system (neglecting symmetry). T is the number of different atom types or types of molecular fragments that are considered within the calculation and s is the number of different sites they can occupy within the structure. For example for a 20-atomic cluster consisting of silver and gold atoms 2^{20} different structures exist. In contrast to the GEO described in section 7.1 there exists no NP-hard problem for

such a discrete Inverse Design task.
A certain type of chemical group is located at a certain position or not. Here, it is not possible that a position is occupied by 0.3 of the chemical fragment A and 0.7 of group B. There is either 1.0 of A and 0.0 of B at a position or 0.0 of A and 1.0 of B at a position. But Inverse Design studies are not necessarily performed within discrete search spaces. The LCAP (linear combination of atomic potentials) method for example can be performed either within a discrete [88] or a continuous search space [89]. Figure 7.2 depicts a small section of some discrete search space for property optimization, as it also exists for our PooMa approach used within this thesis.

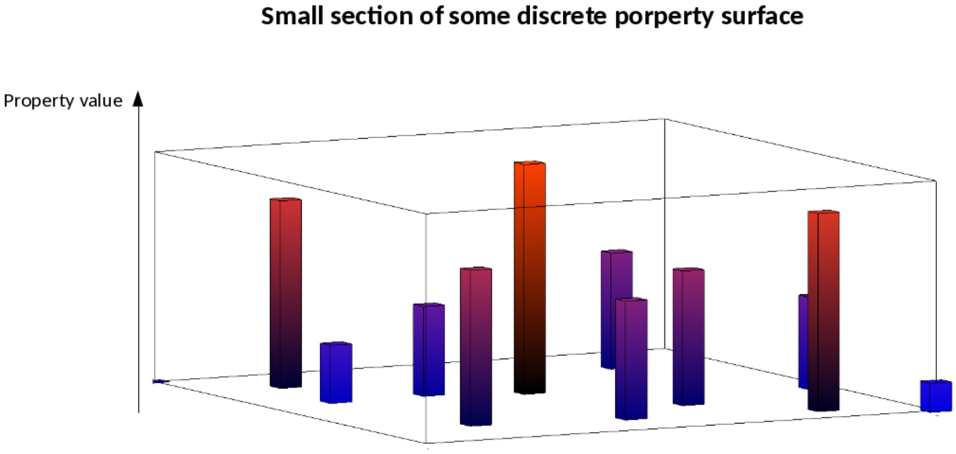

Figure 7.2: Section of some discrete property search space, as it exists for property optimizations based on a variation of discrete variables, e.g. compositions. A single bar represents one certain composition and the height represents a certain property value. A high and a low bar correspond to a large and a small property value, respectively. The colour gradient ranges from blue (small property value) to red (large property value).

The variation that is introduced within the system of interest is a variation of discrete variables (e .g. composition), therefore there is no continuous surface as for the structural-energetic optimization of section 7.1 (see Figure 7.1), but instead the search space can be understood as consisting of bars. Each of the bars represents a different structure, e.g. composition of a system, and only these structural values can be adopted by the system, since values in between have no physical or chemical meaning. Such an unphysical structure may contain something like 0.7 times atom type A and 1.9 times atom type B and so on. The height of a bar represents the size of the property value of this structure. A higher bar corresponds to a larger property value and vice versa, which is additionally highlighted by a colour gradient in Figure 7.2.

As mentioned above structural values in between the different bars do not describe a realistic chemical system, but ID approaches as the LCAP, make use of such "alchemical" structures. Here, the actually discrete search space is transformed into a continuous one [32, 89, 90], where also physically and chemically unrealistic compositions of structures are possible upon optimization, which is finally "corrected", e.g. via rounding a non-integer composition up to the next-nearest integer. Thereby a chemically and physically meaningful structure is obtained. Thereby the optimization is guided by property gradients [89]. The discrete version of the LCAP approach does not consider alchemical structures and it uses property gradients in order to "jump" to positions on the property hypersurface, representing real molecules [88].

7.3 Global and local optimization techniques

7.3.1 Local optimization techniques

Regardless of which optimization problem has to be solved, the use of efficient and sophisticated optimization procedures is fundamental. In general, a distinction has to be made between local and global optimizations. A local optimization is the search for an optimum within a spatially limited area, i.e. it is the task of finding the optimal value within several neighbouring values. The nearby values are larger (minimum search) or smaller (maximum search) than the optimum or in both cases some of them can also be equal to the optimal value. In the latter case one speaks of degenerate local minima. For instance, a given molecular structure can be optimized locally with respect to its interatomic distances, bond angles etc., so that the forces, acting on each atom, are lowered. Among several possible neighbouring geometries, which differ in some structural parameters that one is identified, which exhibits the lowest energy. In contrast, a GEO is the search for the overall energy minimum within the whole search space, i.e. the purpose is to identify the global energy minimum. Among all locally optimized systems (e.g. of same size and/or composition) that one with the lowest energy value is identified. Within the investigations of alkali metal clusters in part II local and global structural-energetic optimizations are combined. The applied GO procedure includes the local optimization of single systems. Each single cluster is optimized locally and among all the locally relaxed cluster structures that one with the lowest total energy is identified. The same applies to the GPO, discussed in part III, where the goal is to identify that structure within the whole search space, which exhibits the optimal property value. Also here, each chemical system is optimized locally concerning its structural parameters and among all locally relaxed structures that one is sought, that posseses the optimal performance concerning a property different from the total energy. Also for this GPO local optimizations are of fundamental importance. According to eqs. 7.3 and 7.4 in section 7.2 the property to calculate depends on the Hamiltonian and the Hamiltonian depends on structural parameters of the chemical system. The local optimization should yield a structure with realistic interatomic distances and bond angles. A well optimized structure is an indispensable condition to obtain a reliable description of the systems' properties. Without having identified the local energy minimum of a structure, a calculated property value may not be meaningful and trustworthy.

Concerning the algorithms used for local relaxations, GEOs and GPOs, as performed within this thesis, do not fundamentally differ. A vast amount of algorithms exists to adress this issue. What they all have in common is the basic principle of finding a minimum for a function f. In the case of local geometry optimization the function f is the total energy of a molecule or an other chemical system. The argument x is represented by the position-space coordinates of the atoms. Some of these optimization algorithms, like steepest descent or conjugate gradient approaches, use the gradient of the function to be optimized. For example, within the steepest descent method [91], the atoms are moved along the forces that act on them. The force is the gradient of the total energy with respect to the position-space coordinates. Other methods, so-called *Newton* approaches additionally make use of the second derivative as information on the characteristics of the PES [92]. In this thesis several local optimization techniques are applied, e.g. a *quasi-Newton* algorithm [92], the steepest descent [91] and the conjugate gradient [93] method. A detailed description of these approaches can be found in the corresponding chapters.

7.3.2 Global optimization techniques

Among the locally optimized structures, the global energy minima or the global property optima are identified via a GO algorithm. As for the local optimizations a large variety of approaches exists, which makes it impossible to explain all of them in detail. A generalized, simplified flowchart for a global optimization procedure is depicted in figure 7.3. Depending on the used GO algorithm this procedure may become arbitralily complex and the scheme in figure 7.3 would have to be adjusted accordingly. The single steps shown in this simplified figure may differ more or less from the actual procedures of the applied optimization methods. But the main principles are included and should give an idea about the general functioning of the GO procedures used within this thesis.

A GO begins with an intitialization, e.g. the setting up of parameters and reading in of input parameters. Some counting variable k is set to its initial value. In some way

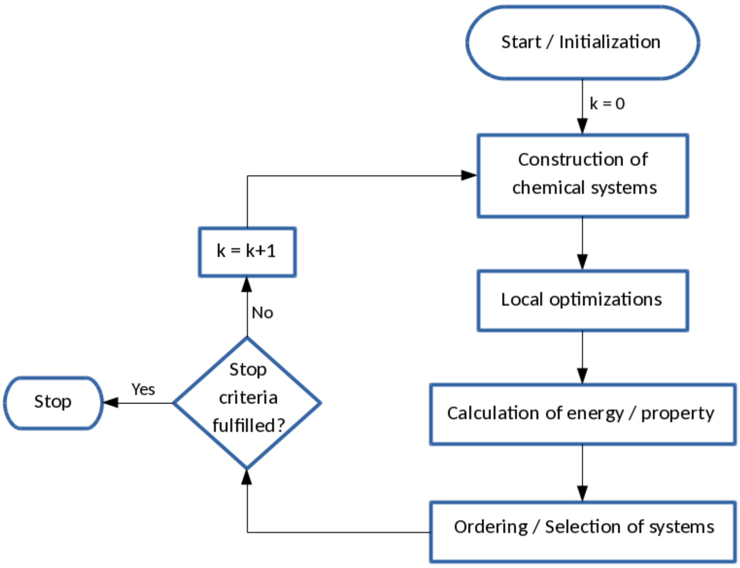

Figure 7.3: Generalized workflow of GO procedures as used within this thesis. Each of the elements depicted is a fundamental part of the used GOs, but the details and the complexity of the different algorithms vary.

or other the chemical systems that are supposed to be investigated, are constructed. Subsequently these systems are relaxed locally, e.g. by one of the algorithms mentioned in the previous section 7.3.1. The total energy of each the systems is calculated and, in case of a property optimization, the corresponding property values are determined. Then, the systems are ordered according to their energy or property value and some procedure is used to select the promising candidate structures. Afterwards it is checked whether predefined stop criteria (or a single stop criterion) are (is) fulfilled. If this is the case, the GO is stopped. Otherwise the algorithm continues and the counting variable k is increased by one. The next step of the GO procedure starts with the construction of new systems, which are again subjected to local relaxations and a subsequent property / energy calculation. The whole procdedure is repeated until a predefined termination criterion has been reached.

One quantity, which has always been used to describe the quality of a global optimization algorithm is the number of function evaluations, which are needed to identify the global optimum [94]. How many structures have to be investigated until this optimum is obtained? Here, the problem arises that it is usually not certain that the global optimum has been found, i.e. there is no universal criterion, which guarantees its identification and the convergence of the GO algorithm. As described above, some stop criteria have to be defined, which specify the end of a global optimization procedure. In doing so, it can only be assumed that the global optimum was obtained. Therefore one may also talk of putative global optima.

Another challenge met in the field of global optimization is the choice of the theoretical method, which is used to model the interactions between the particles within the chemical structures. In order to find the global optimum a huge amount of chemical systems have to be optimized locally. Therefore one local relaxation should not take too much time. Accurate, but computationally expensive approaches like the HF or beyond-HF methods (sections 6.2.1 and 6.2.4) are normally not suitable for a GO task. Also DFT methods (section 6.3) are only feasible, if using a very small (minimal) basis set within the KS approach. Therefore, simpler, faster, but less accurate theoretical methods are used for GO problems. Applying these models, one has to take the deficiencies of the corresponding method into account, especially, when examining and interpreting the results of the calculations. The theoretical approaches employed in this thesis are described in detail in the corresponding sections. The interactions between the atoms of the alkali clusters are modeled by a simple potential, the MEAM (see section 9.1), and the DFTB method (see sections 12.2.1 and 13.3.1) is used to describe the electronic structure of the systems within the property optimization studies.

Global energy minima of clusters: algorithms

In order to identify the global energy minima of clusters frequently applied GO algorithms are simulated annealing [95, 96, 97], basin hopping [98, 99, 100], genetic algorithms (GA) [94, 101, 102] or particle swarm optimizations [103, 104]. An approach, specifically designed for the GO of clusters, is the *Aufbau-Abbau* algorithm. This approach was developed in our working group by V. Grigoryan and M. Springborg. It has been applied succesfully to the global optimization of several metal clusters, for instance Ni [105] and Cu clusters [106]. It is also used for the GEO of alkali metal clusters in this thesis.

In principle, the *Aufbau-Abbau* algorithm combines a random and regular search for cluster structures. Initially, for each cluster size N, so-called random calculations are performed. Within a calculation each cluster is generated randomly and subsequently it is relaxed to its local energy minimum. A certain, predefined number of clusters is calculated until the program stops (stop criterion) and the best, energetically lowest-lying structures of this cluster size N are kept. These "best" isomers serve as input structures for the *Aufbau* and *Abbau* calculations. Within an *Abbau* calculation a low-lying cluster of size $N + 1$, obtained from the random calculations for cluster size $N + 1$, is used to create clusters of size N. This is done by removing successively each of the atoms of the cluster with $N+1$ atoms. Each time an atom is removed, a cluster with N atoms is obtained, which is optimized locally. Again, the best performing clusters, i.e. the most stable ones, are kept. For an *Aufbau* calculation a cluster of size $N-1$ is used as input to create N atomic clusters. To the structure with $N-1$ atoms one atom is added randomly and a N-atom cluster is obtained. This cluster is also relaxed locally. The procedure is repeated many times and again, the lowest-lying isomers of cluster size N are kept. The most-stable clusters obtained from the random, the *Aufbau* and *Abbau* calculations are compared and the lowest-energy isomers are identified. The *Aufbau* and *Abbau* calculations may be performed until no new lowest-lying isomers for a certain cluster size are found. In practice, in an *Aufbau* or an *Abbau* calulation, always a predefined number of clusters is calculated until the program stops and convergence is assumed.

Here, just a rough overview of the *Aufbau-Abbau* algorithm is given. This procedure can be designed arbitralily complex and extensive. A detailed description of the procedure that was used for the GO of the alkali clusters in this thesis can be found in section 9.2.

Global property optima: algorithms

A key challenge in a GPO is to find structures on the hypersurface that have optimal property values, since in the most cases, the variable parameters (see eqs. 7.3 and 7.4) exhibit no simple relationship with the sought property $\hat{P}$ [87]. As explained in the previous section, one can distinguish between property optimizations within a discrete or a continuous search space. A prominent example for approaches using discrete chemical structures are genetic algorithms (GA). GAs have found wide application in the optimization of properties [32, 107, 108, 109]. Further discrete methods are best first search [90, 110], the dead-end elimination algorithm [90, 111, 112] or the Monte Carlo optimization [8, 113, 114]. The LCAP approach, introduced before, uses a property gradient to screen continuous or discrete search spaces [50, 88, 89, 115]. Again, the explanation of the various algorithms is beyond the scope of this work and we limit the short discussion below to the genetic algorithms, since we also use this kind of optimization procedure for the global optimizations within our PooMa method.

A GA is a type of evolutionary algorithm, based on populations, which was developed in the 1960s and 1970s [87, 116, 117]. The basic idea of GAs is the incorporation of concepts of Darwinian biological evolution into optimization algorithms [32, 87]. Today they belong to the standard optimization methods in materials design [32, 101, 102, 107, 108]. Examples include the study of Collins *et al.*. They optimized the CO_2 uptake of metal-organic frameworks (MOFs) [109] and used a GA for varying the functional groups inside the pores of the MOFs. A GA has also been applied by Froemming and Henkelman to investigate the catalytic properties of bimetallic core-shell nanoparticles [118]. Here, various combinations of transition metals have been optimized with respect to the reduction of oxygen.

Generally within a GA an initial population of chemical structures (candidates) is created randomly. This is followed by a local relaxation and the calculation of the performance function (property) for each structure. This initial population (parents) is then subjected to different operations, where the parents are recombined or mutated to form new candidate structures (children). The children are locally optimized and theirs fitness functions are evaluated, too. Out of the parents and children, a certain number of structures is selected that serve as parents to form the next generation of children. The selection can be made according to various criteria. But the primary and overarching objective is to keep that structures with the best property values in order to optimize a predefined property. This whole procedure is repeated until a predefined abort criterion is fulfilled. In more detail, the main elements of a GA are:

1. The encoding method. Usually, the chemical structures are encoded within a GA. This can be accomplished in various ways, e.g. by the use of binaries [87, 119] or integers [52]. With regard to biological concepts, a structure may be imagined as a chromosome and a single integer or binary may be thought of as a gene. Thereby a certain gene (integer or binary) represents a certain atom, functional group or any other physical/chemical object. Furthermore there are real-coded GAs [120], using real numbers as representation for the genes (chemical groups).

2. The fitness function. It describes the performance of each candidate structure. Within a GPO it represents the property to be optimized, whereat this property is a function of the genes (chemical groups) of each chromosome (structure). Because a large number of structures has to be evaluated within an unbiased GPO an important issue is to have a simple mathematical description of the property to be investigated. This also includes the need for approximations in order to reduce the computing time.

3. The selection process. Out of the candidate structures of the previous generation (parents) and current generation (children) a particular number of structures is selected. These form the parents for the subsequent generation. A large number of different selection procedures exist [119, 121]. For instance, it is possible to select only a certain number of candidates, for example those with the best performance.

Or the selected structures may also include some randomly chosen candidates to introduce more variability into the algorithm [87]. Furthermore, there is the so-called Roulette Wheel method, where the probability for a structure to be selected is proportional to its performance [119].

4. The recombination operations. Genes (chemical groups) are exchanged between parent structures. The most simple and most widely used recombination process is the one point crossover operation. A random point within two parents is chosen and the parents are cut at this position. The equally sized parts are swapped and thereby genetic information (chemical groups) is exchanged between the two parents. New structures (children) are formed. Well-performing structural parts of the parents are combined for the purpose of generating even better performing children that incorporate good genes (chemical groups) of both parents. There are also GAs that use a certain probability to decide whether a recombination between two parents takes place or not [119]. Moreover, also multiple point crossover operations are possible and a many other recombination procedures [119].
5. The mutation operations. Genes (chemical groups) within children may be mutated. One simple mutation process is the substition of one gene by another one, e.g. the exchange of an atom type at a certain position into another atom type. Also for mutation operations many different possibilities exist [101, 122]. Mutations increase the diversity within a population and may prevent a premature convergence, so that the algorithm does not get caught in a local optimum [123]. At the same time, it has to be considered that the mutation rate should not be too large, because this may lead to a slow convergence with too much randomization counteracting the basic idea of a GA [87].
6. Convergence criteria. Termination criteria have to be chosen, but it is not possible to define any criterion that guarantees that the global optimum has been identified. So one has to make a decision when convergence of a GA can be assumed. Therefore different stop criteria have been developed and used in GAs [119, 124]. For instance, a GA may stop if a predefined maximum number of generations has been calculated or some predefined criteria are met by the structures of a population [119].

GAs are widely used optimization algorithms. Hence, a huge variety of procedures exist that differ more or less from each other. A more comprehensive description would go beyond the scope of this thesis. In the discussion above only the main ideas of this type of algorithms should be outlined. The details concerning the GAs used for the

GPOs within this thesis can be found in sections 12.2.2 and 13.3.2 of the corresponding chapters.

Part II

Global energy optimization of Li and Na clusters

8 Introduction

Clusters are nanoparticles that can be made of up to 1 to 10 billion atoms or molecules [35]. Due to the increasing demand for miniaturization in technological devices, nanoscience is a popular field of research. In order to manipulate chemical systems on the nanoscale a thorough understanding of the behaviour of nanoparticles on the atomic level is required. Clusters exhibit size-dependent properties, which are different from the bulk material. Therefore, the investigation of the clusters' properties with varying cluster size N is basic research, whereat theoretical and experimental studies complement each other [35, 37].

Alkali metal clusters belong to the most intensively studied types of clusters. One reason for this is that they posses a rather simple electronic structure with one valence electron per atom, which is why they are used as model systems to test theoretical methods [125]. But alkali clusters are also of practical importance: for example the formation of Li clusters within Li-ion batteries can lead to malfunctions [126] or the redox potential of Li clusters may be used for advanced battery technologies [127].

The measurement of mass abundance spectra by Knight *et al.* [128, 129] revealed interesting aspects regarding the size dependent stability of alkali clusters. Clusters with a certain number of atoms N, i.e. $N = 2, 8, 20, 40$, occur more frequently, indicating a higher stability of these sizes. This phenomena is explained via electronic effects, where clusters with a number of valence electrons corresponding to electronic shell closings, exhibit a especially high stability. These cluster sizes are called electronic magic numbers. Theoretical predictions via the spherical jellium model [130, 131, 132] verify these findings. But this is only true for closed-shell clusters, whereas for so-called open-shell clusters, with a number of valence electrons different from electronic shell-closings, a reduced stability and a lower abundance in mass spectra is observed. According to the Jahn-Teller theorem these open-shell systems distort and as a consequence they can not be described using the spherical jellium approach [37, 133], but for instance with the more advanced ellipsoidal Clemenger-Nilsson shell model [134]. For larger Na cluster sizes, with the number of atoms $N > 2000$, peaks of high intensity appeared in abundance mass spectra, which can be explained by geometrical shell closings [135]. The adoption of certain geometries with a large volume-to-surface ratio (e.g. icosahedra), enhances the stability due to an increase of the average coordination number and a decrease of the surface energy of the cluster [35]. According to the electronic magic numbers, these geometrical stabilized clusters are called geometrical magic numbers. Magic numbers, based on icosahedra or decahedra for example can posses N = 13, 55, 147, 309, 561, 923, 1415, 2057, ... atoms [135]. In experiments, it was discovered that for hot, liquid clusters electronic shell effects are present, whereas for cold and solid clusters geometrical magic numbers are observed [136, 137]. But often this distinction is not very clear and, for smaller cluster sizes, an interplay between electronic and geometrical effects can be identified [136]. Both types of effects have been disvovered for a huge number of different cluster types and not only for alkali clusters [35, 136].

A large variety of properties of alkali clusters (and of course of clusters in general) are of scientific interest. These include the polarizability [138, 139, 140], optical [141, 142, 143], thermal [144, 145, 146] or magnetic properties [147, 148]. As mentioned before, in many cases experiments are not sufficient to fully understand and to explain certain phenomena in cluster science. But the prediction of the alkali clusters' properties via theoretical calculation is only reliable, if the geometries of the clusters have been identified accurately. Hence, a lot of effort has been put into the application of computational methods to alkali clusters and the determination of their structural-energetic minima. More advanced levels of theory as *ab initio* methods [149, 150, 151] (section 6.2) as well as DFT studies [152, 153, 154] (section 6.3) and simpler, computationally less demanding model potentials [155, 156] have been used for structural-energetic optimizations of alkali clusters. An unbiased structural-energetic GO can only be performed using a simple description of the interactions between the atoms in order to reduce computational time and to faciliate the extensive investigation of the huge search spaces. This has already been performed within several studies. Tevekeliyska *et al.* used a density-functional tight binding approach to identify global energy minima of Na clusters with up to 20 atoms [157]. As GO procedure a genetic algorithm was chosen. Within the same work Na clusters with up to 60 atoms have been optimized, whereat the embedded atom method (EAM) was combined with the *Aufbau-Abbau* algorithm [157]. In 2011 Kostko *et al.* performed a GO for neutral and anionic Na_N clusters ($N \leq 80$) with a Gupta (G) potential and an unbiased basin hopping optimization [156]. Two model potentials, namely Murrell-Mottram (MM) and Gupta, have been applied to Na clusters with up to 380 atoms, also in combination with the basin-hopping approach [155].

Hereinafter a GO of Li_N and Na_N clusters for $N = 2-150$ is presented. Up to six isomers are considered for each cluster size N. A modified embedded atom method (MEAM) is used to describe the interatomic interactions within the clusters. The putative GEM are determined via a combination of the *variable metric/quasi-Newton* method for local structural relaxations and the *Aufbau-Abbau* algorithm. Moreover, a detailed energetic and structural analysis is performed. Due to the simplicity of the used computational method, the MEAM, and its analytical form, an extensive investigation of the clusters' PES can be performed. To the best of our knowledge this is the first time a study considers up to six isomers for two types of alkali clusters within this size range. Interestingly, not all cluster geometries are solely dictated by packing effects with a high coordination of the atoms, but which are planar or also linear.

This part of the thesis is structured as follows: first the technical details of this study are presented, including a description of the MEAM (section 9.1), and the used optimization algorithms (section 9.2). This is followed by a detailed analysis and discussion of the results (chapter 10). The chapter concludes with a final summary and an outlook (chapter 11).

9 Technical details

9.1 The computational method: MEAM

Formally the EAM has its roots in DFT and the underlying idea is based on the quasi-atom model of an impurity within a host system, which was constructed by Stott and Zaremba in 1980 [158]. The original EAM of Daw, Baskes and Foiles was initially developed to describe metals and has been used to calculate many different properties of these systems [159, 160, 161, 162]. The basic assumption of this method is to treat the metallic system as a kind of host in which each of the systems' atoms is embedded. If an atom is embedded into the host at a certain position i, this atom "feels“ an electron density ρ_i^h at this site, which is caused by all the other atoms constituting the host. This gives rise to the so-called embedding energy $F_i(\rho_i^h)$, which is a function of the hosts' electron density ρ_i^h at this position i. Moreover, the embedded atom i interacts with each other atom j in the host via a short-ranged potential $\phi(r_{ij})$ that is a function of the interatomic distance r_{ij}. Within the EAM the total energy of a N-atomic system can be described as a sum of two energetic contributions:

$$E_{\text{total}} = \sum_{i=1}^{N} F_i(\rho_i^h) + \frac{1}{2} \sum_{\substack{i,j=1 \\ i \neq j}}^{N} \phi(r_{ij}), \tag{9.1}$$

with the local electron density ρ_i^h at site i being a simple superposition of spherically averaged atomic electron densities $\rho_j^a(r_{ij})$. The functions to calculate the total energy E_{total}, i.e. the embedding function, the electron density and the pair potential function, are obtained from fitting data of experiments or higher-level theory like *ab initio* methods. For use in calculations these functions are tabulated and interpolated via cubic splines.

Furthermore, there are analytic embedded atom methods, which have been used for various different applications [163, 164, 165, 166]. As the name suggests, analytical mathematical functions and no spline descriptions are used to describe the quantities appearing within equation 9.1. The parameters of such analytical functions can be obtained from several properties, e.g. the cohesive energy or the elastic constants of the considered metals [163, 166]. Additionally modified EAM models exist, in which an additional term is added to the total energy expression as an adjustment to the assumed superposition of spherically atomic electron densities [167, 168, 169].

The semiempirical EAM has been successfully applied to wide range of metal clusters, including homoatomic systems [105, 106, 157, 170, 171] as well as nanoalloys [172, 173, 174, 175]. As a simple model potential the EAM is particularly suitable for the search of the lowest-energy structures of clusters, which has made it a popular computational method to perform global optimizations [105, 106, 157, 174, 175]. In this thesis an analytic MEAM is used to calculate the energy of Li and Na clusters. It was initially developed for bulk alkali metals and applied to various properties of these systems, e.g. the Debye temperature, heat capacity or surface energy [176]. The results were in good accordance with other theoretical methods and experiments, therefore we were optimistic that an application to alkali clusters would be successful. Initial, preliminary investigations, published as bachelor thesis [177], showed the applicability of this analytic modified EAM to sodium clusters. Three isomers of Na_N clusters (with $2 \leq N \leq 60$) had been considered for the global optimization process. Due to the short time available for the bachelor thesis, only a limited investigation of the clusters' PES was possible. This was not a problem within the present study, where a very thorough GEO of the clusters and a comprehensive structural and energetic analysis could be performed. Each cluster size could be studied in more detail, more isomers and larger cluster sizes could be considered. Additionally, some minor errors have been removed, which enhances the efficiency and accuracy of the source code, used for the GEO of the alkali clusters. Moreover, it should be stressed that none of the results, obtained within the bachelor project, have been used for the investigations within the present study.

According to the MEAM, used in the present study, the total energy of a system can be described via three terms [176], where the first two terms, the embedding energy $F(\rho_i^h)$ and the pair potential $\phi(r_{ij})$, are also included in the original version of the EAM [159, 160]. The embedding energy depends on the interatomic distances r_{ij} through the hosts' electron density ρ_i^h at position i, whereas the pair potential directly depends on the distance between two atoms, with one atom being located at position i and the other one being located at position j. The electron density ρ_i^h originates from the presence of the other atoms of the system. The third energetic contribution $M(P_i^h)$ is the aforementioned modification term that corrects the assumption of linearly superposing spherically atomic electron densities and it is a function of the second order of the hosts' electron density P_i^h at site i [176]. Hence, the total energy of a system consisting of N atoms can be described by the following equation:

$$E_{\text{tot}} = \sum_{i}^{N} F(\rho_i^h) + \frac{1}{2} \sum_{\substack{i,j=1 \\ i \neq j}}^{N} \phi(r_{ij}) + \sum_{i}^{N} M(P_i^h) \tag{9.2}$$

The electron density of the host ρ_i^h and the the second order term P_i^h are sums of the corresponding atomic contributions $f^a(r_{ij})$:

$$\rho_i^h = \sum_j f^a(r_{ij}) \tag{9.3}$$

$$P_i^h = \sum_j (f^a(r_{ij}))^2. \tag{9.4}$$

The atomic electron densities $f^a(r_{ij})$ in turn are calculated as

$$f^a(r_{ij}) = \left(\frac{r_1}{r_{ij}}\right)^{4.5} \left(\frac{r_{\text{cut2}} - r_{ij}}{r_{\text{cut2}} - r_1}\right)^2, \tag{9.5}$$

with r_1 being the nearest-neighbour interatomic distance in an undistorted perfect bcc crystal. The cut-off distance r_{cut2} is decribed via $r_{\text{cut2}} = r_4 + 0.9(r_5 - r_4)$, is therefore located between the fourth r_4 and fifth r_5 nearest-neighbour distance in an undistorted perfect bcc lattice [176].

The analytical description of the embedding energy is

$$F(\rho_i^h) = -\left[F_0 - \gamma \ln\left(\frac{\rho_i^h}{\rho_e}\right)\right]\left(\frac{\rho_i^h}{\rho_e}\right)^n \tag{9.6}$$

with the MEAM parameters F_0, γ, and n and ρ_e representing the electron density of a bcc lattice in equilibrium. The formula for the calculation of the modification term is [176]

$$M(P_i^h) = \alpha\left\{1 - \exp\left[-100\left(\ln\left(\frac{P_i^h}{P_e}\right)\right)^2\right]\right\}, \tag{9.7}$$

with α and P_e representing a model parameter and the second-order equilibrium electron density for a bcc alkali metal, respectively. Moreover, the pair potential is truncated between the third and fourth nearest-neighbour distance of an undistorted bcc crystal, after the distance $r_{\text{cut1}} = r_3 + 0.9(r_4 - r_3)$. A power series expansion is used to describe the pair potential $\phi(r_{ij})$ [176],

$$\phi(r_{ij}) = \sum_{m=-1}^{3} k_m \left(\frac{r_{ij}}{r_1}\right)^m, \tag{9.8}$$

where the k_m represent model parameters of the MEAM. For the calculation of the clusters' energies the MEAM and the parameters of the original work of Hu and Masahiro [176] were used. Several properties of the alkali metals, like the lattice constants a, the cohesive energies and the elastic constants have been calculated within their study and the values for the model parameters of the MEAM were adjusted to accurately reproduce these quantities. These parameter values are listed in in table 9.1.

Table 9.1: Values for the parameters of the analytic MEAM used within this thesis. Lattice parameters a are in Å, F_0, γ, α, k_m are in eV and n is dimensionless. Adapted by permission from Springer Nature: Springer, *J. Clust. Sci.*, Global Optimization of Li and Na Clusters: Application of a Modified Embedded Atom Method, K. Huwig, V. G. Grigoryan and M. Springborg, Copyright 2019.

Parameter	**Li**	**Na**
a	3.491	4.225
F_0	0.96797	0.33292
γ	0.55765	0.57694
α x (10^{-6})	45.23040	7.66488
k_{-1}	4.51824	1.93482
k_0	-13.85574	-6.86288
k_1	14.90406	7.90187
k_2	-6.81276	-3.74485
k_3	1.13050	0.63419
n	0.320	0.465

9.2 The global optimization algorithm

The applied GO algorithm is a two-step procedure, where the first step includes the random creation of clusters and the local relaxation of the generated structures. As local optimization procedure a *variable metric/quasi-Newton* method [92] is used. Due to the analytical form for the energy within the MEAM model it is possible to calculate analytical expressions for the derivatives of the energy. The first order derivatives of the energy, the forces, are needed for the local optimizations. Due to this simplicity of the semiempirical MEAM, the local relaxations are very fast. Thus, for each cluster size many millions of clusters can be calculated, which enables an extensive investigation of the PES. In the subsequent second step, the up to six lowest-energy isomers of the "random" calculations are used as input structures for the *Aufbau-Abbau* algorithm. The energetic minima obtained in the second step are compared to that of the first one and the best, energetically lowest, structures are chosen. Using this optimization procedure, we are convinced that we could identify the global energetic minima or at least that clusters, that are very close to them.

9.2.1 The "random" calculations: unbiased optimizations

Random cluster generation

The concept of cluster creation that is used within this work, was developed by M. Valtchev [178] and it was adjusted to the present task. First, an initial volume V_0 is created, by using crystallographic data of the metal under investigation. In this case this initial volume is represented by the volume of a primitive bcc unit cell of the alkali metals. Furthermore, to take into account the size of the corresponding cluster, the volume of the primitive cell is multiplied by the number of atoms N in the cluster:

$$V_0 = N\frac{a^3}{2}. \tag{9.9}$$

a is the lattice constant of the respective alkali metal (see table 9.1). One calculation of a certain cluster size involves the optimization of many millions or for larger sizes hundred thousands of single clusters. Instead of creating each cluster of a certain size within the same, constant volume, variations are imposed upon this volume throughout a calculation. The shape of the confining volume may be prismatic or elliptic and the size of the volume is varied between $0.88 * V_0$ and $1.12 * V_0$ in increments of 0.04. In addition to the inclusion of compressed and enlarged volumes, the side ratios of the volumes are also varied. For the side ratios $x : y : z$ it is sufficient to change the values for x and y [178]. Hence, the considered side ratios $x : y : 1$ can range from $1 : 1 : 1$ to $10 : 10 : 1$, where x and y are allowed to adopt only integer values. In this context it is taken into account that there may be ratios that are permutative identical, e.g. $4 : 5 : 1$ and $5 : 4 : 1$ and they are not both considered. After the creation of the confining volume, the cluster is generated by placing the clusters' atoms randomly within this volume. Afterwards this initial random geometry is locally relaxed using the *variable metric/quasi-Newton* method [92].

The *variable metric/quasi-Newton* method

Variable metric/quasi-Newton methods are popular optimization algorithms and have been successfully applied to the local optimizations of other metal clusters, such as Ni or Cu clusters [105, 106]. They have proved to be reliable, effective local optimization

procedures, eminently suited for unbiased structural optimizations.
The original, exact *Newton* algorithm is a method that needs the inverse of the Hessian matrix to determine the minimum values of some function f. In practice this exact *Newton* method, in most cases, is not suitable. The calculation of the Hessian that includes the second derivatives of the function f, is often computationally too demanding [92]. So-called *quasi-Newton* methods avoid the calculation of the true Hessian, and therefore the determination of the second derivative, by using an approximation to the inverse of Hessian [92]. Information on the gradient, the first derivative of f, is involved in the construction of the approximated Hessian. This reduces the computational cost for the optimization drastically and has made the *quasi-Newton* methods very popular in science and engineering. The general procedure of these algorithms is visualized in a simplified form in figure 9.1.

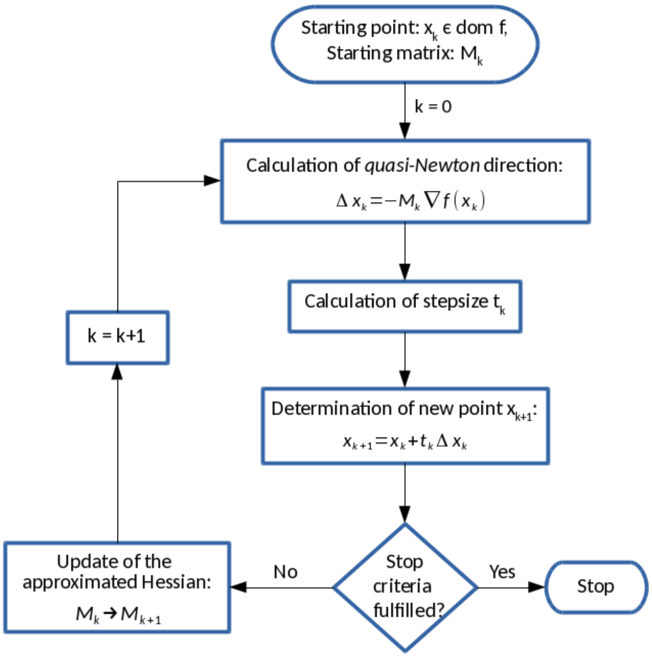

Figure 9.1: Simplified flowchart showing the general workflow of a *quasi-Newton* algorithm, as used within this study of the GO of alkali clusters.

Starting with an inital argument value $x_k = x_0$ and an initial approximation to the inverse Hessian $M_k = M_0$, the *quasi-Newton* direction is determined [179]. The latter specifies the search direction of the optimization Δx_k, which gives the direction on the PES one has to move to reach the next point in space x_{k+1}. The approximation M_k to the inverse Hessian matrix H_k^{-1} and the gradient of the function f at the point x_k, $\nabla f(x_k)$, are used to calculate Δx_k. The matrix M_k is positive definite [92, 179], which ensures that starting from x_k one moves in a downhill direction on the PES towards a minimum value. Next, the parameter t_k is computed, which represents the size of the step one moves along the search direction. Subsequently, the new point x_{k+1} is determined using Δx_k and t_k [179]. Afterwards the stop criteria are checked, which may be the reaching of some tolerance value and/or a maximum number of iteration steps k. If the stop criteria are fulfilled the algorithm stops, if not, the matrix M_k is updated to yield a new approximated matrix M_{k+1} to the true inverse H_{k+1}^{-1} [179]. The next iteration step $k = k+1$ again starts with the calculation of the *quasi-Newton* direction Δx_{k+1} using the updated matrix M_{k+1} and the recent gradient information $\nabla f(x_{k+1})$. There are different versions of *variable metric/quasi-Newton* algorithms, with the Davidon-Fletcher-Powell (DFP) and Broyden-Fletcher-Goldfarb-Shanno (BFGS) algorithm being the two most popular ones [92, 179]. These versions differ in how the approximated Hessian is updated. In this study the BFGS method is used for the local optimization of the single cluster structures. The designation "*variable metric*" is derived from the fact that the positive definite matrix M_k defines a metric. Due to the updating process of the matrix M_k, in each iteration step another metric is defined, i.e. the metric is variable.

The efficiency of the applied *quasi-Newton* algorithm, together with the simplicity of a simple model potential as the MEAM and especially its analytical formulae and the possibility to use the gradient in an analytic form, lead to a fast and effective screening of the PES of the clusters. A large number of clusters could be generated and optimized within each calculation. For the 20-atomic Na cluster about 12.5 million single clusters have been examined during one calculation, what took approximately $42h$. Eight such calculations for Na_{20} have been performed in total, which gives roughly 100 million systems that have been investigated for this cluster size. In general for each cluster size eight to ten of these calculations have been carried out and even larger cluster sizes have been studied extensively (e.g. 5 million clusters in total for Na_{150}). For each cluster size, the results of each of the eight to ten calculations are examined and the six energetically lowest isomers are identified, which are used afterwards in the *Aufbau-Abbau* procedure.

9.2.2 The *Aufbau-Abbau* algorithm

The second step within the GO procedure is the *Aufbau-Abbau* method. In principle, this algorithm consists of two parts: on the one hand the *Aufbau* and on the other the *Abbau* process. To perform an *Aufbau* calculation for a cluster M_N with N atoms an optimized cluster with $N-1$ atoms is needed as an input structure. This $N-1$-atom cluster has been obtained in a previous *Aufbau-Abbau* step or in a "random calculation"

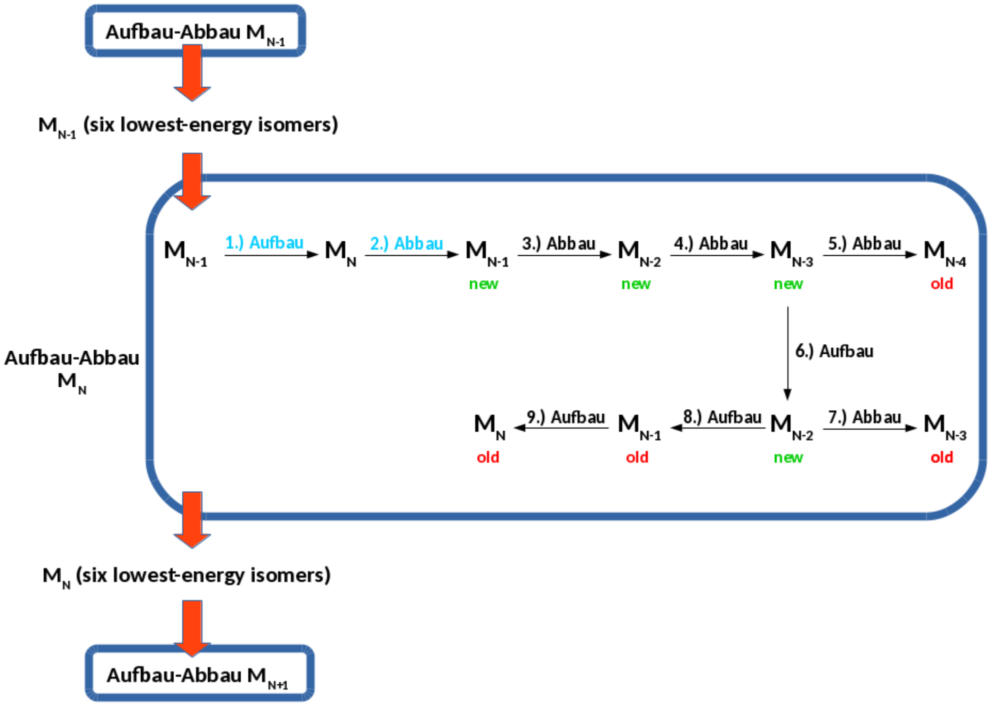

Figure 9.2: Example for the workflow of the *Aufbau-Abbau* algorithm used within this study. Adapted by permission from Springer Nature: Springer, *J. Clust. Sci.*, Global Optimization of Li and Na Clusters: Application of a Modified Embedded Atom Method, K. Huwig, V. G. Grigoryan and M. Springborg, Copyright 2019.

for this cluster size $N-1$. An atom is added at a random position of the $(N-1)$-atom cluster and a cluster with N atoms is obtained, which is subsequently optimized locally using the previously discussed *quasi-Newton* method. The whole process of the addition of an atom to the $(N-1)$-atomic input structure as well as the local relaxation are repeated many thousands or million of times, which enables a further extensive study of the clusters' PES. In contrast, an *Abbau* calculation makes use of an optimized cluster with $(N+1)$ atoms as input system, whereat by removal of an atom a N-atomic cluster is obtained. Afterwards the M_N cluster is locally relaxed. Each single atom of the M_{N+1} input structure is removed once, resulting in $N+1$ different structures with N atoms that are considered within one *Abbau* calculation.

The workflow of the *Aufbau-Abbau* algorithm, as used within this study, is shown in the sketch in figure 9.2. Starting with the smallest cluster size, this algorithm is performed successively. As an example we show the *Aufbau-Abbau* procedure, for the general case of a N-atomic cluster M_N.

The optimization process for the M_{N-1} cluster just has been finished and now we arrive at the cluster size N. The recent six energetically lowest isomers for the $(N-1)$-atomic cluster among the results of the "random calculations" and the *Aufbau-Abbau* algorithm have been identified and are used as input structures for the *Aufbau* calculations of the N-atom cluster M_N (step 1 in figure 9.2). Therefore, six *Aufbau* calculations are performed within step 1. Among the results of the six *Aufbau* calculations of step 1 the energetically lowest structures of the M_N cluster are chosen and compared to that of "random calculations". Again, the six energetic minimum structures of this cluster size are identified and used as input for the following six *Abbau* calculations (step 2), which in turn gives $(N-1)$-atom clusters. The results of this *Abbau* step are compared to the previous lowest-energy isomers of the M_{N-1} cluster and the best structures are kept. These two initial *Aufbau* and *Abbau* steps that are higlighted in light-blue, are always performed for each cluster size N. But the following step 3 is only performed, if new structures for the $(N-1)$-atomic cluster have been identified in step 2, i.e. at least one new lowest-energy isomer is among the six most stable structures. We may now assume that this is the case and a new set of six energy minima has been found for M_{N-1} (denoted by the green coloured "new" in figure 9.2). With this current set of minimum structures *Abbau* calculations are performed (step 3) and optimized $(N-2)$-atomic clusters are obtained. These structures are compared to the current set of lowest-energy minima of cluster size $N-2$ and the best ones are kept. Due to the identification of new energy minima, again *Abbau* calculations have to be performed (step 4). This sequence of *Abbau* steps is carried through until a size is reached, where no new set of structures is obtained (denoted by the red coloured "old" in figure 9.2). We may now assume that this is the case for the *Abbau* calculations that yield clusters of the size $N-4$ (step 5). Therefore the subsequent step 6 is a *Aufbau* procedure, using the recent six energetically lowest isomers of the M_{N-3} clusters as input. Within the results of these calculations, new structures are found for the $(N-2)$-atom cluster. Due to this fact, also *Abbau* calculations have to be performed with current best isomers of this size (step 7). Since this does not lead to new energy minima for cluster size $N-3$, one proceeds with the next *Aufbau* procedure (step 8). Although step 8 does not result in a new set of isomers for the M_{N-1} cluster, the *Aufbau* calculations of step 9 to yield M_N clusters have to be performed with the current set, because new structures for the $(N-1)$-atomic cluster have already been found in step 2. The application of the *Aufbau-Abbau* procedure in this form guarantees, that in case of the identification of new isomers for a certain cluster size, *Aufbau* as well as *Abbau* calculations are performed, using the updated set of structures as input. The optimization process outlined above is assumed to be finished, if no new lowest-energy isomers are identified for the examined cluster sizes. The workflow depicted is complicated and, if performed manually, also time-consuming as well as error-prone. Hence, to perform all the calculations as well the analyses and identifications of the lowest-energy isomers automatically, a self-written bash script was used.

10 Results and discussion

10.1 Smaller cluster sizes

10.1.1 Dimers of Li and Na

The discussion of our results starts with the smallest clusters, the dimers Li_2 and Na_2. Since the used MEAM approach [176] was initially developed for bulk alkali metals, this also offers the opportunity to check the accuracy of our approach. Alkali metals in the solid state and the corresponding bulk properties may be described well with the MEAM, but can nanoparticles like clusters also be treated with this method? Therefore we compare the bond lengths of the optimized Li_2 and Na_2 dimers to experimental results as well as to those of other theoretical methods. This is shown in table 10.1.

The bond length for Li_2 obtained with the MEAM is in very good agreement with the experimental determined value [180] and deviates less from experiment than the listed DFT calculations [181, 182]. Also the MEAM result for the Na dimer is satisfactory and is in good accordance with other studies, but exhibits a larger deviation from the experimentally determined bond length [180] than it is the case for Li_2. For Na_2, DFT studies using B3LYP as the exchange-correlation functional [183] yield a more accurate Na_2 bond length than the MEAM potential of the present work and the MP2 calculations of Ref. [184]. The latter two studies slightly overestimate the sodium dimer bond length. Nevertheless, the results for Li_2 as well as Na_2 obtained with the MEAM are in good agreement with other studies. Taken together with the findings for the bulk alkali metals in Ref. [176] we are convinced that the application to larger cluster sizes will also be successful.

Additionally in figure 10.1 we exemplarily show the energy curve, the most simple type of PES, for the diatomic Li cluster calculated with the MEAM potential. It can be recognized that a well-defined energy minimum exists at an interatomic distance of $r_{\mathrm{min}} = 2.674$ Å.

10.1.2 Clusters with up to ten atoms

In the ensuing discussions about cluster structures the notation $\mathrm{M}_{N.k}$ will be used. Here the letter M denotes the type of alkali metal (Li or Na) and N represents the number of atoms in the cluster. The number of the isomer is denoted by k, where the order is according to increasing energy. A higher number k indicates an isomer with a larger

Table 10.1: Bond lengths of the optimized lithium and sodium dimer obtained with the MEAM potential compared to the results of experimental and other theoretical studies. MEAM, exp., DFT, MP2 denotes modified embedded atom method, experiment, density functional theory and second-order Møller-Plesset perturbation theory, respectively. Adapted by permission from Springer Nature: Springer, *J. Clust. Sci.*, Global Optimization of Li and Na Clusters: Application of a Modified Embedded Atom Method, K. Huwig, V. G. Grigoryan and M. Springborg, Copyright 2019.

Li_2	**R(Å)**	**Method**	**Na_2**	**R(Å)**	**Method**
	2.674	MEAM		3.166	MEAM
	2.673	exp.[180]		3.079	exp.[180]
	2.714	DFT[181]		3.054	DFT[183]
	2.691	DFT[182]		3.153	MP2 [184]

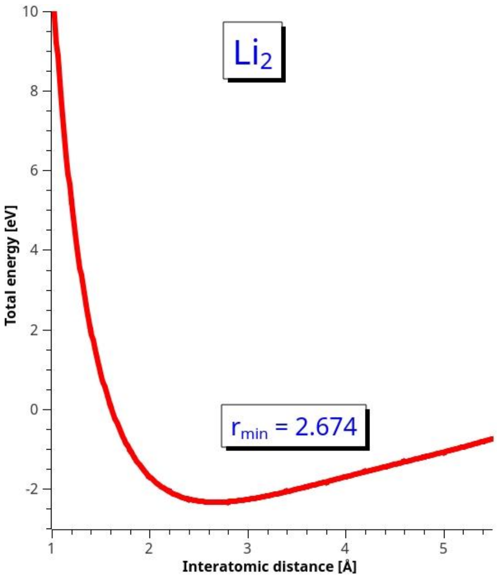

Figure 10.1: Total energy curve for the Li_2 cluster calculated with the MEAM potential.

energy value, i.e. an isomer with a less stable structure.

The cluster geometries obtained with the MEAM are compared to the results of various other methods at different levels of theory, like *ab initio* studies, DFT calculations or model potentials. As mentioned before, in this study up to six isomers are considered for each cluster size. But in general, we focus on the three lowest-energy isomers within the following discussions and only in special cases the fourth, fifth or sixth isomer is considered. Tables including the point groups of all six isomers of Li and Na clusters are enclosed within the appendix A.

Clusters with $N = 3 - 6$ atoms

Table 10.2 lists the symmetries for the three energetically most stable Li_N clusters (with $N = 3 - 6$) of this work compared to the results of other investigations. The structures for the putative global energy minima within this size range are depicted in figure 10.2. Within the MEAM the GEM for the three-atomic Li cluster is the equilateral triangle with the symmetry group D_{3h}, whereas the other studies yield an isosceles triangle with the C_{2v} point group. The reduction of symmetry for the results of the other studies occurs due to a Jahn-Teller distortion [37, 185]. The *ab initio* as well as the DFT calculations listed in table 10.2 explicitly include electrons, but this is not the case for the MEAM used in this work. The simple MEAM model does not encompass electronic degrees of freedom and a Jahn-Teller distortion, an electronic effect, can not be depicted. Experimental investigations substantiate the existence of a Jahn-Teller effect for $\mathrm{Li}_{3.1}$ [186]. Only the DFT calculations of Ref. [185] yield an equilateral triangle. But it is the second-lowest energy isomer of this study with a quartet electronic state and lies 1.31 eV higher in energy than the energetic minimum, the isosceles triangle. For the MEAM a linear geometry ($D_{\infty h}$) is found as second isomer, which represents the third isomer of the DFT calculations of reference [185]. The third most stable structure yielded by the MEAM has a C_{2v} point group and has a large apex angle of about 129.1°. In contrast to the obtuse triangle of our study, the angle at the vertex of the C_{2v} structures of the other studies is smaller [185, 187, 188].

The MEAM exhibits the tetrahedron (T_d) for $\mathrm{Li}_{4.1}$. Compared with the other investigations that yield a planar rhombus with D_{2h} symmetry [185, 187, 188, 189, 190], the result for the model potential is dictated by packing effects. From an energetic point of view the MEAM prefers a high coordinated cluster geometry like a tetrahedron. The rhombus is also obtained with the MEAM, but as the second-lowest energy isomer $\mathrm{Li}_{4.2}$. It is 114 meV less stable than the aforementioned tetrahedron. With the exception of the DFT study of Jones *et al.* [185], where a Jahn-Teller distorted tetrahedron is the second isomer, such a structure is not reported by the other investigations listed in table 10.2. Furthermore, another study, not listed in table 10.2, using configuration interaction and coupled-cluster methods, reports a stable tetrahedron in a no-pair bonding state [191]. The existence of a planar rhombus is also confirmed via experiments [192]. However, comparing the structural parameters of the rhombus $\mathrm{Li}_{4.2}$ obtained with the MEAM with that of the other investigations it becomes obvious that the diagonal and the side bond exhibit almost the same length (3.007 Å and 2.929 Å) for the MEAM structure, whereas this is not the case for the rhombus of the other calculations. Here the side bond is noticeable larger than the diagonal [188, 189]. Finally we obtain a bended rhombus for the third-most stable isomer $\mathrm{Li}_{4.3}$ that has a C_{2v} point group. The calculations of Ref. [189] produce a similar cluster as second isomer. The square (D_{4h}) is the third isomer of this study, which is the fourth-lowest energy structure for the semiempirical MEAM.

The lowest-energy structure for Li_5 is the trigonal bipyramide (D_{3h}), which is not the GEM for the other calculations. A distorted bipyramidal geometry with a C_{2v} point group is reported as the second or first isomer within a few other studies [185, 189, 193]. For the DFT calculations of Ref. [185] also a stable, undistorted D_{3h} bipyramide in a quartet state exists. The lowest-energy structure found with some *ab initio* [189] and DFT [187, 194] methods is a 2D structure with a C_{2v} symmetry. This planar cluster geometry is also obtained with our MEAM model, but due to its preference of higher coordinated structures, it is the fourth most stable isomer for Li_5. However, it should be noted that normally planar structures are not the result of semiempirical model potentials as the MEAM. For the latter $\mathrm{Li}_{5.2}$ is a pyramid with a square base (C_{4v}) that is only reported within two other studies [193, 194], but as an anionic system and not as a neutral cluster. The tetrahedron with one additional atom occupying an edge is the second metastable isomer for the MEAM. This C_{2v} structure is also obtained for Ref. [193] as third isomer and, in a symmetry reduced version (C_2), as second isomer for the DFT calculations of Ref. [194].

A distorted octahedron (C_{4h}) is the GEM for Li_6 within this work as well as for other studies [185, 187, 193, 194] listed in table 10.2. The MEAM yields a trigonal bipyramid with one atom capping a trigonal face (C_{2v}) as second isomer. Also the *ab initio* calculations of Ref. [189] give this structure as third most-stable geometry for the six-atomic Li clusters. $\mathrm{Li}_{6.3}$ is a capped square pyramid, with the additional Li atom also capping a trigonal face (C_s). The latter cluster has not been obtained within any other study listed. The pentagonal pyramid with a flattened geometry and a C_{5v} point group is the first [189] or second [187, 193, 194] isomer for other investigations and represents the fourth metastable cluster in our work. The DFT calculations of Ref. [185] yield the corresponding planar cluster with a D_{5h} symmetry as second isomer. Among the most stable clusters of the other studies another two-dimensional structure (D_{3h}) is mentioned, which is not included within the six Li_6 isomers produced by the MEAM. As to be expected for a model potential like the MEAM lower-coordinated geometries are less-stable and no planar clusters are found among the six lowest-energy isomers for cluster sizes with more than five atoms. Concerning the order of stability, and especially the putative global energy minima, already for cluster sizes $N = 4$ 3D structures are energetically favoured compared to planar systems.

Table 10.2: The symmetry of smaller lithium clusters ($N = 3-6$) obtained with the MEAM compared to other studies. The three lowest-energy isomers are listed. MEAM, DFT, and AI denotes modified embedded atom method, density functional theory, and *ab initio* calculations, respectively. Adapted by permission from Springer Nature: Springer, *J. Clust. Sci.*, Global Optimization of Li and Na Clusters: Application of a Modified Embedded Atom Method, K. Huwig, V. G. Grigoryan and M. Springborg, Copyright 2019.

N	Ref.	Method	$N.1$	$N.2$	$N.3$	***N***	Ref.	Method	$N.1$	$N.2$	$N.3$
3	Here	MEAM	D_{3h}	$D_{\infty h}$	C_{2v}	**5**	Here	MEAM	D_{3h}	C_{4v}	C_{2v}
	[187]	DFT	C_{2v}	C_{2v}			[187]	DFT	C_{2v}		
	[188]	AI	C_{2v}				[189]	AI	C_{2v}	C_{2v}	D_{3h}
	[189]	AI	C_{2v}				[185]	DFT	C_{2v}	C_{2v}	D_{3h}
	[185]	DFT	C_{2v}	D_{3h}	$D_{\infty h}$		[193]	AI	C_{2v}	C_{2v}	C_{2v}
							[194]	DFT	C_{2v}	C_2	
4	Here	MEAM	T_d	D_{2h}	C_{2v}	**6**	Here	MEAM	C_{4h}	C_{2v}	C_s
	[187]	DFT	D_{2h}				[187]	DFT	D_{4h}	C_{5v}	D_{3h}
	[188]	AI	D_{2h}				[189]	AI	C_{5v}	D_{3h}	C_{2v}
	[189]	AI	D_{2h}	C_{2v}	D_{4h}		[185]	DFT	D_{4h}	D_{5h}	D_{3h}
	[185]	DFT	D_{2h}	C_{3v}			[193]	AI	D_{4h}	C_{5v}	D_{3h}
	[190]	AI	D_{2h}				[194]	DFT	D_{4h}	C_{5v}	D_{3h}

Concerning the MEAM structures for the Na clusters within the size range $N = 3-6$, it becomes obvious that they correspond, by and large, to the geometries of the Li clusters presented above. Therefore, for sodium, this cluster size range is not discussed in detail here and the geometries of the putative GEM structures are just mentioned briefly. $\mathrm{Na}_{3.1}$ is an equilateral triangle (D_{3h}) as to be expected without Jahn-Teller effect, $\mathrm{Na}_{4.1}$ is a tetrahedron (T_d), the trigonal bipyramid is obtained for $\mathrm{Na}_{5.1}$ and an

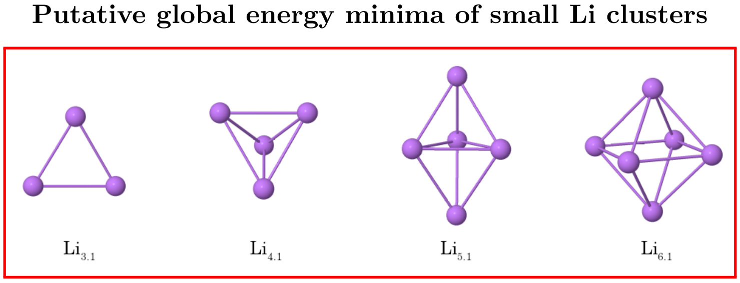

Figure 10.2: Structures of the putative global minima for Li_N clusters for $N = 3 - 6$ obtained with the MEAM. Adapted by permission from Springer Nature: Springer, *J. Clust. Sci.*, Global Optimization of Li and Na Clusters: Application of a Modified Embedded Atom Method, K. Huwig, V. G. Grigoryan and M. Springborg, Copyright 2019.

undistorted octahedron with the point group O_h represents the global optimum for the six-atomic Na cluster.

Clusters with $N = 7 - 10$ atoms

Due to the slight geometric differences between the optimized Li and Na clusters of the present study, for the cluster sizes $N = 7 - 10$ only the sodium clusters are presented. As before for the Li clusters, the point groups of the three lowest-energy isomers of the Na clusters obtained with the MEAM are compared to the results of various other theoretical methods (see table 10.3). The MEAM global minimum structures $Na_{7.1}$ up to $Na_{10.1}$ are depicted in figure 10.3.

As to be expected, the results for the sodium clusters obtained with other semiempirical methods like the Gupta (G) [195] potential are very similar to that of the MEAM, whereas DFT [154] as well as *ab initio* [149, 151] methods yield cluster structures, which exhibit similar differences as in the case of the Li clusters. Concerning the six lowest-energy isomers for the two alkali metals, small differences may occur for the energetic ordering and in a few cases also a structure may be found for Li, which is not obtained for Na and vice versa. The linear $Na_{4.6}$ can be mentioned as an example for this. Being the sixth most-stable structure for Na, this geometry is not among the six isomers of Li_4.

The lowest-energy structure $Na_{7.1}$ is the pentagonal bipyramid (D_{5h}) within the MEAM, which is in accordance with all the other studies, listed in table 10.3 [157, 184, 195, 196]. In our work the first and second metastable isomer for the seven-atomic Na cluster are a singly capped octahedron (C_{3v}) and a bicapped trigonal bipyramid (C_2), respectively. Also in Ref. [196] a second isomer is reported. Its geometry corresponds to our fifth

most stable structure: a tricapped tetrahedron with a C_{3v} point group.
For Na_8 the MEAM yields a bisdisphenoid with D_{2d} symmetry as GEM, which is also obtained with the other model potentials [157, 195] and with the DFTB method [157]. A fully capped octahedron is the first isomer within the other investigations [184, 196, 197]. The mono-capped pentagonal bipyramid (C_s) is the second isomer within our study and is also reported as first metastable isomer in Ref. [197]. The latter study yields a dodecahedral cluster as third lowest-energy structure.
Both, the MEAM and the EAM [157] model yield a doubly capped pentagonal bipyramid as putative energetic minimum for Na_9. The most-stable clusters obtained with the other methods exhibit other geometrical structures [184, 195, 196], e.g. a monocapped tetrahedron is reported in reference [196].
$Na_{10.1}$ is a triply capped pentagonal bipyramid within the MEAM model, the Gupta [195] calculations, and the semiemprirical Murrell-Mottram (MM) [195] potential. This C_{3v} structure is not the result for the other investigations. Hückel calculations [196] yield a cluster with a C_{4v} symmetry, whose geometry can be described as an octahedron with four capping atoms. The DFT studies of Ref. [198] as well as the listed *ab initio* calculations [184] mention a bicapped antiprism with a C_2 point group as lowest-energy cluster. Moreover, a trapezoidal antiprism is the second most-stable ten-atomic Na cluster for the MEAM and exhibits a D_{2h} symmetry.
For $N = 7 - 10$ the energetic ordering of the six isomers of the Li_N clusters is similar to that of the Na_N clusters. Also here, cluster geometries occur for Li that are not found for Na and vice versa. In general the geometries of the putative energy minima for Li and Na clusters do not differ within the size range $N = 7 - 10$. An exception: The undistorted bisdisphenoid (D_{2d}) is the first metastable cluster $Li_{8.2}$ and $Li_{8.1}$ is a bisdisphenoidal structure with a reduced symmetry (C_{2v}).

10.2 Energetic and structural analysis of the alkali metal clusters

Concerning the large amount of data produced upon the global optimization of the Li and Na clusters, it is not feasible to discuss each single cluster size in detail. Rather, we focus on identifying energetic and structural trends using several analytical tools.

Table 10.3: Point groups of smaller sodium clusters ($N = 7 - 10$) obtained with the MEAM compared to other studies. Only the three most stable isomers are listed. Adapted by permission from Springer Nature: Springer, *J. Clust. Sci.*, Global Optimization of Li and Na Clusters: Application of a Modified Embedded Atom Method, K. Huwig, V. G. Grigoryan and M. Springborg, Copyright 2019.

N	Ref.	Method	$N.1$	$N.2$	$N.3$
7	Here	MEAM	D_{5h}	C_{3v}	C_2
	[195]	G	D_{5h}		
	[157]	DFTB	D_{5h}		
	[157]	EAM	D_{5h}		
	[196]	H	D_{5h}		
	[184]	AI	D_{5h}		
8	Here	MEAM	D_{2d}	C_s	D_{3d}
	[195]	G	D_{2d}		
	[157]	DFTB	D_{2d}		
	[157]	EAM	D_{2d}		
	[196]	H	T_d	C_s	
	[184]	AI	T_d		
	[197]	DDTB	T_d	C_s	D_{2d}
9	Here	MEAM	C_{2v}	C_s	C_1
	[195]	G	D_{3h}		
	[157]	EAM	C_{2v}		
	[157]	DFTB	C_1		
	[196]	H	C_{2v}	C_s	
	[184]	AI	C_{2v}		
10	Here	MEAM	C_{3v}	D_{2h}	C_2
	[195]	G	C_{3v}		
	[196]	H	C_{4v}	C_{4v}	C_{2v}
	[184]	AI	C_2	D_{4d}	C_{4v}
	[195]	MM	C_{3v}		
	[198]	DFT	C_2		

Putative global energy minima of small Na clusters

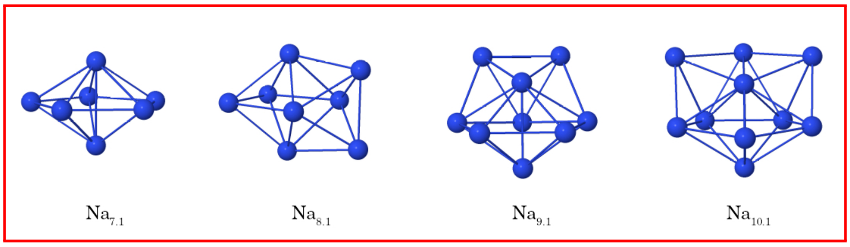

Figure 10.3: Structures of the putative global minima for Na_N clusters for $N = 7 - 10$ obtained with the MEAM. Adapted by permission from Springer Nature: Springer, *J. Clust. Sci.*, Global Optimization of Li and Na Clusters: Application of a Modified Embedded Atom Method, K. Huwig, V. G. Grigoryan and M. Springborg, Copyright 2019.

10.2.1 Energy and stability: trends

For the two most stable isomers of each cluster size, obtained with the MEAM, we calculated the binding energy per atom. The corresponding curves (first isomer: solid line, second isomer: dashed line) are depicted in figure 10.4. With increasing cluster size N the binding energy per atom increases monotonically for both alkali metal clusters. Additionally, one can recognize a fine structure with several tips, especially pronounced for the curve of the putative global minima. These cluster sizes represent structures with a larger binding energy, i.e. a higher stability, than the neighbouring sizes. Overall, the curves for the first and second isomers do not differ very much for both alkali metals. Moreover, the dotted, horizontal lines depict the corresponding binding energies of the Li and Na bulk material (1.63 eV/atom for Li, 1.11 eV/atom for Na). The binding energy of the clusters converges towards the bulk value without reaching it within the investigated cluster size range.

Binding energy as function of cluster size

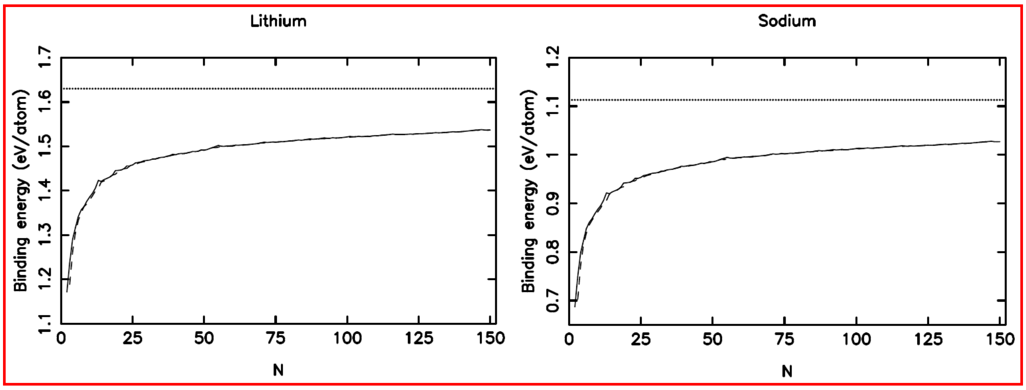

Figure 10.4: Binding energy per atom for the the first and second isomers of Li_N (left panel) and Na_N clusters (right panel) for $2 \leq N \leq 150$. The solid and dashed lines represent the values for the lowest-energy and second lowest-energy isomers, respectively. The dotted, horizontal lines depict the corresponding bulk values. Adapted by permission from Springer Nature: Springer, *J. Clust. Sci.*, Global Optimization of Li and Na Clusters: Application of a Modified Embedded Atom Method, K. Huwig, V. G. Grigoryan and M. Springborg, Copyright 2019.

The fine structure within the curves mentioned above can be investigated in more detail. Two quantities concerning the stability of the clusters can provide further insights into this phenomena. First, the stability function gives the stability of a certain cluster size compared to the stability of neighbouring cluster sizes. It is calculated as:

$$S(N) = E_{\text{tot}}(N+1) + E_{\text{tot}}(N-1) - 2 \cdot E_{\text{tot}}(N). \tag{10.1}$$

Here, N is the total number of atoms in the cluster. The other quantity describing the stability is the difference in the total energy of the two most-stable isomers. Both stability criteria are depicted in figure 10.5.

Stability criteria: stability function and energy difference

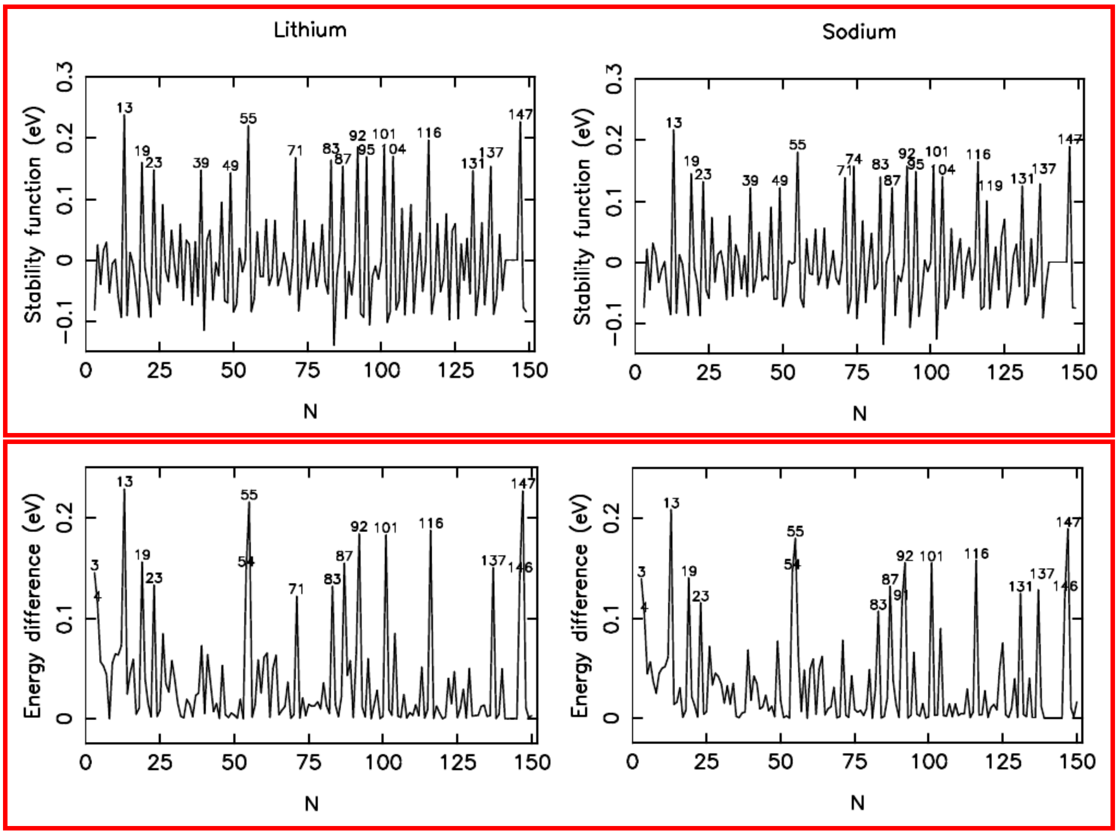

Figure 10.5: Stability criteria for the Li and Na clusters. The upper and the lower panels depict the stability function and the energy difference between the first and second isomers, respectively. Pronounced maxima within the upper panels are so-called magic cluster sizes. Adapted by permission from Springer Nature: Springer, *J. Clust. Sci.*, Global Optimization of Li and Na Clusters: Application of a Modified Embedded Atom Method, K. Huwig, V. G. Grigoryan and M. Springborg, Copyright 2019.

Within the two upper panels the stability function $S(N)$ for the Li and Na clusters is depicted. Peaks within these panels, i.e. pronounced maxima, describe cluster sizes with higher stabilities, if compared to the neighbouring sizes. It can also be noticed that these so-called magic sizes, represented by the tips in figure 10.4, also posses a larger binding energy per atom. Except for the cluster sizes $N = 74$ and $N = 119$ lithium and sodium have the same magic numbers. As to be expected for a model potential including packing effects, the Mackay icosahedra at $N = 13$, 55 and 147 exhibit the largest peaks for Li and Na. Furthermore, for Li several smaller peaks at $N = 26, 46, 107$ and 109 can be found, which are not highlighted in the figure. The stability function for Na shows some less pronounced maxima at $N = 26$, 31 and 46.

Other studies, using the EAM [157], the Gupta (G) [155, 199] or the Murrell-Mottram (MM) potential [155] yield magic sizes for sodium that most often correspond to that of the present study. However, frequently magic sizes are obtained with the MEAM that have not been found within the investigations, previously mentioned, i.e. the magic clusters at $N = 74$, 83, 87, 95, 104, 131 and 137 identified with the MEAM, have not been listed within the other studies. Sometimes, the different model potentials also yield structures with different symmetries for the same magic number, e.g. Na_{101} or Na_{116} for the present study and the MM method. But there are also magic numbers that have not been identified using the MEAM, i.e. $N = 45$, 47, $N = 29$, 81 or $N = 28$, 42 for the EAM, the G and MM model, respectively. The DFTB method [157] yields magic cluster sizes for Na that are quite different from those of the model potentials, and which are in good agreement with the jellium model or mass-spectrometric investigations [37, 128, 132]. Here, electronic shell-closing effects are the reason for pronounced peaks, i.e. a higher stability of certain cluster sizes. Electrons are not explicitly included within simple potentials like the MEAM, the EAM or the G and MM method. So, electronic effects can not be described with these methods and the resulting structures are rather dictated by packing effects. Here, also odd magic numbers are obtained. Comparing the MEAM results for the Li clusters to the magic numbers obtained with the jellium model [132] similar observations can be made.

Whether a cluster size belongs to the magic numbers depends on the investigated system and on the theoretical method that is used to describe the interactions among the atoms of that system. Therefore, it is difficult to predict such magic sizes in advance. Electronic shell-closings effects as well as geometric packing effects may influence the existence of the magic numbers. In this connection, the used computational method is of great importance. This may be explained by a simple example. For the MEAM the lowest-energy isomer for Li_{19} and Na_{19} is the highly-symmetrical double icosahedron with a C_{5v} point group. It is a highly-coordinated structure, which is dictated by the packing-effects that are included within the MEAM. In our study $\mathrm{Li}_{19.1}$ as well as $\mathrm{Na}_{19.1}$ exhibit a pronounced stability compared to the neighbouring cluster sizes and they belong to the magic clusters. The twenty-atom clusters $\mathrm{Li}_{20.1}$ and $\mathrm{Na}_{20.1}$, the double-icosahedron with an additional atom attached to a pentagonal ring, are of lower symmetry (C_s) and stability. The DFT calulations of Ref. [198] that explicitly include

electrons and therefore electronic effects, yield a magic Na_{20} cluster with a honeycomb-like geometry. Here, Na_{19} is no magic number. In this study the pronounced stability for the twenty-atom cluster agrees well with the experimental findings of Ref. [128], where the stability of these cluster sizes is explained via the filling of electronic shells for $N = 8$, 20, 40, … in accordance with the jellium model. These electronic effects can not be depicted by the MEAM, since electrons are not explicitly included within this method. Rather, the previously mentioned packing effects influence the geometries of the clusters and the (non-)existence of magic numbers for certain cluster sizes. In section 10.2.4 a more detailed discussion on the magic cluster sizes can be found.
The lower panels in figure 10.5 show the other stability criterion: the energy difference between the first and second isomers of the Li and Na clusters. In many cases, the cluster sizes with pronounced peaks found for the energy difference correspond to maxima of the stability function $S(N)$. Also here exceptions exist. For example for the three-atomic cluster, the energies of equilateral triangles $Li_{3.1}$/$Na_{3.1}$ are well below that of the linear second isomer. Therefore, at $N = 3$ there is a maximum for the energy difference. But the three-atomic lithium and sodium clusters are no magic clusters (see upper panels in figure 10.5).

10.2.2 Structural trends

Coordination and shape

Next we analyzed trends concerning the structural arrangements within the clusters. Figure 10.6 shows the average coordination number (ACN, upper panels), the minimum coordination number (MCN, middle panels) and the average bond distance (ABD). In case of the ACN (upper panels), we defined that two atoms are bonded, if their distance is less than 3.26 Å for Li and 3.94 Å for Na. In order to obtain these values, we averaged the nearest-neighbour (Li: 3.02 Å, Na: 3.66 Å) and the second nearest-neighbour interatomic distance (Li: 3.49 Å, Na: 4.23 Å) for bulk Li/Na. As to be expected, with increasing cluster size an increase in the ACN can be noticed. This is due to the decreasing number of atoms that is located in the surface region with increasing system size. Moreover, there is a fine structure within the curves describing the ACN. This fine structure is more pronounced for smaller-sized clusters and is smaller for larger cluster sizes: for Li after $N = 130$ and for Na after $N = 120$. For both alkali metal clusters the bcc coordination number of eight is reached at about $N = 50$. For larger cluster sizes even higher values for the ACN are found. In summary, it can be said that, at about $N = 50$

the bulk value is exceeded and is not reached again within the size range under study. A less dense packing, as found within the bcc lattice is unfavourable for the clusters within this size range and more compact structures are preferred. Therefore, larger sizes would have to be studied in order to investigate in which size range a transition to the less dense bcc packing occurs.

The two middle panels in figure 10.6 depict the MCN. A cluster growth with additional atoms attached to the surface of a cluster can be understood in terms of a low value between one and four for the MCN. Atoms that are added to a position inside a cluster or new arrangements of surface atoms are indicated by higher MCN values in figure 10.6. The ABD for the two alkali metal clusters is depicted in the lower panels in figure 10.6. In both cases, the average bond distance of the bcc bulk systems (Li: 3.02 Å, Na: 3.66 Å) is exceeded. Again, as observed for the ACN, the bulk properties are not reached within the studied cluster size range.

Coordination analysis

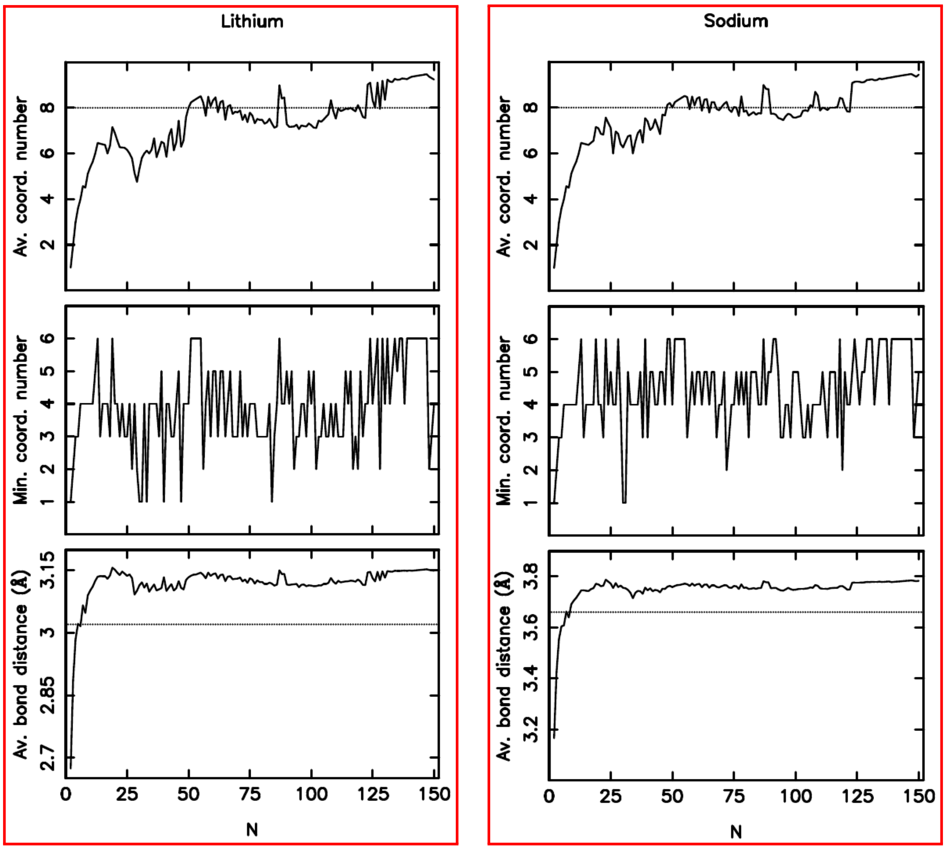

Figure 10.6: Analyses of the coordination within the clusters. The two upper panels, the two middle panels and the two botton panels depict the average coordination number, the minimum coordination number and the average bond distance, respectively. The left panels show the results for the Li clusters and the right panels the corresponding analyses for the Na clusters. Adapted by permission from Springer Nature: Springer, *J. Clust. Sci.*, Global Optimization of Li and Na Clusters: Application of a Modified Embedded Atom Method, K. Huwig, V. G. Grigoryan and M. Springborg, Copyright 2019.

Moreover, the overall shape of the lithium and sodium clusters might be of interest. Suitable quantities to describe these properties are the moments of inertia [105, 106]. Here, we considered the 3×3 matrix, including the following elements:

$$I_{\sigma\tau} = \frac{1}{u_l^2} \sum_{n=1}^{N} (R_{n,\sigma} - R_{0,\sigma}) \cdot (R_{n,\tau} - R_{0,\tau}). \tag{10.2}$$

$u_l = 1$ Å is the unit length, the variables σ and τ denote the directional components x, y and z and $\vec{R}_0$ represents the center of the corresponding cluster. The latter is calculated as

$$\vec{R}_0 = \frac{1}{N} \sum_{n=1}^{N} \vec{R}_n, \tag{10.3}$$

with the position of the nth atom $\vec{R}_n$. The three eigenvalues $I_{\alpha\alpha}$, belonging to the aforementioned 3×3 matrix, can be used to classify the clusters according to their shapes. Here, three shape categories can be distinguished. Clusters of overall spherical shape posses three identical eigenvalues, whereas cigar-shaped systems exhibit two large and one small eigenvalues. One large and two small eigenvalues are found for clusters with a lens shape. Another parameter, which can be used to describe the spatial extension of a cluster is the average $\langle I_{\alpha\alpha} \rangle$ of the previously mentioned eigenvalues. Assuming that we have a homogeneous sphere with N atoms, it is beneficial to scale the average $\langle I_{\alpha\alpha} \rangle$ by $N^{-5/3}$. In doing so, roughly N independent values are obtained. The normalized average, as well es the shapes of the clusters for all six isomers are shown in the upper and middle panels of figure 10.7.

Analyzing the two middle panels reveals that Li and Na exhibit an overall spherical shape for same cluster sizes. According to our analysis for both alkali metal clusters the putative global minima at $N = 4$, 6, 13, 26, 28, 34, 55, 92 and 147 as well as $\mathrm{Li}_{146.3}$ and $\mathrm{Na}_{146.2}$ are of spherical shape (bottom set of rows). Except for $\mathrm{Li}_{6.1}$, a distorted octahedron (C_{4h}), all lowest-lying isomers are of high symmetry. Comparing with the stability function in the upper panels of figure 10.5, one recognizes that the magic clusters at $N = 13$, 55, 92 and 147 are also overall spherical. Also $\mathrm{Li}_{146.3}$ and $\mathrm{Na}_{146.2}$ exhibit high symmetries, i.e. both posses a I_h point group. Further examination of the cluster shapes shows cluster size ranges, in which a certain shape seems to be dominant. For the sizes ranges $55 < N < 74$ and $94 < N < 111$ almost all six isomers of both alkali metal clusters predominantly exhibit cigar-like shapes (middle set of rows). Lens-shaped clusters can be found for Li for the cluster sizes $45 < N < 54$, $77 < N < 85$, and $111 < N < 140$

and for Na for $45 < N < 51$, $78 < N < 85$, and $111 < N < 138$ (top set of rows). A dominating shape can not be identified for smaller lithium or sodium clusters $\mathrm{Li}_N/\mathrm{Na}_N$ with $N < 45$. Within this size range more cigar-shaped systems can be found than spherical or lens-shaped structures.

The two upper panels in figure 10.7 show the average $\langle I_{\alpha\alpha} \rangle$. Here, for both alkali metals all six isomers exhibit similar trends. Smaller average values, for $50 < N < 55$ and $N > 140$, indicate more spherical shaped clusters. For the maximum eigenvalue difference $\Delta_{\max} I_{\alpha\alpha}$ (lower panels in figure 10.7) similar observations can be made. Spherical shaped clusters posses small eigenvalue differences, which is true for the cluster size ranges around $N = 55$ and $N = 90$ as well as for clusters with more than 140 atoms.

Growth pattern and similarity studies

In figure 10.8 we study the growth patterns of the lithium and sodium clusters. Here, the question arises: how similar is a N-atomic cluster to another cluster consisting of $N - 1$ atoms? How can a cluster with N atoms be build from a $(N-1)$-atom structure? In order to investigate this issue we employ a similarity function S_d using interatomic distances. [105, 106] All interatomic distances d_i (with $i = 1, 2, \cdots, N(N-1)/2$) between the atoms of the cluster with $N - 1$ atoms are calculated and subsequently these distances are sorted in increasing order. In a following step we take the cluster with N atoms and remove a single atom, thereby creating a $(N - 1)$-atom cluster. So, we obtain N structures with $N - 1$ atoms out of the N-atomic cluster. The interatomic distances d'_i are calculated for each of those newly generated clusters and they are also sorted in increasing order. Next, we use the interatomic distances to calculate the quantity

$$q_d = \left[\frac{2}{N(N-1)} \sum_{i=1}^{N(N-1)/2} (d_i - d'_i)^2 \right]^{1/2} . \tag{10.4}$$

N values for q_d are obtained and we keep the smallest one, $q_{d,\min}$. Subsequently, the similarity function S_d is computed using this minimum value for q_d:

$$S_d = \frac{1}{1 + q_{d,\min}/u_l}, \tag{10.5}$$

with $u_l = 1$ Å. There is a high degree of similarity between the two structures if the value for S_d is close to 1. The top panel in figure 10.8 depicts this similarity function for the comparison of the most-stable isomers of the $(N - 1)$-atomic and the N-atom Li (left) and Na (right) clusters. Due to the similarity function not being close to 1 for cluster sizes $N \leq 42$, a rather complex growth pattern is indicated for these smaller clusters. For

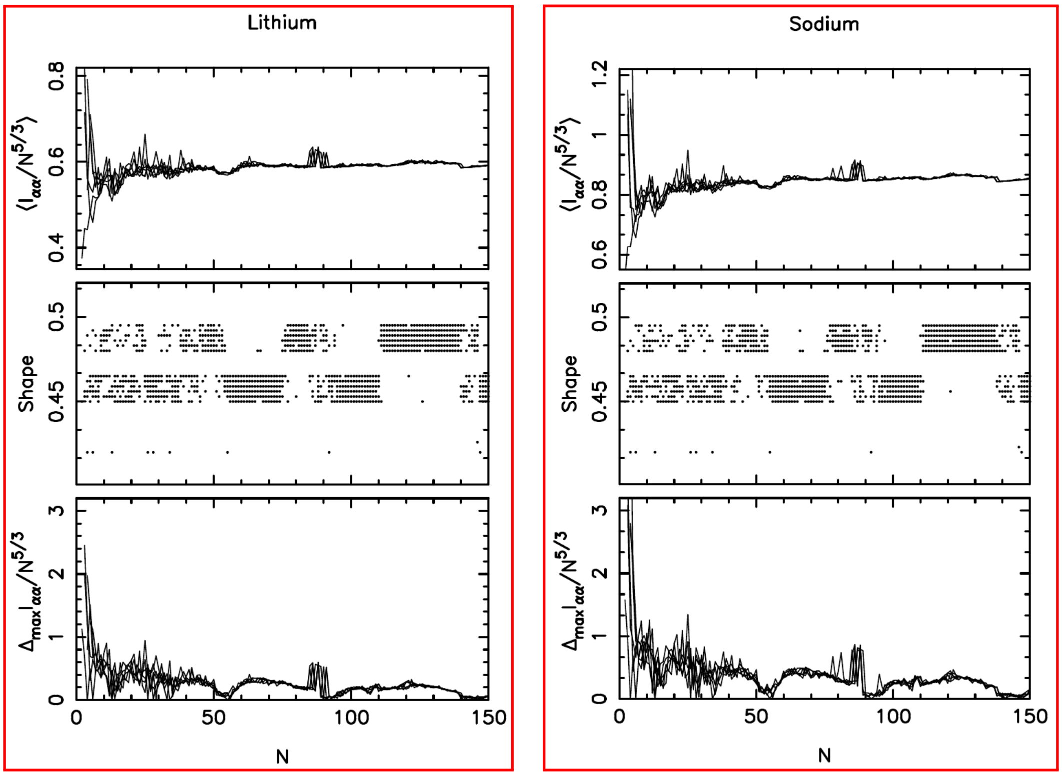
Shape analysis

Figure 10.7: Analysis of the shape of the Li (left) and Na clusters (right). Three quantities are used to describe the clusters' shape. The two upper panels depict the average of the eigenvalues $\langle I_{\alpha\alpha}\rangle$ (scaled by $N^{-5/3}$). The middle panels shows the overall shape of the clusters and the bottom panels depict the maximum eigenvalue difference. Within the middle panels, clusters of spherical, cigar and lens shape are depicted in the bottom, the middle and the top set of rows, respectively. Adapted by permission from Springer Nature: Springer, *J. Clust. Sci.*, Global Optimization of Li and Na Clusters: Application of a Modified Embedded Atom Method, K. Huwig, V. G. Grigoryan and M. Springborg, Copyright 2019.

both alkali metals the cluster sizes around $10 \leq N \leq 24$ are exceptions and a pronounced similarity can be observed within this size range. Furthermore, there are larger peaks for Li ($N = 6-9, 25-29, 32-34, 40-42, 87, 90$) and Na ($N = 6-9, 25-30, 32, 41, 42, 87, 90$), representing a lower degree of similarity for the N- and $(N-1)$-atom structures for these cluster sizes. With a few exceptions (C_2 for $N = 90$), the aforementioned Li and Na clusters often are of higher symmetry. The low similarity indices found for several cluster sizes, indicate that also the energetically higher-lying isomers may contribute to the growth patterns of the alkali metal clusters. It can be noticed that in many cases, the most stable isomers of a cluster size N are not very similar to a structure with $N-1$ atoms.

In order to study the role of the metastable cluster structures we also calculate the similarity function S_d for the comparison of the lowest-energy isomers of the N-atomic clusters with all six isomers of the clusters with $N-1$ atoms. Also here, the lowest value $q_{d,\min}$ is kept and S_d is calculated. The results of this investigation are depicted in the middle panel of figure 10.8. Obviously, many of the pronounced peaks (e.g. at $N = 87$ and $N = 90$) that could be identified within the uppermost panels, disappeared within the middle panels. Several metastable isomers of cluster size $N-1$ are more similar to the first isomer of a N-atom structure than the corresponding $(N-1)$-atomic system of lowest energy. Especially for larger cluster sizes, i.e. $N > 133$ for Li and $N > 127$ for Na, a high degree of similarity can be observed, with S_d being close to 1.

Which of the isomers with $N-1$ atoms exhibits the highest degree of similarity to the most-stable N-atom cluster? We adress this issue within the bottom panels in figure 10.8. For Li as well as for Na for smaller cluster sizes with $N \leq 24$, the lowest-energy isomers show the largest similarity. This is different for the larger clusters, where also the higher-lying isomers play a pivotale role in the growth process. This finding is in accordance with the results depicted in the upper two panels in figure 10.8. In order to understand the complex growth patterns of the alkali metal clusters it is necessary to take into account the most-stable as well as the higher-lying isomers of these systems.

How similar are the Li/Na clusters and the corresponding bcc crystal? We will investigate this question below. In order to calculate the similarity function S_r [105, 106] the clusters' radial distances

$$r_n = |\vec{R}_n - \vec{R}_0|, \tag{10.6}$$

have to be determined. Here, $\vec{R}_n$ and $\vec{R}_0$ represent the position vector of the *nth* atom and the center of the cluster, respectively. The radial distances r_n are calculated for

Growth patterns of Li and Na clusters

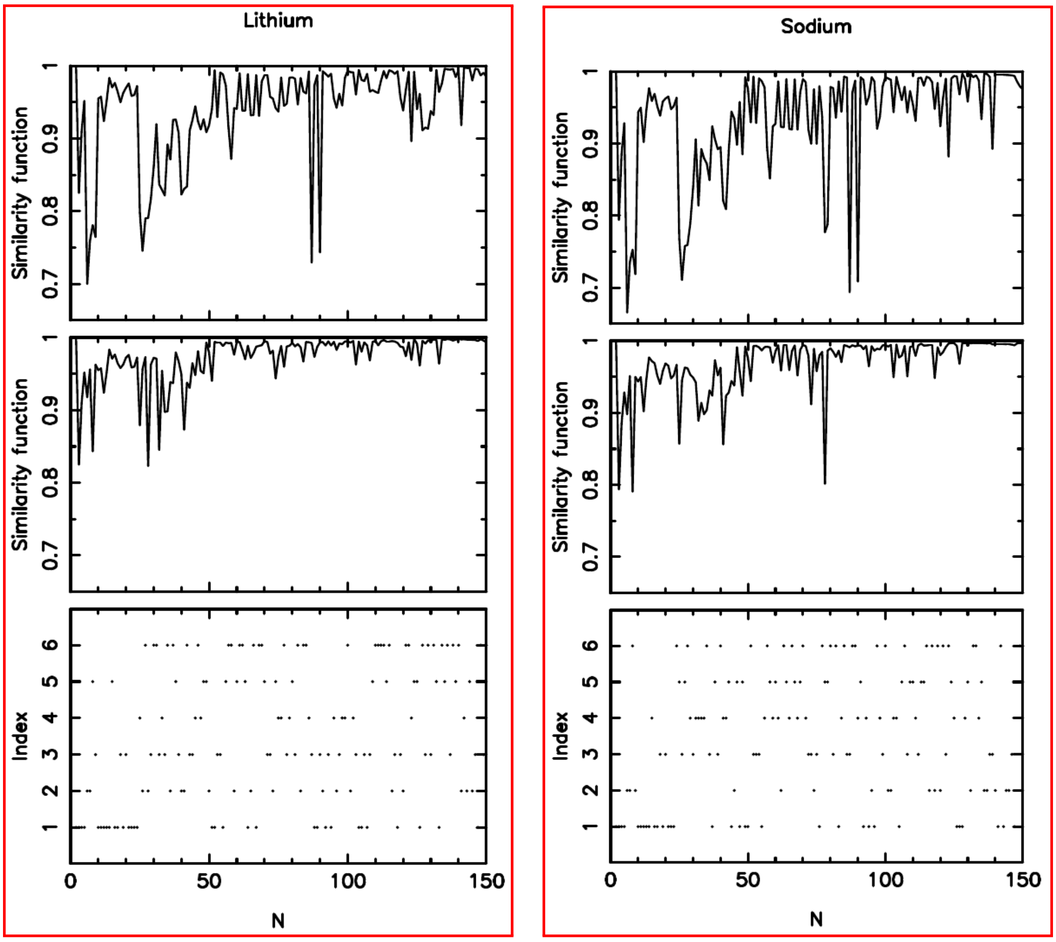

Figure 10.8: The growth patterns of Li (left panels) and Na clusters (right panels) are investigated using similarity functions. The two upper panels depict this similarity function, when comparing the most stable N-atomic cluster to the lowest-lying isomer with $(N-1)$ atoms. The two middle panels show the function, when the most stable cluster with N atoms is compared to each of the six isomers with $(N-1)$ atoms. The two lower panels depict which of the isomers in the latter case exhibits the highest degree of similarity to the N-atom cluster. Adapted by permission from Springer Nature: Springer, *J. Clust. Sci.*, Global Optimization of Li and Na Clusters: Application of a Modified Embedded Atom Method, K. Huwig, V. G. Grigoryan and M. Springborg, Copyright 2019.

each atom of a cluster and subsequently these distances are sorted in increasing order. Also for a spherical bcc fragment radial distances r'_n are calculated and sorted. Due to the non-uniqueness of the center of a crytal reference system three different centers were taken into account: the position of an atom within the crystal, the middle of the nearest-neighbour bond and the middle of a second-nearest-neighbour bond. Using the calculated radial distances r_n and r'_n, the quantity

$$q_r = \left[\frac{1}{N} \sum_{n=1}^{N} (r_n - r'_n)^2 \right]^{\frac{1}{2}} \tag{10.7}$$

is calculated. With the help of this q_r, it is possible to calculate the radial similarity function

$$S_r = \frac{1}{1 + \frac{q_r}{u_l}}, \tag{10.8}$$

with $u_l = 1$ Å being the unit length. The value of the similarity function S_r is close to 1, if there is a high similarity between a cluster and a bcc reference system. Moreover, according to our experience, only for values roughly above $S = 0.7$ any similarity exists between the two systems, which are compared.

In figure 10.9 the similarity functions S_r between all six isomers of the clusters and the three different bcc reference systems is shown (Li: left panels, Na: right panels). The upper, middle and lower panels depict this comparison with the bcc fragments with the center being placed at an atom, at the middle of a nearest-neighbour bond and at the middle of a second-nearest neighbour bond, respectively. In all three cases at least a marginal similarity between the Li and Na clusters and the corresponding crystal fragments can be found. The fragments with the centers being placed at the middle of a nearest- (middle panel) and second-nearest-neighbour bond (bottom panel) generally exhibit a little larger similarity to the clusters of the considered size range than the fragment with the center at an atomic position. In the latter case, the values for S_r range between 0.5 and 0.7, whereas the similarity functions takes values between 0.6 and 0.8 in the two lower panels. But within the upper panel it can be noticed that the cluster size range around $N = 17$ shows a larger similarity to the fragment with values above 0.8 for the similarity function S_r.

Figure 10.10 shows the similarity function S_r, when comparing to an isocahedral Li/Na cluster with 309 atoms (top panel) and three different fragments of a corresponding fcc crystal (three lower panels). The lattice constants of Ref. [200] were used to build the fcc reference systems. For both alkali metals a high similarity between the icosahedral

Similarity of the clusters with bcc fragments

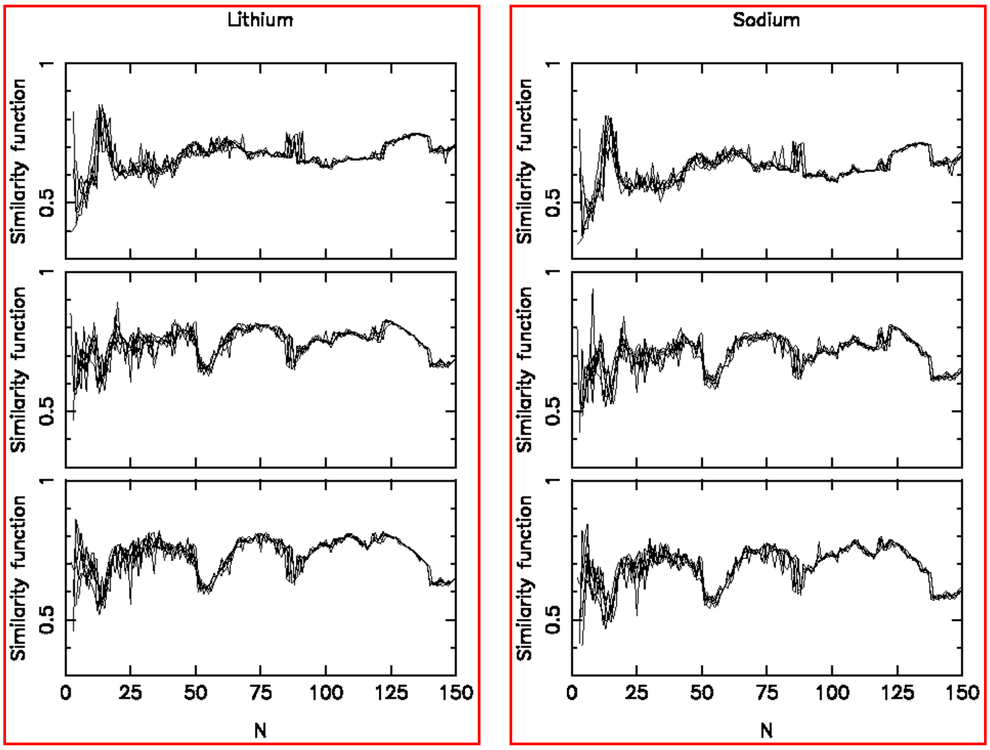

Figure 10.9: The similarity function, when comparing the Li and Na clusters to different bcc fragments (Li: left panels, Na: right panels). The center of the fragments are placed at the position of an atom (upper panels), at the middle of a nearest-neighbour bond (middle panels) and at the middle of a second-nearest neighbour bond (lower panels).

Mackay structures of cluster size $N = 13, 55$ and 147 and the 309-atom structure can be found. These are results to be expected. Due to the existence of icosahedral structural motifs for the cluster sizes around 13, 55 and 147 also these clusters exhibit similarity function values up to around 0.9. For both alkali metals a cluster at $N = 3$ shows a quite large similarity, with $S > 0.8$, to the icosahedron. This pronounced peak corresponds to the linear $\mathrm{Li}_{3.2}/\mathrm{Na}_{3.2}$. Obviously, these structures contain no icosahedral motifs, but the linear atomic arrangement within these clusters can be found within the 309-atom icosahedra. This leads to a relatively large similarity function S_r for this cluster size. The peaks at $N = 25$ correspond to the fourth most-stable isomers $\mathrm{Li}_{25.4}/\mathrm{Na}_{25.4}$. Both structures posses a D_{5d} point group. This fivefold symmetry belongs to a pentagonal subgroup of the icosahedral symmetry group. The three bottom panels on the left and right in figure 10.10 depict the similarity function, when comparing the clusters to a spherical fcc fragment with the center located at an atom (second top panel), at the middle of a nearest-neighbour bond (second lowest panel) and at the center of the cube (lowest panel). Here, similar observations can be made like for the comparison of the cluster structures with the bcc fragments, with the values for S_r in general ranging from 0.6 to 0.9. For the center being placed at the middle of a nearest-neighbour bond (second-lowest panel), on average the similarity function is slightly larger than for the other two fcc reference systems. Moreover, the most pronounced peaks occur for smaller clusters around $N = 4, 6, 8, 13$ (second uppermost and lowest panel) and for larger cluster sizes around $N = 55$ (second upper panel). So, for both, the bcc as well as the fcc case the fragments and the clusters are more or less similar to each other, with the similarity in principle being relatively small.

The radial distances r_n as function of the cluster size are depicted in figure 10.11 for the lowest energy isomers of the Li (left panel) and Na clusters (right panel). Only curves for the first isomers are shown, because the meta-stable isomers exhibit very similar function profiles. Each of the small horizontal lines in this figure represents at least one single atom for a N-atom cluster, that posseses this value. Shell constructions are visible around $N = 13$ as well as for $N = 55$. A drop in the radial distances indicates the formation of the first ($N = 13$) and second ($N = 55$) Mackay icosahedron, the lowest-energy isomers for Li and Na at these cluster sizes. A less smooth shape of the curves with sudden drops can be found for $N < 90$ for Li and Na. Again, this indicates a shell construction, where the magic clusters $\mathrm{Li}_{87.1}$ and $\mathrm{Na}_{87.1}$ are formed. Furthermore, one can identify shell constructions below and above $N = 140$, including the formation of the third Mackay icosahedron at $N = 147$.

As mentioned before, the structures of the Li and Na clusters are often quite similar (see

Similarity of the clusters to icosahedral structures and fcc fragments

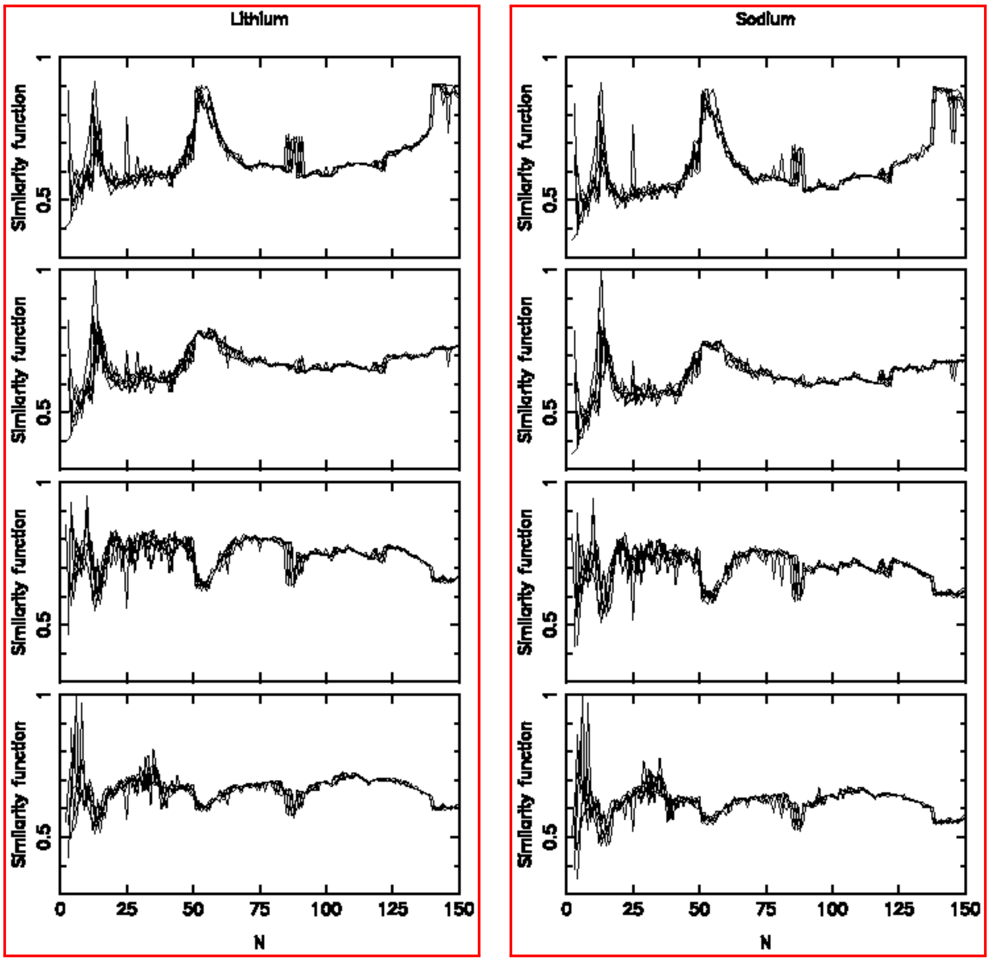

Figure 10.10: The similarity function, when comparing the Li and Na clusters to a 309-atomic icosahedron and different fcc fragments (Li: left panels, Na: right panels). The center of the fragmens are placed at the position of an atom (upper panels), at the middle of a nearest-neighbour bond (middle panels) and at the center of the cube (lower panels). Adapted by permission from Springer Nature: Springer, *J. Clust. Sci.*, Global Optimization of Li and Na Clusters: Application of a Modified Embedded Atom Method, K. Huwig, V. G. Grigoryan and M. Springborg, Copyright 2019.

Radial distances within the clusters

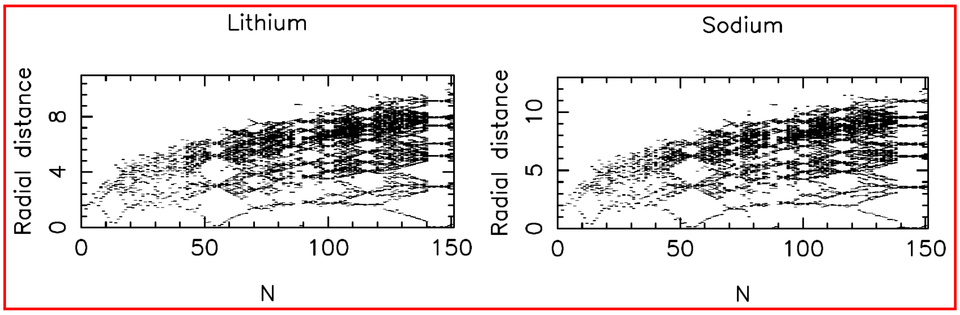

Figure 10.11: The radial distribution for lowest-energy isomers of the Li (left panel) and Na (right panel) clusters. Here, the radial distances (in Å) are shown as function of the cluster size N. Each small line within the panels indicates (at least) one atom with such a radial distance. Adapted by permission from Springer Nature: Springer, *J. Clust. Sci.*, Global Optimization of Li and Na Clusters: Application of a Modified Embedded Atom Method, K. Huwig, V. G. Grigoryan and M. Springborg, Copyright 2019.

e.g. the discussion on the smaller clusters in section 10.1.2). In the following a more detailed investigation of this observation is presented. In order to study the similarity of the clusters, the similarity function using the radial distances S_r (equations 10.6–10.8) is employed. The results of these calculations are shown in figure 10.12. To enable the comparison of the two systems the atomic coordinates of the clusters have been rescaled. First, the most stable N-atom Li isomers are compared to the lowest-energy structures of the Na_N clusters (top left panel) and vice versa (top right panel). Frequently pronounced peaks occur, while for the majority of the clusters, the similarity function is close to 1. The minima, located at $N = 33$, 40, 48, $72 - 74$, 78 and 139, indicate relatively large structural differences for the most-stable isomers of the Li and Na clusters for these cluster sizes. In this case, also the higher-lying isomers may have to be investigated. Therefore, the middle panels in figure 10.12 depict the similarity between the Li and Na clusters, when considering all six isomers of lithium (left middle panel) and sodium (right middle panel). It can be noticed that many of the minima that could be observed in the uppermost panels, can not be identified within the middle panels of figure 10.12 anymore. This means that there are also a few cluster sizes, for which a metastable cluster geometry of the one system exhibits a larger similarity to the first isomer of the other system. Predominantly this is due to a different energetic ordering of the lithium and sodium cluster for a certain cluster size (see tables with cluster structures in the appendix A). But there are also some cluster geometries for one system, which do not belong to the six most-stable structures of the other system. Such cases are indicated by the remaining pronounced peaks in the middle panel of figure 10.12. Moreover, the bottom panels depict, which of the six lowest-lying isomers of the one system (left: Na, right: Li) shows the highest degree of similarity to the putative global minima of the other system (left: Li, right: Na). Obviously, also in accordance with chemical intuition and experience, in most cases the most-stable cluster geometries of Li and Na clusters correspond to each other. This can be explained by the very similar chemical as well as physical properties of both alkali metals, which is a consequence of the same electronic configuration of the valence-shell of Li and Na. However, as recognized before, there are also cluster sizes, for which meta-stable isomers of the one system exhibit a higher similarity to the minimum structure of the other system. From the bottom panels of figure 10.12 it can be seen that the second-most stable isomers are the most common ones among the energetically higher-lying structures.

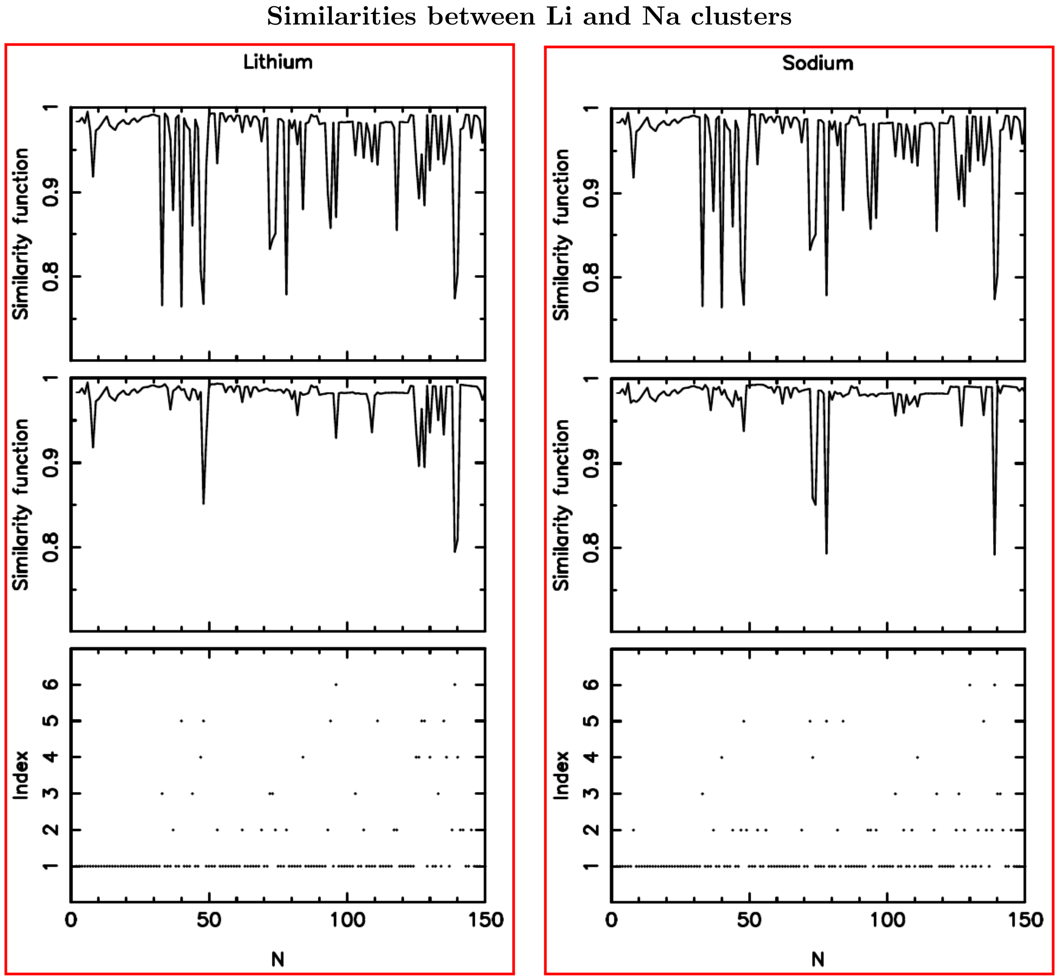

Figure 10.12: The Li and Na clusters (lithium: left, sodium: right) are compared to each other employing the similarity function using the radial distances. The upper two panels depict the similarity of the lowest-lying isomers of both systems. The two middle panels show the similarity function, in case of comparing all six sodium cluster isomers of a certain cluster size to the putative global minimum structure of Li of the same size (left panel) and vice versa (right panel). Which isomer is the most similar to the global minimum of a Li (left panel) or a Na cluster (right panel) is depicted within the bottom panels. Adapted by permission from Springer Nature: Springer, *J. Clust. Sci.*, Global Optimization of Li and Na Clusters: Application of a Modified Embedded Atom Method, K. Huwig, V. G. Grigoryan and M. Springborg, Copyright 2019.

10.2.3 Clusters with special structural features

As previously mentioned in section 10.1.2, sometimes the MEAM yields clusters that are usually not the result of that kind of model potentials. Such clusters showing special structural features may be planar/linear or may exhibit another certain exceptional atomic arrangement. Planar or linear cluster geometries are special within an approach like the MEAM, because such potentials show a strong preference for densely packed, highly-coordinated structures. Exceptional atomic arrangements may be very symmetric clusters with interesting geometries, e.g. star-shaped clusters.

Smaller clusters with special structural features

The smaller MEAM clusters with special atomic arrangements are depicted in figure 10.13. Additionally theirs point groups and the energy difference to the corresponding putative global minima of this cluster size are shown. Clusters with linear geometries and $D_{\infty h}$ symmetries are found for $\mathrm{Li}_{3.2}$, $\mathrm{Na}_{3.2}$ as well as $\mathrm{Na}_{4.6}$. Furthermore the MEAM yields two-dimensional structures for clusters with 4 and 5 atoms. $\mathrm{Li}_{4.2}$ and $\mathrm{Na}_{4.2}$ both are planar rhombuses, each with a D_{2h} symmetry. A simple square (point group: D_{4h}) is obtained for $\mathrm{Li}_{4.4}$ as well as $\mathrm{Na}_{4.3}$. Additionally the five-atom clusters $\mathrm{Li}_{5.4}$ and $\mathrm{Na}_{5.5}$ are planar and each posseses a C_{2v} point group. However, these linear and planar clusters are always less stable than the corresponding lowest-energy isomers. From figure 10.13 it can be noticed that the higher coordinated global minima are at least 100 meV lower in energy than these clusters. Although the MEAM predicts these clusters as being stable, theirs stabilities are significantly lower than that of the compact, high coordinated and three-dimensional lowest-energy isomers. In general, such low coordinated linear or planar structures are the result of higher-level theory like *ab initio* or DFT approaches and for these methods these structures are often the most-stable isomers [184, 185, 187].

Larger clusters with special structural features

Also some of the larger alkali metal clusters exhibit interesting structural arrangements. These are depicted in figure 10.14. Since in most cases the geometries of the Li and Na clusters do not differ, only the sodium clusters are shown.

$\mathrm{Na}_{22.6}$ is a hexagonal double antiprism, where the two hexagonal faces each are capped by a single sodium atom. This structure with D_{6h} symmetry is not among the six lowest-energy isomers of the Li clusters. For Na, the putative global minimum structure for this cluster size is a triple icosahedron minus an atom at a pentagonal ring. This GM structure is 46 meV more stable than $\mathrm{Na}_{22.6}$.

Smaller clusters exhibiting special structural features.

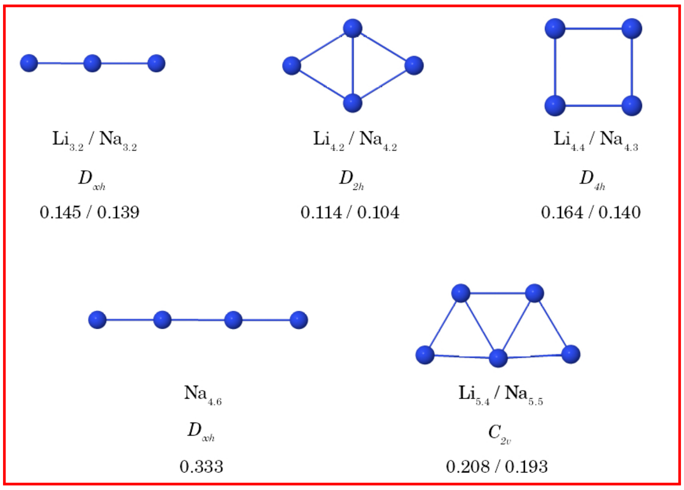

Figure 10.13: Planar and linear cluster geometries for cluster sizes $N = 3, 4, 5$. Below the structure the second line shows the symmetry (point group) and the third line denotes the energy difference between each of the structures and the putative global minimum in eV obtained with the MEAM for this cluster size. Again the Li and Na clusters exhibit similar geometries. Therefore, we only show the structures of the sodium clusters. Adapted by permission from Springer Nature: Springer, *J. Clust. Sci.*, Global Optimization of Li and Na Clusters: Application of a Modified Embedded Atom Method, K. Huwig, V. G. Grigoryan and M. Springborg, Copyright 2019.

A star-shaped cluster geometry is obtained for $\mathrm{Li}_{34.2}/\mathrm{Na}_{34.3}$. It exhibits a D_{5h} point group and is ten-pointed. The DFT calculations of Ref. [154] yield this cluster geometry for the 34-atom Na cluster as lowest-energy isomer.
Bimetallic clusters may adopt pancake-like geometries [201, 202]. Such a flat, highly-symmetric atomic arrangement (point group: D_{6h}) is also obtained for the monometallic $\mathrm{Li}_{38.4}$ and $\mathrm{Na}_{38.5}$ clusters.

Larger clusters exhibiting special structural features.

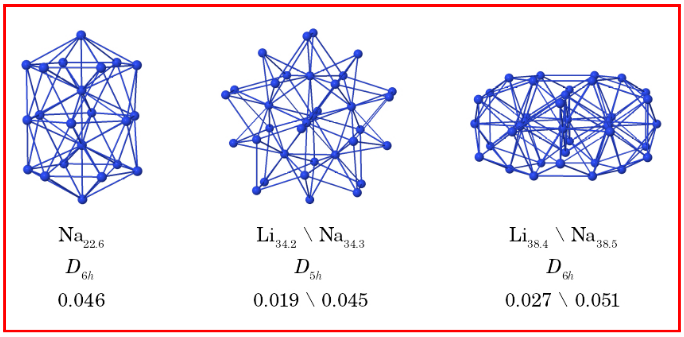

Figure 10.14: Larger clusters with special geometries. Below the structure the second line shows the symmetry (point group) and the third line denotes the energy difference between each of the structures and the putative global minimum in eV obtained with the MEAM for this cluster size. Again the Li and Na clusters exhibit similar geometries. Therefore, we only show the structures of the sodium clusters. Adapted by permission from Springer Nature: Springer, *J. Clust. Sci.*, Global Optimization of Li and Na Clusters: Application of a Modified Embedded Atom Method, K. Huwig, V. G. Grigoryan and M. Springborg, Copyright 2019.

10.2.4 The magic cluster sizes for Li and Na

In this section we study the magic cluster sizes for Li and Na obtained with the MEAM in more detail. They are compared to the results of other studies, with the cluster sizes of the other investigations not necessarily belonging to the magic numbers for these calculations. In most cases, Li and Na posses the same magic numbers and cluster geometries. Therefore, only the structures of the sodium clusters are depicted.

Magic numbers for cluster sizes $N \leq 80$

For smaller cluster sizes $N \leq 80$ the magic numbers as well as their point groups are listed in table 10.4. Moreover, in figure 10.15 the corresponding cluster structures for Na are depicted. For the 74-atom system the lowest-energy isomer for Li exhibits a different geometry than the Na cluster and $\mathrm{Li}_{74.1}$ does not belong to the magic cluster sizes, but

$Na_{74.1}$ does. In general, most of the magic numbers show a compact atomic arrangement with a high symmetry. But some of the clusters are also of lower symmetry (e.g. Li_{49}). For $N = 13$, the MEAM yields the first Mackay icosahedron for both alkali metals (point group: I_h). This geometry is build up successively beginning with the doubly-capped pentagonal bipyramid at $N = 9$. Atom by atom is added, whereat for example the tri-capped ($N = 10$) and quadruply-capped ($N = 11$) pentagonal bipyramides are formed until the 13-atom isosahedron is obtained. This finding mainly agrees with the results of the other investigations for $Na_{13.1}$ (see table 10.4). All model potentials (EAM [157], G [195], MM [195]) yield the first Mackay icosahedron as $Na_{13.1}$, whereas clusters with C_2 symmetry are obtained with the DFTB approach [157] and DFT reoptimized Gupta calculations [156]. Moreover, the DFT-GGA (GGA = generalized-gradient approximation) study of Ref. [154] list the icosahedron for Na_{13} as third isomer. For $Li_{13.1}$ the results of the DFT calculations of Ref. [181] correspond to the results of our model calculations, while a lower-symmetry cluster (C_s) is obtained within another study [187].

For our study, the double icosahedron $Li_{19.1}$/$Na_{19.1}$ (point group: D_{5h}) is a magic number. Again, the EAM [157], the G [195] and the MM [195] method also give this structure in accordance with our calculations. As for Na_{13} the DFT reoptimized Gupta calculations [156] and the DFTB computations [157] yield sodium clusters with lower symmetry. Both DFT studies listed in table 10.4 do not yield the double icosahedral structure for $Li_{19.1}$. Instead of the D_{5h} geometries, clusters with C_{2v} symmetry are obtained within these investigations [181, 187].

At $N = 23$ we obtain the triple icosahedron as putative global minimum for Li and Na. Also for this magic size the results of the other model calculations [157, 195] for sodium agree with our investigations.

The magic numbers obtained with the MEAM model for Na and that reported for the EAM study of Ref. [157] coincide up to this cluster size. At $N = 39$ and 49 the MEAM yields magic clusters, which do not belong to the magic sizes for this EAM calculations. The magic clusters $Li_{39.1}$/$Na_{39.1}$ both posses a D_5 point group and they exhibit a similar geometry like the C_5 structures for $Na_{39.1}$ obtained with the G and MM potential [195]. Compared to $Na_{49.1}$ (C_{3v}), $Li_{49.1}$ is slightly distorted and has a reduced symmetry with a C_3 point group. Both, the Li and Na cluster with 49 atoms are derived from the second Mackay icosahedron at $N = 55$ by removing a face consisting of six atoms. Concerning the other studies for Na listed in table 10.4, only the MM calculations [195] yield the same geometry with a C_{3v} point group, whereas the Gupta potential [195] gives a C_{5v} structure and the DFT reoptimized Gupta computations [156] give a cluster with lower symmetry (C_1).

For the cluster size $N = 55$ the results of the present study for Na correspond to that of the other theoretical investigations that are listed in table 10.4. All calculations yield the undistorted second Mackay icosahedron (point group: I_h). This is confirmed by other theoretical [154] and experimental [203] studies. Using photoelectron spectroscopy and melting experiments the latter predict a closed-shell icosahedron for the 55-atom Na cluster. The DFT calculations of reference [204] confirm the the Mackay icosahedron as lowest-energy structure for Li_{55}.

$\mathrm{Li}_{71.1}$ and $\mathrm{Na}_{71.1}$ exhibit a prolate shape and have a C_5 point group. Here, the G as well as the MM calculations agree with our study. This structure may be described as 55-atomic Mackay icosahedron with an additional cap, consisting of 16 atoms, attached to its vertex [155]. Within reference [156] the 71-atom cluster is a less twisted, higher symmetric version of the clusters found with the MEAM model.

Being a magic number for sodium, the cluster of size $N = 74$ is not magic for lithium. $\mathrm{Na}_{74.1}$ is of high symmetry with a D_{3d} point group, whereas the lowest-energy isomer for Li_{74} exhibits a lower C_2 symmetry. For the G model [195] the most-stable 74-atomic Na cluster exhibits a similar geometry as our D_{3d} structure, but posseses a lower symmetry (C_{2h}). The dihedral atomic arrangement for $\mathrm{Na}_{74.1}$, found within the present study, is also obtained for the calculations of reference [195] (MM potential) and [156] (DFT reoptimized Gupta calculations).

Magic numbers for cluster sizes $N > 80$

Next, we discuss the larger magic numbers for $80 < N \leq 150$. The point groups of the Li and Na clusters obtained with the MEAM as well as the results of other investigations are shown in table 10.5. Also in this size range the geometries of the magic lithium and sodium clusters are largely the same, which is why only the structures of the Na clusters are shown in figure 10.16.

The MEAM yields dihedral 83-atom magic clusters (D_3) for Li and Na. The G potential [195] also predicts this geometry and symmetry for this cluster size. A distorted version of this structure (point group: C_1) is obtained with the MM model [195].

While our MEAM calculations give prolate 87-atomic Li and Na clusters (point group: D_{5h}), both the G and the MM potential yield other structures, with C_s (G) and C_{2v} (MM) symmetries. The D_{5h} geometries of our study are build up by a shell construction, where a 16-atom cap is attached to the top of the second isomers $\mathrm{Li}_{71.2}$ and $\mathrm{Na}_{71.2}$. This construction can also be noticed, when examining figure 10.11 in section 10.2.2, where a abrupt drop in the radial distance can be observed below $N = 90$ for both alkali metals. At $N = 92$ the Li and Na clusters exhibit a tetrahedral symmetry, which is substantiated

Table 10.4: The symmetries of smaller magic alkali clusters (Li and Na) for cluster sizes $N \leq 80$ obtained in the present study. They are compared to structures of other investigations. Adapted by permission from Springer Nature: Springer, *J. Clust. Sci.*, Global Optimization of Li and Na Clusters: Application of a Modified Embedded Atom Method, K. Huwig, V. G. Grigoryan and M. Springborg, Copyright 2019.

N	Ref.	Method	Li	Na	***N***	Ref.	Method	Li	Na
13	Here	MEAM	I_h	I_h	**39**	Here	MEAM	D_5	D_5
	[181]	DFT	I_h	—		[195]	G	—	C_5
	[187]	DFT	C_s	—		[195]	MM	—	C_5
	[157]	DFTB	—	C_2	**49**	Here	MEAM	C_3	C_{3v}
	[157]	EAM	—	I_h		[195]	G	—	C_{5v}
	[195]	G	—	I_h		[195]	MM	—	C_{3v}
	[195]	MM	—	I_h		[156]	G/DFT	—	C_1
	[156]	G/DFT	—	C_2	**55**	Here	MEAM	I_h	I_h
						[204]	DFT	I_h	—
19	Here	MEAM	D_{5h}	D_{5h}		[157]	EAM	—	I_h
	[181]	DFT	C_{2v}	—		[195]	G	—	I_h
	[187]	DFT	C_{2v}	—		[195]	MM	—	I_h
	[157]	DFTB	—	C_1		[156]	G/DFT	—	I_h
	[157]	EAM	—	D_{5h}	**71**	Here	MEAM	C_5	C_5
	[195]	G	—	D_{5h}		[195]	G	—	C_5
	[195]	MM	—	D_{5h}		[195]	MM	—	C_5
	[156]	G/DFT	—	C_s		[156]	G/DFT	—	D_5
23	Here	MEAM	D_{3h}	D_{3h}	**74**	Here	MEAM	C_2	D_{3d}
	[157]	EAM	—	D_{3h}		[195]	G	—	C_{2h}
	[195]	G	—	D_{3h}		[195]	MM	—	D_{3d}
	[195]	MM	—	D_{3h}		[156]	G/DFT	—	D_{3d}

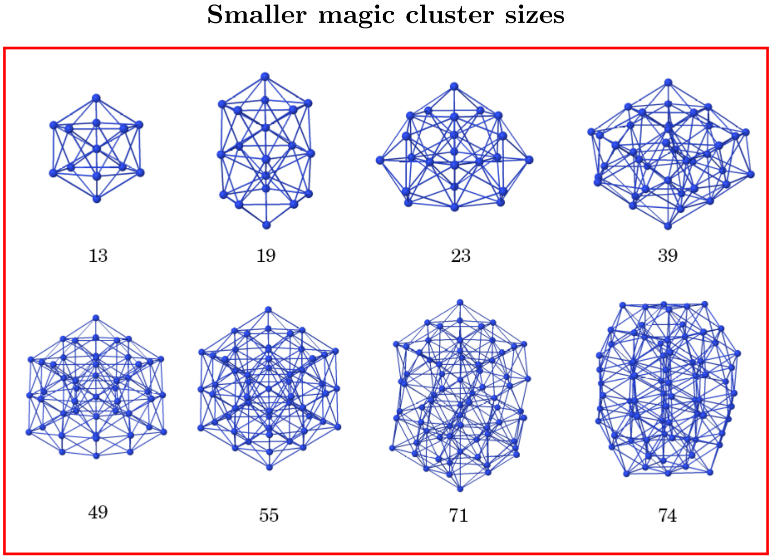

Figure 10.15: Structures for the magic cluster sizes with $N \leq 80$. Since the geometries of the Li and Na clusters predominantly match, only the sodium clusters are shown. Adapted by permission from Springer Nature: Springer, *J. Clust. Sci.*, Global Optimization of Li and Na Clusters: Application of a Modified Embedded Atom Method, K. Huwig, V. G. Grigoryan and M. Springborg, Copyright 2019.

by the results obtained for the Gupta potential of reference [195]. As for the 83-atomic cluster the MM calculations [195] predict a less symmetric cluster geometry with a C_1 point group.

$Li_{95.1}$ and $Na_{95.1}$ both show a rotational symmetry and posses a C_3 point group. This is in accordance with the other investigations listed in table 10.5, but where, for example, $Na_{95.1}$ is not a magic number for the Gupta method [195].

The 101-atom Li cluster exhibits a D_3 point group, whereat $Na_{101.1}$ is distorted and less symmetric (C_3). Furthermore, the magic size at $N = 104$ posseses a twofold rotational symmetry (point group for $Li_{104.1}$/$Na_{104.1}$: C_2). Here, the two other model potentials (G and MM) [195] yield different geometries and point groups for the 104-atom cluster (D_5 (G), C_1 (MM)). Moreover, this cluster size is no magic number for these two approaches [155].

For Na (as well as Li), the lowest-energy isomer with 116 atoms has a D_5 symmetry and is a distorted, twisted version of the $Na_{116.1}$ cluster obtained with the MM model (D_{5h}) [195]. The Gupta calculations yield a different structure with a C_{5v} point group, which is no magic number for this model potential [155, 195]. Experimental investigations also predict a 116-atom magic cluster for Na [203].

Within the other investigations (see table 10.5) the 131- and 137-atom Na clusters do not belong to the magic cluster sizes and are only identified as magic numbers for our MEAM calculations [155]. $\mathrm{Li}_{131.1}$ and $\mathrm{Li}_{137.1}$ are also magic according to our study. Furthermore, the point groups of the MEAM structures obtained for these cluster sizes differ from those of the other model potentials. $\mathrm{Na}_{131.1}$ and $\mathrm{Li}_{131.1}$ both posses a C_{2v} symmetry, whereas the sodium clusters for the other calculations exhibit lower symmetries (G: C_s and MM: C_2) [195]. Also the geometries of the 137-atomic Li and Na systems differ among the considered studies. Here, we identify a C_{3v} point group for $\mathrm{Li}_{137.1}$ and $\mathrm{Na}_{137.1}$, but for $\mathrm{Na}_{137.1}$ a D_{5d} and C_{2v} symmetry is predicted by the Gupta and MM model [195], respectively.

This is different for the cluster with 147 atoms. Our MEAM approach yields the third Mackay icosahedron for $\mathrm{Li}_{147.1}/\mathrm{Na}_{147.1}$ which is in accordance with the results of the other studies that are shown in table 10.5 [195, 204]. The existence of a icosahedral geometry for the 147-atomic Na cluster is also predicted by experimental investigations [203].

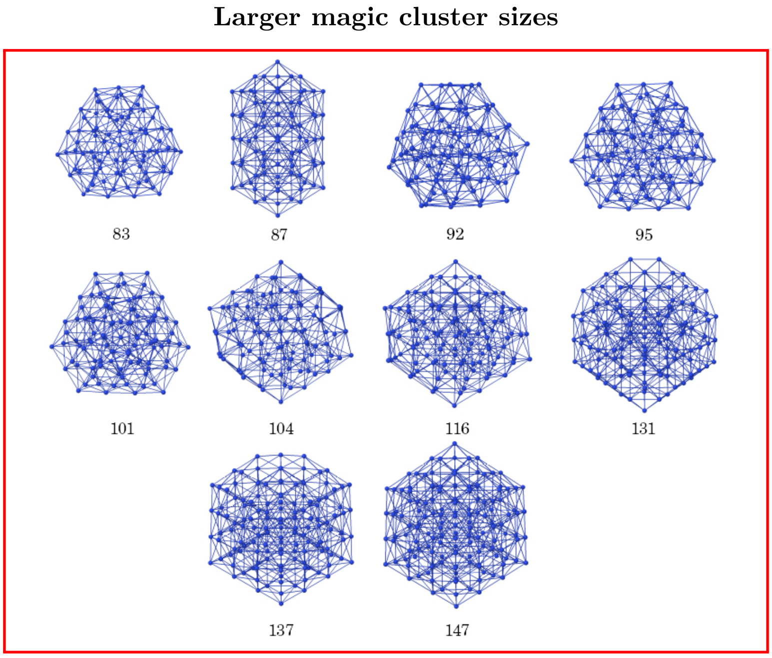

Figure 10.16: Structures for the magic cluster sizes with $N > 80$. Since the geometries of the Li and Na clusters predominantly match, only the sodium clusters are shown. Adapted by permission from Springer Nature: Springer, *J. Clust. Sci.*, Global Optimization of Li and Na Clusters: Application of a Modified Embedded Atom Method, K. Huwig, V. G. Grigoryan and M. Springborg, Copyright 2019.

Table 10.5: The symmetries of larger magic alkali clusters (Li and Na) for cluster sizes $N > 80$ obtained in the present study. They are compared to structures of other investigations. Adapted by permission from Springer Nature: Springer, *J. Clust. Sci.*, Global Optimization of Li and Na Clusters: Application of a Modified Embedded Atom Method, K. Huwig, V. G. Grigoryan and M. Springborg, Copyright 2019.

$\boldsymbol{N}$	Ref.	Method	Li	Na	$\boldsymbol{N}$	Ref.	Method	Li	Na
83	Here	MEAM	D_3	D_3	**104**	Here	MEAM	C_2	C_2
	[195]	G	—	D_3		[195]	G	—	D_5
	[195]	MM	—	C_1		[195]	MM	—	C_1
87	Here	MEAM	D_{5h}	D_{5h}	**116**	Here	MEAM	D_5	D_5
	[195]	G	—	C_s		[195]	G	—	C_{5v}
	[195]	MM	—	C_{2v}		[195]	MM	—	D_{5h}
92	Here	MEAM	T	T	**131**	Here	MEAM	C_{2v}	C_{2v}
	[195]	G	—	T		[195]	G	—	C_s
	[195]	MM	—	C_1		[195]	MM	—	C_2
95	Here	MEAM	C_3	C_3	**137**	Here	MEAM	C_{3v}	C_{3v}
	[195]	G	—	C_3		[195]	G	—	D_{5d}
	[195]	MM	—	C_3		[195]	MM	—	C_{2v}
101	Here	MEAM	D_3	C_3	**147**	Here	MEAM	I_h	I_h
	[195]	G	—	D_3		[204]	DFT	I_h	—
	[195]	MM	—	D_3		[195]	G	—	I_h
						[195]	MM	—	I_h

11 Conclusions and outlook

An energetic and structural global optimization of alkali metal clusters has been performed using a simple, semiempirical modified embedded atom method (MEAM). For both, Li and Na clusters we considered cluster sizes N with $2 \leq N \leq 150$ and up to six isomers per cluster size. A two-step optimization procedure has been employed. Initially, the clusters are generated randomly and the *variable metric/quasi-Newton* method is used to relax the structures locally. From those calculations we keep up to six lowest-energy isomers for each cluster size, which serve as input structures for the following *Aufbau-Abbau* algorithm. A bash script is used to automatize this second step. Moreover we have performed a detailed energetic and structural analysis of the obtained Li and Na clusters, including the magic numbers and the growth patterns. We obtained interesting results, which are surprising to some extent. But the majority of our findings are to be expected for a model potential like the MEAM.

We were able to perform a thorough investigation of the clusters' potential hypersurfaces, because the optimization of a single cluster structure is quite fast. This is due to the analytical formulae for the total energy of a system within the MEAM. The first derivatives of these expressions, which are needed for local relaxations with the *quasi-Newton* approximation, are derived easily. Even for larger cluster sizes it is possible to optimize millions of clusters. Based on this extensive studies, it can be assumed that our identified putative global minima are realistic within the framework of a semiempirical model potential.

The bond length of the Li and the Na dimer obtained with MEAM are in accordance with the findings of other theoretical approaches and experimental studies. Already for smaller cluster sizes $N \leq 3$, it becomes obvious that the MEAM prefers compact clusters with higher coordinated atoms. As for other model potentials, i.e. the Gupta or Murrell-Mottram method, the cluster structures of the MEAM are dictated by packing effects. But the latter method exhibits some special features. Some of the metastable isomers of the cluster sizes $N = 3, 4$ and 5 are of planar and/or linear geometries. Such cluster structures are normally obtained with higher-level theory, but not with simple, semiempirical model potentials as the MEAM.

The cluster sizes that have been investigated within this study are not large enough to reach the bulk properties of lithium or sodium. This becomes obvious, when examining the binding energy, the coordination numbers and bond lengths between the atoms of the clusters. Additionally, a more dense atomic arrangement than within bcc crystals can be found for some of the clusters of considered size range.

Concerning the analysis of the clusters' shapes, there are cluster size ranges in which a certain shape is predominant and the lowest-energy isomers of Li and Na clusters almost exclusively exhibit spherical, compact shapes. In principle, lithium and sodium show the same cluster shapes for similar cluster sizes. Analysis of the growth patterns reveals that also metastable isomers seem to play a role in the growth process of the Li and Na clusters. A rather simple growth pattern can not be identified for the whole cluster size range under study and in order to understand the growth processes of clusters the importance of considering several isomers becomes evident.

As already indicated by the shape analyis, the geometries of most of the putative global energy minima of the Li and Na clusters correspond to each other, which is also largely true for higher-lying isomers. This is in accordance with chemical intuition. Li and Na posses a similar valence shell configuration and exhibit similar chemical and physical properties. Hence, both systems might prefer similar cluster geometries, too. And indeed, as our findings show, this is the case for the lithium and sodium clusters. Furthermore, the clusters have been compared to bcc as well as fcc crystal fragments. In both cases the clusters exhibit some similarity to the corresponding crystal reference systems, although this resemblance is not very pronounced for the majority of the clusters.

We also performed a detailed analysis of the magic cluster sizes. With our approach we almost exclusively obtain the same magic sizes for the Li and Na clusters, which also posses the same geometries and symmetries. Many of the magic numbers predicted by the MEAM for Na are also found for other model potentials, e.g. the strongly pronounced energetic maxima at $N = 13,\ 55$ and 147, representing the highly-symmetric Mackay icosahedra. Additionally, there are several clusters of enhanced stability, which have not been mentioned in previous studies. These include the magic sizes $N = 74,\ 83,\ 87,\ 95,\ 104,\ 131$ and 137. However, other studies yield some magic numbers that have not been identified with the present approach. Except for a few low-symmetric magic clusters, e.g. the 95-atom cluster (point group: C_3) and the cluster with 104 atoms (point group: C_2), most of the magic clusters are of higher symmetry, with a compact, almost spherically-shaped geometry. Theoretical methods that include electronic degrees of freedom, yield even magic numbers. With the MEAM, which does not explicitly include electronic but packing effects, even and also odd magic numbers are obtained.

A large amount of data has been produced during this global optimization study, since we have considered Li_N and Na_N clusters with $2 \leq N \leq 150$ and up to six isomers for each cluster size. Following studies may make use of this huge quantities of data and push forward the research activities on the alkali metal clusters. With regard to the "direct approach“, discussed in the very beginning of this thesis in chapter 5, various properties of the minimum structures may be calculated. Examples include the thermodynamic or the vibrational behaviour of the Li and Na clusters. Additionaly, many of the clusters' properties, e.g. the melting behaviour, require the lowest-energy isomer and also the metastable cluster structures. Here, only considering the global minimum structure may lead to unreliable and inaccurate cluster properties.

Part III

Global property optimization: sunlight harvesting and adsorption properties

The previous part II of this thesis dealt with the automatic computational determination of the lowest-energy structures of certain systems (global energy optimization, GEO), in this case: alkali metal clusters. The present part adresses the question of the automatic computational identification of optimal structures concerning properties different from the total energy. We call it a global property optimization (GPO). In the following, two different GPO tasks are presented: the optimization of organic solar cell materials and the optimization of the adsorption properties of transition-metal surfaces.
Chapter 12 presents the optimization of benzene with varying functional groups with respect to solar-energy harvesting properties [205]. Here, benzene is chosen as simple model system to represent a dye-sensitized solar cell material. In reality, more complex systems like substituted porphyrins are used for dye-sensitized solar cells (DSSCs). Hence, the use of the model system benzene within this study should be considered as a first approach and that, in principle, it is possible to determine automatically systems with optimal properties different from energy. The sunlight harvesting properties are approximated by using simple mathematical descriptions that may have an influence on the solar light absorption and conversion of sunlight. Therefore, the properties presented are to be considered as recommendations that may have a more or less strong influence on the optical properties of real systems for DSSCs. Depending on the considered system also other properties may be important and a decision which of them should be considered has to be made with regard to the corresponding system.

In chapter 13 our inverse design (ID) approach (PooMa) is extended to optimize transition metal surfaces with respect to their adsorption performance of simple molecules. Since we are interested in strong interactions between the surface and the molecules and because of they have been studied extensively, Ni, as well as Ti surfaces have been chosen as test systems. Within these adsorption studies, a single simple property is considered, the adsorption energy. A glance at the literature shows that the latter is actually always used to describe the adsorption properties of surfaces and therefore we consider it to be a good approach for our study.

Within both GPO studies, described within this thesis, our goal is to investigate many systems and to identify trends. Trends that show, which substitution pattern or which surface composition may be ideal for a certain property. Therefore, we do not seek for a maximal accuracy and we rather use many approximations that allow for an extensive search of the property hypersurfaces, in analogy to the use of the simple MEAM potential for the GEO of the alkali metal clusters. This makes our ID approach quite simple and fast with no need for expensive hardware. Additionally, since we perform theoretical studies, no expensive laboratory equipment is needed. Therefore we call our approach the "Poor Man's Material optimization" (PooMa).

Within the GPO of molecules for applications in dye-sensitized solar cells, we define an organic backbone, e.g. porphyrine or in this study benzene. To this core system various substituents, single atoms and functional groups, may be attached. The goal is to indentify automatically the type and positions of substituents that optimize a predefined optical property. In the case of adsorption properties, the core is represented by a transition metal surface. The position on this surface may be occupied by a metal atom or a vacancy. Here, the number and positions of atoms and vacancies on the surface, which give the optimal adsorption performance is determined automatically. In addition, we also consider different adsorption sites on the surfaces.

In principle, the PooMa approach can be applied to many different problems, but there are some basic principles which the different PooMa studies have in common. The following points are essential components of our PooMa approach, which are adapted according to the systems and properties under study [52, 205]:

1. The representation of chemical compounds by an array of N integers. Each integer describes a different kind of substituent or component within the system, e.g. an atom, a functional group or a vacancy. For a certain optimization problem within PooMa there are K such different components which can be chosen. With N being the number of positions that can be occupied by the K different chemical groups, this gives K^N possible systems for such an optimization task. Due to the consideration of symmetry, this number may be reduced.

2. An underlying electronic-structure method which is essential for the calculated properties. The property values depend on the electronic and structural parameters obtained with the used theoretical approach. In principle there is no limitation to one certain method, although it has been shown that the parametrized density functional tight-binding (DFTB) method is ideally suited for our purposes. The DFTB method combines speed and accuracy, enabling to study a large amount of systems within a short period of time and, at the same time, to retain a relatively high accuracy.

3. A simple genetic algorithm (GA) as GO algorithm and efficient local optimizations. The GA procedure is used to scan a discrete search space (see figure 7.2 in section 7.2) and to identify structures with optimal property values. Prior to property calculation each system is relaxed locally to yield well-converged structures. These local optimizations are required to obtain reliable property values. In principle, also other suitable global optimization procedures may be used within our PooMa

approach. However, genetic algorithms have the advantage that they can give more, different optimal systems.

4. A fast way of molecule/compound construction. This includes an efficient method to attach functional groups and atoms at given sites of an organic backbone (DSSCs) as well as a simple way of generating slabs, molecules and slab-molecule systems for the adsorption studies. The requirement for an efficient construction of chemical compounds may be extended to any GPO task treated with PooMa.
5. Identification and the subsequent mathematical definition of suitable properties. In this connection we use simple mathematical descriptions of the sought properties, yielding one property value for each system, which can be optimized for. Here, we optimize for a smallest or largest property value. Thereby, it may be necessary to consider the size-dependency of certain properties, i.e. to focus on intensive properties. Here, it should be avoided that the largest system yields the largest property value.

12 Solar energy harvesting

12.1 Introduction

The DSSC (also called Grätzel cell) has been invented by Grätzel and co-workers in 1991 [206]. The basic working principle of these types of solar cells is depicted in figure 12.1.

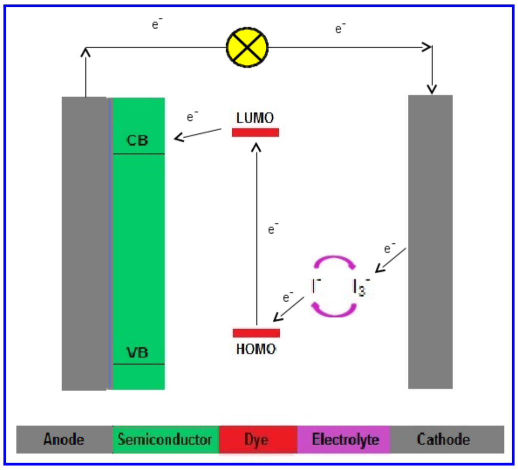

Figure 12.1: Simplified representation of the basic working principle of a DSSC.

An organic molecule, a dye, is used as sunlight absorbing component (colored red in figure 12.1). If the dye absorbs a photon, an electron e^- is excited from an occupied orbital (e.g. HOMO) of the organic molecule to a virtual orbital (e.g. LUMO). Thereby a hole is created in the starting orbital, resulting in an electron-hole pair. Subsequently, the electron is transported to an electrode, with a semiconductor material, e.g. TiO_2 (colored green in figure 12.1). From the anode (colored grey in figure 12.1), e.g. a Pt-coated electrode the e^- migrates to the counterelectrode, the cathode, and reduces the electrolyte ion (colored purple in figure 12.1). The reduced ion transportes the electron to the organic molecule and transfers it to the dye. This whole process converts sunlight into an electric current that can be used as an energy source.

But what makes a well-performing dye-based solar cell? With reference to the working principle shown in figure 12.1 and our previous study [52] one can define several criteria that are of fundamental importance for DSSCs. The following list is not exhaustive, but includes several key points:

1. The HOMO-LUMO energy gap and also the gap between other occupied orbitals

and virtual ones should not be too large and rather small, in order to faciliate absorption processes within the organic molecule [52]. Systems that fulfill this requirement are organic molecules including conjugated electronic structures and/or transition metals.

2. If an organic dye absorbs a photon, an electron is excited into a virtual orbital and leaves a hole in its starting orbitals: a electron-hole pair is created. If the two orbitals are spatially too close to each other, an undesired phenomena may occur, the recombination of the electron and the hole [52]. The possibility for recombination can be reduced by using donor (D) and acceptor (A) groups within the molecule. A conjugated π bridge seperates the D and A groups and therefore these molecules are called D-π-A systems.

3. An easy transfer of the excited electrons to the semiconductor has to be guaranteed. To create strong bonds between the dye and the electrode so-called anchor groups are used that attach the molecule to the semiconductor [52]. Here, the Fermi level of the electrode material should be lower than the HOMO level of the organic dye in order to faciliate the electron transport into the conduction band (CB) of the electrode.

4. The last criterion is related to the mediator, the redox system. The redox couple transports the electrons from the counterelectrode to the dye. To ensure the electron transfer from the ion to the molecule, the LUMO level of the ions should lie above the HOMO level of the organic dye.

It becomes obvious that the DSSCs are relatively complex, multi-faceted systems with various variable parameters and components. A lot of efforts have been put into the development of these solar cells to improve the conversion efficiency, stability, costs and other relevant properties [207, 208]. These include the investigation of different organic molecules [207, 209], different electrode materials [208, 210, 211] and several types of electrolytes [207, 208, 212]. The complexity of DSSCs, concerning components, conditions and parameters can not be completely depicted by theoretical approaches, including this work. Therefore choices have to be made, which part of the system DSSC should be considered and what can be neglected. Here, we limit our studies to the investigation of the light absorbing component, the organic dyes. The performance of the organic sensitizer is a central issue and the dye is the fundamental component within the DSSC. A sensitizer without suitable properties may not lead to an at least acceptable conversion of light into electric current.

But the task of finding organic molecules with desired solar harvesting properties is not an easy one. Various organic systems with different atomic compositions and including many different possible functional groups exist. Hence, a strictly experimental approach is not able to deal with the vast amount of possible chemical structures. The use of theoretical calculations comes into play. They are able to reduce the amount of costs, and to save time that otherwise would be needed for pure experimental studies. Theoretical models are needed that are simple enough to screen large search spaces and which are still accurate enough to yield acceptable results. Since such theoretical methods make use of many approximations (see chapter 6 in part I) and, as mentioned above, one has to reduce the complexity of the DSSCS, theory can only be understood as an assistance to experiments. This is also true for the present study, where our results can be interpreted as suggestions for the improvement of the performance of dyes for solar cell applications. Experimental investigations can not be completely replaced by theoretical studies, but theory may help to reduce the amount of experiments in order to faciliate a more targeted research on DSSCs. A prescreening of a large chemical space may substitute time-consuming, expensive experimental "trial-and-error" approaches.

In general, a dye can be thought of as an organic backbone, a core, to which different functional groups are attached. Prominent organic backbones that are used frequently as sensitizers are porphyrins [213, 214, 215], BODIPY [216, 217, 218] or bipyridine ligands [219, 220]. In this work, we study benzene derivatives as a simple model system to show that in principle, it is possible to determine automatically that substitution patterns of organic molecules that exhibit desired properties concerning solar energy harvesting. Without the need for considering all possible systems, our ID method is able to identify that molecules with optimal values for a predefined property. There are also other ID studies on dye-based solar cells. In Ref. [50] a LCAP approach is used to study a variably substituted phenylacetylacetonate backbone. Also alchemical structures are considered within this optimization process and the actually discrete hypersurface is smoothened out (see section 7.2). Hence, their optimization takes place within a continuous search space in contrast to our approach, where, as outlined in section 7.2, we investigate a discrete search space. The composition, i.e. the substitution patterns of the organic molecules span a dicrete space. A certain functional group is attached to a certain position or not. There is nothing in between. In our case, the compositions of the chemical structures are discrete variables. In principle, this decreases the dimensionality of our optimization task. This is a fundamental difference between our GPO, the PooMa, and that of Ref. [50] and it also distinguishes the PooMa approach from the GEO of the alkali metal clusters (see chapter 7 of the present thesis). The global optimization of the Li and

Na clusters is also performed within a continuous search space, with the position-space coordinates representing continuous variables.
The technical details of our ID method are presented in section 12.2, which is followed by a detailed discussion of the results of our GPO in section 12.3. In section 12.4 a brief conclusion will be drawn from the obtained results and an outlook on further studies on solar energy harvesting and other optimization tasks using PooMa is provided.

12.2 Technical details

First, the underlying computational method, the density functional theory tight-binding method (DFTB), is discussed (subsection 12.2.1). Subsequently, the local optimization algorithm, i.e. the steepest descent method and the global optimization procedure, i.e. the genetic algorithm, are introduced in subsection 12.2.2. In subsection 12.2.3 the way of molecule construction will be presented briefly. And finally, subsection 12.2.4 deals with the solar energy harvesting properties that are considered within this study.

12.2.1 The computational method: DFTB

The simple semiempirical MEAM model used for the GEO of clusters (part II, section 9.1), is efficient and suitable to perform unbiased global optimizations, where a large number of systems has to be considered. Also bigger systems with hundreds of atoms can be treated with such methods. This can not be achieved by more accurate HF or DFT approaches. One problem of such model potentials as the used analytic MEAM or force field approaches, is the limited transferability [221]. They are parametrized for a specific element or a few similar elements, but can not be just applied to any arbitrary ones. Moreover, quantum effects are not included explicitly within these methods, what may reduce the accuracy. This may also influence the outcome of such calculations and therefore this has to be taken into account when interpreting the results obtained with such methods (see part II, chapter 10).
The density functional tight-binding (DFTB) method [222, 223, 224] is an approach, which is computationally inexpensive and therefore suitable for unbiased GO tasks. Based on DFT, the DFTB method inludes quantum and electron correlation effects [221], resulting in a higher accuracy compared to model potentials. Furthermore, the parametrization process is less complicated and includes only the performance of several DFT calculations, faciliating transferability [221, 225]. In order to derive the first-order non-SCC DFTB method used in this study, one starts with the KS-DFT (see section 6.3.2 in part I of the present thesis). Therefore, it is necessary to remember the expression for

the total energy of a system according to the KS approach. Equation 6.31, in a slight modified form, reads:

$$E_{\text{tot}}[\rho] = \sum_{\substack{\alpha\beta \\ \beta>\alpha}} E_{\alpha\beta} + \sum_k n_k \left\langle \psi_k \left| -\frac{\hbar^2}{2m_e}\Delta + v_{ext}(\vec{r}) + \frac{1}{2}\int \frac{e^2\rho(\vec{r}\,')}{4\pi\epsilon_0|\vec{r}-\vec{r}\,'|}d\vec{r}\,' \right| \psi_k \right\rangle \\ + E_{xc}[\rho], \tag{12.1}$$

with $E_{\alpha\beta}$ being the nuclear repulsion energy between the nuclei α and β and the remaining terms representing the electronic KS energy. Now the electron density $\rho(\vec{r})/\rho(\vec{r}\,')$ is replaced with some reference density $\rho_{ref}(\vec{r})/\rho_{ref}(\vec{r}\,')$ and its perturbation, a small charge fluctuation $\delta\rho(\vec{r})$: $\rho(\vec{r}) = \rho_{ref}(\vec{r}) + \delta\rho(\vec{r})$. Inserting this into equation 12.1 and using the short notation $\rho_{ref} = \rho_{ref}(\vec{r})$, $\rho'_{ref} = \rho_{ref}(\vec{r}\,')$ and $\delta\rho = \delta\rho(\vec{r})$, yields [225]:

$$E_{\text{tot}}[\rho_{ref}+\delta\rho] = \sum_{\substack{\alpha\beta \\ \beta>\alpha}} E_{\alpha\beta} + \sum_k n_k \left\langle \psi_k \left| -\frac{\hbar^2}{2m_e}\Delta + v_{ext}(\vec{r}) + \int \frac{e^2\rho'_{ref}}{4\pi\epsilon_0|\vec{r}-\vec{r}\,'|}d\vec{r}\,' + v_{xc}[\rho_{ref}] \right| \psi_k \right\rangle \\ - \frac{1}{2}\int\int \frac{e^2\rho'_{ref}(\rho_{ref}+\delta\rho)}{4\pi\epsilon_0|\vec{r}-\vec{r}\,'|}d\vec{r}d\vec{r}\,' - \int v_{xc}[\rho_{ref}](\rho_{ref}+\delta\rho)d\vec{r} \\ + \frac{1}{2}\int\int \frac{e^2\delta\rho'(\rho_{ref}+\delta\rho)}{4\pi\epsilon_0|\vec{r}-\vec{r}\,'|}d\vec{r}d\vec{r}\,' + E_{xc}[\rho_{ref}+\delta\rho]. \tag{12.2}$$

Since the Coulomb energy

$$\int \frac{e^2\rho'_{ref}}{4\pi\epsilon_0|\vec{r}-\vec{r}\,'|}d\vec{r}\,', \tag{12.3}$$

within term two of equation 12.2 is counted twice, the third term

$$\frac{1}{2}\int\int \frac{e^2\rho'_{ref}(\rho_{ref}+\delta\rho)}{4\pi\epsilon_0|\vec{r}-\vec{r}\,'|}d\vec{r}d\vec{r}\,' \tag{12.4}$$

is introduced as a correction. The Coulomb term itself is divided into two different energetic contributions, where one is related to the density ρ_{ref}/ρ'_{ref} (within term two in equation 12.2 / equation 12.3) and the other to the fluctuation $\delta\rho/\delta\rho'$ (term five in equation 12.2) [225]

$$\frac{1}{2}\int\int \frac{e^2\delta\rho'(\rho_{ref}+\delta\rho)}{4\pi\epsilon_0|\vec{r}-\vec{r}\,'|}d\vec{r}d\vec{r}\,'. \tag{12.5}$$

Finally, the new exchange-correlation expression within term two of equation 12.2

$$v_{xc}[\rho_{ref}], \tag{12.6}$$

is corrected by the fourth term in equation 12.2

$$\int v_{xc}[\rho_{ref}](\rho_{ref} + \delta\rho)d\vec{r}. \tag{12.7}$$

A Taylor series expansion of the exchange-correlation energy E_{xc} around $\rho_{ref} + \delta\rho$ up to the second order leads to the following expression for E_{xc} [221, 224, 225]:

$$\begin{aligned} E_{xc}[\rho_{ref} + \delta\rho] = E_{xc}[\rho_{ref}] + \int \left.\frac{\delta E_{xc}}{\delta\rho}\right|_{\rho_{ref}} \delta\rho d\vec{r} \\ + \frac{1}{2}\int\int \left.\frac{\delta^2 E_{xc}}{\delta\rho\delta\rho'}\right|_{\rho_{ref}} \delta\rho\delta\rho' d\vec{r}d\vec{r}' \end{aligned} \tag{12.8}$$

Combination of equation 12.2 and 12.8 gives an expression for the second-order expansion of the KS total energy

$$\begin{aligned} E_{\text{tot}}[\rho_{ref} + \delta\rho] = & \sum_{\substack{\alpha\beta \\ \beta>\alpha}} E_{\alpha\beta} + \sum_k n_k \left\langle \psi_k \left| -\frac{\hbar^2}{2m_e}\Delta + v_{ext}(\vec{r}) + \int \frac{e^2 {\rho'}_{ref}}{4\pi\epsilon_0|\vec{r}-\vec{r}'|}d\vec{r}' + v_{xc}[\rho_{ref}] \right| \psi_k \right\rangle \\ & - \frac{1}{2}\int\int \frac{e^2 {\rho'}_{ref}(\rho_{ref} + \delta\rho)}{4\pi\epsilon_0|\vec{r}-\vec{r}'|}d\vec{r}d\vec{r}' - \int v_{xc}[\rho_{ref}](\rho_{ref} + \delta\rho)d\vec{r} \\ & + \frac{1}{2}\int\int \frac{e^2 \delta\rho'(\rho_{ref} + \delta\rho)}{4\pi\epsilon_0|\vec{r}-\vec{r}'|}d\vec{r}d\vec{r}' + E_{xc}[\rho_{ref}] + \int \left.\frac{\delta E_{xc}}{\delta\rho}\right|_{\rho_{ref}} \delta\rho d\vec{r} \\ & + \frac{1}{2}\int\int \left.\frac{\delta^2 E_{xc}}{\delta\rho\delta\rho'}\right|_{\rho_{ref}} \delta\rho\delta\rho' d\vec{r}d\vec{r}' \end{aligned} \tag{12.9}$$

By rewriting this equation and making use of the relation $(\delta E_{xc}/\delta\rho)_{\rho_{ref}} = v_{xc}[\rho_{ref}]$ [225], one can simplify expression 12.9 to

$$E_{\text{tot}}[\rho_{ref}+\delta\rho] = \sum_{\substack{\alpha\beta\\ \beta>\alpha}} E_{\alpha\beta} - \frac{1}{2}\int\int \frac{e^2\rho_{ref}{\rho'}_{ref}}{4\pi\epsilon_0|\vec{r}-\vec{r}'|}d\vec{r}d\vec{r}' - \int v_{xc}[\rho_{ref}]\rho_{ref}d\vec{r} + E_{xc}[\rho_{ref}]$$
$$+ \sum_k n_k \left\langle \psi_k \left| -\frac{\hbar^2}{2m_e}\Delta + v_{ext}(\vec{r}) + \int \frac{e^2{\rho'}_{ref}}{4\pi\epsilon_0|\vec{r}-\vec{r}'|}d\vec{r}' + v_{xc}[\rho_{ref}] \right| \psi_k \right\rangle$$
$$+ \frac{1}{2}\int\int \left(\frac{e^2}{4\pi\epsilon_0|\vec{r}-\vec{r}'|} + \left.\frac{\delta^2 E_{xc}}{\delta\rho\delta\rho'}\right|_{\rho_{ref}} \right) \delta\rho\delta\rho' d\vec{r}d\vec{r}'. \tag{12.10}$$

Equation 12.10 can be further simplified and the various energetic contributions can be summarized in three terms, according to up to which order the density fluctuations are considered:

$$E_{\text{tot}}[\rho_{ref}+\delta\rho] = E^0[\rho_{ref}] \ + \ E^1[\rho_{ref},\delta\rho] \ + \ E^2[\rho_{ref},(\delta\rho)^2]. \tag{12.11}$$

$E^0[\rho_{ref}]$ is the zeroth-order term with respect to the density fluctuations that includes the first four energetic contributions in equation 12.10 [221]. $E^1[\rho_{ref},\delta\rho]$ is the first-order and $E^2[\rho_{ref},(\delta\rho)^2]$ the corresponding second-order energy term that represent the fifth and sixth energetic term of equation 12.10, respectively [221]. For the first-order non-SCC DFTB, used within this study, only the first two terms are relevant and they will be discussed in more detail in the following.

The non-SCC DFTB

The first-order contribution to the total energy is,

$$E^1[\rho_{ref},\delta\rho] = \sum_k n_k \left\langle \psi_k \left| -\frac{\hbar^2}{2m_e}\Delta + v_{ext}(\vec{r}) + \int \frac{e^2{\rho'}_{ref}}{4\pi\epsilon_0|\vec{r}-\vec{r}'|}d\vec{r}' + v_{xc}[\rho_{ref}] \right| \psi_k \right\rangle, \tag{12.12}$$

whereat we can introduce the reference Hamiltonian $\hat{H}^0$ as a short-hand notation [225], which yields the much simpler expression

$$E^1[\rho_{ref}] = \sum_k n_k \left\langle \psi_k \left| \hat{H}^0[\rho_{ref}] \right| \psi_k \right\rangle. \tag{12.13}$$

Here, the operator $\hat{H}^0$ solely depends on the reference electron density ρ_{ref} and not on the fluctuation term $\delta\rho$, and therefore also $E^1[\rho_{ref}]$ depends only on the reference density ρ_{ref} [225]. As for the KS-DFT, within the DFTB method the molecular orbitals ψ_k are written as a linear combination of non-orthogonal atomic orbitals [222, 223]

$$\psi_k(\vec{r}) = \sum_{\mu_\alpha} c_{\mu_\alpha k} \phi_{\mu_\alpha}, \tag{12.14}$$

with $c_{\mu_\alpha k}$ being the expansion coefficients and ϕ_{μ_α} representing the atomic basis functions belonging to atom α. A minimal basis set is used within the DFTB approach and only valence electrons are treated explicitly [221]. The remaining electrons are considered within a frozen core approximation [52]. The functions ϕ_{μ_α} are Slater-type orbitals, obtained from SCF-LDA calculations [224]. As discussed in section 6.3.2, the use of the LCAO ansatz results in secular eigenvalue problems

$$\sum_{\nu_\beta} c_{\nu_\beta k}(H^0_{\mu_\alpha \nu_\beta} - \epsilon_k S_{\mu_\alpha \nu_\beta}) = 0, \tag{12.15}$$

where μ_α and ν_β denote the μth/νth orbital belonging to atom α/β. The Hamiltonian matrix elements $H^0_{\mu_\alpha \nu_\beta}$ and the overlap matrix elements $S_{\mu_\alpha \nu_\beta}$ take the following forms:

$$H^0_{\mu_\alpha \nu_\beta} = \langle \phi_{\mu_\alpha} | \hat{H}^0 | \phi_{\nu_\beta} \rangle \tag{12.16}$$

and

$$S_{\mu_\alpha \nu_\beta} = \langle \phi_{\mu_\alpha} | \phi_{\nu_\beta} \rangle, \tag{12.17}$$

where, according to a superposition of atomic potentials [223], the operator H^0 is

$$\hat{H}^0 = \hat{T} + V_{eff}(\rho^\alpha) + V_{eff}(\rho^\beta). \tag{12.18}$$

$\hat{T}$, $V_{eff}(\rho^\alpha)$ and $V_{eff}(\rho^\beta)$ represent the kinetic energy, the potential of atom α and the potential of atom β, respectively. The matrix elements $H^0_{\mu_\alpha \nu_\beta}$ are calculated using a two-centre approximation and three-centre terms are neglected [223]. For the DFTB method the two-center elements of the Hamiltonian matrix $H^0_{\mu_\alpha \nu_\beta}$ as well as that of the overlap matrix $S_{\mu_\alpha \nu_\beta}$ are tabulated as functions of the interatomic distance within so-called Slater-Koster (SK) files. No integrals have to be evaluated during a calculation and these elements are just read from the SK files and interpolated to the actual distance between a pair of atoms [222]. The atomic potentials $V_{eff}(\rho^\alpha)/V_{eff}(\rho^\beta)$ in equation 12.18 are functions of the atomic electron densities ρ^α/ρ^β of the neutral atoms α/β. The reference density ρ_{ref} is a simple superposition of this atomic densities. The functions $\phi_{\mu_\alpha}/\phi_{\mu_\beta}$ as well as the atomic reference electron densities ρ^α/ρ^β are obtained via DFT calculations using the KS approach.

Depending on the atomic orbitals considered, the Hamiltonian matrix elements $H^0_{\mu_\alpha \nu_\beta}$ can be represented as follows:

$$H^0_{\mu_\alpha \nu_\beta} = \begin{cases} \epsilon^{free\,atom}_{\mu_\alpha}, & \text{for } \mu_\alpha = \nu_\beta \\ \langle \phi_{\mu_\alpha} | \hat{H}^0 | \phi_{\nu_\beta} \rangle, & \text{for } \alpha \neq \beta \\ 0, & \text{otherwise.} \end{cases} \tag{12.19}$$

Once the atomic orbitals ϕ_{ν_α} as well as the initial electron density ρ_α have been determined, it is possible to solve the secular equation system 12.15. This gives the electronic energy E^1 (equation 12.13) within the DFTB method [221] as

$$E^1[\rho_{ref}] = \sum_k n_k \left\langle \psi_k \middle| \hat{H}^0 \middle| \psi_k \right\rangle = \sum_k n_k \sum_{\mu_\alpha \nu_\beta} c_{\mu_\alpha k} c_{\nu_\beta k} H^0_{\mu_\alpha \nu_\beta} = \sum_k n_k \epsilon_k, \tag{12.20}$$

where n_k is the occupation number of the kth KS orbital and ϵ_k its corresponding energy. As E^1 the energy term E^0 solely depends on the reference density ρ_{ref} [221]. Within the DFTB method $E^0[\rho_{ref}]$ is approximated as a sum of interatomic repulsive potentials $U^{rep}_{\alpha\beta}$ [221, 225]:

$$E^0[\rho_{ref}] \approx E^{rep} = \frac{1}{2} \sum_{\alpha\beta} U^{rep}_{\alpha\beta}. \tag{12.21}$$

Also the repulsive potentials are calculated using only two-center approximations. They can be fitted to polynomial functions [222, 223, 226]

$$U^{rep,pol}_{\alpha\beta} = \sum_{i=2}^{NP} c_i (r_{cut} - r)^i, \tag{12.22}$$

with NP being the order of the polynomial, r representing the interatomic distance and the coefficients c_i and the cutoff distance r_{cut} being tabulated in the SK files. Besides there is a spline repulsive, where, depending on the interatomic distance r the repulsive term is described as [226] by an exponential function or a spline. If the distance r between two atoms is smaller than the starting distance of the first spline, the exponential function

$$e^{-a_1 r + a_2} + a_3, \tag{12.23}$$

is used to describe the repulsive interaction, where the parameters a_1, a_2 and a_3 are tabulated in the SK files. For larger interatomic distances r a spline repulsive interaction would be, for instance,

$$c_0 + c_1(r - r_0) + c_2(r - r_0)^2 + c_3(r - r_0)^3, \tag{12.24}$$

with the parameters c_0, c_1, c_2 and c_3 as well as the starting distance r_0 also being tabulated in the SK files. According to the non-SCC DFTB approach the total energy of a system becomes [221, 225]

$$E_{\text{tot}}^{\text{nSCC}} = E^1[\rho_{ref}] + E^0[\rho_{ref}] = \sum_k n_k \epsilon_k + \frac{1}{2}\sum_{\alpha\beta} U_{\alpha\beta}^{rep}. \tag{12.25}$$

No integrals have to be solved and all relevant energetic quantities that are needed to compute E_{tot} are obtained from KS-DFT calculations and are read from the SK files. This makes the DFTB approach a very efficient and fast method [221] and, since it is based on the DFT level of theory, a high accuracy can be achieved. Within the non-SCC DFTB used in this study charge fluctuations are not considered and the third energy term in equation 12.11 is neglected. Therefore, the secular eigenvalue equations 12.15 do not have to be solved self-consistently. Calculations including the self-consistent charge treatment can take up to five to ten times longer than the non-SCC DFTB method [221].

12.2.2 The global optimization algorithm

Property optimizations are performed using a genetic algorithm. In order to obtain reliable properties, each constructed molecule is optimized locally by the steepest descent method. In the following two subsubsections the basic concepts of the used algorithms are presented.

Local structural relaxations: the steepest descent relaxation

The steepest descent (gradient descent) method is an algorithm for searching local minima. Upon minima search of a function f, the gradient vector g_k is calculated [91] and the path along the steepest descent of the gradient is followed [91].

The basic workflow of the steepest descent relaxation for a function f is shown figure 12.2. One starts with a initial guess, a starting point for the function's argument, x_0 and an initial gradient vector g_0 [91]. The initial gradient g_0 is calculated using the known vector b and the known symmetric, positive-definite matrix A. In each iteration step k the step size α_k is determined, the new point x_{k+1} is computed and finally the new gradient vector g_{k+1} is calculated. If the termination criteria are fulfilled, e.g. a predefined threshold value is reached, the algorithm stops, convergence is reached. If not, the loop variable is incremented by one and the optimization is continued. The whole procedure is repeated until convergence is reached.

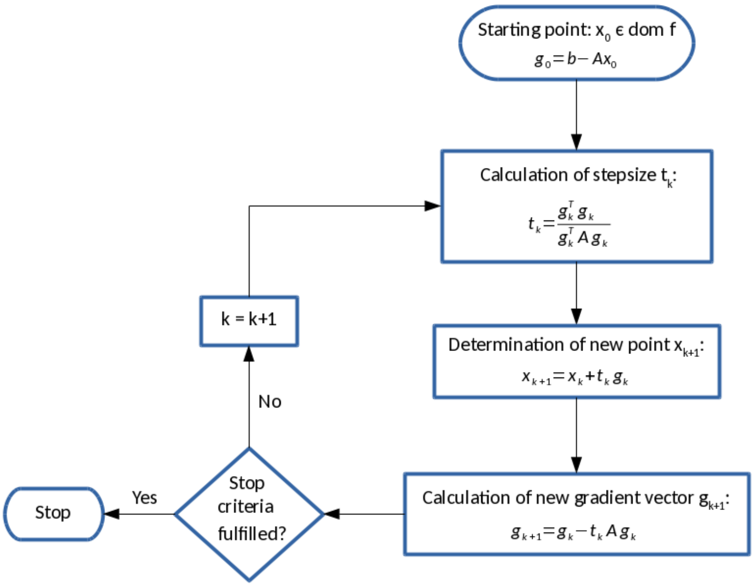

Figure 12.2: Simplified flowchart showing the general workflow of a steepest descent algorithm, as used for local relaxations within this study.

Optimization of solar energy harvesting properties: the genetic algorithm

We use a simple GA for the automatic property optimization. The organic backbone of the molecules is kept fixed during the calculations, only the substitution pattern is varied. Different functional groups and atoms can be attached to this core and the GA automatically determines which substituents at which sites yield optimal property values. Each molecule is encoded as a string of N integers and the substituents adopt integer values from 1 to K. On these strings of integers the GA is applied.

The applied evolutionary algorithm can be devidided into the following steps [52, 205]:

1. Creation of the initial generation. $2P$ parent molecules are generated randomly. It is ensured that there are no identical or symmetry equivalent molecules.

2. To obtain well-converged structures, local optimizations are performed for each molecule of the recent generation.

3. The performance function is calculated and the different candidates are ordered according to theirs property values. Depending on the chosen property, the optimal

value can be the smallest (minimum search) or largest one (maximum search).

4. The molecules are separated randomly into P pairs.
5. A crossover procedure is used to create two children from each pair of molecules. Each of these two molecules, represented by N integers, is divided randomly into two parts, with one part consisting of $N - M$ and the other one consisting of M integers with $0 < M < N$. Upon interchanging the parts between the molecules, it is ensured that each child consists of N integers, i.e. the parts of length M and length $N - M$ are recombined.
6. To prevent premature convergence also mutations are introduced. A random number is used to determine, whether a mutation takes place or not. A structure is mutated by the random exchange of one integer into another.
7. It is checked that all $4P$ structures, parents and children, are different. This also includes the test for symmetricall equivalent molecules. If there are duplicate structures the steps 4, 5 and 6 are repeated.
8. The children structures are relaxed locally and their performance functions are calculated (see steps 2 and 3).
9. The $2P$ best performing molecules are selected out of the $4P$ parents and children. These structures represent the parents of the subsequent generation.
10. The two termination conditions are checked: either a certain number of the $2P$ molecules are unchanged for several consecutive generations or a predefined maximum number of generations has been reached. The first termination condition is the desired one, showing a convergence of the applied GA.

Figure 12.3 shows the working flow of the used GA. As discussed for the model system benzene in section 12.3, the used GA is able to identify certain functional groups that occur repeatedly as substituents within the benzene molecules. These groups may enhance the performance of a molecule for a certain property, i.e. there are substituents which seem to be beneficial for a certain solar energy harvesting property. In this context, it is important to note that we do not test the created molecules for being synthesizable in a laboratory. The molecular fragments and atoms occuring more frequently within the substitution patterns of the molecules should be understood as recommendations. The inclusion of such a substituent within a molecular sensitizer may lead to an enhanced performance of this system.

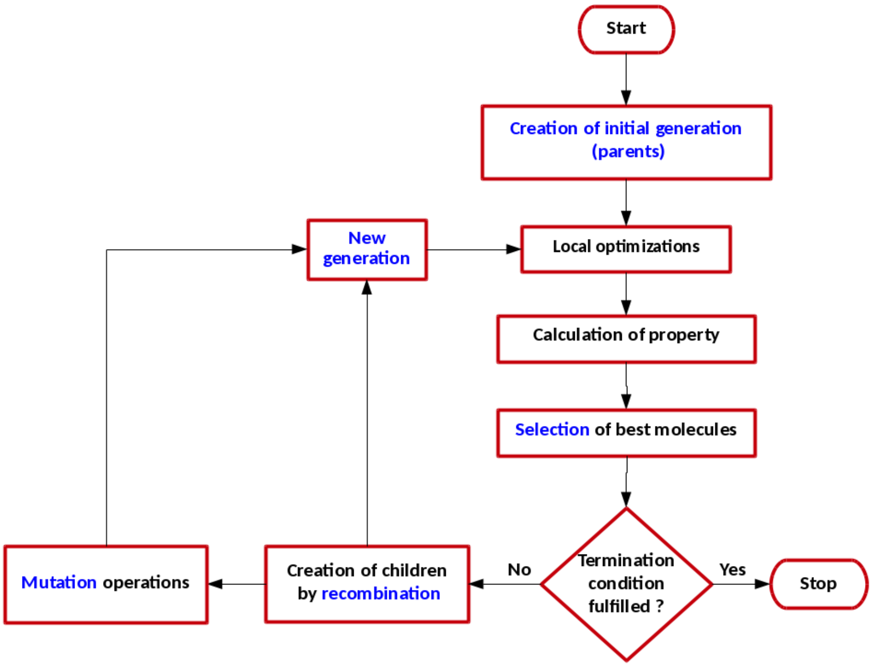

Figure 12.3: Simplified flowchart showing the workflow of the genetic algorithm used within this study.

12.2.3 Molecule construction

An important component within our PooMa approach is the efficient construction of the molecules. For the former study on Silicium-Germanium clusters [52] the cluster generation was a rather simple task. Only single Si or Ge atoms, having the same number of valence electrons, were allowed to occupy positions within a cluster. This is very different from the current study, where different functional groups may have a different number of atoms and also a different number of valence electrons. Also the substituents' orientation in space has to be considered. Depending on which site of the molecule a substituent is attached, this orientation may vary.

Within our approach a molecule consists of two parts. One part is the "naked" organic backbone, a core, and the other one are the functional groups that can be attached to this core system. Concerning molecules used as sensitizers for solar cells, the backbone may include an anchor group that fixes the dye at the electrode (see figure 12.1, the DSSC working principle). An anchor group facilitates the electron transport from the molecule to the electrode.

A subroutine within our source code reads in the structural data from an input file. This file contains all relevant information about the systems to investigate, e.g. position-space coordinates, types of atoms and number of electrons of the organic core and the functional groups. Within this subroutine the molecules are constructed according to the following procedure (figure 12.4). The first step involves the building of the ”naked” organic backbone (1). Subsequently at each substituent site of the ”naked” core, ”empty“ sites are defined. Each ”empty” site includes two different types of information: a typical position (2) and a typical orientation. If a substituent is attached to the organic backbone it is positioned relative to the ”empty“ site and according to the typical orientation of this site. Within our global optimization procedure many molecules have to be investigated and the optimization of a single molecule should be fast and efficient. Therefore, it is extremely important to have a good guess for the initial structure of a molecule prior to relaxation. Therefore, the position-space coordinates of the functional groups are defined in such a way that each substituent has a typical distance relative to the empty sites as well as a realistic orientation. Within the last step of molecule construction the functional groups are attached to the ”empty” sites of the core (3).

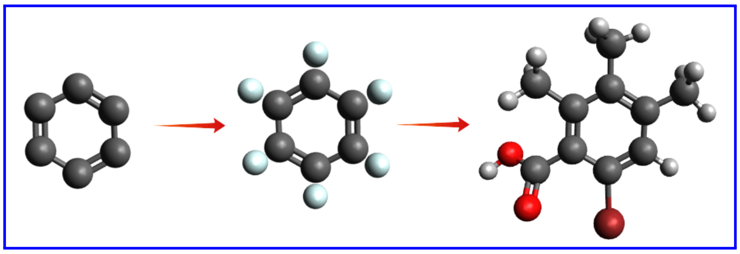

Construction of molecules within the PooMa approach for DSSCs

Figure 12.4: The way of molecule construction for benzene derivatives used within this study. The process involves three steps: 1) definition of the ”naked“ organic backbone, 2) definition of ”empty” substituent sites, 3) final molecule after attachement of the functional groups. Reproduced/Adapted from K. Huwig, C. Fan, and M. Springborg. From properties to materials: An efficient and simple approach. *J. Chem. Phys.*, 147(23):234105, 2017, with the permission of AIP Publishing.

Functional groups and anchor groups are attached the same way to the organic backbone. But whereas the ”normal“ functional groups are always varied during a calculation, the anchor groups can kept fixed at a certain substituent site of core.

Within this study 18 different functional groups are considered as possible substituents: –CH_3 , –H, –CN, –F, –Cl, –Br, –I, –OH, –OCH_3, –NH_2 , –$N(CH_3)_2$, –CHO, –COOH, –$HC{=}CH_2$, –C≡CH, –NO_2 , –SH, and –SCH_3. Moreover, –COOH is used as a fixed anchor group.

12.2.4 Solar energy harvesting: the properties

For a GPO the definition of suitable properties is of crucial importance. The identification of such properties that may be important for solar energy harvesting, is not always a simple task. There is not a structural parameter or electronic property, which alone determines the suitability of a molecule as dye sensitizer. As discussed in section 12.1 there is a subtle interplay between different parameters that influence the performances of the organic molecules. Therefore we defined several properties that we consider as being important for the performance to approach the optical performance of DSSCs. The performance functions described below can be understood as suggestions, which may have a more or less strong influence on a real sensitizers light harvesting properties. Furthermore, as described within our earlier work [52], some of the chosen properties may be correlated. Our GO algorithm searches for these molecules that exhibit an optimal value concerning a predefined property. As mentioned above in subsection 12.2.3 the size, i.e. the number of atoms and valence electrons, of the systems within this study varies. Now the problem appears that the chosen properties may increase with system size, leading to the largest or smallest systems as optimal solutions. To prevent this, intensive properties are defined in cases where molecule size plays a role. Within our previous study on the solar energy harvesting properties of SiGe clusters [52], where the number of atoms and valence electrons stayed constant during a calculation, this was not necessary.

Various properties concerning light harvesting are investigated within this study and for each computation a single property is optimized. In order to take into account the problem of varying molecule size during a calculation and to obtain intensive quantities, properties that depend on the number of orbitals of a system are divided by the number of valence electrons N_e of the system. Hereinafter we discuss the optimized properties. In detail, these are

a. The HOMO-LUMO gap G. It is the energetic difference between the highest occupied molecular orbital (HOMO) and the lowest unoccupied molecular orbital (LUMO). The value for G shall be as small as possible:

$$G = \epsilon_{\mathrm{LUMO}} - \epsilon_{\mathrm{HOMO}} \tag{12.26}$$

b. The sunlight absorption A. It is described as a sum of spectral functions $P(\epsilon_u - \epsilon_o)$, which represent the probabilities for single electron excitations. ϵ_u and ϵ_u are the energies of an unoccupied and an occupied orbital, respectively. As weigthing factor the oscillator strength f_{ou} is used. A should be as large as possible. Removing size dependency through division by N_e the absorption A is:

$$A = \frac{\sum_{o,u} f_{ou} P(\epsilon_u - \epsilon_o)}{N_e}, \tag{12.27}$$

with o and u denoting an occupied and an unoccupied orbital, respectively. The black-body approximation is used to describe the probabilities $P(\epsilon_u - \epsilon_o)$:

$$P(\epsilon_u - \epsilon_o) = \frac{8\pi(\epsilon_u - \epsilon_o)^3}{(2\pi\hbar c)^3} \left[exp\left(\frac{\epsilon_u - \epsilon_o}{k_b T} \right) - 1 \right]^{-1}. \tag{12.28}$$

The oscillator strength f_{ou} is approximately calculated as

$$f_{ou} = \frac{4}{3}(\epsilon_u - \epsilon_o)|\vec{d}_{ou}|^2 = \frac{4}{3}(\epsilon_u - \epsilon_o)|\sum_{\alpha} \vec{R}_\alpha q_{\alpha,ou}|^2, \tag{12.29}$$

with $\vec{d}_{ou}$ representing the transition dipole moments for the transition $o \rightarrow u$ that are calculated using the Mulliken transition charges $q_{\alpha,ou}$ and the position-space coordinates $\vec{R}_\alpha$ of the corresponding atoms α. f_{ou} is described according to the TD-DFTB (time-dependent density functional tight-binding) approach [227]. Due to the use of non-SCC DFTB in our study and since we only take one-electron excitations into account we use a simplified expression for f_{ou} compared to the original expression.

c. The light-harvesting efficiency LHE. A larger value for the LHE means a larger capacity for sunlight harvesting of the molecule. Only transitions $o \rightarrow u$ with energies lower than a predefined threshold are considered to calculate this property. Here it is computed according to

$$LHE = \frac{\sum_{o,u}(1 - 10^{-f_{ou}})}{N_e}. \tag{12.30}$$

d. The orbital overlap O_{av}. This is one of the properties that are related to the spatial distribution of the molecular orbitals (MOs). In order to prevent the recombination of electron-hole pairs a small spatial overlap between occupied and virtual MOs is preferable. The overlap O_{ou} between an occupied orbital and an unoccupied one is calculated as:

$$O_{ou} = \sum_{\alpha} |q_{\alpha,o} \cdot q_{\alpha,u}|, \tag{12.31}$$

with $q_{\alpha,o}$ and $q_{\alpha,u}$ being the atomic gross Mulliken populations of occupied orbital o and unoccupied orbital u on atom α. For all possible transition $o \to u$ O_{ou} is calculated and its transition probability is taken into account by multiplication with $f_{ou}P(\epsilon_u - \epsilon_o)$. Summation over all possible transitions and division by the number of valence electrons N_e yields the average value O_{av}:

$$O_{av} = \frac{\sum_{o,u} f_{ou}P(\epsilon_u - \epsilon_o)O_{ou}}{N_e}. \tag{12.32}$$

e. The orbital distance D_{av}. The spatial distance between an occupied and a virtual MO should be large to reduce the possibility for the recombination of electron-hole pairs. As in the case for the overlapping of MOs, a single distance D_{uo} between pair of occupied/unoccupied orbitals is calculated in terms of atomic gross Mulliken populations:

$$D_{uo} = |\sum_{\alpha} q_{\alpha,u}\vec{R}_{\alpha} - \sum_{\alpha} q_{\alpha,0}\vec{R}_{\alpha}|, \tag{12.33}$$

To obtain an average value, we sum up over the different transitions $o \to u$, weight them and divide by N_e:

$$D_{av} = \frac{\sum_{o,u} f_{ou}P(\epsilon_u - \epsilon_o)D_{uo}}{N_e}. \tag{12.34}$$

f. The spatial distribution DL of the LUMO on the anchor group (ag). Since an efficient transfer of electrons between the sensitizer molecules and the semiconductor is desirable, the participation of the atoms of anchor group in forming the LUMO should be not too small. Here, the distribution DL is computed as:

$$DL = \sum_{\alpha \in ag} q_{\alpha,LUMO}, \tag{12.35}$$

with the atomic gross Mulliken populations $q_{\alpha,LUMO}$.

g. The reorganization energies λ_+ and λ_-. Electrons, charges, are transferred between molecules within the dye-sensitized solar cells. The theoretical background of such charge transfers is described via the Marcus theory [228, 229]. According to this model the charge transfer rate k_{tr} is:

$$k_{tr} \propto \frac{1}{\sqrt{\lambda}} t^2 exp(-\frac{\lambda}{4k_B T}), \tag{12.36}$$

with λ, t, T and k_B being the reorganization energy, the transfer integral, the temperature and the Boltzmann constant, respectively. The calculation of the complex transfer integral t is computational too demanding for our PooMa approach, since it depends on the spatial distance and orientation between neighbouring sensitizer molecules. In contrast to that, the reorganization energy λ can be calculated for a single molecule according to the following simple expressions:

$$\begin{aligned} \lambda_+ &= (E_0^+ - E_+^+) + (E_+^0 - E_0^0), \\ \lambda_- &= (E_0^- - E_-^-) + (E_-^0 - E_0^0), \end{aligned} \tag{12.37}$$

where λ_+ and λ_- representing the reorganization energies for holes and electrons, respectively. E_0^+ and E_0^- are the total energies of the cationic and anionic molecule in the neutral geometry, whereas the energies of the neutral molecules in the equilibrium cationic and anionic geometry are described by E_+^0 and E_-^0. Moreover E_+^+, E_-^- and E_0^0 are the total energies for the cationic, anionic and neutral molecules in the corresponding optimized geometries, respectively. The transfer of electrons between the molecules should be fast and efficient and therefore a small value for the reorganization energies is desirable. To describe the performance of each molecule with a single number the average value of λ_+ and λ_- is determined.

12.3 Results and discussion

In this study benzene is used to study solar energy harvesting properties. The anchor group –COOH is attached to one of the six substituent sites of benzene and is kept fixed at this position throughout a calculation. To the remaining sites, five out of the 18 different functional groups can be attached. In consideration of symmetry equivalent structures approximately $\frac{1}{2}18^5 \simeq 10^6$ different molecules are possible. In this context, the investigation of each single molecule is not feasible. A simple ID method seems to be ideally suited for such an optimization task.

In the following the results of this GPO are presented and it can be stated that our

PooMa method is able to yield interesting results regarding the substitution pattern of the benzene derivatives. The present study demonstrates that our approach basically is suitable to optimize molecules with respect to their use in DSSCs and it is possible to extract valuable information out of the results. Here, the benzene derivatives are not studied for their own purpose and rather should be considered as a simple model system to present the ideas and possibilities of our method.

12.3.1 Energy gap, sunlight absorption and light-harvesting efficiency

Figure 12.5 shows the five best performing molecules concerning the HOMO-LUMO gap G, i.e. that systems with the lowest values for G. It can be recognized that there are some functional groups (circled) that occur frequently. Referring to the use of a genetic algorithm as optimization procedure, these substituents can be seen as good gene fragments. Each of the molecules shown in figure 12.5 contains electron-withdrawing substituents, such as –CHO or –NO_2, as well as electron-donating groups, e.g. –OH or –NMe_2. Extended conjugated π-electron systems together with electron-donating and -withdrawing functional groups are known to be beneficial to reduce the energy gap between HOMO and LUMO [230].

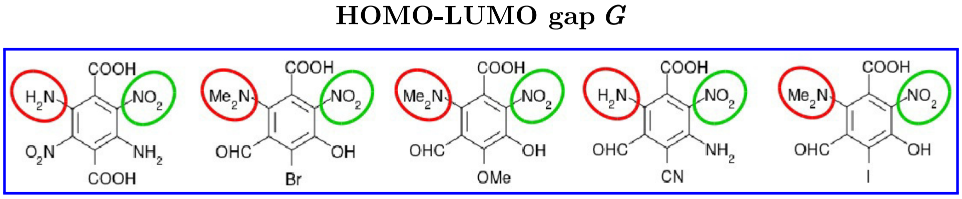

Figure 12.5: The five benzene derivatives, exhibiting the optimal (smallest) values for the HOMO-LUMO gap G. The marked substituents occur more frequently within the substitution pattern of the best molecules. The molecules' performances decreases from left to right. Reproduced/Adapted from K. Huwig, C. Fan, and M. Springborg. From properties to materials: An efficient and simple approach. *J. Chem. Phys.*, 147(23):234105, 2017, with the permission of AIP Publishing.

Next we discuss the results obtained when optimizing the light absorption A (top row) and the light-harvesting efficiency LHE (bottom row) (see figure 12.6). In both cases, molecules with property values that are supposed to be as large as possible, are considered to be optimal solutions. The multiple occurence of functional groups with conjugating effects within the best candidates, e.g. –CHO, –NMe_2 or –C≡CH is in accordance with physical and chemical understanding. Moreover, iodine as a substituent seems to be beneficial for the LHE, but this can not be explained so easily using chemical intuition.

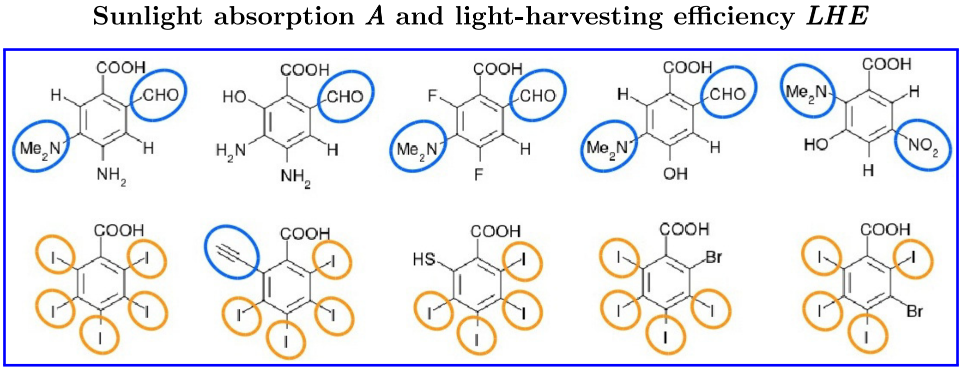

Figure 12.6: The top row depicts the five benzene derivatives exhibiting optimal (largest) values for the sunlight absorption A. The bottom row depicts molecules with the best (largest) values for the light-harvesting efficiency LHE. Substituents with a conjugating effect as well as iodine are excplicitly marked. For both properties, the molecules' performance decreases from left to right. Reproduced/Adapted from K. Huwig, C. Fan, and M. Springborg. From properties to materials: An efficient and simple approach. *J. Chem. Phys.*, 147(23):234105, 2017, with the permission of AIP Publishing.

12.3.2 Spatial orbital distribution and reorganization energies

In the following the spatial separation between occupied and unoccupied orbitals is considered. In figure 12.7 the benzene derivatives with the best values for the average orbital distance D_{av} (top row) and average orbital overlap O_{av} (bottom row) are shown. In order to prevent electron-hole recombination a large value for D_{av} and a small value for O_{av} is desireable. Refering to the molecules with large average orbital distance, all shown structures have a certain fragment in common: an electron-withdrawing (–CHO) and an electron-donating group (–NMe_2) opposite each other, i.e. located in para position. For the two best-performing molecules two such para-positioned pairs of electron-donating and -withdrawing groups occur within their substitution patterns. Molecules with a small average orbital overlap almost exclusively posses electron-donating functional groups, such as –SMe or –NMe_2. Except the fluorine atom within the third best structure (bottom row in figure 12.7) with its strong -I effect, no electron-withdrawing groups appear. Concerning D_{av} and O_{av} a simple explanation for the obtained substitution patterns based on physical and/or chemical assumptions is not easily found.

In case of benzene derivatives with a high propertion of the LUMO on the anchor group (figure 12.8) the occurrence of two opposing amino groups within each molecule is obvious. Also here, electron-donating functional groups are predominant, except the fluorine atoms within the three best structures. No groups with strong -M effect, such as –NO_2

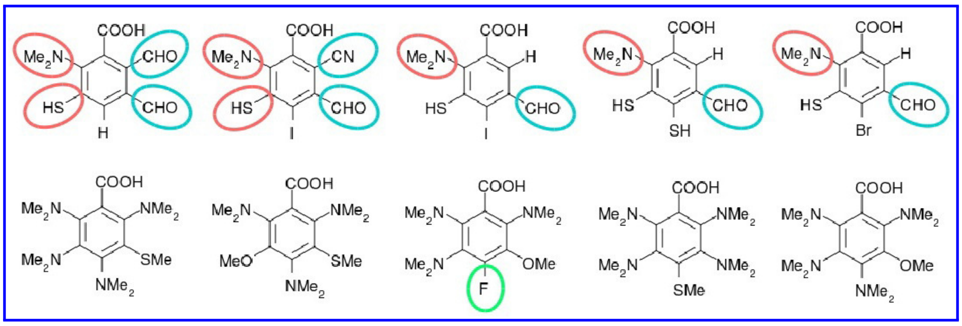

Spatial orbital distance D_{av} and orbital overlap O_{av}

Figure 12.7: The five benzene derivatives, exhibiting the optimal (largest) values for the spatial orbital distance D_{av} and the best (smallest) values for the orbital overlap O_{av}. Marked substituents occur more frequently within the substitution pattern of the best molecules. For D_{av} the appearence of para-positioned electron-withdrawing and -donating substituents within each of the molecules depicted is noticeable. Except the circled fluorine atom, electron-donating groups are predominant for molecules with small orbital overlap O_{av}. For both properties, the molecules' performance decreases from left to right. Reproduced/Adapted from K. Huwig, C. Fan, and M. Springborg. From properties to materials: An efficient and simple approach. *J. Chem. Phys.*, 147(23):234105, 2017, with the permission of AIP Publishing.

appear as substituents. It seems to be beneficial to have a high proportion of the LUMO on the electron-withdrawing –COOH anchor group, if there are no other strong electron-withdrawing groups within the molecule, i.e. there is no competition between the –COOH and such functional groups. Due to the appearence of fluorine substituents within the two best molecules, the order of the optimal structures is not easily understood in terms of chemical intuition. Such electron-withdrawing groups are completely absent within the fourth and fifth benzene derivatives. Again results are obtained that may only have been predicted partially using chemical expertise.

The best performing molecules with respect to the reorganization energy λ are shown in figure 12.9. It can be noticed that each molecule has two electron-withdrawing (-M effect) nitro groups in meta position to each other and an electron-donating (+M effect) SH group. Due to the mesomeric effects of these functional groups these molecules posses a highly delocalized π electron system and several resonance structures are possible for these molecules. Therefore, only a small change of the total energy and of structural parameters upon formation of anions and cations may be expected for these benzene derivatives.

Spatial distribution of the LUMO *DL*

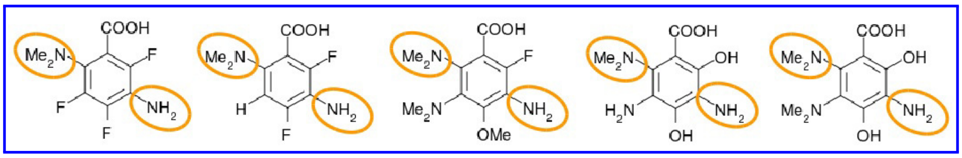

Figure 12.8: The five benzene derivatives, exhibiting the optimal (largest) values for the spatial distribution of the LUMO on the –COOH anchor group. The marked substituents occur more frequently within the substitution pattern of the best molecules. Reproduced/Adapted from K. Huwig, C. Fan, and M. Springborg. From properties to materials: An efficient and simple approach. *J. Chem. Phys.*, 147(23):234105, 2017, with the permission of AIP Publishing.

Averaged reorganization energy *λ*

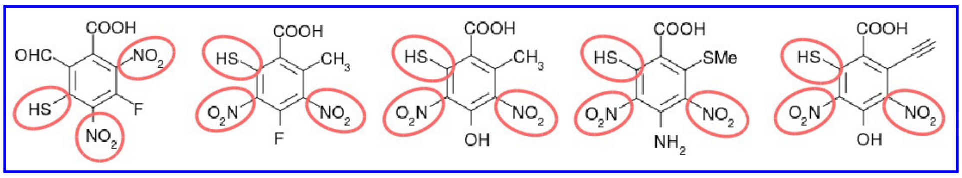

Figure 12.9: The five benzene derivatives, exhibiting the optimal (smallest) values for the averaged reorganization energy λ. The marked substituents occur more frequently within the substitution pattern of the best molecules. Reproduced/Adapted from K. Huwig, C. Fan, and M. Springborg. From properties to materials: An efficient and simple approach. *J. Chem. Phys.*, 147(23):234105, 2017, with the permission of AIP Publishing.

12.4 Conclusion and outlook

The use of benzene within the present study should be considered as a test case. The primary purpose of this study was to show the capabillities of our GPO technique, the PooMa approach. Properties related to solar energy harvesting have been optimized automatically using a genetic algorithm. The calculations yield best performing molecules that are not necessarily realistic since we make use of many approximations and we do not test the constructed molecules for being synthesizable. But the type of functional groups as well as their arrangements may include valuable information for other systems considered as sensitizer molecules.

With our theoretical approach we are able to investigate huge search spaces within a short period of time, without the need for studying each single system. We obtain results that may include concrete suggestions for the substitution patterns of molecules. The prescreening of large search spaces may assist computationally more demanding theoretical calculations as well as experiments. The approximate nature of our method enables us to forego expensive computational ressources and to use relatively cheap hardware (laptop, desktop). For this reason we call our approach the Poor Man's Materials Optimization (PooMa).We emphasize that the prescreening of a large search space is an initial step towards the design of new materials with optimal properties. In this case, many systems have to be investigated, which makes the use of very accurate and expensive computational approaches unfeasible. An unbiased global optimization requires a fast and approximated approach that enables to study a large amount of systems. Thereby the approximations should not be too crude, leading to unusable results and one should know about bottlenecks and drawbacks of the applied method. As mentioned above the molecules should be considered as suggestions that may assist further theoretical and experimental studies.

The PooMa method involves a genetic algorithm for global property optimization, local structural relaxations in order to obtain reliable properties and a efficient way of molecule construction. As underlying method of electronic structure calculation, which is used to determine the structures and the properties of the molecules, the non-SCC DFTB approach is used. PooMa is not limited to the use of DFTB as electronic structure method and in principle any other method, including more accurate ones, can be applied. The choice of the method depends on the chemical/physical problem to be investigated and has to be selected for each case individually. A further key point of our approach is to find mathematical descriptions of the properties to be optimized.

As described in our previous studies on SiGe clusters [52] our optimization algorithm does not always yield the structure with the overall best property, but at least well performing candidate solutions. But also this may give some valuable information on the systems of interest. The current study predicts the best molecules to have similar substitution patterns or rather to have several functional groups in common. A certain functional group or several groups that are beneficial for several different properties can not be identified. But from the results it can be concluded, which substituents may be advantageous for a certain property and this may be a good starting point for further investigations. As in the case of the SiGe clusters [52] the results of the calculations can not always be explained using chemical and/or physical intuition, e.g. for the orbital overlap O_{av} and distance D_{av}, whereas for the absorption A, the distribution of the LUMO DL and the HOMO-LUMO gap G it is possible to understand the results in terms of chemical/physical effects.

In this study we only considered the simple model system benzene. The PooMa approach has already been applied succesfully to more relevant sensitizer systems, i.e. porphyrins [215], cyanopyridone [231] or thiophene oligomers [232]. But, of course, this approach is not limited to the optimization of sensitizer molecules for solar cell applications. Many other GPO tasks are possible, such as the investigation of the adsorption properties of transition metal surfaces as described in chapter 13.

13 Adsorption on transition metal surfaces

13.1 Introduction

The adsorption of atomic or molecular species on surfaces is a broad field of research. Various applications exist, where the interaction between atoms/molecules and surfaces plays a fundamental role: catalytic processes [233, 234, 235, 236], gas-sensing/toxic gas adsorption [237, 238, 239, 240], surface poisoning effects during technological processes [241, 242, 243], hydrogen storage [244, 245, 246, 247] and many more [248, 249, 250, 251]. Among the different surface systems, transition-metal (TM) surfaces, especially theirs catalytic properties, are of particular interest and importance [252, 253, 254]. Therefore the interaction of molecules and atoms with TM surfaces has been the subject of many experimental [252, 255, 256, 257] and theoretical studies [243, 258, 259, 260, 261]. Computational investigations often involve the calculation of properties of single crystal surfaces concerning the adsorption of certain molecules relevant for industrial processes or just in order to gain basic knowledge about interactions between adsorbates and abdsorbents. For example, in regard of undesired sulfur poisoning during industrial processes the (111), (100), (110) and (211) surfaces of eight different fcc transition metals have been studied in terms of the adsorption of atomic sulfur [243]. Within another work calculations for a various number of different atomic and molecular species, as well as fragments of molecules adsorbed on the Cu(111) surface have been performed and analyzed using DFT-GGA [262]. Moreover, the interaction between water molecules and metal surfaces is of technological importance: adsorption and dissociation on H_2O on the (111), (100) and (110) surfaces of Ni have been studied with the GGA-PBE method [263]. To understand the influence of several simultaneously adsorbed molecules on the adsorption performance of the surfaces, also different levels of coverage are taken into account [264, 265]. Being the energetically most stable adsorption sites, in almost all cases the high symmetry adsorption sites on the single crystal surfaces are considered for the adsorption processes. Furthermore, defects and steps as well as strain were shown to have a positive effect on the adsorption properties of transition metal surfaces [266, 267, 268, 269] and also other types of adsorbents [270, 271, 272]. Also dopant atoms, incorporated within the surfaces may alter the performance of adsorbent systems or catalytic surfaces [273, 274, 275].

Here we extend our PooMa approach, previously applied to organic sensitizers for solar cells (see chapter 12), to the adsorption properties of single crystal TM surfaces. Here, we do not define an organic backbone but a TM slab consisting of several atomic layers. Instead of varying functional groups attached to an organic core, the number of atoms/vacancies and their postions within the uppermost layer of the slab are varied, i.e. a position within the uppermost layer can either be occupied by a TM atom or a vacancy. Furthermore, several different non-high-symmetry adsorption sites are taken into account. A simple GA is used to determine automatically the slab with that composition, which yields the best performance concerning the adsorption of a certain molecule. A discrete search space is screened in order to determine the structure with the best property, i.e. the optimal adsorption energy. The objectives associated with such a property optimization are numerous. It would be conceivable, for example, to prescreen these property hypersurfaces, in order to identify optimal surfaces for toxic gas adsorption or for catalytic purposes. In this regard we focus mainly on strong interactions, where molecules are chemisorbed on the corresponding surfaces and neglect long-range interactions. Such an approximation is also necessary in order to make this unbiased global optimization computationally feasible. As test systems, the single crystal surfaces Ni(111) and Ti(0001) are used as adsorbents. CO as molecular adsorbate for Ni(111) and H_2 for Ti(0001) are considered. Various studies on Ni(111)/CO [264, 276, 277, 278] and Ti(0001)/H_2 [279, 280, 281] or Ti(0001)/H [282, 283] have been reported. Together with the fact of relatively strong adsorbent-absorbate interactions and their technological relevance these systems are considered as suitable adsorbent/absorbate combinations for our testing purposes. In general, the surfaces are modelled via so-called slabs. A slab consists of several atomic layers of the system to investigate [262, 264]. Also within this study this "slab-approach“ is used.

In section 13.3 the technical details, e.g. the used computational approach, the optimization algorithm and details on the construction of the periodical slab systems, are discussed. The subsequent section 13.4 deals with the results of the present study as well as the difficulties that arose during these investigations. Finally conclusions are drawn and future perspectives are described within section 13.5.

13.2 Theoretical background

13.2.1 Periodic calculations

Periodic structures, such as crystals, or crystal surfaces may be envisaged as very large molecules. Since calculations on the entire systems are practically not feasible, symmetry properties of these structures are utilized and only a relative small section of such a system is considered explicitly within a calculation. Here, the ideal infinite periodical structure consists of repeated units with periodic boundary conditions. Wavefunctions to describe a system consisting of N units are supposed to fullfill the cyclic boundary conditions [284]

$$\psi_k(\vec{r} + N \cdot \vec{a}) = \psi_k(\vec{r}). \tag{13.1}$$

a is the length of a unit, the lattice vector. Moving about N units along the system gives again the initial state. For an infinite system, there is an infinite number of units and an infinite number of molecular orbitals $\psi_k = \psi_k(\vec{r} + N \cdot \vec{a})$. Functions that obey the cyclic boundary conditions in equation 13.1 for $N \to \infty$ are the so-called Bloch functions [284]

$$\psi_k = \sum_{l=0}^{\infty} e^{ikla} \chi_l = \sum_{l=0}^{\infty} [\cos(kla) + i \cdot \sin(kla)] \chi_l, \tag{13.2}$$

where the factors e^{ikla} represent the coefficients of this linear combination [284] and the χ_l are translational images of each other. Within the first Brillouin zone [285] there is an infinite number of values for the wavenumber k, where k may adopt the following values:

$$-\frac{\pi}{a} \leq k \leq \frac{\pi}{a}. \tag{13.3}$$

Due to the fact that the crystal orbitals are described via trigonometric functions (equation 13.2), only the wavefunctions for $0 \leq k \leq \frac{\pi}{a}$ have to be considered. They contain the complete information on the system of interest.

Two- and three-dimensional systems, e.g. surfaces and crystals, are described via a two-component ($\vec{k} = (k_x, k_y)$) and three-component ($\vec{k} = (k_x, k_y, k_z)$) wavevector [284], respectively. For the simplest two-dimensional case, a square-grid [286], the first Brillouin zone is a square with dimensions

$$-\frac{\pi}{a} \leq kx,\ ky \leq \frac{\pi}{a}. \tag{13.4}$$

But, because of the symmetry properties of the Bloch functions, only the area $0 \leq k_x,\ k_y \leq \frac{\pi}{a}$ is of relevance. This area already contains all relevant information on the system. Similarly, a three dimensional system is completely described with the three components of the wavevector $\vec{k}$: k_x, k_y and k_z. They take values between 0 and $\frac{\pi}{a}$. In practical calculations, points within the first Brillouine zone of the corresponding material are sampled via so-called k-points. There are several ways to generate the k-points that describe a structure. They may be defined explicitly as k-point coordinates, or they may be generated automatically via some scheme [287].

13.2.2 Adsorption on Ni(111) and Ti(0001) surfaces

Adsorption of CO on Ni(111)

In principle, on Ni(111) four different high symmetry adsorption sites exist. Figure 13.1 depicts a Ni(111) surface, with these positions being marked: the onefold ontop (o) position, the twofold bridged (b) adsorption site and two threefold positions, fcc (f) and hcp (h). At the ontop site, the adsorbate is adsorbed atop of one single adsorbent atom and at the bridged position adsorption takes place atop two adsorbent atoms. For the fcc as well as the hcp site the adsorbate is located above three surface atoms. The threefold sites differ in the arangement of the Ni atoms within the second layer beneath the adsorption position. For the hcp site a Ni atom of the second layer is directly below the adsorption position. This is not the case for the fcc site.

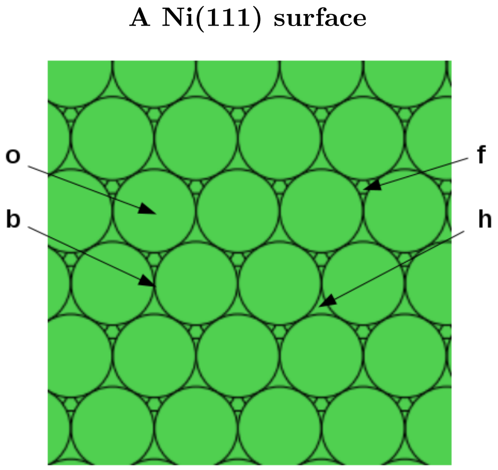

Figure 13.1: Sketch of a Ni111 surface. The different high-symmetry adsorptions sites are marked with arrows. The letters o, b, f and h denote the ontop, bridge, fcc and hcp adsorption position, respectively.

As for many other surfaces [278], the CO molecule prefers to adsorb on Ni(111) in a vertical upright position with the carbon atom pointing towards the surface. According to the Blyholder model [278, 288, 289, 290] two dominating interactions exist between CO and the metal surface. First of all, there is donation of electrons from the 5σ

orbital (lone pair, centered on carbon) of the CO molecule to the conduction band (vacant d orbitals) of Ni. Subsequently a back-donation from Ni to CO occurs. Here, electrons are transfered from the metal's valence band (consisting of filled d orbitals) to the antibonding $2\pi^*$ orbital of CO.
Concerning the stability of the different adsorption sites for CO on Ni(111), for the low coverage adsorption the following order (in increasing stability) can be concluded [264, 277, 278]:

$$\text{ontop} < \text{bridge} < \text{fcc} \lesssim \text{hcp}.$$

In general, the stability of the two threefold adsorption positions, fcc and hcp, is significantly higher than that of the one- or twofold adsorption sites. But the values for the adsorption energies for the fcc and hcp site are always very close to each other, with the hcp position in most cases being a little more stable than the fcc site [264, 276, 277, 278]. Experimental investigations confirm the hollow sites on Ni(111) to be favoured adsorption position for CO [257, 291]. The preference for certain adsorption sites also depends on the coverage of the surface [264, 277]. Since coverage effects are neglected within this study and we only consider the low-coverage regime, i.e. there is no interaction between the adsorbate molecules, this will not be discussed in detail here.

Adsorption of H_2 on Ti(0001) surfaces

Also the Ti(0001) surface exhibits four different high-symmetry adsorption sites. These are the same as for Ni(111): ontop (o), bridge (b), fcc(f) and hcp(h). Figure 13.2 depicts a sketch of a Ti(0001) surface with the high-symmetry sites being marked with arrows. H_2 is known to show a strong tendency for dissociative adsorption on Ti(0001) surfaces [279, 281]. Especially the d electrons of the Ti atoms on the surface contribute to the dissociation process [281]. Initally, when the H_2 molecule approaches the surface the s electrons of the Ti surface atoms and the MOs of H_2 overlap. The s states of the Ti atoms are fully occupied and due to the Pauli exclusion principle repulsion effects occur [281]. However, the resulting energy barrier is rather small since the d states of Ti are mainly unoccupied and the orbitals of H_2 and the d states of the Ti surface interact [281]. Electrons are transferred from the H_2 molecule to the conduction band (vacant d orbitals) of Ti. Electrons from the valence band (filled d orbitals) of Ti are back-donated to the antibonding MO of H_2 [281]. These interactions lengthen the H-H bond and enhance the dissociation of the molecule [281]. Once H_2 is dissociated, the single H atoms tend to occupy the hollow adsorption sites on Ti(0001), i.e. the

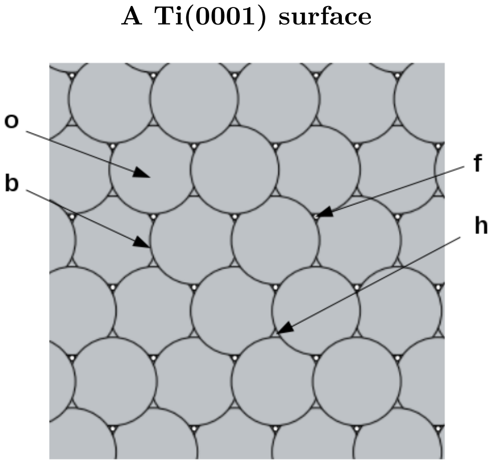

Figure 13.2: Sketch of a Ti(0001) surface. The different high-symmetry adsorptions sites are marked with arrows. The letters o, b, f and h denote the ontop, bridge, fcc and hcp adsorption position, respectively.

fcc and hcp positions [279]. Here, the two hydrogen atoms may occupy neighbouring threefold sites (unfavoured) or separated hollow positions (favoured) [279]. The general preference for hydrogen adsorption on threefold sites is confirmed experimentally as well as theoretically [292, 293]. Moreover it is known that the fcc and hcp hollow sites seem to be nearly degenerate concerning the stability for H adsorption [292].

13.3 Technical details

At the beginning of part III of this thesis, the essential components of the PooMa approach are listed. Also our extention of the PooMa approach that is needed for the issues of this chapter makes use of these essential elements and they are discussed in this section. First, the used computational approaches, SCC-DFTB [224] and DFT-LDA method, are discussed (subsection 13.3.1). This is followed by a description of the applied local and global optimzation algorithms in subsection 13.3.2: the conjugate gradient relaxation and the GA, respectively. The way of constructing the adsorbents, adsorbates and the adsorbent-adsorbate pairs can be found in subsection 13.3.3. This section concludes with a definition of the adsorption property that shall be optimized (subsection 13.3.4).

The code used to perform the calculations within this study, was written in the Python programming language. The basic simplicity of the Fortran code, used previously for the study of DSSCs, was maintained and combined with the flexibility and efficiency pro-

vided by available Python modules and tools, i.e. the Atomic Simulation Environment (ASE) [1, 2]. As before within our earlier PooMa code each chemical compound is represented by an array of integers within the GA. Special functions implemented in ASE are used to build up the structures before optimization and property calculation. Different types of chemical systems can be built using ASE, e.g. molecules, crystals or surfaces. This offers a high flexibillity concerning the optimization problems that can be treated. The method of electronic structure calculation is also included by using ASE modules. Hence, a current theoretical method can easily be changed into another approach. Many methods and packages are supported as calculators by ASE: simple potentials like effective-medium theory or the embeded atom method, packages like Quantum Espresso [294, 295], SIESTA [296], VASP [297] or DFTB+ [298]. Furthermore, local structural optimizations can either be performed with optimization algorithms as implemented in the package of the used calculator or with one of algorithms included in ASE [1, 2].
Among the different operations that are performed during a global property optimization, the local relaxations are the most time consuming procedures. Thus, the code has been parallelized with respect to the local optimizations of the pure adsorbents and the adsorbent-adsorbate systems and several systems can be relaxed simultaneously. This is realized by employing the Python package multiprocessing [3]. Summarizing the above, it can be stated that the Python modules of ASE are helpful for a further development of our PooMa approach, e.g. by offering a higher flexbillity concerning the uses of different electronic structure methods. Moreover, the simple ways of constructing various chemical systems with ASE is another advantage of the present approach.

13.3.1 Computational methods: DFTB and DFT

Two different methods of electronic structure calculation are used within this study: the DFTB approach as well as DFT in the local density approximation.

The SCC-DFTB

In order to obtain the total energy within the SCC-DFTB, the second-order term $E^2[\rho_{ref}, \delta\rho]$ has to be added to the total energy expression of the non-SCC DFTB method (equation 12.25 in section 12.2.1). This yields [221, 224, 225]:

$$E_{\text{tot}}^{\text{SCC}} = E^1[\rho_{ref}] + E^0[\rho_{ref}] + E^2[\rho_{ref}, \delta\rho]. \tag{13.5}$$

With this correction, charge fluctuations are taken into account, which gives a better description of e.g. heteronuclear systems [225]. The second-order energy term is

$$E^2[\rho_{ref},\delta\rho] = \frac{1}{2}\int\int\left(\frac{e^2}{4\pi\epsilon_0|\vec{r}-\vec{r}'|} + \left.\frac{\delta^2 E_{xc}}{\delta\rho\delta\rho'}\right|_{\rho_{ref}}\right)\delta\rho\delta\rho' d\vec{r}d\vec{r}', \tag{13.6}$$

with the density fluctuations $\delta\rho$ being approximated by atomic charge fluctuations Δq_α that in turn are calculated using the Mulliken population analysis [221, 225]. The integral in equation 13.6 is approximated via

$$\gamma_{\alpha\beta} = \gamma_{\alpha\beta}(U_\alpha, U_\beta, R_{\alpha\beta}), \tag{13.7}$$

where $\gamma_{\alpha\beta}$ is a function of the Hubbard parameters U_α and U_β of atom α and β and their interatomic distance $R_{\alpha\beta}$ [299]. The Hubbard parameter (chemical hardness) U_α is the second derivative of the energy E_{at} of the atom α concerning the total charge q_{at} of that atom [299]:

$$U_\alpha = \frac{1}{2}\frac{\partial^2 E_{\text{at}}}{\partial q_{\text{at}}^2}. \tag{13.8}$$

Using these approximation the expression for the second-order energy term in equation 13.6 can be simplified to [224]:

$$E^2[\rho_{ref},\delta\rho] \approx \frac{1}{2}\sum_{\alpha\beta}\gamma_{\alpha\beta}\Delta q_\alpha \Delta q_\beta. \tag{13.9}$$

Hence, the total energy within the SCC-DFTB [299] is:

$$E_{\text{tot}}^{\text{SCC}} = \sum_k n_k\epsilon_k + \frac{1}{2}\sum_{\alpha\beta}U_{\alpha\beta}^{rep} + \frac{1}{2}\sum_{\alpha\beta}\gamma_{\alpha\beta}\Delta q_\alpha \Delta q_\beta. \tag{13.10}$$

As for the non-SCC case a LCAO ansatz is used to describe the molecular orbitals, what leads to a secular equation system of the form:

$$\sum_{\nu_\beta} c_{\nu_\beta k}(H_{\mu_\alpha\nu_\beta} - \epsilon_k S_{\mu_\alpha\nu_\beta}) = 0, \tag{13.11}$$

with the $H_{\mu_\alpha\nu_\beta}$ representing the corrected charge self-consistent Hamiltonian elements that are calculated as [299]:

$$H_{\mu_\alpha\nu_\beta} = H^0_{\mu_\alpha\nu_\beta} + \frac{1}{2}S_{\mu_\alpha\nu_\beta}\sum_\zeta \Delta q_\zeta(\gamma_{\alpha\zeta} + \gamma_{\beta\zeta}). \tag{13.12}$$

Since the atomic charges Δq_ζ depend on the orbitals ψ_k, the secular equations 13.11 have to be solved self-consistently with respect to the atomic charges [221]. With the SCC-

DFTB method a higher accuracy is achieved at the expense of computational efficiency. The DFTB calculations within this study are performed with the DFTB+ package [298], which is used as a calculator within the ASE framework.

DFT-LDA

Besides DFTB, DFT is considered as a theoretical method for testing purposes within this study. Here, the SIESTA package [296] is chosen as calculator within ASE. SIESTA is a self-consistent DFT code that uses strictly localized basis functions [296]. Due to the use of a flexible LCAO scheme a wide range of applications is possible: fast and less accurate calculations using a minimal basis set and also very accurate computations with multiple zeta basis sets and polarization functions [296]. Within the framework of our GPO, the use of SIESTA with a minimal (or at least very small) basis set should be suitable and appropriate.

When using DFT, the main issue is to find an expression for the exchange-correlation functional $E_{xc}[\rho(\vec{r})]$. Within DFT-LDA the exchange-correlation functional solely depends on the local electron density at a point in position-space and is not a function of the gradient of the electron density $\nabla\rho(\vec{r})$ as for GGA methods. Spatially slowly varying electron densities are treated quite well, whereas for stronger density variations the GGA method is superior. Nevertheless DFT-LDA often yields surprisingly good results for various types of chemical systems [300, 301]. Since we are more interested in qualitative results and a high accurracy plays a minor role for our studies, the LDA is sufficient for our purposes, especially for test calculations.

Within the LDA (spin degeneration) or LSDA (local spin density approximation, different electronic spin states), the exchange-correlation functional $E_{xc}[\rho(\vec{r})]$ is approximated by the exchange-correlation energy $\epsilon_{xc}(\rho(\vec{r}))$ of a particle moving in an homogeneous electron gas of density $\rho(\vec{r})$:

$$E_{xc}^{LDA} = \int \epsilon_{xc}(\rho(\vec{r}))\rho(\vec{r})d\vec{r}. \tag{13.13}$$

This form of calculating the energy of a uniform electron gas has, e.g. been treated by Ceperley and Alder in 1980 [302]. Usually the exchange-correlation energy of a single particle $\epsilon_{xc}(\rho(\vec{r}))$ is split into two energetic terms: an exchange ϵ_x and a correlation ϵ_c contribution [303]. For ϵ_x an explicit formula is given. For the correlation energy ϵ_c of a particle there exist several parametrized expressions, like the Vosko-Wilk-Nusair (VWN) [304], the Perdew-Wang (PW) [305] or the Perdew-Zunger (PZ) [303] parametrization. In this study we use LDA with the PZ parametrization.

Additionally, within our calculations we tested different basis sets: the minimal, single-zeta (SZ) basis set, the double-zeta (DZ) basis set and the single-zeta basis set including polarisation functions (SZP).

13.3.2 The global optimization algorithm

As for the optimization of solar energy harvesting properties a simple GA is used for the GO of the adsorption properties. Well-converged structures are needed in order to obtain reliable properties and therefore each single system is optimized locally. Here, the DFTB method is used together with the conjugate gradient (CG) relaxation and when using DFT-LDA the Limited-memory Broyden-Fletcher-Goldfarb-Shanno algorithm (L-BFGS) is applied. First, the two local optimization algorithms are briefly discussed and subsequently the used GA is presented.

Local structural relaxations: the Conjugate gradient and the Limited-memory BFGS algorithm

In case of using DFTB as electronic-structure method, the CG algorithm turned out to work best concerning the structural relaxation of the surface systems. For test calculations also the L-BFGS is employed.

The CG algorithm, developed by M. Hestens and E. Stiefel in 1952 [93], is an improvement of the steepest descent relaxation. The steepest descent relaxation uses the updated gradient as the new search direction. The optimization proceeds along the direction of the largest descent [91]. This may be inefficient and many steps have to be taken to reach the minimum point. In contrast to that, the CG method uses conjugate vectors p_k as search directions. The vectors p_k are A-conjugate [91]:

$$p_k^T A p_k = 0, \tag{13.14}$$

with A being a symmetric, positive-definite matrix. The search direction is not that of the maximal descent, but it is ensured that the search proceeds along a descent direction. Within the CG relaxation the vectors p_k describe the conjugate descent directions, which are calculated using the gradient vectors g_k [91]. The flowchart in figure 13.3 depicts the basic operating principle of the CG algorithm. Initially an arbitrary starting point x_0 is used to calculate the initial gradient vector g_0 as well as the initial conjugate search direction p_0 [91]. The step size α_k and subsequently the new point x_{k+1} are determined. After updating the gradient vector ($g_k \rightarrow g_{k+1}$), it is checked whether convergence is reached or not. If some termination criterion is fulfilled, the algorithm stops, otherwise it continues. The new conjugate search direction p_{k+1} is computed as linear combination of the recent gradient vector g_{k+1} and the previous conjugate search direction p_k [91]. The local optimizations of the chemical systems has been performed with the CG method as implemented in DFTB+ code [298].

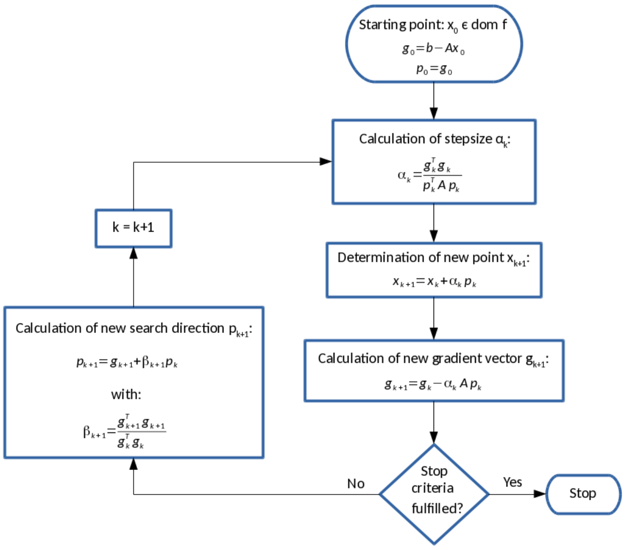

Figure 13.3: Simplified flowchart showing the general workflow of a conjugate gradient algorithm, as used for local relaxations within this study.

The L-BFGS algorithm is an approximation to the BFGS method, presented in section 9.2.1 [306, 307]. The BFGS algorithm is a *quasi-Newton* approach, that stores an approximated version of the inverse Hessian matrix. The L-BFGS method only stores a few vectors instead of a whole matrix, reducing the amount of computer memory needed [306, 307]. Especially larger optimization tasks are treated with LBFGS algorithms. Since this local optimization procedure is used only for testing purposes within this study and the *quasi-Newton* method has been discussed in section 9.2.1, a detailed presentation of the L-BFGS is not provided within this section. Local optimizations have either been performed with the L-BFGS method as implemented in DFTB+ [298] or as implemented in ASE [1, 2].

Optimization of adsorption properties: the genetic algorithm

As for the optimization of the solar energy harvesting properties (section 12.2.2) a simple GA is used. Prior to a calculation one defines the adsorbent system to be investigated and the molecule that is supposed to be adsorbed. The low-index surface types are used as a kind of framework and it is varied, whether an atom or a vacancy occupies a position within the uppermost layer of the slab. It is possible to consider different low-index surface types of one transition metal within one calculation, e.g. fcc111, fcc100 and fcc110 for a fcc TM like Ni. Except for the local optimizations of the slabs and the slabs with added adsorbate, where the positions of the slab atoms are adjusted, the corresponding surface type acts as a fixed framework. The uppermost layer of a slab may include no vacancy at all or only one atom, an adatom, remains within the top layer. Any possibility between no vacancies and a single remaining atom can be considered. Strings with integers are used to present the slabs within the GA and all operations during the GA are applied to these strings. Here, adsorbents atoms and vacancies are represented by different integers.

To keep the approach as unbiased as possible, not only high-symmetric adsorption positions can be considered for the adsorbate, but also different, non-high symmetry sites. At the same time, it can also be chosen that the adsorbate is added to the slab in a less-symmetric orientation with respect to the surface, i.e. in a different orientation than a vertical or horizontal one. Therefore, the adsorbate molecule can be rotated through angles with respect to x, y or z axes. Figure 13.4 shows a CO molecule in such a tilted position added to a Ni(111) slab. This strategy also takes into account the fact that in reality most of the molecules to be adsorbed on a surface do not necessarily approach the surface in high symmetric orientations and at high symmetric adsorption sites. Built-in functions of ASE are used for rotating the molecular adsorbates.

A Ni(111) surface and a CO molecule

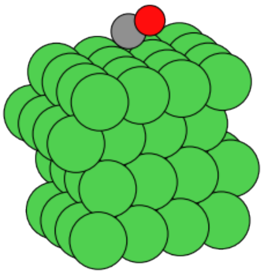

Figure 13.4: A 4x4x4 Ni(111) slab with a tilted CO molecule as adsorbate approaching the surface. Green balls denote nickel atoms and the grey and red ball denote a carbon and an oxygen atom, respectively.

At the moment one single orientation of a molecule can be considered within a calculation. But the PooMa source code used for the present study may be developed further in the future to include several orientations within one calculation. Hence, besides the variation of the number of vacancies within the uppermost layer of the slab, also the adsorption positions may be varied and each system can be identified via its number and positions of vacancies, its surface type and the adsorption site, at which the adsorbate molecule is placed.

The used GA is very similar to that described in section 12.2.2 and it can be divided into the following steps:

1. An initial pool of $2P$ different slabs is created randomly. All relevant information on the system, including the molecule's adsorption site, are defined. It is ensured that there are no identical systems within the pool.
2. Each of the pure slabs without adsorbate is optimized locally and subsequently the relaxed adsorbate molecule is added to each of the optimized slabs and the obtained adsorbent-adsorbate systems are relaxed locally, too.
3. The perfomance function is calculated for each single slab and the different candidate structures are ordered according to the optimal property value.
4. The pool of $2P$ slabs is seperated randomly into P pairs.
5. The pairs of slabs are subjected to recombination operations. For each pair of slabs, each of the two, represented by a string of N integers, is cut into two parts consisting of M and $N - M$ integers with $0 < M < N$. The two equivalent parts of the two parent structures are interchanged, resulting again in two strings, each with N integers. For each of the generated children its surface type and adsorption site is chosen randomly out of its parents' surface types and adsorption sites.
6. Mutation operations are performed. Using a random number it is decided if a recently generated child is mutated or not. Four different mutation operations are possible, with random numbers determining which of these operations is executed. For example, a certain number of randomly chosen positions within the uppermost layer of the slab is subjected to substition mutations. An adsorbent atom is exchanged into a vacancy and vice versa, i.e. the one integer describing the corresponding object (atom or vacancy) is exchanged into the other one. Moreover, permutation mutations are possible, where the integers in the string, representing the structure, are randomly shuffled. Another possible operation is the shift of the integers by a random number of places. Here, integers that are shifted beyond

the last position in string, are re-introduced at the beginning of the string. The last mutation process that is considered, is the simple exchange of the surface type and adsorption site into another combination of type and site. If only one cell type is considered within an investigation, only the adsorption site is exchanged. It is always checked, that no duplicate structures exist among the $4P$ parent and children slabs. If a structure is duplicate, this slab is discarded and a new child is created by recombination of two parents. Also in this child mutations may be introduced.

7. The children slabs are optimized locally, the relaxed adsorbate is added to the slab and the adsorbent-adsorbate system is also relaxed. Subsequently the performance function is calculated for each system and all structures (parents and children) are ordered according to their property value.
8. Out of the $4P$ parents and children, the $2P$ best performing slabs are selected and serve as parents for the next generation of slabs.
9. It is checked, whether one of the termination conditions is fulfilled: either a predefined maximum number of calculated generations is reached or a predefined number of best peforming structures stays unchanged for a predefined number of generations. The latter criterion is the desired one, since no better structures have been obtained within a longer period of time and convergence of the calculation can be assumed.

13.3.3 Construction of the systems

All of the chemical systems within this study are constructed using building functions implemented in ASE [1, 2]. Within the GA each of the structures is represented by a string of integers: here we use the atomic number of the element the surface consists of to represent the slab atoms. Besides the atomic number for the adsorbent atoms, vacancies are represented by any integer different from the atomic number of the adsorbent atom, e.g. by the atomic number of another element. This could be considered as a dummy atomic number, which is just a placeholder. These strings, including the different integers for atoms and vacancies, are subjected to the operations within the GA as described in the previous section 13.3.2. Through the use of different integers, the positions of the vacancies within the strings, and hence within the surface, are marked. Initially each slab is built without vacancies using the string with atomic numbers and subsequently the atoms at the marked positions within the surface are deleted to yield the slab with defects. The slabs are easily built using so-called ASE *Atoms* objects and functions of the *ase.build* module. This functions are used to build up chemical structures, that can be optimized locally and whose properties can be calculated. For example, in order to built up a 4x4 Ti(0001) slab with four layers (a 4x4x4 structure) and a vacuum of 10 Å on both sides of the slab the one-line command [1, 2]

$$\mathbf{Adsorbent = ase.build.hcp0001(Ti,size{=}(4,4,4),vacuum{=}10.0)} \tag{13.15}$$

has to be used within the Python code. This results in a defect-free adsorbent in which the vacancies are incorporated by deleting the corresponding atoms out of the uppermost layer. The molecule to be adsorbed, e.g. H_2, is obtained using the following function [1, 2]:

$$\mathbf{Adsorbate = ase.build.molecule('H2')}. \tag{13.16}$$

Using ASE, one can resort to a large database of different molecules. After optimization of the pure slab, again a function of the *ase.build* module is employed to add the adsorbate to the slab. Thereby, an adsorbent-adsorbate system is obtained. This can be realized by the one-line command [1, 2]

$$\mathbf{ase.build.add\_adsorbate(Adsorbent,Adsorbate,height,position,offset,mol\_index)}, \tag{13.17}$$

with height, position, offset and mol_index representing the initial height of the molecule above the slab prior to local relaxation, the x-y position of the molecule on the surface, the offset of the adsorbate and the index of the atom of the adsorbate, which is located above the adsorption position, respectively. Figure 13.5 shows the constructed defect free slab (1), the same slab including the vacancies (2) and the final adsorbent-adsorbate system (3).

To speed up the calculations, i.e. the local relaxations of the slab systems, it is common to fix the atoms of a certain number of layers of a slab during the relaxation processes [243, 261, 262, 264]. This has also been done in the present study. The number of layers that is kept fixed may vary depending on the investigated system or because of other reasons. The number of moved/fixed layers within the present investigations are indicated at the corresponding places in section 13.4.

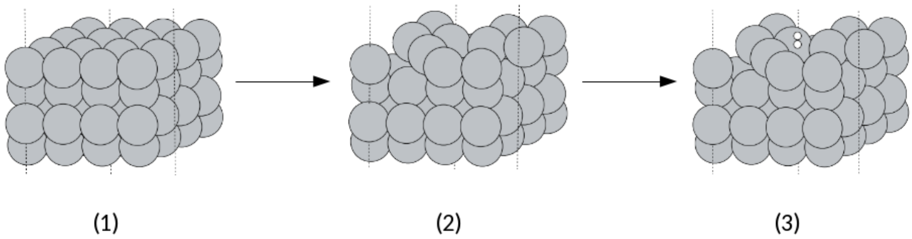
Construction of slab systems including vacancies

Figure 13.5: Example for the construction of the slab systems. Big, grey balls denote Ti atoms and small, white balls denote H atoms: Ti slab without vacancies (1), Ti slab including vacancies (2) and the Ti slab with added adsorbate H_2.

13.3.4 Adsorption: the property

A widely used quantity to describe the adsorption properties of surfaces is, of course, the adsorption energy E_{ads} [239, 259, 271, 276]. Also in our study, we make use of this quantity. The adsorption energy is calculated using the following simple formula

$$E_{\text{ads}} = E_{\text{slab+mol}} - E_{\text{slab}} - E_{\text{mol}}, \tag{13.18}$$

with $E_{\text{slab+mol}}$, E_{slab} and E_{mol} representing the total energy of the relaxed adsorbent-adsorbate system, the total energy of the relaxed adsorbent and the total energy of the relaxed adsorbate, respectively. Due to the simple mathematical description of the adsorption energy, it is suitable to be considered as property within our PooMa approach. Hence, it requires more local optimizations, i.e. the local optimization of the adsorbate, the pure adsorbent and the adsorbent-adsorbate system.
With regard to the definition of the adsorption energy in equation 13.18 a negative value for E_{ads} corresponds to an exothermic adsorption process and a positive value for E_{ads} to an endothermic one. Furthermore, the more negative the value for E_{ads} is, the stronger the adsorption is.

13.4 Results and discussion

Several problems occured concerning the use of DFTB+ as a calculator in combination with Ni(111) as adsorbent. These difficulties and the tests with SIESTA as alternative to DFTB+ are described in section 13.4.1. But also with SIESTA as a calculator problems arose, which complicate the use SIESTA within our PooMa approach. Simultaneously further tests with the DFTB+ have been performed. This time Ti(0001) surfaces were considered. Ti as adsorbent turned out to be less problematic than Ni. Owing to a lack of time the technical problems concerning the use of SIESTA could not be solved anymore within this thesis. Therefore at least Ti was used to test the extention of our PooMa approach. This is described in section 13.4.2. To reduce the computational cost of the calculations, not all layers of a slab are moved during a relaxation and some of the bottom layers are kept fixed. As previously mentioned, this is a common procedure, when studying the adsorption properties of surfaces using theoretical methods [261, 264, 283]. The different calculational parameters, e.g. the slab sizes or the number of k-points, are listed at the corresponding parts in this section.

13.4.1 Testing the electronic structure methods: Ni slabs

Test calculations with SCC-DFTB

Initially, test calculations with DFTB+, implemented as calculator in ASE, have been performed. These tests were carried through in order to check the suitability of the method and, especially, the Slater-Koster (SK) files. Ni as adsorbent and CO as adsorbate molecule have been chosen. The SK files for Ni, C and O have been taken from the trans3d [308] and mio set [309] available on dftb.org [4]. The trans3d set has been developed to describe the interaction between 3d transition metals with C, O, N, and H atoms, but it was initially not tested for periodic systems. Other studies mention the use of this SK file set in order to calculate the properties of Fe surfaces [310, 311]. Since they do not give a reference for the trans3d SK files, it is not clear if their used set coincides with the SK set used within this thesis and Ref [308]. Nevertheless, for the first test calculations the trans3d set has been used. Concerning the good transferability of the DFTB method we were confident that our tests would be succesfull.

Unless not explicitly mentioned, the following calculations have been performed without spin-polarization. It is reported that the consideration of spin, has a more quantitative than a qualitative impact on the results of the adsorption calculations for Ni [312, 313, 314]. Since we are more interested in the qualitative order of adsorption energies and our purpose is to identify trends, the consideration of magnetization might not be necessary. Moreover, the inclusion of spin increases the computational cost, which is not practical for an unbiased GPO as PooMa. Nevertheless, for the sake of comparison, also spin-polarized test calculations have been performed in certain cases. To determine the k-point mesh, the difference in the total energy per atom obtained from single-point calculations of the pure slabs have been used as criterion. Several calculations have been performed, successively increasing the k-points. Starting with a grid of 2x2x1 and continuing with 3x3x1, 4x4x1, 5x5x1 etc. it was checked, whether the difference in the total energy per atom of the slabs of two subsequent calculations, e.g. with 3x3x1 and 4x4x1 k-points, is about 1 meV or lower. When the difference between two successive meshes was lower than this value, convergence was assumed and the lower mesh of these two was used for the calculations. In the case that the computational cost did not increase to much, just to be sure, sometimes also the larger of the two meshes was chosen. Throughout all investigations the mixing of charges within the SCC cycles was performed with the Broyden charge mixer, using a mixing parameter of 0.1. Calculations for bulk fcc Ni, using the equation of state analysis, yield a lattice constant of 3.636 Å. This is in fair agreement with the experimental value of 3.520 Å [315].

The following slab calculations have been performed with a 4x4x1 k-point mesh. The maximum force component was allowed to be 0.001 atomic units (= au, Hartree per Bohr), the SCC tolerance was set to 0.0001 electrons and a vacuum of 10 Å was added on each side of the slab. Moreover, an electronic temperature of 0.00001 Hartree was used within these calculations. This was necessary in order to reach charge-self-consistency within the SCC cycles and/or to improve the SCC convergence. The need for a finite temperature for electrons is observed quite frequently, when investigating metallic or near-metallic systems with the SCC-DFTB method [316, 317].

Initially, we wanted to perform test calculations in order to ckeck the qualitative ordering of the different adsorption sites for CO on Ni(111). Here, we wanted to investigate, if the SCC-DFTB method is able to reproduce the known order of stability for CO adsorption on Ni(111): ontop $<$ bridge $<$ fcc $\lesssim$ hcp (see section 13.2.2). But unexpected results were obtained. The atoms that were allowed to move upon local relaxation, moved a lot and no intact (111) structure could be obtained after optimization. This effect becomes stronger, if the number of relaxed layers is increased and it also influences the value of the adsorption energy E_{ads}. Due to these problems, checking the order of stabilty of the different adsorption sites on Ni(111) was not pursued any longer. Instead, we wanted to understand the reason for the strange behaviour of the slab atoms upon relaxation. In figure 13.6 4x4x4 sized Ni(111) slabs with CO as adsorbate, initially on a bridge adsorption site, are depicted, prior to local optimization (left) and after local relaxation (right).

Also the adsorption energy E_{ads} and the number of relaxed layers are shown below the optimized structures. The calculations for the two slabs with size 4x4x4 only differ in the number of layers, which are relaxed. It can be noticed that the atoms within the slabs moved a lot upon relaxation and the final structures seem to be relatively disordered compared to the initial ones. The Ni(111) structure is no longer intact. Moreover,

Adsorption tests for CO on Ni(111) I

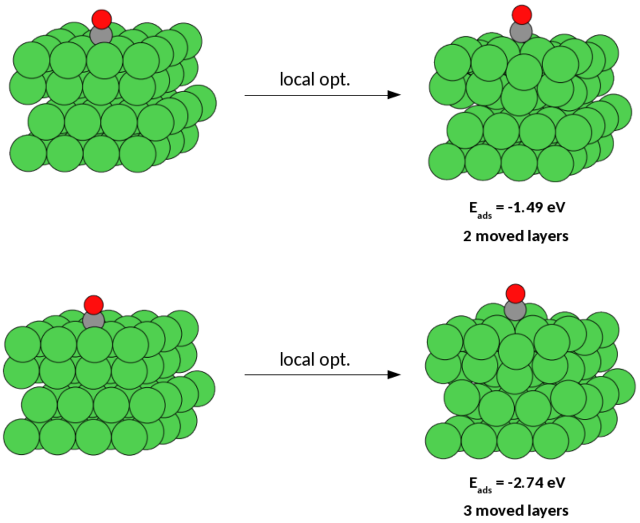

Figure 13.6: Results obtained from local optimizations of Ni111/CO adsorbent-abdsorbate systems (size of Ni(111): 4x4 and 4 layers). The two upper systems represent the initial (left) and final (right) structure, when two layers are moved during relaxation. The two lower slab systems represent the initial (left) and final (right) structure, when three layers are moved during relaxation. For both optimizations the structures on the left show the Ni slab and the CO molecule in their relaxed geometries, assembled as adsorbent-adsorbate systems, prior to their local optimization. Additionally the corresponding adsorption energies E_{ads} and the number of layers, moved during the optimization, are shown below the relaxed adsorbent-adsorbate systems.

comparing the values for the adsorption energy for the two cases, it becomes obvious that they differ more than 1 eV. More atoms are moved during the optimization depicted in the lower part of figure 13.6, and more degrees of freedom are allowed, which results in a lower adsorption energy E_{ads}. This can also be observed for larger sized systems. In figure 13.7 Ni(111) slabs of size 4x4x5 are shown, before (left) and after (right) they have been relaxed locally.

In the upper part in figure 13.7 three and in the lower part four layers have been relaxed during optimization. The previous observations are also made for the 5-layer systems. Performing further calculations with varying parameters, e.g. force tolerance, slab size in x and y direction, number of layers, vacuum, k-points and different adsorption positions, similar observations can be made. In figure 13.8 some more results are shown, i.e. a relaxed 6x6x6 sized adsorbent-adsorbate system with four relaxed layers (left part in figure 13.8) and a relaxed 4x4x8 slab with three relaxed layers (right part in figure 13.8).

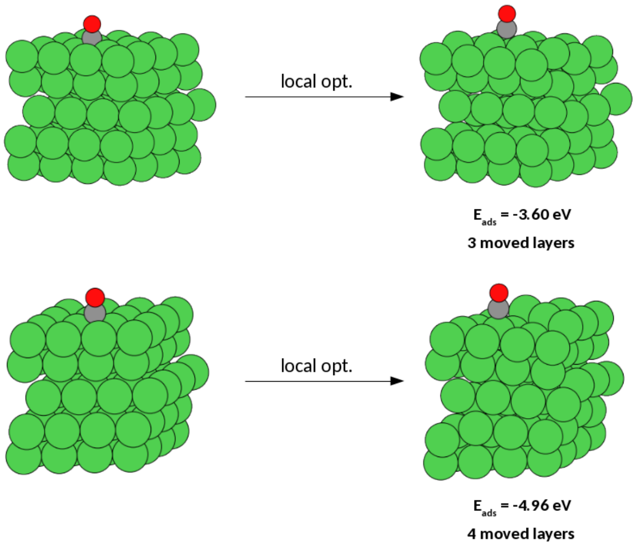

Adsorption tests for CO on Ni(111) II

Figure 13.7: Results obtained from local optimizations of Ni111/CO adsorbent-abdsorbate systems (size of Ni(111): 4x4 and 5 layers). The two upper systems represent the initial (left) and final (right) structure, when three layers are moved during relaxation. The two lower systems represent the initial (left) and final (right) structure, when four layers are moved during relaxation. For both optimizations the structures on the left show the Ni slab and the CO molecule in their relaxed geometries, assembled as adsorbent-adsorbate systems, prior to the local optimization of the adsorbent-adsorbate system. Additionally the corresponding adsorption energies E_{ads} and the number of layers that are moved during the optimization, are shown below the relaxed adsorbent-adsorbate systems.

Both results have been obtained using a 4x4x1 k-point mesh, a force tolerance of 0.005 au and a SCC tolerance of 0.005. In both cases the electronic temperature was set to $1 * 10^{-7}$. The slabs depicted shall illustrate that regardless of the used system size or calculational parameters, it was not possible to obtain reasonable results, which could have been used for further investigations. It is also noticeable that, if more atoms are allowed to relax during a relaxation, a stronger distortion and a drastically reduced adsorption energy E_{ads} is obtained. For the slab on the left in figure 13.8 144 atoms were allowed to relax and this yields an adsorption energy of -13.41 eV. For the slab on the right in figure 13.8 only 48 atoms could relax during the local optimization, which results in an adsorption energy of -2.47 eV. By providing more degrees of freedom, i.e. by increasing the number of relaxed atoms during a relaxation an increasing stability of the adsorbent-adsorbate systems can be observed after the optimization (compare also figures 13.6 and 13.7). The crucial point is now that upon the local optimization

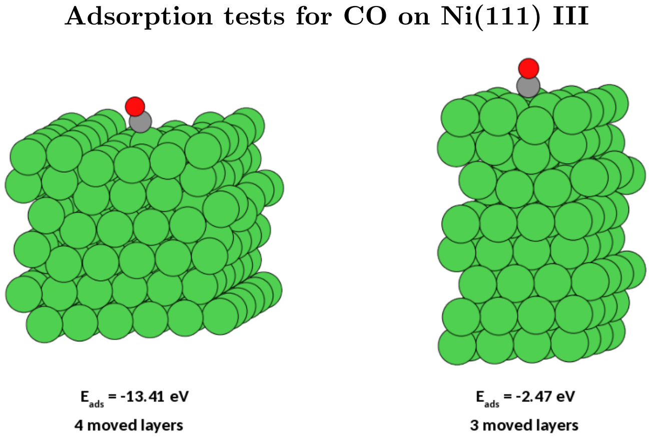

Figure 13.8: Two locally relaxed Ni(111)/CO adsorbent-adsorbate systems. On the left part a 6x6x6 slab is depicted. Four layers were allowed to move during the optimization process for this structure. On the right part a 4x4x8 slab is shown. Three layers of atoms were allowed to move during the relaxation. Below the structures, the corresponding adsorption energies and the number of moved layers are depicted.

of the adsorbent-adsorbate systems, the slabs do not remain within the structure of the Ni(111) surface. One may expect more or less small corrections concerning the interatomic distances between the slab atoms and the retention of the fcc(111) geometry upon local optimization. But instead the system relaxes out of this geometric structure to reach another local minimum. The presence of an adsorbate molecule leads to a distorted structure and it seems that the slabs are not really stable and therefore the adsorption energies E_{ads} depicted in the figures 13.6, 13.7 and 13.8 are not useful to describe the adsorption properties of the surfaces. These values are mainly determined by the amount of slab atoms that are allowed to relax during the relaxations and in the present case by the disorder that arises within the slabs during these local optimizations. Interestingly, however, the disorder of the slab does not occur, when optimizing the pure slab. Only, if an adsorbate is present this behaviour of the slab atoms can be noticed. To exclude that the neglect of spin-polarisation is responsible for the rearrangement of the slab atoms, also calculations considering the magnetization of Ni have been executed. But a similar disorder within the optimized adsorbent-adsorbate systems could be identified for these calculations.

Guo *et al.* described the adsorption of organic molecules on bcc Fe(110) slabs [310, 311], also using DFTB as electronic structure method. They state that they used the trans3d SK set, but without giving a reference in their works. Hence, it is not possible to declare with absolute certainty that this SK set is the same as that one used within this thesis.

In their study they do not report any unexpected behaviour or deformation of the slabs upon adsorption processes. But trying to reproduce some results of Ref. [310] was not succesfull and distorted slabs have been obtained after the optimization process. Also the adsorption of CO was tested, which led to distorted Fe slabs. We tested different parameters and settings and each time similar results, distorted slabs, were obtained. Relaxed Fe(110) slabs of size 4x4x4 (upper part) and 5x5x4 (lower part) are shown on the right in figure 13.9. These results have been obtained using a 4x4x1 k-point mesh, however, convergence was already achieved for a 3x3x1 grid. A maximum force tolerance of 0.001 au, a SCC-tolerance of 0.0001 electrons and an electronic temperature of 0.00001 au was used. Furthermore, CO was positioned above an ontop adsorption site before the local relaxation.

Adsorption tests for CO on Fe(110)

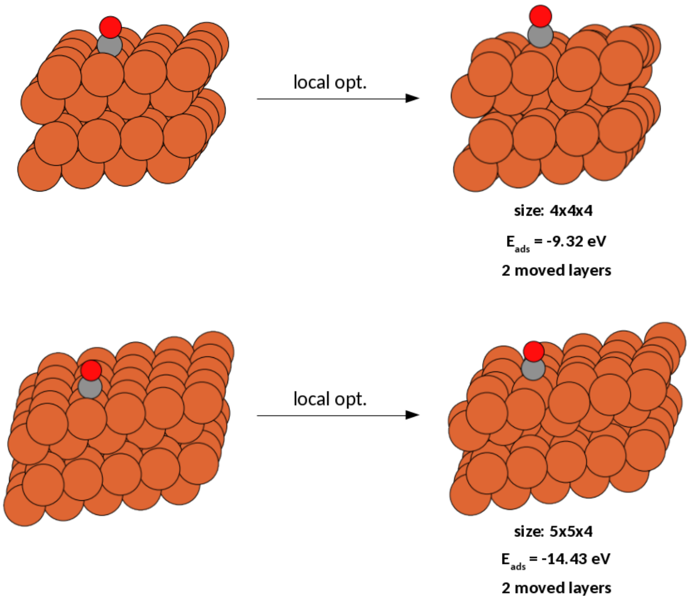

Figure 13.9: Adsorption tests for the Fe(110) surface. Prior to optimization (left part) the CO molecule was added to an ontop adsorption site. In the upper part the relaxation of a 4x4x4 sized Fe(110) slab is shown and in the lower part the optimization of a 5x5x4 sized slab is depicted. In both cases, a disordered slab system is obtained (right part).

From the distortion of the structures and the rearrangement of the slab atoms in both cases it can be deduced that also the Fe(110) slab cannot be described properly. Also the adsorption energies, depicted below the relaxed adsorbent-adsorbate systems, verify this conclusion. Trying to get in contact with the corresponding author of the DFTB studies of Ref. [310, 311] to obtain some information was not succesfull.

First, it should be noted that with the DFTB method and the SK files of Ni and Fe of the trans3d set, no reasonable results could be obtained within this study. We wanted to find out the reason for the rearrangement of the slab atoms upon the adsorption processes. A disorder in the slab after optimization can only be observed in case of the presence of an adsorbate molecule and a relaxed pure slab does not show such atomic rearrangements. The slab without molecule is of higher symmetry than the system with adsorbate and the adsorbate molecule can be considered as some kind of disturbance. Therefore, we thought to continue researching in that direction. We were interested in the behaviour of the slab when a symmetry reduction would be imposed on the pure slab without adsorbate. Hence, the pure 4x4x4 Ni(111) slab was optimized, with varying initial positions of one randomly selected atom within the top layer of the slab. This one atom was moved out of plane of the layer upwards in z-direction prior to optimization and then the slab was relaxed locally. Thereby a symmetry reduction was imposed on the pure slab. Several optimizations have been performed, successively increasing the initial displacement of that atom. For the calculations discussed below, if not otherwise mentioned, the top two layers were allowed to relax, whereas the two bottom layers were kept fixed. Many such calculations with varying parameters have been performed and similar results have been obtained. Accordingly, only some of these results have been selected for discussion. The parameters for the calculations depicted in figure 13.10 are the same as for the adsorption tests of CO on Ni(111) depicted in figure 13.6 and 13.7.

On the left in the upper part of figure 13.10 a Ni(111) slab prior to optimization is shown. No atom is initially moved out of plane of the surface. The local relaxation yields the slab on the right, which exhibits an undistorted structure. The positions of the atoms changed to a small extent, but the fcc111 structure is maintained. In the lower part of figure 13.10, on the left, it can be noticed that an atom has been moved in the z-direction out of plane of the uppermost layer. This initially distorted slab is optimized locally, which results in the structure shown on the bottom right in figure 13.10. Upon relaxation the initially displaced atom does not move down to the "regular" position within the top layer. It remains/moves about 0.6 Å above the plane of the uppermost layer. Particularly striking is the fact that the total energy of the relaxed slab E_{slab}, shown below the optimized slab in figure 13.10, is lower in the distorted case. For a stable Ni(111) slab one would expect the undistorted, symmetric structure to be lower in energy than the slab with displaced atom in the lower part of figure 13.10. But the undistorted Ni(111) system is 168 meV higher in energy and therefore less stable than the distorted one. Several of such optimizations have been performed with increasing

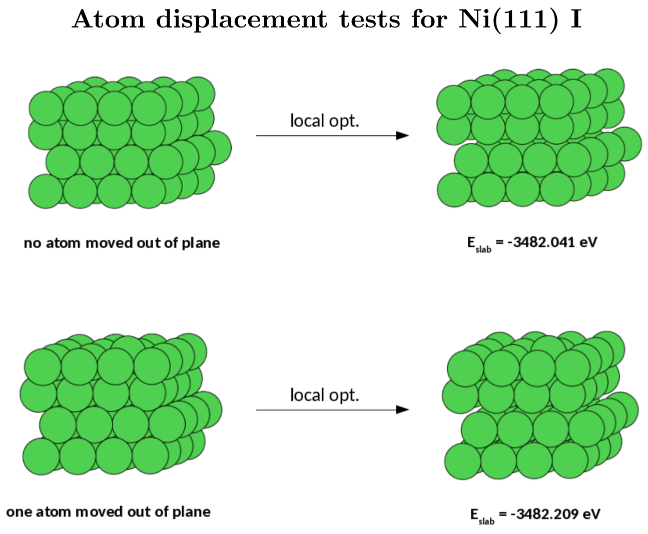

Figure 13.10: Displacement tests for Ni(111). The upper part of the figure depicts the optimization of a pure, defect-free Ni(111) slab. On the left the structure is shown before optimization. No atom has been displaced initially, prior to relaxation. On the right the relaxed slab is shown, which posseses a symmetric, undistorted structure. The lower part depicts also the relaxation of a pure, defect-free slab, but with an initially displaced atom (left). Upon relaxation of that system, the initially moved atom does not return to a position within the plane of the uppermost layer. It remains in a position about 0.6 Å above the plane. The total energy of the optimized slab, shown below the relaxed slabs, is lower for the initially distorted slab.

initial displacement of the atom as shown in the lower part of figure 13.10. The smallest displacement considered was 0.1 Å and at a displacement of 0.4 Å or larger the atom does not move back into the plane of the top layer. But the atom migrates to a position 0.6 Å above the plane of the top layer. A larger displacement of an atom, e.g. about 1.8 Å even leads to a large disorder in the Ni(111) system, with the fcc111 structure not remaining intact. In this case, also a lower energy than for the structures depicted in figure 13.10 is obtained. Such a disordered Ni(111) slab is shown in figure 13.11.

The behaviour described above is even more pronounced when changing the element from Ni to Fe. Below the results for a 4x4x4 Fe(110) slab are discussed examplarily. The allowed maximum force on the atoms was set to 0.005 au. The other calculational parameters were the same as in the case of the Ni(111) slabs. Also here, Fe(110) slabs of different sizes and different calculational parameters have been tested and each time similar results have been obtained. Strong rearrangements within the Fe(110) slabs occur

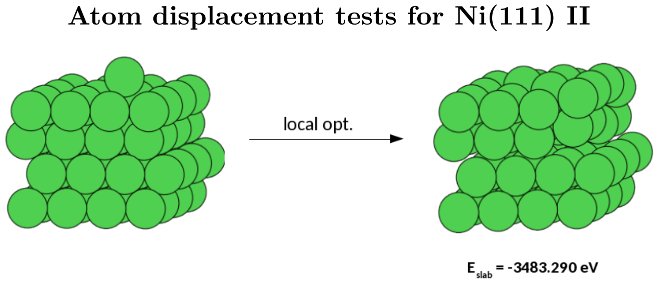

Figure 13.11: Further atom displacement tests for Ni(111). A larger displacement of an atom of the top layer is considered. On the left the Ni(111) slab is shown before the local relaxation. One atom has initially been moved about 1.8 Å above the plane of the uppermost layer. The resulting structure after the optimization is distorted and its total energy, shown below the relaxed slab, is even lower than the energy of the systems shown in figure 13.10.

upon adsorption processes (see figure 13.9) as well as during the atom displacement tests. For the Fe(110) slab a very small displacement of an atom is enough to lead to a disorder in the structure. This is shown exemplarily in figure 13.12 where the upper part depicts the local relaxation of an initially undistorted Fe(110) slab. The bottom part shows the starting structure and the final slab for a optimization of an initially distorted slab. Here, a very small displacement of an atom of about 0.1 Å upwards out of the plane of the top layer leads to a strong disorder within the Fe slab after the optimization. The total energies of the relaxed slabs are shown below the corresponding structures and it can be noticed that the disordered Fe(110) system is about 5 eV lower in energy than the undistorted one.

Concerning these results one is able to draw some conclusions. As long as the transition metal slabs posses a higher symmetric geometry and a higher ordered structure before the local optimization, the system will retain that geometry (state) upon relaxation. Only the interatomic distances between the slab atoms change to some extent during this optimization process. But the overall structure is maintained. This suddenly changes if a more or less strong symmetry reduction or a disturbance is imposed on the system. This was done by adding an adsorbate or by an initial displacement of a slab atom. If such a disturbance is suffieciently large, neither the Ni nor the Fe slabs yield an undistorted structure after the optimization. Instead, a disordered arrangement of the slab atoms (see for example figures 13.7, 13.8 or 13.12) or a slab atom remaining above its surface position are the result. This strongly indicates that these slabs are not stable when using the DFTB method with this SK files. Hence, they are not suitable to describe properly the adsorption properties or at least the interaction among the slab atoms. This leads

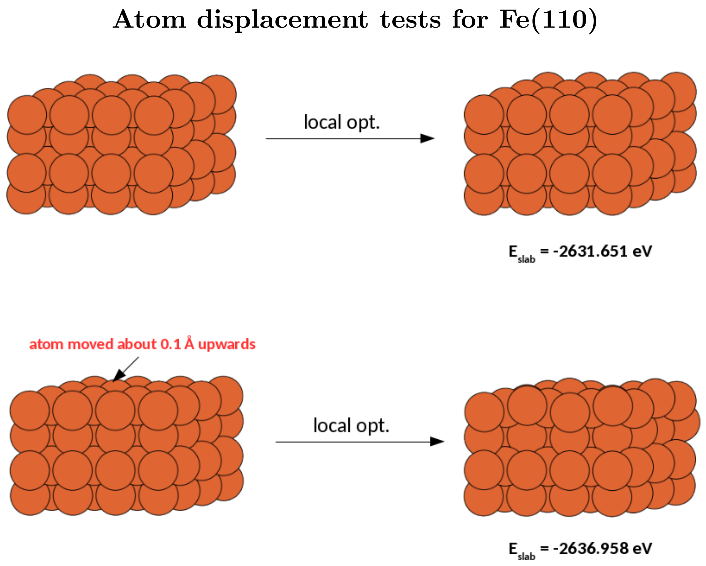

Figure 13.12: Atom displacement tests for Fe(110). The upper part of the figure depicts the local optimization of an initially undistorted slab. No atom has been displaced prior to optimization and the resulting structure after the relaxation is a symmetric undistorted Fe(110) slab. The lower part shows the relaxation of a slab, which exhibits a small distortion prior to relaxation. On the left the corresonding atom is moved about 0.1 Å above the plane of the top layer (the moved atom is marked by an arrow). This small distortion leads to a disordered structure after relaxation (right). The disordered relaxed slab is about 5 eV lower in energy than the symmetric, undistorted system, shown on the right in the upper part of the figure.

to the unreasonable and unusable results shown above.

Several possbilities exist to address this problem. Maybe the solution lies in the creation of other SK files, which are adapted to the problem of describing Ni and Fe slabs. But then the SK files for all possible diatomic interactions have to be set up. In the case of the Ni(111)/CO system the parametrization of nine diatomic interactions would have to be performed and nine SK files would have to be created. Although there are straightforward procedures to create such SK files this is a time-consuming procedure. It would somehow counteract the spirit of our approach, the PooMa method, with its simple, uncomplicated basic idea. For each further adsorbate molecule that would be considered, a whole set of SK files would have to be created. Actually one of the resaons for the preference of the DFTB method for our PooMa approach is its transferabillity and the existence of a large amount of SK files for different applications. But, as could be seen above, there are limitations concerning this transferabillity. Of course, in case of not having any other alternative, the creation of further SK files is a necessary work and would have been also our next step. But we wanted to maintain the spirit of PooMa and make use of the gained flexibility, when using ASE. Therefore we decided to change the calculator within ASE from DFTB+ to SIESTA. The test calculations using SIESTA are discussed in the following section. Simultaneously, we started to investigate the adsorbent-adsorbate system Ti(0001)/H_2 using DFTB+. These calcualtions are presented in section 13.4.2.

Test calculations with DFT-LDA using SIESTA

By using localized atomic orbitals, SIESTA is a fast and efficient DFT package and compared to plane-wave DFT codes a much smaller computational effort is needed [296]. This makes SIESTA the calculator of choice, when treating large chemical systems or GO tasks with DFT. Hence, we were optimistic that we could employ SIESTA with a small, ideally minimal, basis set within our PooMa approach. Our intention was to obtain a reliable qualitative description of the adsorption processes on transition metal surfaces, while keeping the computational cost as low as possible.

Again the combination Ni(111)/CO has been considered as adsorbent-adsorbate system. The potential files used for the elements were downloaded from the *Virtual Vault for Pseudopotentials* [5]. The difficulties that arose during the DFTB calculations on Ni(111)/CO, discussed in the previous section 13.4.1, did not occur for the DFT calculations performed with SIESTA and no disordered slabs have been obtained. Therefore, we started our investigations by examining the high symmetry adsorption sites on the Ni(111) surface. But it turned out that a single zeta (minimal) basis set including polarisation functions is needed to describe the adsorption properties properly. Neither the pure minimal (single zeta) nor the double zeta basis turned out to be suitable. Below a more detailed discussion, concerning this issue, will follow.

The EOS analysis, using SIESTA as a calculator, yielded a lattice constant of 3.503 Å for bulk Ni, which is in good agreement with the experimental value of 3.524 Å [315]. In order to minimize the computational costs, first the minimal basis set was tested. But it quickly became evident that the single-zeta (SZ) basis is not sufficient to describe the adsorption of CO on Ni(111). Several parameters and different calculational settings have been tested, but with the minimal basis the ontop as well the bridge site turned out to be not stable enough for the CO molecule to remain and to be adsorbed. For both high-symmetry sites the CO molecule migrates to a neighbouring higher coordinating threefold adsorption site upon local relaxation. In general, the two threefold sites, fcc and hcp, exhibit a higher stability with respect to CO adsorption than the ontop and bridge positions, which results in a more negative adsorption energy [264, 276]. But in the present case, when using the single zeta basis set, these sites are rather unstable for a CO adsorption. This behaviour of the CO molecule on Ni(111), when using the minimal basis set, is examplarily shown in figure 13.13.

Ontop and bridge adsorption tests on Ni(111) using a minimal basis set

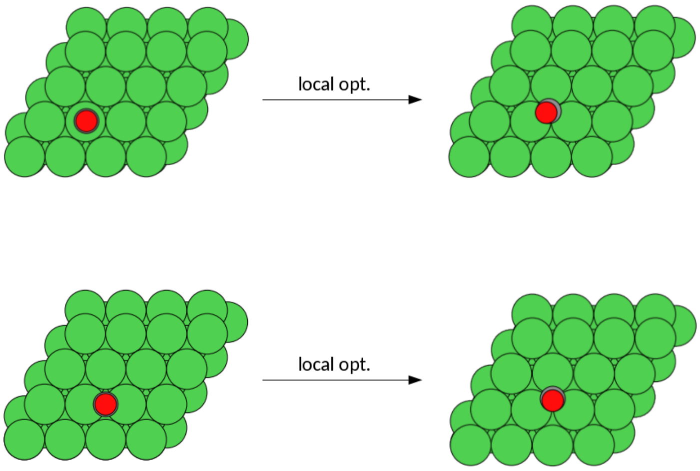

Figure 13.13: Ni(111) surfaces with CO molecules added to ontop and bridge positions prior to relaxation (left side). Upon optimization the CO molecules migrate away from the intial positions towards a threefold adsorption site. The upper part of the figure depicts CO initally located above an ontop site and the bottom part depicts CO initially located above a bridge adsorption site.

On the left upper part in the figure, a Ni(111) slab with CO above the ontop site is shown prior to relaxation. On the right upper part the adsorbent-adsorbate system is shown after the relaxation, where the CO molecule migrated to the neighbouring fcc site. The lower left part of figure 13.13 shows the CO molecule at the bridge position before the optimization. The optimized slab-adsorbate system is shown on the right, with CO moved to a near fcc position. The migration of the CO molecule from the one- and twofold adsorption sites to the threefold positions of course severely complicates the investigation of the different adsorption sites on Ni(111). This may not be a proper representation of this adsorbent-adsorbate system for our purposes. Changing the minimal to the double-zeta (DZ) basis set corrects for the description of the ontop adsorption, but in case of the bridge adsorption, the CO molecule still moves towards a neighbouring threefold site. However, when using a SZ basis with additional polarisation functions (SZP) each high-symmetry adsorption site on Ni(111) can be described. For the minimal and the DZ basis the orbitals might be too strictly localized on the atoms. This rigidness and inflexibility may be the reason that stabilizing interactions between the

CO molecule and the one- and twofolded sites on Ni(111) can not be treated properly. So, only by using polarisation functions, distortions (polarisations) of the orbitals of CO and Ni upon the adsorption process may be describable. Hence, throughout the test calculations with SIESTA, the SZP basis set was used.

Convergence tests have been performed to determine the number of k-points as described in section 13.4.1. Thereby, a k-point mesh of 4x4x1 was identified as providing accurate results. A vacuum of 15 Å was selected, although it may be possible to use a smaller vacuum, since the qualitative description of the adsorption properties is not affected much by this parameter. Local optimizations have been performed with the L-BFGS algorithm and a force tolerance of 0.05 eV/Å. For the SCF cycles density-matrix mixing was used. Self-consistency was assumed, if the maximum difference between the input and the output of each element within the density matrix was below 0.001. For the mixing of the density matrix the Pulay mixer has been employed with a mixing weight of 0.01. Furthermore, during the geometry optimizations, the two top layers of the slabs and the adsorbate molecule were allowed to relax. The atoms of the remaining layers were kept fixed at their inital positions.

Next, test calculations for the x and y dimensions of the slab and the number of layers of the slab are performed. Here, the variation in the adsorption energy as well as the qualitative order of the various high-symmetry adsorptions sites on Ni(111) serve to identify the suitable size of a system. We took into account that our GO approach makes it necessary to reduce the computational costs for local optimizations of the slab systems. A quantitative description of the adsorption energies is less import for our PooMa approach. We want to identify trends and give suggestions, concerning structural arrangements and chemical groups that might be beneficial for a certain property. Therefore, the focus is on obtaining a reliable, qualitative view of the adsorption chatracteristices, i.e. the order of stability of the different high-symmetry adsorption sites on Ni(111). Moreover, especially for initial tests of our approach a qualitative description of the adsorption properties is sufficient.

Results for this test calculations are shown in table 13.1. For the larger sized slabs, e.g. 5x5x3 and 6x6x3 also larger k-point meshes have been tested, but no significant differences to the use of 4x4x1 k-points could be observed.

The entries 1 to 4 in table 13.1 depict the adsorption energies for an increasing number of layers, whereas entry 5 and 6 show the results of the calculations for a larger x and y extention of the slabs. For the different slab sizes the values for E_{ads} differ quantitatively, whereat it can be noticed that the difference decreases with increasing number of layers (entries 1-4) and also with increasing extention in x and y direction (entries 1, 5 and 6).

Table 13.1: Adsorption energies for CO on the high-symmetry adsorption sites of Ni(111) for different slab sizes.

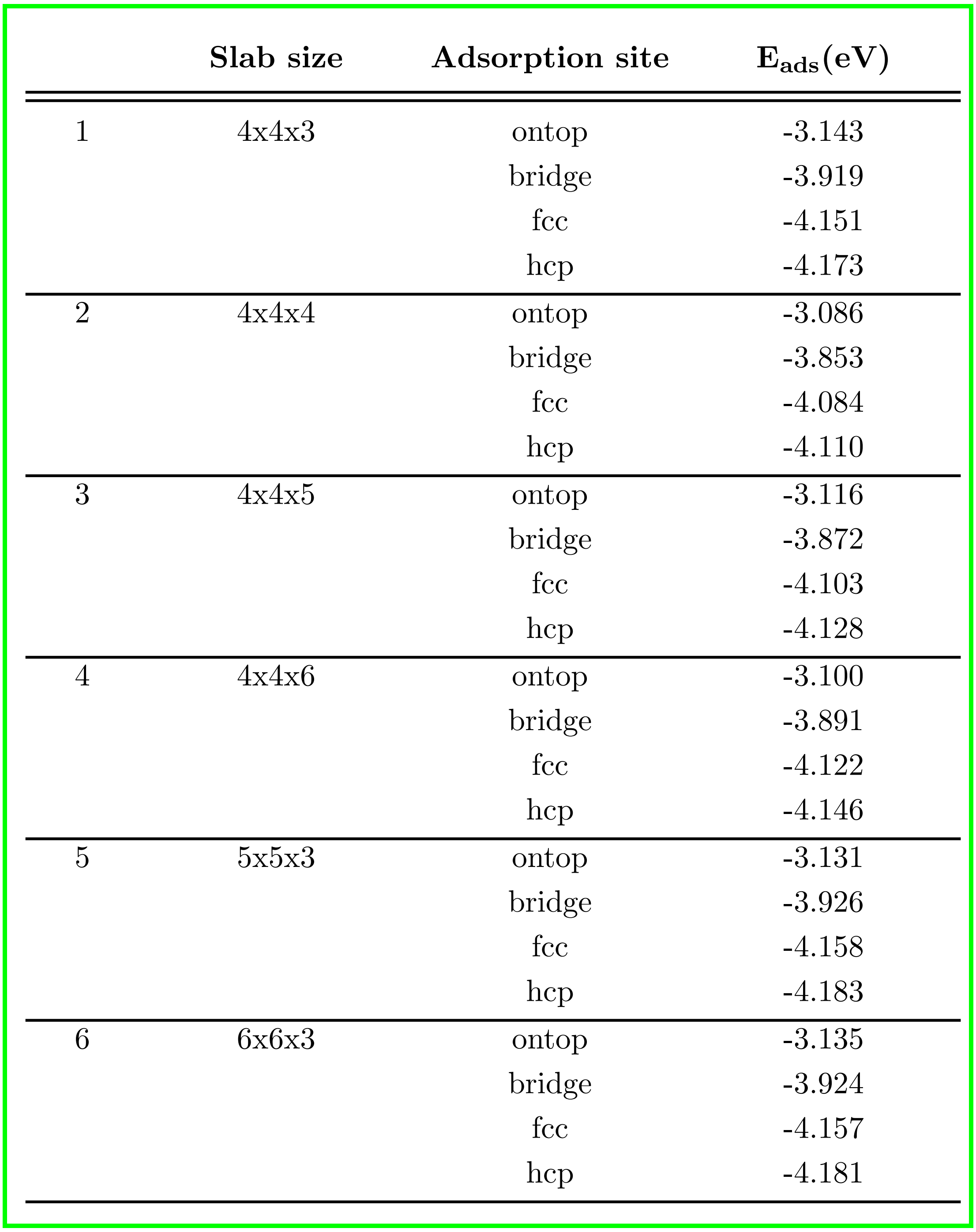

	Slab size	Adsorption site	E_{ads}(eV)
1	4x4x3	ontop	-3.143
		bridge	-3.919
		fcc	-4.151
		hcp	-4.173
2	4x4x4	ontop	-3.086
		bridge	-3.853
		fcc	-4.084
		hcp	-4.110
3	4x4x5	ontop	-3.116
		bridge	-3.872
		fcc	-4.103
		hcp	-4.128
4	4x4x6	ontop	-3.100
		bridge	-3.891
		fcc	-4.122
		hcp	-4.146
5	5x5x3	ontop	-3.131
		bridge	-3.926
		fcc	-4.158
		hcp	-4.183
6	6x6x3	ontop	-3.135
		bridge	-3.924
		fcc	-4.157
		hcp	-4.181

For all slab sizes the order of stability of the different high-symmetry adsorption sites is ontop < bridge < fcc < hcp. This is in accordance with the results of various DFT calculations, e.g. Refs. [264], [277] or [278]. Also factors like the coverage play an important role for the adsorption properties [264, 277], but we limit our discussions to the adsorption of one single molecule, i.e. a low-coverage of the Ni(111) surface. In relative terms, all slab sizes shown exhibit a lower stability concerning the ontop adsorption. This is apparent in the relatively low values for E_{ads} compared to the other adsorption sites, which also agrees with the results of other studies [264, 277, 278]. As known from literature [264, 277, 278] and also in accordance with chemical intuition the two threefold adsorption sites, i.e. fcc and hcp, are quite close in stability. Since a reliable, qualitative description is already achieved for the 4x4x3 slab and for initial tests of our approach a small, conmputational inexpensive system may be sufficient, we decided to continue our investigations with this slab size.

But some technical problems occured concerning the use of SIESTA with the parallelization of the PooMa code. During the relaxation of the slabs the programm accesses some files. When performing local optimizations of several slabs in parallel it may happen that during different optimizations the same file is accessed at the same time, which causes some error. This problem could be addressed by performing the relaxations in different folders, e.g. one folder for the optimization of one structure, as it was also done, when using DFTB+ as a calculator. In doing so, one single folder is assigned to a single local optimization and each optimization accesses its files in its own folder. But this could not be implemented in case of SIESTA and it seems to be a more difficult task. The different calculators that can be used within ASE have a different way of creating and accessing theirs input and output files. Unfortunately, due to the advanced time, further investigations in this direction could not be realized within this doctoral thesis. Furthermore, simultaneously with the tests of SIESTA for Ni, the DFTB method has been applied to Ti(0001) surfaces and promising results have been obtained. Hence, and also due to the lower computational effort of the DFTB method compared to DFT, we decided to continue with Ti. The results with Ti(0001) as adsorbent to test our PooMa approach are presented in section 13.4.2. The investigations using SIESTA as a calculator may serve as basis for further studies, which also may try to solve the technical issues described above.

13.4.2 Testing the PooMa approach: Ti slabs and H_2 adsorption

Testing the applicability of DFTB with Ti0001/H_2

The Ti(0001) surface was chosen as adsorbent and the simple H_2 molecule as adsorbate. The *tiorg* [318] and the *mio* [309] SK sets have been employed for the calculations. For bulk hcp Ti the lattice parameters have been determined via a EOS analysis, which yields the following parameters: a = 2.988 Å, c = 4.884 Å and a/c = 1.634. They are in good agreement with the experimental values of a = 2.951 Å, c = 4.686 Å and c/a = 1.588 [318].

No distorted Ti slabs, as obtained for Ni using DFTB, can be observed upon optimization. Also atom displacement tests, as described for the Ni slabs in section 13.4.1 have been performed. In the case of Ti(0001) as surface, atoms displaced prior to optimization, do not remain above the plane of the top layer upon relaxation. The initially displaced Ti atom always migrates to its "ideal" position within the top layer of the Ti(0001) surface. Regardless of a vertical displacement upwards above the surface or a horizontal and vertical displacement, the atom moves to the surface position, even for a larger displacements about 1.8 Å.

Test calculations with the SCC-DFTB method have been performed to determine the number of k-points. A k-point mesh of 4x4x1 is sufficient. A vacuum of 10 Å is added on both sides of the slab. An electronic temperature of 0.00001 Hartree is employed, the Broyden charge mixing parameter is set to 0.1 and the atoms within the two uppermost layers are allowed to relax, whereas the other layers are kept at fixed positions. The strong tendency of H_2 to dissociate on Ti(0001), as described in section 13.2.2, is also observed for the DFTB calculations within this study. Moreover, the single H atoms also prefer to occupy the hollow adsorption sites on the Ti(0001) surface.

In order to determine a suitable slab size and to check the performance of DFTB with the combination Ti0001/H_2 further tests have been performed. Figure 13.14 depicts a sketch of the Ti(0001) surface with three possible adsorption positions for the two H atoms after dissociation of the H_2 molecule [279].

Here, the hydrogen atoms may be located in neighbouring hollow sites after dissociation, i.e. one atom is located at position 1 and the other one in position 2 (1-2 adsorption). Or the H atoms are located in separated threefold sites, i.e. 1-3 or 1-4 adsorption. According to the configuration interaction (CI) calculations of Ref. [279] the 1-2 adsorption position is less stable compared to the other two arrangements. Here, two H atoms are located adjacent to each other, one atom occupying a fcc the other one occupying a hcp site. For the 1-4 position, the hydrogen atoms are opposite each other with one Ti atom in

Ti(0001) surface with different adsorption positions for dissociated H_2 molecules

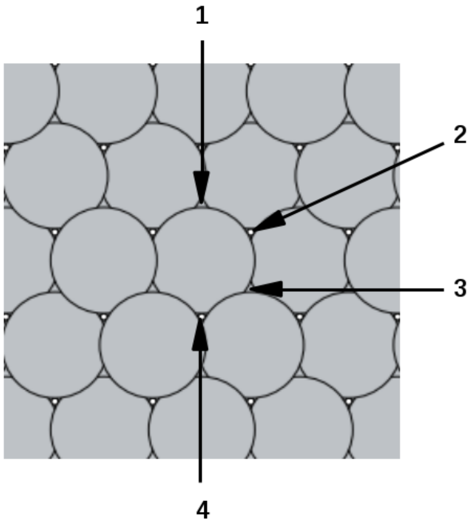

Figure 13.14: Sketch of a Ti(0001) surface. After dissociation, the H atoms tend to migrate to the threefold adsorption sites on Ti(0001). Three arrangements of the H atoms after dissociation are considered. The hydrogen atoms may be located in adjacent hollow sites (1-2), or in seperated threefold sites (1-3 and 1-4).

between.

We calculated the order of the three adsorption sites, 1-2, 1-3 and 1-4 for different Ti(0001) slab sizes. The results are shown in table 13.2.

The single H atoms are placed on the corresponding positions prior to local relaxation to speed up the optimization procedure for these calculations. In order to check the order of stability of the different adsorption sites, this procedure is sufficient. With two exceptions (entries 7 and 10 in table 13.2) for each slab size in table 13.2 the order corresponds to that found in Ref. [279]. The 1-2 site is always less stable than the 1-3 and 1-4 positions. The latter two are closer in energy. Except for the 5x5x3 (entry 7) and 6x6x3 sized slab (entry 10) the 1-3 site is slightly more stable than the 1-4 site, which is also in accordance with the results of Ref. [279]. In general, the adsorption values for different slab sizes differ quantitatively, but agree qualitatively. Our investigations predict the same order of stability for these three sites as the CI calculations of Ref. [279]. Moreover, we performed the same calculations with the non-SCC DFTB approach and the results are basically very similar to those of the self-consistent method. Concerning the slab size, a smaller system, e.g. 3x3x4, might be sufficient for initial tests of our PooMa aaproach.

Table 13.2: Adsorption energies for dissociated H_2 at three different sites of Ti(0001) for different slab sizes. The sites 1-2, 1-3 and 1-4 denote the position of the hydrogen atoms on the Ti surface according to figure 13.14.

	Size	**Site**	$\mathbf{E_{ads}(eV)}$		**Size**	**Site**	$\mathbf{E_{ads}(eV)}$
1	3x3x3	1-2	-2.237	7	5x5x3	1-2	-2.070
		1-3	-2.418			1-3	-2.200
		1-4	-2.411			1-4	-2.209
2	3x3x4	1-2	-2.296	8	5x5x4	1-2	-2.625
		1-3	-2.508			1-3	-2.817
		1-4	-2.463			1-4	-2.785
3	3x3x5	1-2	-2.292	9	5x5x5	1-2	-2.625
		1-3	-2.512			1-3	-2.853
		1-4	-2.465			1-4	-2.787
4	4x4x3	1-2	-2.373	10	6x6x3	1-2	-1.993
		1-3	-2.546			1-3	-2.174
		1-4	-2.533			1-4	-2.212
5	4x4x4	1-2	-2.403	11	6x6x4	1-2	-2.856
		1-3	-2.620			1-3	-3.021
		1-4	-2.570			1-4	-2.977
6	4x4x5	1-2	-2.417	12	6x6x5	1-2	-2.854
		1-3	-2.629			1-3	-3.044
		1-4	-2.572			1-4	-2.999

Tests with Ti(0001)/H_2: The PooMa approach

Due to the time-consuming problems met during the investigation of the other adsorbent-adsorbate systems (see section 13.4.1) only a few test calculations with our PooMa approach could be performed. A genetic algorithm (see section 13.3.2 for details) is used to optimize the adsorption properties of the Ti(0001) surfaces automatically. A slab size of 3x3x4 is employed. These test calculations have been performed using the non-SCC DFTB method, which is sufficient for testing the genetic algorithm. Each position within the uppermost layer of the slab may be occupied by a Ti atom or a vacancy. Here, we consider any arrangement and composition, ranging from a slab without any vacancy to a single adatom within the uppermost layer. Our program automatically determines that compositions/arrangements, which exhibit the best adsorption properties, i.e. the lowest adsorption energy (see equation 13.18). To each slab the H_2 molecule is added in a tilted, non-symmetric orientation. Figure 13.15 depicts an example of such an adsorbate-adsorbate system prior to relaxation.

Ti(0001) surface with vacancies and a H_2 molecule

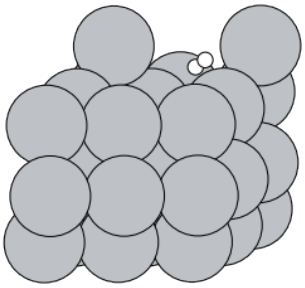

Figure 13.15: A Ti(0001) slab, including several vacancies, with a tilted H_2 molecule as adsorbate approaching the surface. Grey and white balls denote titanium and hydrogen atoms, respectively.

Four different non-high-symmetry adsorption sites are considered for each slab, which gives in total $4 \cdot (2^9 - 1) = 2044$ adsorbent-adsorbate systems for the 3x3x4 sized slabs. Up to eight vacancies within the uppermost layer are considered. For this relatively small number of structures, it is practical to calculate the adsorption energy for each single system. In order to check the efficiency of our genetic algorithm we calculated the performance of each of the 2044 slab systems and compared to the structures that were automatically determined by our PooMa approach. Especially the calculation of each of the 2044 single systems becomes more feasible when using the non-SCC approach. Four calculations have been performed, and in all cases our approach was able to identify the best performing adsorbent-adsorbate system, after 30, 26, 35 and 36 generations. With a pool size of 16 structures within each generation, the optimal solution could be determined after 480, 416, 560 and 576 calculated structures, respectively. These values are well below the total number of 2044 possible systems and additionally it has to be remembered that one or more slabs would be generated more than once within such a calculation. The occurence of duplicate structures within the children and parent systems is prevented. Directly, after construction of a system, it is checked, if the system is already included within the structure pools. But, of course, it is possible that a structure is generated again in subsequent generations. A system that is not included within the best structures due to its worse performance, is removed from the structure pool and it may be created again within subsequent generations. Therefore, a slab may be generated more than once. Moreover, in most cases, also the second best adsorbent-adsorbate system is identified by our genetic algorithm.

Examining the results of the calculations in more detail, reveals that the hydrogen atoms seem to have a high preference for certain positions on a surface. Within our present calculations we consider four different adsorption sites for each slab system. Starting with different initial configurations, i.e. the hydrogen molecule being added to different positions on the surface, may lead to very similar structures after optimization. The positions of the hydrogen atoms only differ marginally, when comparing two of these structures, and also the values for the adsorption energies are quite close. So, the hydrogen molecule dissociates and the single hydrogen atoms migrate to similar positions on the surface upon relaxation, although the initial structures (prior to optimization) are different. An example for this phenomena is depicted in figure 13.16.

In order to obtain different final configurations for the slabs, it might be considered as well that the initial positions of the H_2 molecule have to differ more than the positions shown on the left in figure 13.16. But, it may not be easy (or impossible) to identify, when two initial configurations differ enough in order to lead to different structures after optimization.

Firstly, the finding above demonstrates that there are indeed certain positions on the Ti(0001) surface, where the hydrogen atoms preferably adsorb. The structures with hydrogen adsorbed on these sites seem to represent well-defined minima. But, although the structures are different prior to relaxation, the preference for certain adsorption sites leads to very similar (in principle the same) structures after optimization and to duplicate systems within the results. This could be prevented by including a structure similarity test after the optimization of the single adsorbent-adsorbate systems, but due to the lack of time this task could not be accomplished within the present thesis. Therefore,

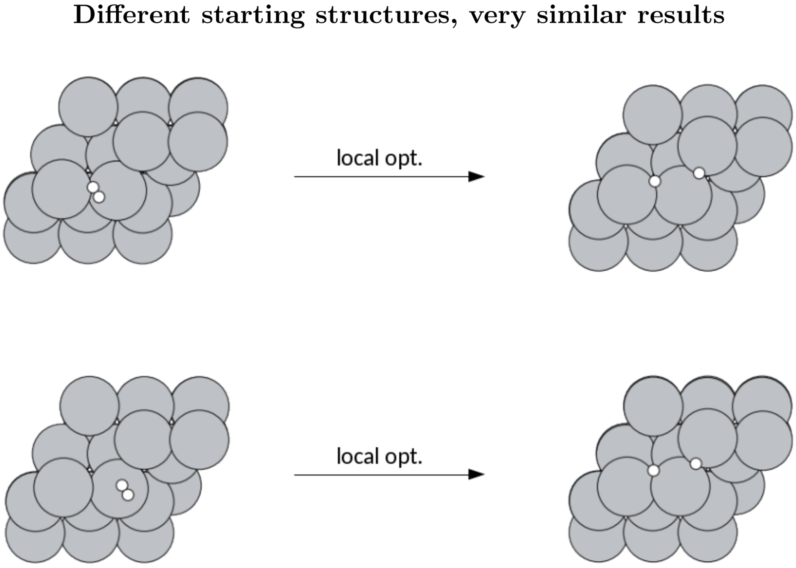

Figure 13.16: Adsorption of H_2 on Ti(0001). The same adsorbent with different adsorption positions is shown. Prior to relaxation, the H_2 molecule is located at different positions on the Ti(0001) surface (left top and left bottom part). Upon relaxation the H_2 molecule dissociates and in both cases the hydrogen atoms migrate to very similar positions on the surface. Therefore the final structures are very similar.

future investigations may solve this problem and improve the efficiency of the present PooMa approach.

In figure 13.17 we show the four best performing adsorbent-adsorbate systems in their final configurations, obtained with our genetic algorithm. Each of the structures exhibits several vacancies/adatoms within the uppermost layer of the slab. Obviously vacancies or adatoms are beneficial for the dissociative adsorption of the H_2 molecule.

In general, the hydrogen atoms prefer to be adsorbed at sites, where they are surrounded by several Ti atoms. This is in accordance with the findings that H tends to occupy the threefold adsorption sites on a defect-free Ti(0001) surface (see section 13.4.2). For each structure depicted in figure 13.17 hydrogen is located in higher-coordinating spacings. Except for the preference of higher-coordinating adsorption sites, the exact positions of the hydrogen atoms on many of the surfaces depicted in figure 13.17 are not easily understood in terms of chemical intuition and this makes predictions difficult. But, this shows that our PooMa approach is able to yield unexpected and interesting results. For the non-SCC DFTB method the adsorption energies for the dissociative adsorption of H_2 on defect-free 3x3x4 Ti(0001) slabs are roughly 200 meV higher than that of the best-performing adsorbent-adsorbate system in figure 13.17 (system to the left). In their *ab*

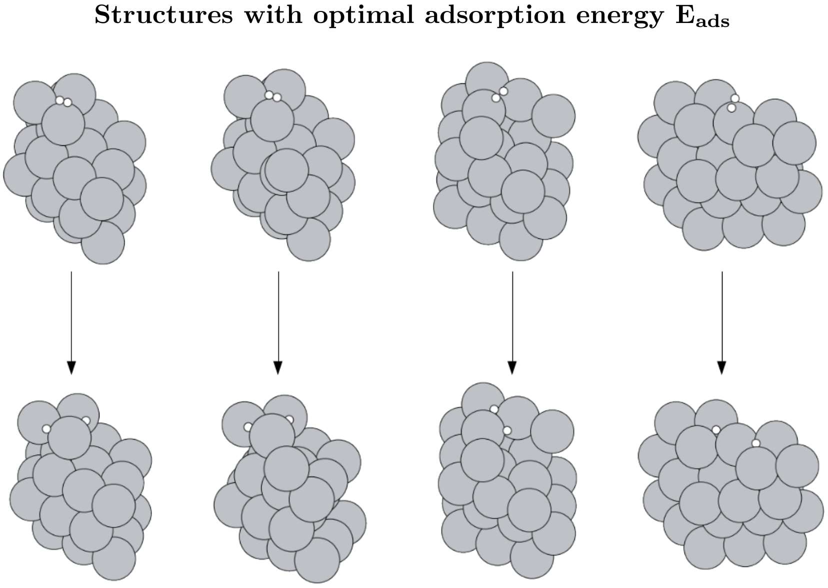

Figure 13.17: H_2 adsorption: the four best-performing Ti(0001) slabs, i.e. the slabs with the lowest adsorption energies, identified with our genetic algorithm. The initial structures (prior to relaxation, top structures), as well as the final structures (after relaxation, bottom structures) are shown. The adsorption energy increases (the performance decreases) from left to right. Grey and white balls denote titanium and hydrogen atoms, respectively.

initio studies Cremaschi and Whitten investigated the adsorption of hydrogen atoms on Ti(0001) with an additional Ti adatom on the surface. Here, they also observed a strong exothermic adsorption process [319]. Our PooMa approach is able to yield interesting adsorbent-adsorbate systems. According to our first test calculations vacancies/adatoms may have a positive influence on the performance of Ti(0001) concerning dissociative H_2 adsorption. Further investigations may also use the self-consistent charge DFTB method as a calculator within the present PooMa approach, which, for reasons of time, could not be performed within the present study. It may be of interest to study, to what extent the present results differ from the structures that are obtained with the SCC treatment.

13.5 Conclusion and outlook

In the present study we have developed an extension of our PooMa approach in order to optimize the adsorption properties of surfaces. Here we have made use of the many possibilities offered by ASE [1, 2] and its high flexibility concerning the construction of chemical systems and the use of electronic structure methods. As in our previous studies [52, 205, 215] the DFTB method was chosen as theoretical approach and a genetic algorithm as global optimization procedure. As variation we implemented, whether a position within the top layer of the slab is occupied by a slab atom or a vacancy and we also considered different adsorption sites. Hence, our approach is supposed to identify slabs with such arrangements/compositions, which optimize the adsorption energy.

Before the usage of a certain adsorbent-adsorbate system in combination with our PooMa method we have tested the corresponding systems. Problems occured with Ni(111)/CO. The SK files [308] used to describe the atomic interactions did not yield stable Ni slabs within our investigations. We changed the calculator from DFTB+ to SIESTA (DFT). Here, we obtained promising results for the qualitative description of the different high-symmetry adsorption sites for CO on Ni(111). But, due to technical problems, SIESTA could not be combined succesfully with our parallelized PooMa approach until now.

In parallel with the calculations using SIESTA, we started to investigate the system Ti(0001)/H_2. With DFTB+ as calculator and the SK files from Ref. [318] none of the difficulties arose that we have previously observed for Ni. The strong tendency of H_2 for dissociative adsorption on Ti could also be identified when using the DFTB method. Furthermore we have investigated the hydrogen adsorption in threefold hollow sites on Ti(0001). From a qualitative point of view, our results using the DFTB approach (non-SCC and SCC) agree very well with literature.

On the basis of these satisfying results we have performed first test calculations with our PooMa approach. The H_2 adsorption on Ti(0001) slabs of size 3x3x4 has been studied. Up to eight vacancies within the uppermost layer of the slabs have been considered. A tilted initial orientation of the H_2 molecule on the surface was used and different adsorption sites have been taken into account. In order to speed up the calculations, the DFTB method without self-consistent charge treatment has been utilized for this initial tests. H_2 tends to adsorb dissociatively on Ti(0001) with certain positions being particularly favourable for the adsorption of atomic hydrogen. Although, having different initial structures prior to local relaxation it frequently happened that the final structures after optimization are very similar. At the moment, our PooMa code includes a structure similarity test directly after structure generation but before local relaxation. This has to be complemented in future studies by a further similarity test after the local optimization of the adsorbent-adsorbate systems. The obtained results show that vacancies and/or adatoms might be beneficial for the adsorption energy of H_2 on Ti(0001). As is to be expected, after dissociation the hydrogen atoms prefer such sites on the Ti(0001) surface, where they are coordinated by several Ti atoms. But the exact location of the hydrogen atoms after relaxation is not easily explained via chemical intuition. As for the organic dyes discussed in section 12.3, the automatic optimization of materials' properties may lead to interesting and unexpected results.

Besides the improvement of the present approach further investigations with the PooMa method may also include calculations using the self-consistent DFTB approach. Moreover, other adsorbent-adsorbate systems can be studied and not only transition-metal surfaces could be used as adsorbent. For instance, the adsorption properties of metal oxides as well as that of graphene may be of interest. Depending on the system the present source code may have to be modified, too. But, as described above, problems may arise. Therefore it is indispensable to test the chosen adsorbate-adsorbate system before using it with the PooMa approach. Due to the complexity of the interactions during an adsorption process and the many calculational parameters that can be varied, a thorough preliminary investigation is necessary. This study represents some fundamental work on the global optimization of adsorption properties with PooMa. Additionally first test calculations within this global property optimization task have been performed and interesting results could be obtained.

14 Summary

In the present work, global optimizations of various materials properties have been performed. The properties under consideration were: the energy/structure of alkali-metal clusters, the solar energy harvesting properties of organic molecules and the adsorption performance of transition metal surfaces.

Theoretical investigations are a valuable tool in order to assist experimental research. Due to the enormous amount of possible chemical compounds, which constitute chemical space, often pure experimental studies are not feasible. But using theoretical tools for optimizing materials properties, one also faces the challenge of huge search spaces. Efficient algorithms that help to screen these large search spaces are essential. Within the three studies, presented in this thesis, different search spaces are investigated using different optimization procedures.

For the structural-energetic global optimization (global energy optimization) a cluster's energy is a function of the position-space coordinates of the cluster's atoms. The position-space coordinates are continuous variables and therefore a cluster's PES is a continuous search space. A N-atomic non-linear cluster exhibits a $(3N-6)$-dimensional PES, with the number of non-equivalent energy minima increasing exponentially with increasing cluster size. Already for medium-sized clusters this gives an enormous amount of possible minimum structures. This is called the NP-hard problem. In order to screen the potential energy surfaces of the alkali metal clusters efficiently, we combined a simple model potential, the MEAM, with a suitable global optimization algorithm, the *Aufbau-Abbau* method. The analytic formulae of the MEAM enabled us to calculate the derivatives of the total energy with respect to nuclear coordinates in analytical form. Hence, the local optimization of a single cluster, even a larger one, is quite fast. This gave us the opportunity to screen the search spaces of the clusters extensively and to calculate millions of clusters for each cluster size. Having produced a huge amount of data during the optimization of the clusters, i.e. up to six isomers for Li_N and Na_N clusters with $2 \leq N \leq 150$, a detailed energetic and structural analyses was subsequently carried out. We could observe that Li and Na exhibit similar cluster geometries and that metastable isomers have to be taken into account when studying the growth patterns of the alkali metal clusters.

The solar-energy harvesting properties, e.g. the sunlight absorption or the HOMO-LUMO gap, are functions of the substitution patterns of benzene molecules. The substitution patterns are discrete variables. Either one or another functional group is attached to a certain position in the benzene molecule. There exists only one unique structure with a certain substitution pattern within this search space and the property hypersurfaces that are considered within this study, are discrete. The number of possible organic molecules depends on the number of types of substituents T that can be attached to the organic backbone and the number of sites S within the organic core that are available for substitution. This gives T^S different structures (without symmetricall eqivalent systems). For the present study a fixed anchor group, –COOH, is attached to one of the positions of benzene and 18 different functional groups are considered. Including symmetry, there are 18^5 possible organic molecules that would have to be investigated. Although no NP-hard problem, this large number of structures makes it necessary to use efficient optimization algorithms. Our PooMa approach uses a simple genetic algorithm to screen this discrete search space. The simple DFTB method without self-consistency is used to describe the electronic structure of the molecules. The genetic algorithm and the DFTB method are combined with an efficient way of molecule construction, leading to fast global optimization procedure for the solar energy harvesting properties. Seven different properties are taken into account, including the sunlight absorption and properties concerning the spatial arrangement of the orbitals of the molecules. We obtain results that can partially be explained using chemical intuition. But some of the molecules exhibit substitution patterns, which can not be explained that easily.

Also the adsorption properties of the transition metals are investigated using the PooMa approach. Similar to the global optimization of the organic molecules for solar cell applications, we screen a discrete search space. The composition of the uppermost layer of a transition metal slab, where a position can be occupied either with a transition metal atom or a vacancy forms the set of discrete variables. Furthermore, different adsorption sites on one slab are considered. Again, we combined a genetic algorithm with the DFTB method. Furthermore, through the use of ASE we were able to obtain further flexibility and simplicity within the PooMa approach. We chose Ni(111)/CO and Ti(0001)/H_2 as adsorbent-adsorbate systems that should be investigated. But with the used SK files we could not obtain stable Ni(111) slabs. This problem could not be observed for Ti(0001) and we pursued our studies with Ti(0001) as adsorbent and H_2 as molecular adsorbate. To test our PooMa approach a small slab size, i.e. 3x3x4, was chosen. The positions within the top layer of the slab can either be occupied by a Ti atom or a vacancy and a slab may contain no vacancy at all or up to eight vacancies. In the latter case only one adatom is left within the top layer. Four different adsorption sites are considered, which makes in total $4 \cdot (2^9 - 1)$ potentially different structures. In some cases, a different adsorption site on the same surface yields a very similar structure after local relaxation.

Here, the present PooMa source code would have to be improved for future investigations, e.g. by an additional check for duplicate structure after the local relaxation of the adsorbent-adsorbate systems. Our results show that vacancies/adatoms on a Ti(0001) surface may be beneficial for the adsorption performance of Ti(0001) surfaces. The H_2 molecule tends to dissociate on Ti(0001) with the hydrogen atoms occupying higher coordinating adsorption sites.

Appendices

A Appendix to part II: Symmetries of Li and Na clusters

A.1 Point groups of lithium clusters Li_2 - Li_{150}

Table A.1: Point groups for the six most stable lithium clusters Li_2 - Li_{50} obtained with the MEAM. Adapted by permission from Springer Nature: Springer, *J. Clust. Sci.*, Global Optimization of Li and Na Clusters: Application of a Modified Embedded Atom Method, K. Huwig, V. G. Grigoryan and M. Springborg, Copyright 2019.

$\boldsymbol{N}$	$N.1$	$N.2$	$N.3$	$N.4$	$N.5$	$N.6$	$\boldsymbol{N}$	$N.1$	$N.2$	$N.3$	$N.4$	$N.5$	$N.6$
2	$D_{\infty h}$						27	C_{2v}	C_s	C_{3v}	C_{2v}	C_s	C_s
3	D_{3h}	$D_{\infty h}$	C_{2v}				28	T	C_s	C_s	C_1	C_1	D_2
4	T_d	D_{2h}	C_{2v}	D_{4h}	C_{2v}		29	D_{3h}	C_s	C_2	C_s	C_3	C_1
5	D_{3h}	C_{4v}	C_{2v}	C_{2v}	C_1	C_{3v}	30	C_{2v}	C_1	C_{2v}	C_{2v}	C_1	C_1
6	C_{4h}	C_{2v}	C_s	C_s	C_{5v}	C_s	31	C_s	C_2	C_1	C_1	C_s	C_s
7	D_{5h}	C_{3v}	C_2	C_{3v}	C_s	C_{2v}	32	C_3	C_{2v}	C_s	D_{5h}	C_2	C_1
8	C_{2v}	D_{2d}	C_s	D_{3d}	C_{2v}	C_s	33	C_{5v}	C_s	C_2	C_s	D_3	C_1
9	C_{2v}	C_s	C_{2v}	C_2	C_s	D_{3h}	34	T	D_{5h}	D_{2d}	C_s	C_1	C_2
10	C_{3v}	D_{2h}	C_1	C_2	C_{2v}	C_1	35	D_3	C_2	D_3	C_1	C_2	C_{3v}
11	C_{2v}	C_2	C_{2v}	C_1	C_2	C_2	36	C_2	C_1	C_2	C_1	C_1	C_1
12	C_{5v}	C_s	D_{3h}	C_1	D_{2d}	C_s	37	C_3	C_2	C_2	C_1	C_1	C_2
13	I_h	C_s	C_s	C_s	C_s	D_{3h}	38	C_3	C_5	C_1	D_{6h}	C_3	C_1
14	C_{3v}	C_{2v}	C_s	C_{3v}	C_1	C_s	39	D_5	C_{6v}	C_1	C_2	C_{5v}	C_1
15	C_{2v}	D_{6d}	C_s	C_s	C_2	C_2	40	D_{6h}	C_2	C_2	C_s	C_1	C_2
16	C_s	C_s	C_2	C_s	C_2	C_s	41	D_3	C_2	C_1	C_s	C_2	C_1
17	C_s	C_2	C_s	C_{3v}	C_s	C_2	42	D_2	C_2	C_2	C_2	C_1	C_2
18	C_s	C_{5v}	C_s	C_1	C_s	C_1	43	C_1	C_1	C_1	C_1	C_1	C_1
19	D_{5h}	C_1	C_1	C_s	C_s	C_2	44	C_2	C_s	C_{2v}	C_1	C_3	C_1
20	C_{2v}	D_{3d}	D_2	C_s	C_s	C_s	45	C_1	C_2	C_s	C_s	C_1	C_1
21	C_1	C_{2v}	C_{2v}	C_s	C_s	C_s	46	C_2	C_1	C_1	C_s	C_2	C_1
22	C_s	C_s	C_1	C_2	C_s	C_1	47	C_{3v}	C_1	C_1	C_1	C_1	C_2
23	D_{3h}	D_{3h}	C_s	C_1	C_1	C_s	48	C_2	C_1	C_1	C_2	C_1	C_1
24	C_{2v}	C_s	D_3	C_s	C_1	C_{2v}	49	C_3	C_{3v}	C_1	C_1	C_1	C_2
25	C_{2v}	C_s	C_3	D_{5d}	C_1	C_1	50	C_s	C_s	C_1	C_2	C_2	C_1
26	T_d	C_s	C_s	C_s	C_1	C_s							

Table A.2: Point groups for the six most stable lithium clusters Li_{51} - Li_{100} obtained with the MEAM. Adapted by permission from Springer Nature: Springer, *J. Clust. Sci.*, Global Optimization of Li and Na Clusters: Application of a Modified Embedded Atom Method, K. Huwig, V. G. Grigoryan and M. Springborg, Copyright 2019.

$\boldsymbol{N}$	$N.1$	$N.2$	$N.3$	$N.4$	$N.5$	$N.6$	$\boldsymbol{N}$	$N.1$	$N.2$	$N.3$	$N.4$	$N.5$	$N.6$
51	C_s	C_s	C_1	C_1	C_s	C_{2v}	76	C_1	C_1	C_1	C_1	C_1	C_s
52	C_{2v}	C_{3v}	C_s	C_1	C_s	C_{3v}	77	C_1	C_1	C_1	C_1	C_1	C_1
53	D_{5d}	C_{2v}	C_{2v}	C_s	C_s	C_1	78	C_1	C_1	C_1	C_1	C_1	C_1
54	C_{5v}	C_{2v}	C_s	C_1	C_1	C_1	79	C_1	C_1	C_1	C_1	C_1	C_1
55	I_h	C_1	C_s	C_s	C_1	C_s	80	C_1	C_2	C_1	C_1	C_1	C_1
56	C_s	C_{3v}	C_{3v}	C_{2v}	C_3	C_1	81	C_1	C_1	C_1	C_2	C_2	C_1
57	C_{2v}	C_s	C_s	C_s	C_s	C_s	82	C_1	C_1	C_1	C_1	C_1	C_1
58	C_{3v}	C_1	C_s	C_s	C_1	C_s	83	D_3	C_1	C_1	C_2	C_1	C_1
59	C_1	C_2	C_{2v}	C_{2v}	C_s	C_1	84	C_3	C_1	C_1	C_1	C_1	C_1
60	C_s	C_1	C_1	C_{2v}	C_s	C_s	85	C_1	C_1	C_1	C_1	D_{5h}	C_s
61	C_{2v}	C_1	C_s	C_1	C_s	C_1	86	C_3	C_{5v}	C_s	C_1	C_3	C_1
62	C_1	C_1	C_{2v}	C_2	C_1	C_s	87	D_{5h}	C_1	C_1	C_1	C_1	C_1
63	C_1	C_1	C_2	C_s	C_1	C_s	88	C_s	C_1	C_1	C_s	C_s	C_s
64	C_s	C_1	C_1	C_1	C_1	C_1	89	C_{2v}	C_1	C_1	C_3	C_1	C_1
65	C_1	C_1	C_1	C_1	C_1	C_2	90	C_2	C_1	C_1	C_2	C_s	C_2
66	C_1	C_1	C_1	C_1	C_1	C_1	91	C_1	C_{2v}	C_1	C_1	C_1	C_1
67	C_2	C_s	C_1	C_1	C_1	C_1	92	T	C_1	C_1	C_1	C_1	C_1
68	C_1	C_1	C_1	C_1	C_1	C_1	93	C_1	C_3	C_1	C_1	C_3	C_1
69	C_1	C_1	C_1	C_1	C_1	C_1	94	C_2	C_1	C_1	C_1	C_1	C_1
70	C_1	C_5	C_1	C_5	C_{5v}	C_1	95	C_3	C_1	C_2	C_1	C_1	C_1
71	C_5	C_{5v}	C_1	C_s	C_1	C_1	96	C_2	C_1	C_1	C_1	C_1	C_1
72	C_2	C_1	C_1	C_1	C_s	C_1	97	C_1	C_1	C_1	C_1	C_1	C_1
73	C_1	C_1	C_1	C_1	C_1	C_1	98	C_1	C_1	C_1	C_1	C_1	C_1
74	C_2	C_1	C_1	C_1	C_1	C_1	99	C_2	C_2	C_2	C_1	C_1	C_1
75	C_1	C_1	C_1	C_1	C_s	C_1	100	C_1	C_1	C_1	C_1	C_3	C_1

Table A.3: Point groups for the six most stable lithium clusters Li_{101} - Li_{150} obtained with the MEAM. Adapted by permission from Springer Nature: Springer, *J. Clust. Sci.*, Global Optimization of Li and Na Clusters: Application of a Modified Embedded Atom Method, K. Huwig, V. G. Grigoryan and M. Springborg, Copyright 2019.

$\boldsymbol{N}$	N.1	N.2	N.3	N.4	N.5	N.6	$\boldsymbol{N}$	N.1	N.2	N.3	N.4	N.5	N.6
101	D_3	C_1	C_1	C_1	C_1	C_1	126	C_1	C_1	C_1	C_1	C_1	C_1
102	C_1	C_1	C_1	C_3	C_1	C_1	127	C_1	C_s	C_s	C_1	C_s	C_1
103	C_1	C_1	C_1	C_1	C_1	C_1	128	C_s	C_s	C_1	C_1	C_s	C_1
104	C_2	C_1	C_1	C_1	C_1	C_1	129	C_s	C_1	C_1	C_1	C_2	C_1
105	C_1	C_1	C_1	C_1	C_1	C_1	130	C_1	C_1	C_1	C_1	C_1	C_1
106	C_1	C_1	C_1	C_s	C_1	C_s	131	C_{2v}	C_2	C_1	C_1	C_1	C_1
107	C_1	C_1	C_1	C_1	C_s	C_1	132	C_1	C_s	C_1	C_1	C_1	C_1
108	C_1	C_1	C_1	C_1	C_1	C_1	133	C_s	C_1	C_1	C_1	C_1	C_1
109	C_1	C_1	C_1	C_1	C_1	C_1	134	C_s	C_s	C_1	C_1	C_1	C_1
110	C_1	C_2	C_2	C_1	C_1	C_1	135	C_1	C_1	C_s	C_1	C_1	C_1
111	C_1	C_1	C_1	C_1	C_1	C_1	136	C_1	C_s	C_s	C_s	C_s	C_s
112	C_1	C_1	C_1	C_1	C_1	C_1	137	C_{3v}	C_1	C_1	C_1	C_1	C_1
113	C_2	C_1	C_1	C_1	C_1	C_1	138	C_s	C_1	C_s	C_s	C_1	C_1
114	C_2	C_1	C_2	C_1	C_2	C_2	139	C_1	C_1	C_s	C_s	C_1	C_1
115	C_1	C_5	C_1	C_1	C_2	C_1	140	C_s	C_s	C_s	C_s	C_s	C_s
116	D_5	C_1	C_1	C_1	C_1	C_1	141	C_2	C_{2v}	C_1	C_1	C_{3v}	C_{2v}
117	C_1	C_1	C_1	C_1	C_1	C_1	142	C_s	C_s	C_s	C_1	C_s	C_s
118	C_2	C_1	C_s	C_1	C_1	C_1	143	C_{2v}	D_{2h}	C_s	C_2	C_s	C_2
119	C_s	C_1	C_1	C_1	C_1	C_1	144	C_{3v}	C_s	C_s	C_1	C_{3v}	C_s
120	C_1	C_1	C_1	C_1	C_1	C_1	145	D_{5d}	C_{2v}	C_{2v}	C_s	C_1	C_1
121	C_1	C_1	C_1	C_1	C_1	C_1	146	C_{5v}	C_s	I_h	C_{3v}	C_1	C_s
122	C_2	C_1	C_1	C_1	C_1	C_1	147	I_h	C_1	C_s	C_s	C_s	C_1
123	C_s	C_1	C_1	C_1	C_1	C_1	148	C_s	C_1	C_1	C_1	C_1	C_s
124	C_s	C_1	C_1	C_1	C_1	C_1	149	C_1	C_s	C_s	C_s	C_s	C_{2v}
125	C_1	C_s	C_s	C_1	C_1	C_1	150	C_3	C_s	C_{3v}	C_1	C_1	C_1

A.2 Point groups of sodium clusters Na$_2$ - Na$_{150}$

Table A.4: Point groups for the six most stable sodium clusters Na$_2$ - Na$_{50}$ obtained with the MEAM. Adapted by permission from Springer Nature: Springer, *J. Clust. Sci.*, Global Optimization of Li and Na Clusters: Application of a Modified Embedded Atom Method, K. Huwig, V. G. Grigoryan and M. Springborg, Copyright 2019.

N	*N*.1	*N*.2	*N*.3	*N*.4	*N*.5	*N*.6	***N***	*N*.1	*N*.2	*N*.3	*N*.4	*N*.5	*N*.6
2	$D_{\infty h}$						27	C_{2v}	C_s	C_1	C_{2v}	C_{3v}	C_1
3	D_{3h}	$D_{\infty h}$	C_{2v}				28	T	C_s	D_2	C_s	C_1	C_1
4	T_d	D_{2h}	D_{4h}	C_{2v}	C_s	$D_{\infty h}$	29	D_{3h}	C_3	C_s	C_2	C_2	C_{2v}
5	D_{3h}	C_{4v}	C_{2v}	C_s	C_{2v}	C_{3v}	30	C_{2v}	C_1	C_{2v}	C_{2v}	C_2	C_s
6	O_h	C_{2v}	C_{2v}	C_s	C_s	C_{5v}	31	C_s	C_2	C_1	C_2	C_1	C_s
7	D_{5h}	C_{3v}	C_2	C_1	C_{3v}	C_s	32	D_3	C_{2v}	C_2	C_1	C_{2v}	C_1
8	D_{2d}	C_s	D_{3d}	C_{2v}	C_{2v}	D_{3d}	33	C_2	C_s	C_{5v}	C_1	C_1	C_s
9	C_{2v}	C_s	C_1	C_{2v}	D_{3h}	C_s	34	T	C_s	D_{5h}	C_2	C_2	C_2
10	C_{3v}	D_{2h}	C_2	C_{2v}	C_1	C_s	35	D_3	C_3	C_2	C_1	C_2	C_{2v}
11	C_{2v}	C_{2v}	C_1	C_2	C_2	C_1	36	C_1	C_1	C_2	C_s	C_1	C_1
12	C_5	C_s	C_1	D_{3h}	D_{2d}	C_s	37	C_2	C_3	C_2	C_1	C_1	C_1
13	I_h	C_s	C_s	C_s	C_s	D_{3h}	38	C_3	C_5	C_1	C_3	D_{6h}	C_1
14	C_{3v}	C_{2v}	C_s	C_1	C_s	C_{2v}	39	D_5	C_{5v}	C_{6v}	C_1	C_1	C_s
15	C_{2v}	D_{6d}	C_s	C_s	C_2	C_1	40	C_s	C_1	C_2	C_1	D_{6h}	C_1
16	C_s	C_s	C_2	C_s	D_{3h}	C_2	41	C_3	C_s	C_1	C_2	C_2	C_2
17	C_s	C_2	C_s	C_{3v}	C_2	C_s	42	D_2	C_2	C_2	C_1	C_2	C_s
18	C_s	C_{5v}	C_s	C_1	C_1	C_s	43	C_1	C_s	C_1	C_1	C_1	C_1
19	D_{5h}	C_1	C_1	C_s	C_s	C_s	44	C_s	C_1	C_2	C_1	C_{2v}	C_s
20	C_{2v}	D_{3d}	D_2	C_s	C_s	C_s	45	C_1	C_s	C_1	C_1	C_1	C_1
21	C_1	C_{2v}	C_{2v}	C_s	C_1	C_s	46	C_2	C_{2v}	C_1	C_1	C_s	C_1
22	C_s	C_s	C_1	C_2	C_1	D_{6h}	47	C_1	C_1	C_1	C_{3v}	C_s	C_1
23	D_{3h}	D_{3h}	C_s	C_1	C_1	C_s	48	C_s	C_s	C_1	C_s	C_2	C_1
24	C_{2v}	C_s	C_3	C_{2v}	C_s	C_1	49	C_{3v}	C_1	C_1	C_1	C_2	C_1
25	C_{2v}	C_3	C_s	D_{5d}	C_1	C_1	50	C_s	C_s	C_2	C_1	C_2	C_s
26	T_d	C_s	C_s	C_1	C_s	C_1							

Table A.5: Point groups for the six most stable sodium clusters Na_{51} - Na_{100} obtained with the MEAM. Adapted by permission from Springer Nature: Springer, *J. Clust. Sci.*, Global Optimization of Li and Na Clusters: Application of a Modified Embedded Atom Method, K. Huwig, V. G. Grigoryan and M. Springborg, Copyright 2019.

$\boldsymbol{N}$	$N.1$	$N.2$	$N.3$	$N.4$	$N.5$	$N.6$	$\boldsymbol{N}$	$N.1$	$N.2$	$N.3$	$N.4$	$N.5$	$N.6$
51	C_s	C_s	C_1	C_{2v}	C_s	C_s	76	C_1	C_s	C_1	C_1	C_1	C_1
52	C_{2v}	C_{3v}	C_1	C_s	C_s	C_{3v}	77	C_1	C_1	C_1	C_1	C_1	C_1
53	C_{2v}	D_{5d}	C_{2v}	C_s	C_s	C_1	78	C_1	C_1	C_1	C_1	C_1	C_1
54	C_{5v}	C_{2v}	C_s	C_s	C_s	C_1	79	C_1	C_1	C_1	C_1	C_1	C_1
55	I_h	C_s	C_s	C_s	C_1	C_s	80	C_1	C_1	C_1	C_1	C_1	C_1
56	C_{3v}	C_{3v}	C_{2v}	C_1	C_s	C_s	81	C_1	C_1	C_1	C_2	C_s	C_1
57	C_{2v}	C_1	C_1	C_1	C_s	C_s	82	C_1	C_1	C_s	C_1	C_1	C_1
58	C_{3v}	C_1	C_1	C_1	C_1	C_s	83	D_3	C_1	C_2	C_1	C_1	C_1
59	C_1	C_1	C_2	C_2	C_{2v}	C_{2v}	84	C_1	C_1	C_1	C_3	C_1	C_1
60	C_s	C_1	C_s	C_1	C_1	C_{2v}	85	C_1	C_1	C_1	C_1	D_{5h}	C_s
61	C_{2v}	C_1	C_s	C_1	C_1	C_s	86	C_3	C_{5v}	C_s	C_1	C_{2v}	C_1
62	C_1	C_1	C_{2v}	C_s	C_s	C_1	87	D_{5h}	C_1	C_1	C_1	C_1	C_1
63	C_1	C_1	C_s	C_s	C_1	C_s	88	C_s	C_s	C_1	C_s	C_s	C_s
64	C_s	C_1	C_1	C_1	C_1	C_3	89	C_{2v}	C_1	C_1	C_1	C_1	C_1
65	C_1	C_1	C_1	C_1	C_1	C_2	90	C_2	C_1	C_1	C_2	C_1	C_2
66	C_1	C_1	C_s	C_1	C_1	C_1	91	C_1	C_1	C_1	C_1	C_1	C_1
67	C_2	C_s	C_{3v}	C_1	C_s	C_1	92	T	C_1	C_1	C_1	C_1	C_1
68	C_1	C_1	C_1	C_1	C_1	C_1	93	C_3	C_1	C_3	C_1	C_1	C_1
69	C_1	C_1	C_1	C_1	C_1	C_1	94	C_1	C_1	C_1	C_1	C_2	C_1
70	C_1	C_5	C_5	C_1	C_{5v}	C_{5v}	95	C_3	C_1	C_1	C_1	C_1	C_1
71	C_5	C_{5v}	C_s	C_1	C_1	C_1	96	C_1	C_1	C_1	C_1	C_1	C_1
72	C_s	C_1	C_2	C_1	C_1	C_1	97	C_1	C_1	C_1	C_1	C_1	C_1
73	C_s	C_s	C_1	C_1	C_1	C_1	98	C_1	C_1	C_1	C_1	C_1	C_1
74	D_{3d}	C_1	C_1	C_1	C_1	C_s	99	C_2	C_2	C_1	C_1	C_1	C_1
75	C_1	C_1	C_s	C_1	C_1	C_1	100	C_1	C_1	C_1	C_1	C_1	C_1

Table A.6: Point groups for the six most stable sodium clusters Na_{101} - Na_{150} obtained with the MEAM. Adapted by permission from Springer Nature: Springer, *J. Clust. Sci.*, Global Optimization of Li and Na Clusters: Application of a Modified Embedded Atom Method, K. Huwig, V. G. Grigoryan and M. Springborg, Copyright 2019.

N	$N.1$	$N.2$	$N.3$	$N.4$	$N.5$	$N.6$	**N**	$N.1$	$N.2$	$N.3$	$N.4$	$N.5$	$N.6$
101	C_3	C_1	C_1	C_1	C_1	C_1	126	C_1	C_1	C_1	C_1	C_s	C_1
102	C_1	C_3	C_1	C_1	C_3	C_1	127	C_1	C_s	C_s	C_1	C_1	C_s
103	C_1	C_1	C_1	C_1	C_1	C_1	128	C_s	C_1	C_s	C_s	C_1	C_1
104	C_2	C_1	C_1	C_1	C_1	C_1	129	C_s	C_s	C_s	C_1	C_1	C_1
105	C_1	C_1	C_1	C_1	C_1	C_1	130	C_1	C_s	C_1	C_1	C_1	C_s
106	C_1	C_1	C_1	C_1	C_s	C_1	131	C_{2v}	C_1	C_1	C_1	C_1	C_1
107	C_1	C_1	C_1	C_1	C_s	C_1	132	C_1	C_1	C_s	C_1	C_1	C_1
108	C_1	C_s	C_1	C_1	C_1	C_1	133	C_1	C_1	C_1	C_1	C_s	C_s
109	C_1	C_1	C_1	C_1	C_1	C_1	134	C_s	C_{3v}	C_s	C_1	C_1	C_s
110	C_1	C_2	C_1	C_2	C_1	C_1	135	C_s	C_s	C_1	C_s	C_1	C_s
111	C_2	C_1	C_1	C_1	C_1	C_2	136	C_s	C_s	C_s	C_1	C_s	C_s
112	C_1	C_1	C_1	C_1	C_1	C_2	137	C_{3v}	C_1	C_1	C_1	C_1	C_1
113	C_2	C_1	C_1	C_1	C_1	C_1	138	C_1	C_s	C_{3v}	C_s	C_s	C_1
114	C_2	C_1	C_2	C_1	C_2	C_2	139	C_{2v}	C_s	C_2	C_s	D_{2h}	C_s
115	C_1	C_5	C_1	C_2	C_1	C_1	140	C_s	C_s	C_s	C_s	C_1	C_s
116	D_5	C_1	C_1	C_1	C_1	C_1	141	C_5	C_2	C_{2v}	D_{3d}	C_3	C_1
117	C_1	C_1	C_1	C_1	C_1	C_1	142	C_s	C_s	C_1	C_s	C_s	C_s
118	C_s	C_2	C_s	C_1	C_1	C_1	143	C_{2v}	C_s	C_s	C_2	D_{2h}	C_s
119	C_s	C_1	C_s	C_1	C_1	C_1	144	C_{3v}	C_s	C_s	C_s	C_{3v}	C_1
120	C_1	C_1	C_1	C_1	C_1	C_1	145	C_{2v}	D_{5d}	C_{2v}	C_s	C_{5v}	C_1
121	C_1	C_1	C_1	C_1	C_1	C_1	146	C_{5v}	I_h	C_1	C_s	C_1	C_1
122	C_2	C_1	C_1	C_1	C_1	C_s	147	I_h	C_1	C_s	C_s	C_1	C_s
123	C_s	C_1	C_s	C_s	C_1	C_s	148	C_s	C_s	C_1	C_s	C_1	C_s
124	C_s	C_s	C_s	C_1	C_1	C_s	149	C_s	C_s	C_s	C_s	C_{2v}	C_s
125	C_1	C_1	C_1	C_1	C_1	C_1	150	C_{3v}	C_{3v}	C_1	C_s	C_1	C_s

Bibliography

[1] S. R. Bahn and K. W. Jacobsen. An object-oriented scripting interface to a legacy electronic structure code. *Comput. Sci. Eng.*, 4(3):56–66, 2002.

[2] A. H. Larsen, J. J. Mortensen, J. Blomqvist, I. E. Castelli, R. Christensen, M. Dułak, J. Friis, M. N. Groves, B. Hammer, C. Hargus, E. D. Hermes, P. C. Jennings, P. B. Jensen, J. Kermode, J. R. Kitchin, E. L. Kolsbjerg, J. Kubal, K. Kaasbjerg, S. Lysgaard, J. Bergmann Maronsson, T. Maxson, T. Olsen, L. Pastewka, A. Peterson, C. Rostgaard, J. Schiøtz, O. Schütt, M. Strange, K. S. Thygesen, T. Vegge, L. Vilhelmsen, M. Walter, Z. Zeng, and K. W. Jacobsen. The Atomic Simulation Environment—a Python library for working with atoms. *J. Phys.: Condens. Matter*, 29(27):273002, 2017.

[3] multiprocessing - process-based parallelism. website. online available: `https://docs.python.org/3/library/multiprocessing.html`; last time retrieved: 2020-06-15.

[4] dftb.org the DFTB website. website. online available: `https://www.dftb.org/parameters/download/`; last time retrieved: 2020-06-15.

[5] NNIN/C Pseudopotential Virtual Vault. website. online available: `http://nninc.cnf.cornell.edu/`; last time retrieved: 2020-02-17.

[6] E. J. Llanos, W. Leal, D. H. Luu, J. Jost, P. F. Stadler, and G. Restrepo. Exploration of the chemical space and its three historical regimes. *PNAS*, 116(26):12660–12665, 2019.

[7] R. S. Bohacek, C. McMartin, and W. C. Guida. The art and practice of structure-based drug design: A molecular modeling perspective. *Med. Res. Rev.*, 16(1):3–50, 1996.

[8] A. Franceschetti and A. Zunger. The inverse band-structure problem of finding an atomic configuration with given electronic properties. *Nature*, 402(6757):60–63, 1999.

[9] R. J. Hendershot, C. M. Snively, and J. Lauterbach. High-Throughput Heterogeneous Catalytic Science. *Chem. Eur. J.*, 11(3):806–814, 2005.

[10] D. Farrusseng. High-throughput heterogeneous catalysis. *Surf. Sci. Rep.*, 63(11):487–513, 2008.

[11] L. M. Mayr and D. Bojanic. Novel trends in high-throughput screening. *Curr. Opin. Pharmacol.*, 9(5):580–588, 2009.

[12] C. J. Welch. High throughput analysis enables high throughput experimentation in pharmaceutical process research. *React. Chem. Eng.*, 4(11):1895–1911, 2019.

[13] W. F. Maier, K. Stöwe, and S. Sieg. Combinatorial and High-Throughput Materials Science. *Angew. Chem. Int. Ed.*, 46(32):6016–6067, 2007.

[14] B. J. Battersby and M. Trau. Novel miniaturized systems in high-throughput screening. *Trends Biotechnol.*, 20(4):167–173, 2002.

[15] T. Zech, G. Bohner, and J. Klein. High-throughput screening of supported catalysts in massively parallel single-bead microreactors: Workflow aspects related to reactor bonding and catalyst preparation. *Catal. Today*, 110(1-2):58–67, 2005.

[16] M. G. Bures and Y. C. Martin. Computational methods in molecular diversity and combinatorial chemistry. *Curr. Opin. Chem. Biol.*, 2(3):376–380, 1998.

[17] A. Z. Dudek, T́. Arodz, and J. Gálvez. Computational Methods in Developing Quantitative Structure-Activity Relationships (QSAR): A Review. *Comb. Chem. High Throughput Screen.*, 9(3):213–228, 2006.

[18] J. Bargon, editor. *Computational Methods in Chemistry.* The IBM Research Symposia Series. Plenum Press, New York, U.S., 1980.

[19] H.-J. Zhu. *Organic Stereochemistry: Experimental and Computational Methods, 1st Edition.* Wiley-VCH Verlag GmbH & Co. KGaA, Weinheim, Germany, 2015.

[20] T. Sperger, I. A. Sanhueza, and F. Schoenebeck. Computation and Experiment: A Powerful Combination to Understand and Predict Reactivities. *Acc. Chem. Res.*, 49(6):1311–1319, 2016.

[21] B. M. Szyja and D. Vanpoucke. Computational Chemistry Experiment Possibilities. In V. Blay, L. F. Bobadilla, and A. C. García, editors, *Zeolithes and Metal-Organic Frameworks.*, Atlantis Advances in Nanotechnology, Material Science and Energy Technologies, chapter 9, pages 235–264. Amsterdam University Press, Amsterdam, Netherlands, 2018.

[22] M. Solà, F. De Proft, and F. M. Bickelhaupt. Special Collection: Computational Chemistry. *ChemistryOpen*, 8(7):814–816, 2019.

[23] T. Lookman, F. J. Alexander, and K. Rajan, editors. *Information Science for Materials Discovery and Design.* Springer Series in Materials Science 225. Springer International Publishing, Switzerland.

[24] T. Lookman, P. V. Balachandran, D. Xue, and R. Yuan. Active learning in materials science with emphasis on adaptive sampling using uncertainties for targeted design. *npj Comput. Mater.*, 5(1):21, 2019.

[25] L. M. Ghiringhelli, J. Vybiral, S. V. Levchenko, C. Draxl, and M. Scheffler. Big Data of Materials Science: Critical Role of the Descriptor. *Phys. Rev. Lett.*, 114(10):105503, 2015.

[26] I. V. Tetko, O. Engkvist, U. Koch, J.-L. Reymond, and H. Chen. BIGCHEM: Challenges and Opportunities for Big Data Analysis in Chemistry. *Mol. Inform.*, 35(11-12):615–621, 2016.

[27] A. Agrawal and A. Choudhary. Perspective: Materials informatics and big data: Realization of the "fourth paradigm" of science in materials science. *APL Mater.*, 4(5):053208, 2016.

[28] C. A. Floudas and P. Pardalos, editors. *Optimization in Computational Chemistry and Molecular Biology. Local and Global Approaches.* Nonconvex Optimization and Its Applications, Vol. 40. Springer US, New York, U.S., 2000.

[29] P. M. Pardalos, H. E. Romeijn, and H. Tuy. Recent developments and trends in global optimization. *J. Comput. Appl. Math.*, 124(1-2):209–228, 2000.

[30] B. Hartke. Global optimization. *WIREs Comput. Mol. Sci.*, 1(6):879–887, 2011.

[31] R. Fournier and A. Mohareb. Optimizing molecular properties using a relative index of thermodynamic stability and global optimization techniques. *J. Chem. Phys.*, 144(2):024114, 2016.

[32] J. G. Freeze, H. R. Kelly, and V. S. Batista. Search for Catalysts by Inverse Design: Artificial Intelligence, Mountain Climbers, and Alchemists. *Chem. Rev.*, 119(11):6595–6612, 2019.

[33] D. J. Wales and J. P. K. Doye. Global Optimization by Basin-Hopping and the Lowest Energy Structures of Lennard-Jones Clusters Containing up to 110 Atoms. *J. Phys. Chem. A*, 101(28):5111–5116, 1997.

[34] S. Heiles and R. L. Johnston. Global Optimization of clusters using electronic structure methods. *Int. J. Quantum Chem.*, 113(18):2091–2109, 2013.

[35] R. L. Johnston. *Atomic and Molecular Clusters.* Masters Series in Physics and Astronomy. Taylor & Francis, London, U.K., 2002.

[36] M. D. Morse. Clusters of Transition-Metal Atoms. *Chem. Rev.*, 86(6):1049–1109, 1986.

[37] W. A. de Heer. The physics of simple metal clusters: experimental aspects and simple models. *Rev. Mod. Phys.*, 65(3):611–676, 1993.

[38] Y. Negishi, W. Kurashige, Y. Niihori, and K. Nobusada. Toward the creation of stable, functionalized metal clusters. *Phys. Chem. Chem. Phys.*, 15(43):18736–18751, 2013.

[39] M. Jäger, R. Schäfer, and R. L. Johnston. First principles global optimization of metal clusters and nanoalloys. *Adv. Phys.: X*, 3(1):1516514, 2018.

[40] X. Shao, X. Liu, and W. Cai. Structural Optimization of Silver Clusters up to 80 Atoms with Gupta and Sutton-Chen Potentials. *J. Chem. Theory Comput.*, 1(4):762–768, 2005.

[41] A. Zunger. Inverse design in search of materials with target functionalities. *Nat. Rev. Chem.*, 2(4):0121, 2018.

[42] A. Hakansson, J. Sanchez-Dehesa, and L. Sanchis. Inverse design of photonic crystal devices. *IEEE J. Sel. Areas Commun.*, 23(7):1365–1371, 2005.

[43] A. V. Moroz, M. V. Rybin, K. B. Samusev, and M. F. Liminov. Band gaps in multicomponent photonic crystals: splitting effects and the inverse design problem. *J. Opt. Soc. Am. B*, 26(9):1767–1771, 2009.

[44] D. Xiao. Inverse molecular design of green catalysts for biomass conversion. In *International Summit on Past and Present Research Systems of Green Chemistry.*, volume 3, page 59. Longdom Publishing, August 2014.

[45] F. De Vleeschouwer, W. Yang, D. N. Beratan, P. Geerlings, and F. De Proft. Inverse design of molecules with optimal reactivity properties: acidity of 2-naphtol derivatives. *Phys. Chem. Chem. Phys.*, 14(46):16002–16013, 2012.

[46] B. Li, L. Wang, B. Kang, P. Wang, and Y. Qiu. Review of recent progress in solid-state dye-sensitized solar cells. *Sol. Energy Mater. Sol. Cells*, 90(5):549–573, 2006.

[47] S. De Wolf, A. Descoeudres, Z. C. Holman, and C. Ballif. High-efficiency Silicon Heterojunction Solar Cells: A Review. *Green*, 2(1):7–24, 2012.

[48] X. Liu, Y. Feng, H. Cui, F. Liu, X. Hao, G. Conibeer, D. B. Mitzi, and M. Green. The current status and future prospects of kesterite solar cells: a brief review. *Prog. Photovolt.: Res. Appl.*, 24(6):879–898, 2016.

[49] M. I. Asghar, J. Zhang, H. Wang, and P. D. Lund. Device stability of perovskite solar cells – A review. *Renew. Sustain. Energy Rev.*, 77:131–146, 2017.

[50] D. Xiao, L. A. Martini, R. C. Snoeberger III, R. H. Crabtree, and V. S. Batista. Inverse Design and Synthesis of acac-Coumarin Anchors for Robust TiO_2 Sensitization. *J. Am. Chem. Soc.*, 133(23):9014–9022, 2011.

[51] L. Yu, R. S. Kokenyesi, D. A. Keszler, and A. Zunger. Inverse Design of High Absorption Thin-Film Photovoltaic Materials. *Adv. Energy Mater.*, 3(1):43–48, 2013.

[52] M. Springborg, S. Kohaut, Y. Dong, and K. Huwig. Mixed Si-Ge clusters, solar-energy harvesting, and inverse-design methods. *Comput. Theor. Chem.*, 1107:14–22, 2017.

[53] B. Kim, S. Lee, and J. Kim. Inverse design of porous materials using artificial neural networks. *Sci. Adv.*, 6(1), 2020.

[54] T. S. Choksi, L. T. Roling, V. Streibel, and F. Abild-Pedersen. Predicting Adsorption Properties of Catalytic Descriptors on Bimetallic Nanoalloys with Site-Specific Precision. *J. Phys. Chem. Lett.*, 10(8):1852–1859, 2019.

[55] M. Born and R. Oppenheimer. Zur Quantentheorie der Molekeln. *Ann. Phys.*, 389(20):457–484, 1927.

[56] R. G. Woolley. Quantum chemistry beyond the Born-Oppenheimer approximation. *J. Mol. Struct. (Theochem)*, 230:17–46, 1991.

[57] I. Rahinov, R. Cooper, D. Matsiev, C. Bartels, D. J. Auerbach, and A. M. Wodtke. Quantifying the breakdown of the Born-Oppenheimer approximation in surface chemistry. *Phys. Chem. Chem. Phys.*, 13(28):12680–12692, 2011.

[58] A. Scherrer, F. Agostini, D. Sebastiani, E. K. U. Gross, and R. Vuilleumier. On the Mass of Atoms in Molecules: Beyond the Born-Oppenheimer Approximation. *Phys. Rev. X*, 7(3):031035, 2017.

[59] J. C. Slater. The Theory of Complex Spectra. *Phys. Rev.*, 34(10):1293–1322, 1929.

[60] D. R. Hartree. The Wave Mechanics of an Atom with a Non-Coulomb Central Field. Part I. Theory and Methods. *Math. Proc. Camb. Philos. Soc.*, 24(1):89–110, 1928.

[61] D. R. Hartree. The Wave Mechanics of an Atom with a Non-Coulomb Central Field. Part II. Some Results and Discussion. *Math. Proc. Camb. Philos. Soc.*, 24(1):111–132, 1928.

[62] V. Fock. Näherungsmethode zur Lösung des quantenmechanischen Mehrkörperproblems. *Z. Phys.*, 61(1):126–148, 1930.

[63] V. Fock. „Selfconsistent field" mit Austausch für Natrium. *Z. Phys.*, 62(11):795–805, 1930.

[64] D. R. Hartree and W. Hartree. Self-consistent field, with exchange, for beryllium. *Proc. R. Soc. Lond. A*, 150(869):9–33, 1935.

[65] C. C. J. Roothaan. New Developments in Molecular Orbital Theory. *Rev. Mod. Phys.*, 23(2):69–89, 1951.

[66] G. G. Hall. The molecular orbital theory of chemical valency. VIII. A method of calculating ionization potentials. *Proc. R. Soc. Lond. A*, 205(1083):541–552, 1951.

[67] A. L. Magalhães. Gaussian-Type Orbitals versus Slater-Type Orbitals: A Comparison. *J. Chem. Educ.*, 91(12):2124–2127, 2014.

[68] G. C. Lie and E. Clementi. Study of the electronic structure of molecules. XXI. Correlation energy corrections as a functional of the Hartree-Fock density and its application to the hydrides of the second row atoms. *J. Chem. Phys.*, 60(4):1275–1287, 1974.

[69] C. D. Sherrill and H. F. Schaefer. The Configuration Interaction Method: Advances in Highly Correlated Approaches. volume 34 of *Adv. Quantum Chem.*, pages 143–269. Academic Press, 1999.

[70] E. U. Condon. The Theory of Complex Spectra. *Phys. Rev.*, 36(7):1121–1133, 1930.

[71] F. O. Ellison and H. Shull. Molecular Calculations. I. LCAO MO Self-Consistent Field Treatment of the Ground State of H_2O. *J. Chem. Phys.*, 23(12):2348–2357, 1955.

[72] I. Shavitt. The history and evolution of configuration interaction. *Mol. Phys.*, 94(1):3–17, 1998.

[73] Chr. Møller and M. S. Plesset. Note on an Approximation Treatment for Many-Electron Systems. *Phys. Rev.*, 46(7):618–622, 1934.

[74] J. A. Pople, J. S. Binkley, and R. Seeger. Theoretical models incorporating electron correlation. *Int. J. Quantum Chem.*, 10(S10):1–19, 1976.

[75] R. O. Jones. Density functional theory: Its origins, rise to prominence, and future. *Rev. Mod. Phys.*, 87(3):897–923, 2015.

[76] L. H. Thomas. The calculation of atomic fields. *Math. Proc. Cambridge Philos. Soc.*, 23(5):542–548, 1927.

[77] E. Fermi. Eine statistische Methode zur Bestimmung einiger Eigenschaften des Atoms und ihre Anwendungen auf die Theorie des periodischen Systems der Elemente. *Z. Phys.*, 48(1):73–79, 1928.

[78] P. Hohenberg and W. Kohn. Inhomogeneous Electron Gas. *Phys. Rev.*, 136(3B):B864–B871, 1964.

[79] W. Kohn and L. J. Sham. Self-Consistent Equations Including Exchange and Correlation Effects. *Phys. Rev.*, 140(4A):A1133–A1138, 1965.

[80] P. Bouř. Comparison of Hartree-Fock and Kohn-Sham determinants as wave functions. *J. Comput. Chem.*, 21(1):8–16, 2000.

[81] A. J. Cohen, P. Mori-Sánchez, and W. Yang. Challenges for Density Functional Theory. *Chem. Rev.*, 112(1):289–320, 2012.

[82] D. J. Wales and H. A. Scheraga. Global Optimization of Clusters, Crystals, and Biomolecules. *Science*, 285(5432):1368–1372, 1999.

[83] H. Eyring and M. Polanyi. On Simple Gas Reactions. *Z. Phys. Chem.*, 227(11):1221–1246, 2013.

[84] V. A. Rassolov and S. Garashchuk. Computational complexity in quantum chemistry. *Chem. Phys. Lett.*, 464(4-6):262–264, 2008.

[85] J. D. Whitfield, P. J. Love, and A. Aspuru-Guzik. Computational complexity in electronic structure. *Phys. Chem. Chem. Phys.*, 15(2):397–411, 2013.

[86] J. P. K. Doye and D. J. Wales. On potential energy surfaces and relaxation to the global minimum. *J. Chem. Phys.*, 105(18):8428–8445, 1996.

[87] D. Xiao, I. Warnke, J. Bedford, and V. S. Batista. Chapter 1 Inverse molecular design for materials discovery. In M. Springborg and J.-O. Joswig, editors, *Chemical Modelling: Volume 10.*, Specialist Periodical Reports, pages 1–31. The Royal Society of Chemistry, Cambridge, U.K., 2014.

[88] S. Keinan, X. Hu, D. N. Beratan, and W. Yang. Designing Molecules with Optimal Properties Using the Linear Combination of Atomic Potentials Approach in an AM1 Semiempirical Framework. *J. Phys. Chem. A*, 111(1):176–181, 2007.

[89] M. Wang, X. Hu, D. N. Beratan, and W. Yang. Designing Molecules by Optimizing Potentials. *J. Am. Chem. Soc.*, 128(10):3228–3232, 2006.

[90] D. Balamurugan, W. Yang, and D. N. Beratan. Exploring chemical space with discrete, gradient and hybrid optimization methods. *J. Chem. Phys.*, 129(17):174105, 2008.

[91] J. R. Shewchuk. An Introduction to the Conjugate Gradient Method Without the Agonizing Pain. Edition $1\,\frac{1}{4}$. Technical report, School of Computer Science at Carnegie Mellon University, Pittsburgh, U.S., August 1994.

[92] W. H. Press, S. A. Teukolsky, W. T. Vetterling, and B. P. Flannery. *Numerical Recipes in Fortran 77: the Art of Scientific Computing. Second Edition.*, volume 1 of *Fortran Numerical Recipes.* Cambridge University Press, Cambridge, U.K., 1992.

[93] M. R. Hestenes and E. Stiefel. Methods of Conjugate Gradients for Solving Linear Systems. *J. Res. Natl. Bur. Stand.*, 49(6):409–436, 1952.

[94] B. Hartke. Global geometry optimization of clusters using genetic algorithms. *J. Phys. Chem.*, 97(39):9973–9976, 1993.

[95] R. Kawai and J. H. Weare. From van der Waals to Metallic Bonding: The Growth of Be Clusters. *Phys. Rev. Lett.*, 65(1):80–83, 1990.

[96] Y. Xiang, D. Y. Sun, and X. G. Gong. Generalized Simulated Annealing Studies on Structures and Properties of Ni_n (n=2-55). *J. Phys. Chem. A*, 104(12):2746–2751, 2000.

[97] G. Esperanza Moyano, R. Wesendrup, T. Söhnel, and P. Schwerdtfeger. Properties of Small- to Medium-Sized Mercury Clusters from a Combined *ab initio*, Density-Functional, and Simulated-Annealing Study. *Phys. Rev. Lett.*, 89(10):103401, 2002.

[98] S. Yoo and X. C. Zeng. Global geometry optimization of silicon clusters described by three empirical potentials. *J. Chem. Phys.*, 119(3):1442–1450, 2003.

[99] H. Do and N. A. Besley. Structural optimization of molecular clusters with density functional theory combined with basin hopping. *J. Chem. Phys.*, 137(13):134106, 2012.

[100] R. Ouyang, Y. Xie, and D. Jiang. Global minimization of gold clusters by combining neural network potentials and the basin-hopping method. *Nanoscale*, 7(36):14817–14821, 2015.

[101] S. Kohaut and M. Springborg. Structural, Energetic, and Magnetic Properties of $\mathrm{Ag}_{n-m}\mathrm{Rh}_m$ and $\mathrm{Ag}_m\mathrm{Rh}_{n-m}$ Clusters with $n \leq 20$ and $m = 0, 1$. *J. Clust. Sci.*, 27(3):913–933, 2016.

[102] M. Van den Bossche. DFTB-Assisted Global Structure Optimization of 13- and 55-Atom Late Transition Metal Clusters. *J. Phys. Chem. A*, 123(13):3038–3045, 2019.

[103] S. T. Call, D. Y. Zubarev, and A. I. Boldyrev. Global minimum structure searches via particle swarm optimization. *J. Comput. Chem.*, 28(7):1177–1186, 2007.

[104] J. Lv, Y. Wang, L. Zhu, and Y. Ma. Particle-swarm structure prediction on clusters. *J. Chem. Phys.*, 137(8):084104, 2012.

[105] V. G. Grigoryan and M. Springborg. Structural and energetic properties of nickel clusters: $\boldsymbol{2 \leq N \leq 150}$. *Phys. Rev. B*, 70(20):205415, 2004.

[106] V. G. Grigoryan, D. Alamanova, and M. Springborg. Structure and energetics of $\mathbf{Cu}_{\boldsymbol{N}}$ clusters with $(\mathbf{2} \leq \boldsymbol{N} \leq \mathbf{150})$: An embedded-atom-method study. *Phys. Rev. B*, 73(11):115415, 2006.

[107] S. V. Dudiy and A. Zunger. Searching for Alloy Configurations with Target Physical Properties: Impurity Design via a Genetic Algorithm Inverse Band Structure Approach. *Phys. Rev. Lett.*, 97(4):046401, 2006.

[108] I. Y. Kanal, S. G. Owens, J. S. Bechtel, and G. R. Hutchison. Efficient Computational Screening of Organic Polymer Photovoltaics. *J. Phys. Chem. Lett.*, 4(10):1613–1623, 2013.

[109] S. P. Collins, T. D. Daff, S. S. Piotrkowski, and T. K. Woo. Materials design by evolutionary optimization of functional groups in metal-organic frameworks. *Sci. Adv.*, 2(11), 2016.

[110] D. B. Gordon and S. L. Mayo. Branch-and-Terminate: a combinatorial optimization algorithm for protein design. *Structure*, 7(9):1089–1098, 1999.

[111] R. F. Goldstein. Efficient rotamer elimination applied to protein side-chains and related spin glasses. *Biophys. J.*, 66(5):1335–1340, 1994.

[112] L. L. Looger and H. W. Hellinga. Generalized dead-end elimination algorithms make large-scale protein side-chain structure prediction tractable: implications for protein design and structural genomics. *J. Mol. Biol.*, 307(1):429–445, 2001.

[113] X. Hu, D. N. Beratan, and W. Yang. A gradient-directed Monte Carlo approach to molecular design. *J. Chem. Phys.*, 129(6):064102, 2008.

[114] X. Hu, H. Hu, D. N. Beratan, and W. Yang. A gradient-directed Monte Carlo approach for protein design. *J. Comput. Chem.*, 31(11):2164–2168, 2010.

[115] D. Xiao, W. Yang, and D. N. Beratan. Inverse molecular design in a tight-binding framework. *J. Chem. Phys.*, 129(4):044106, 2008.

[116] J. H. Holland. *Adaptation in natural and artificial systems: an introductory analysis with applications to biology, control, and artificial intelligence.* Complex adaptive systems. MIT Press, Cambridge, Massachusetts, U.S., 1992.

[117] K. Deb. *Multi-Objective Optimization Using Evolutionary Algorithms.* Wiley-Interscience Series in Systems and Optimization. John Wiley & Sons, LTD, Chichester, England, 2001.

[118] N. S. Froemming and G. Henkelman. Optimizing core-shell nanoparticle catalysts with a genetic algorithm. *J. Chem. Phys.*, 131(23):234103, 2009.

[119] J. McCall. Genetic algorithms for modelling and optimisation. *J. Comput. Appl. Math.*, 184(1):205–222, 2005.

[120] H. Kita. A Comparison Study of Self-Adaptation in Evolution Strategies and Real-Coded Genetic Algorithms. *Evol. Comput.*, 9(2):223–241, 2001.

[121] D. Thierens and D. Goldberg. Convergence models of genetic algorithm selection schemes. In Y. Davidor, H.-P. Schwefel, and R. Männer, editors, *Parallel Problem Solving from Nature - PPSN III.*, volume 866 of *Lecture Notes in Computer Science*, pages 119–129, Berlin, Heidelberg, Germany, 1994. Springer Berlin Heidelberg.

[122] K. Chellapilla. Combining mutation operators in evolutionary programming. *IEEE Trans. Evol. Comput.*, 2(3):91–96, 1998.

[123] A. Hertz and D. Kobler. A framework for the description of evolutionary algorithms. *Eur. J. Oper. Res.*, 126(1):1–12, 2000.

[124] D. Greenhalgh and S. Marshall. Convergence Criteria for Genetic Algorithms. *SIAM J. Comput.*, 30(1):269–282, 2000.

[125] J. Koutecký, V. Bonačić-Koutecký, I. Boustani, P. Fantucci, and W. Pewestorf. Electronic Structure and Basic Properties of Small Alkali Metal Clusters. In J. Jortner, A. Pullman, and B. Pullman, editors, *Large Finite Systems.*, pages 303–317, Dordrecht, Netherlands, 1987. Springer Netherlands.

[126] A. K. Kushwaha and S. K. Nayak. Wobbled electronic properties of lithium clusters: Deterministic approach through first principles. *Physica E Low Dimens. Syst. Nanostruct.*, 97:368–374, 2018.

[127] A. K. Kushwaha, M. R. Sahoo, J. Nanda, and S. K. Nayak. Engineering Redox Potential of Lithium Clusters for Electrode Material in Lithium-Ion Batteries. *J. Clust. Sci.*, 28(5):2779–2793, 2017.

[128] W. D. Knight, K. Clemenger, W. A. de Heer, W. A. Saunders, M. Y. Chou, and M. L. Cohen. Electronic Shell Structure and Abundances of Sodium Clusters. *Phys. Rev. Lett.*, 52(24):2141–2143, 1984.

[129] W. D. Knight, W. A. de Heer, K. Clemenger, and W. A. Saunders. Electronic shell structure in potassium clusters. *Solid State Commun.*, 53(5):445–446, 1985.

[130] W. Ekardt. Dynamical Polarizability of Small Metal Particles: Self-Consistent Spherical Jellium Background Model. *Phys. Rev. Lett.*, 52(21):1925–1928, 1984.

[131] W. Ekardt. Work function of small metal particles: Self-consistent spherical jellium-background model. *Phys. Rev. B*, 29(4):1558–1564, 1984.

[132] M. Y. Chou, A. Cleland, and M. L. Cohen. Total energies, abundances, and electronic shell structure of lithium, sodium, and potassium clusters. *Solid State Commun.*, 52(7):645–648, 1984.

[133] H. A. Jahn, E. Teller, and F. G. Donnan. Stability of polyatomic molecules in degenerate electronic states. I. Orbital degeneracy. *Proc. R. Soc. Lond. A*, 161(905):220–235, 1937.

[134] K. Clemenger. Ellipsoidal shell structure in free-electron metal clusters. *Phys. Rev. B*, 32(2):1359–1362, 1985.

[135] T. P. Martin, T. Bergmann, H. Göhlich, and T. Lange. Shell structure of clusters. *J. Phys. Chem.*, 95(17):6421–6429, 1991.

[136] F. Baletto and R. Ferrando. Structural properties of nanoclusters: Energetic, thermodynamic, and kinetic effects. *Rev. Mod. Phys.*, 77(1):371–423, 2005.

[137] T. P. Martin, U. Näher, H. Schaber, and U. Zimmermann. Evidence for a size-dependent melting of sodium clusters. *J. Chem. Phys.*, 100(3):2322–2324, 1994.

[138] W. D. Knight, K. Clemenger, W. A. de Heer, and W. A. Saunders. Polarizability of alkali clusters. *Phys. Rev. B.*, 31(4):2539–2540, 1985.

[139] G. Tikhonov, V. Kasperovich, K. Wong, and V. V. Kresin. A measurement of the polarizability of sodium clusters. *Phys. Rev. A*, 64(6):063202, 2001.

[140] K. R. S. Chandrakumar, T. K. Ghanty, and S. K. Gosh. Theoretical studies on polarizability of alkali metal clusters. In G. Maroulis, editor, *Atoms, Molecules and Clusters in Electric Fields.*, Computational, Numerical and Mathematical Methods in Sciences and Engineering: Volume 1, pages 625–655. Imperial College Press, London, U.K., 2006.

[141] C. Yannouleas, E. Vigezzi, and R. A. Broglia. Evolution of the optical properties of alkali-metal microclusters towards the bulk: The matrix random-phase-approximation description. *Phys. Rev. B*, 47(15):9849–9861, 1993.

[142] A. Rubio, J. A. Alonso, X. Blase, and S. G. Louie. Theoretical Models for the Optical Properties of Clusters and Nanostructures. *Int. J. Mod. Phys. B*, 11(23):2727–2776, 1997.

[143] Z. Guo, B. Lu, X. Jiang, J. Zhao, and R.-H. Xie. Structural, electronic, and optical properties of medium-sized Li_n clusters ($n = 20, 30, 40, 50$) by density functional theory. *Physica E Low Dimens. Syst. Nanostruct.*, 42(5):1755–1762, 2010.

[144] M. Brack, O. Genzken, and K. Hansen. Thermal electronic properties of alkali clusters. *Z. Phys. D: At., Mol. Clusters*, 19(4):51–53, 1991.

[145] F. Calvo and F. Spiegelmann. Geometric Size Effects in the Melting of Sodium Clusters. *Phys. Rev. Lett.*, 82(11):2270–2273, 1999.

[146] A. Aguado, L. M. Molina, J. M. López, and J. A. Alonso. Melting behaviour of large disordered sodium clusters. *Eur. Phys. J. D*, 15(2):221–227, 2001.

[147] C. P. Schulz, P. Claas, D. Schumacher, and F. Stienkemeier. Formation and Stability of High-Spin Alkali Clusters. *Phys. Rev. Lett.*, 92(1):013401, 2004.

[148] X. Liu, H. Ito, and E. Torikai. A numerical study of spin-dependent organization of alkali-metal atomic clusters using density-functional method. *J. Nanopart. Res.*, 14(8):1050, 2012.

[149] V. Bonačić-Koutecký, P. Fantucci, and J. Koutecký. Systematic *ab initio* configuration-interaction study of alkali-metal clusters. II. Relation between electronic structure and geometry of small sodium clusters. *Phys. Rev. B*, 37(9):4369–4374, 1988.

[150] J. Blanc, V. Bonačić-Koutecký, M. Broyer, J. Chevaleyre, Ph. Dugourd, J. Koutecký, C. Scheuch, J. P. Wolf, and L. Wöste. Evolution of the electronic structure of lithium clusters between four and eight atoms. *J. Chem. Phys.*, 96(3):1793–1809, 1992.

[151] L. Kronik, I. Vasiliev, M. Jain, and J. R. Chelikowsky. *Ab initio* structures and polarizabilities of sodium clusters. 115(9):4322–4332, 2001.

[152] G. Gardet, F. Rogemond, and H. Chermette. Density functional theory study of some structural and energetic properties of small lithium clusters. *J. Chem. Phys.*, 105(22):9933–9947, 1996.

[153] A. Banerjee, T. K. Ghanty, and A. Chakrabarti. *Ab initio* Studies of Properties of Small Potassium Clusters. *J. Phys. Chem. A*, 112(48):12303–12311, 2008.

[154] M. Itoh, V. Kumar, T. Adschiri, and Y. Kawazoe. Comprehensive study of sodium, copper, and silver clusters over a wide range of sizes $2 \leq N \leq 75$. *J. Chem. Phys.*, 131(17):174510, 2009.

[155] E. G. Noya, J. P. K. Doye, D. J. Wales, and A. Aguado. Geometric magic numbers of sodium clusters: Interpretation of the melting behaviour. *Eur. Phys. J. D*, 43(1):57–60, 2007.

[156] A. Aguado and O. Kostko. First-principles determination of the structure of Na_N and Na_N^- clusters with up to 80 atoms. *J. Chem. Phys.*, 134(16):164304, 2011.

[157] V. Tevekeliyska, Y. Dong, M. Springborg, and V. G. Grigoryan. Structural and energetic properties of sodium clusters. *Eur. Phys. J. D*, 43(1):19–22, 2007.

[158] M. J. Stott and E. Zaremba. Quasiatoms: An approach to atoms in nonuniform electronic systems. *Phys. Rev. B*, 22(4):1564–1583, 1980.

[159] M. S. Daw and M. I. Baskes. Semiempirical, Quantum Mechanical Calculation of Hydrogen Embrittlement in Metals. *Phys. Rev. Lett.*, 50(17):1285–1288, 1983.

[160] M. S. Daw and M. I. Baskes. Embedded-atom method: Derivation and application to impurities, surfaces, and other defects in metals. *Phys. Rev. B*, 29(12):6443–6453, 1984.

[161] S. M. Foiles, M. I. Baskes, and M. S. Daw. Embedded-atom-method functions for the fcc metals Cu, Ag, Au, Ni, Pd, Pt, and their alloys. *Phys. Rev. B*, 33(12):7983–7991, 1986.

[162] M. S. Daw, S. M. Foiles, and M. I. Baskes. The embedded-atom method: a review of theory and applications. *Mat. Sci. Rep.*, 9(7):251–310, 1993.

[163] R. A. Johnson and D. J. Oh. Analytic embedded atom method model for bcc metals. *J. Mater. Res.*, 4(5):1195–1201, 1989.

[164] R. A. Johnson. Alloy models with the embedded-atom method. *Phys. Rev. B*, 39(17):12554–12559, 1989.

[165] Z. Bangwei and O. Yifang. Theoretical calculation of thermodynamic data for bcc binary alloys with the embedded-atom method. *Phys. Rev. B*, 48(5):3022–3029, 1993.

[166] S. S. Pohlong and P. N. Ram. Analytic embedded atom method potentials for face-centered cubic metals. *J. Mater. Res.*, 13(7):1919–1927, 1998.

[167] O. Yifang, Z. Bangwei, L. Shuzhi, and J. Zhanpeng. A simple analytical EAM model for bcc metals including Cr and its application. *Z. Phys. B: Condens. Matter*, 101(2):161–168, 1996.

[168] Z. Bangwei, O. Yifang, L. Shuzhi, and J. Zhanpeng. An analytic MEAM model for all BCC transition metals. *Physica B Condens. Matter*, 262(3):218–225, 1999.

[169] K. Yang, L. Lang, H. Deng, F. Gao, and W. Hu. Modified analytic embedded atom method potential for chromium. *Model. Simul. Mat. Sci. Eng.*, 26(6):065001, 2018.

[170] A. Sachdev, R. I. Masel, and J. B. Adams. An embedded atom method study of the equilibrium shapes of small platinum and palladium clusters. *Z. Phys. D: At., Mol. Clusters*, 26(1):310–312, 1993.

[171] M. Karabacak, S. Özçelik, and Z. B. Güvenç. Structures and energetics Of Pd_n $(n = 2 - 20)$ clusters using an embedded-atom model potential. *Surf. Sci.*, 507-510:636–642, 2002.

[172] J. M. Montejano-Carrizales, M. P. Iñiguez, and J. A. Alonso. Embedded-atom method applied to bimetallic clusters: The Cu-Ni and Cu-Pd systems. *Phys. Rev. B*, 49(23):16649–16658, 1994.

[173] T. Van Hoof and M. Hou. Structural and thermodynamic properties of $\mathbf{Ag} - \mathbf{Co}$ nanoclusters. *Phys. Rev. B*, 72(11):115434, 2005.

[174] M. Molayem, V. G. Grigoryan, and M. Springborg. Global Minimum Structures and Magic Clusters of Cu_mAg_n Nanoalloys. *J. Phys. Chem. C*, 115(45):22148–22162, 2011.

[175] M. Molayem, V. G. Grigoryan, and M. Springborg. Theoretical Determination of the Most Stable Structures of Ni_mAg_n Bimetallic Nanoalloys. *J. Phys. Chem. C*, 115(15):7179–7192, 2011.

[176] W. Hu and F. Masahiro. The application of the analytic embedded atom potentials to alkali metals. *Model. Simul. Mat. Sci. Eng.*, 10(6):707–726, 2002.

[177] K. Huwig. Structural and energetic investigation of sodium clusters. Bachelor thesis, Universität des Saarlandes, 2012.

[178] M. Valtchev. Algorithmen zur Generierung zufälliger Atomanordnungen in vorgegebenen Formen und Volumina und deren Anwendung in der Strukturoptimierung bimetallischer Cluster. Vertiefungsarbeit, Universität des Saarlandes, 2006.

[179] L. Vandenberghe. ECE236C - Optimization Methods for Large-Scale Systems. 15. Quasi-Newton methods., 2020. online available: `http://www.seas.ucla.edu/~vandenbe/236C/lectures/qnewton.pdf`; last time retrieved: 2020-05-10.

[180] K. P. Huber and G. Herzberg. *Molecular spectra and molecular structure IV. Constants of diatomic molecules.* Van Nostrand Reinhold Company, New York, U.S., 1979.

[181] R. Fournier, J. B. Y. Cheng, and A. Wong. Theoretical study of the structure of lithium clusters. *J. Chem. Phys.*, 119(18):9444–9454, 2003.

[182] B. G. A. Brito, G.-Q. Hai, and L. Cândido. A quantum Monte Carlo study of the structural and electronic properties of small cationic and neutral lithium clusters. *J. Chem. Phys.*, 146(17):174306, 2017.

[183] K. R. S. Chandrakumar, T. K. Ghanty, and S. K. Ghosh. Static dipole polarizability and binding energy of sodium clusters Na_n ($n = 1 - 10$): A critical assessment of all-electron based post Hartree-Fock and density functional methods. *J. Chem. Phys.*, 120(14):6487–6494, 2004.

[184] I. A. Solov'yov, A. V. Solov'yov, and W. Greiner. Structure and properties of small sodium clusters. *Phys. Rev. A*, 65(5):053203, 2002.

[185] R. O. Jones, A. I. Lichtenstein, and J. Hutter. Density functional study of structure and bonding in lithium clusters Li_n and their oxides $\mathrm{Li}_n\mathrm{O}$. *J. Chem. Phys.*, 106(11):4566–4574, 1997.

[186] Ph. Dugourd, J. Chevaleyre, M. Broyer, J. P. Wolf, and L. Wöste. Vibronic structure of the Li_3 ground state. *Chem. Phys. Lett.*, 175(6):555–560, 1990.

[187] H.-S. Hu, Y.-F. Zhao, J. R. Hammond, E. J. Bylaska, E. Aprà, H. J. J. van Dam, J. Li, N. Govind, and K. Kowalski. Theoretical studies of the global minima and polarizabilities of small lithium clusters. *Chem. Phys. Lett.*, 644:235–242, 2016.

[188] S. E. Wheeler, K. W. Sattelmeyer, P. v. R. Schleyer, and H. F. Schaefer III. Binding energies of small lithium clusters (Li_n) and hydrogenated lithium clusters ($\mathrm{Li}_n\mathrm{H}$). *J. Chem. Phys.*, 120(10):4683–4689, 2004.

[189] I. Boustani, W. Pewestorf, P. Fantucci, V. Bonaić-Koutecký, and J. Koutecký. Systematic *ab initio* configuration-interaction study of alkali-metal clusters: Relation between electronic structure and geometry of small Li clusters. *Phys. Rev. B*, 35(18):9437–9450, 1987.

[190] A. Grassi, G. M. Lombardo, G. G. N. Angilella, N. H. March, and R. Pucci. Equilibrium geometries of low-lying isomers of some Li clusters, within Hartree-Fock theory plus bond order or MP2 correlation corrections. *J. Chem. Phys.*, 120(24):11615–11620, 2004.

[191] A. Monari, J. Pitarch-Ruiz, G. L. Bendazzoli, S. Evangelisti, and J. Sanchez-Marin. Full Configuration-Interaction Study on the Tetrahedral Li_4 Cluster. *J. Chem. Theory Comput.*, 4(3):404–413, 2008.

[192] A. Kornath, A. Kaufmann, A. Zoermer, and R. Ludwig. Raman spectroscopic investigation of small matrix-isolated lithium clusters. *J. Chem. Phys.*, 118(15):6957–6963, 2003.

[193] J. F. Pérez, E. Florez, C. Z. Hadad, P. Fuentealba, and A. Restrepo. Stochastic Search of the Quantum Conformational Space of Small Lithium and Bimetallic Lithium-Sodium Clusters. *J. Phys. Chem. A*, 112(25):5749–5755, 2008.

[194] D. Yepes, S. R. Kirk, S. Jenkins, and A. Restrepo. Structures, energies and bonding in neutral and charged Li microclusters. *J. Mol. Model.*, 18(9):4171–4189, 2012.

[195] D. J. Wales, J. P. K. Doye, A. Dullweber, M. P. Hodges, F. Y. Naumkin, F. Calvo, J. Hernández-Rojas, and T. F. Middleton. The Cambridge Cluster Database. website. online available: `http://www-wales.ch.cam.ac.uk/CCD.html`; last time retrieved: 2020-03-23.

[196] R. Poteau and F. Spiegelmann. Distance-dependent Hückel-type model for the study of sodium clusters. *Phys. Rev. B*, 45(4):1878–1888, 1992.

[197] R. Poteau, F. Spiegelmann, and P. Labastie. Isomerisation and phase transitions in small sodium clusters. *Z. Phys. D: At., Mol. Clusters*, 30(1):57–68, 1994.

[198] W. G. Sun, J. J. Wang, C. Lu, X. X. Xia, X. Y. Kuang, and A. Hermann. Evolution of the Structural and Electronic Properties of Medium-Sized Sodium Clusters: A Honeycomb-Like Na_{20} Cluster. *Inorg. Chem.*, 56(3):1241–1248, 2017.

[199] S. K. Lai, P. J. Hsu, K. L. Wu, W. K. Liu, and M. Iwamatsu. Structures of metallic clusters: Mono- and polyvalent metals. *J. Chem. Phys.*, 117(23):10715–10725, 2002.

[200] M. M. Dacorogna and M. L. Cohen. First-principles study of the structural properties of alkali metals. *Phys. Rev. B*, 34(8):4996–5002, 1986.

[201] A. Rapallo, G. Rossi, R. Ferrando, A. Fortunelli, B. C. Curley, L. D. Lloyd, G. M. Tarbuck, and R. L. Johnston. Global optimization of bimetallic cluster structures. I. Size-mismatched Ag-Cu, Ag-Ni, and Au-Cu systems. *J. Chem. Phys.*, 122(19):194308, 2005.

[202] R. Ferrando, J. Jellinek, and R. L. Johnston. Nanoalloys: From Theory to Applications of Alloy Clusters and Nanoparticles. *Chem. Rev.*, 108(3):845–910, 2008.

[203] H. Haberland, T. Hippler, J. Donges, O. Kostko, M. Schmidt, and B. von Issendorff. Melting of Sodium Clusters: Where Do the Magic Numbers Come from?. *Phys. Rev. Lett.*, 94(3):035701, 2005.

[204] M.-W. Sung, R. Kawai, and J. H. Weare. Packing Transitions in Nanosized Li Clusters. *Phys. Rev. Lett.*, 73(26):3552–3555, 1994.

[205] K. Huwig, C. Fan, and M. Springborg. From properties to materials: An efficient and simple approach. *J. Chem. Phys.*, 147(23):234105, 2017.

[206] B. O'Regan and M. Grätzel. A low-cost, high-efficiency solar cell based on dye-sensitized colloidal TiO_2 films. *Nature*, 353(6346):737–740, 1991.

[207] N. Sharifi, F. Tajabadi, and N. Taghavinia. Recent Developments in Dye-Sensitized Solar Cells. *ChemPhysChem*, 15(18):3902–3927, 2014.

[208] J. Gong, K. Sumathy, Q. Qiao, and Z. Zhou. Review on dye-sensitized solar cells (DSSCs): Advanced techniques and research trends. *Renew. Sustain. Energy Rev.*, 68:234–246, 2017.

[209] P. Xu, N. S. McCool, and T. E. Mallouk. Water splitting dye-sensitized solar cells. *Nano Today*, 14:42–58, 2017.

[210] T. Liu, K. Yu, L. Gao, H. Chen, N. Wang, L. Hao, T. Li, H. He, and Z. Guo. A graphene quantum dot decorated $SrRuO_3$ mesoporous film as an efficient counter electrode for high-performance dye-sensitized solar cells. *J. Mater. Chem A.*, 5(34):17848–17855, 2017.

[211] B. N. Nunes, L. A. Faustino, A. V. Muller, A. S. Polo, and A. O. T. Patrocinio. Chapter 8 - Nb_2O_5 dye-sensitized solar cells. In S. Thomas, E. H. M. Sakho, N. Kalarikkal, S. O. Oluwafemi, and J. Wu, editors, *Nanomaterials for Solar Cell Applications.*, pages 287–322. Elsevier, 2019.

[212] Y. Saygili, M. Stojanovic, N. Flores-Díaz, S. M. Zakeeruddin, N. Vlachopoulos, M. Grätzel, and A. Hagfeldt. Metal Coordination Complexes as Redox Mediators in Regenerative Dye-Sensitized Solar Cells. *Inorganics*, 7(3):30, 2019.

[213] L.-L. Li and E. W.-G. Diau. Porphyrin-sensitized solar cells. *Chem. Soc. Rev.*, 42(1):291–304, 2013.

[214] Y. Liang, X. Xue, W. Zhang, C. Fan, Y. Li, B. Zhang, and Y. Feng. Novel D-π-A structured porphyrin dyes containing various diarylamino moieties for dye-sensitized solar cells. *Dyes Pigm.*, 115:7–16, 2015.

[215] C. Fan, M. Springborg, and Y. Feng. Application of an inverse-design method to optimizing porphyrins in dye-sensitized solar cells. *Phys. Chem. Chem. Phys.*, 21(10):5834–5844, 2019.

[216] M. Mao, J.-B. Wang, Z.-F. Xiao, S.-Y. Dai, and Q.-H. Song. New 2,6-modified BODIPY sensitizers for dye-sensitized solar cells. *Dyes Pigm.*, 94(2):224–232, 2012.

[217] S. P. Singh and T. Gayathri. Evolution of BODIPY Dyes as Potential Sensitizers for Dye-Sensitized Solar Cells. *Eur. J. Org. Chem.*, 2014(22):4689–4707, 2014.

[218] H. Klfout, A. Stewart, M. Elkhalifa, and H. He. BODIPYs for Dye-Sensitized Solar Cells. *ACS Appl. Mater. Interfaces*, 9(46):39873–39889, 2017.

[219] M. Chandrasekharam, T. Suresh, S. P. Singh, B. Priyanka, K. Bhanuprakash, A. Islam, L. Han, and M. Lakshmi Kantam. Functionalized styryl bipyridine as a superior chelate for a ruthenium sensitizer in dye sensitized solar cells. *Dalton Trans.*, 41(29):8770–8772, 2012.

[220] M. Urbani, M. Medel, S. A. Kumar, A. K. Chandiran, D. González-Rodríguez, M. Grätzel, M. K. Nazeeruddin, and T. Torres. Cyclopentadithiophene-functionalized Ru(II)-bipyridine sensitizers for dye-sensitized solar cells. *Polyhedron*, 82:132–138, 2014.

[221] M. Elstner and G. Seifert. Density functional tight binding. *Phil. Trans. R. Soc. A*, 372(2011):20120483, 2014.

[222] D. Porezag, Th. Frauenheim, Th. Köhler, G. Seifert, and R. Kaschner. Construction of tight-binding-like potentials on the basis of density-functional theory: Application to carbon. *Phys. Rev. B*, 51(19):12947–12957, 1995.

[223] G. Seifert, D. Porezag, and Th. Frauenheim. Calculations of molecules, clusters, and solids with a simplified LCAO-DFT-LDA Scheme. *Int. J. Quantum Chem.*, 58(2):185–192, 1996.

[224] M. Elstner, D. Porezag, G. Jungnickel, J. Elsner, M. Haugk, Th. Frauenheim, S. Suhai, and G. Seifert. Self-consistent-charge density-functional tight-binding method for simulations of complex materials properties. *Phys. Rev. B*, 58(11):7260–7268, 1998.

[225] A. F. Oliveira, G. Seifert, T. Heine, and H. A. Duarte. Density-Functional based tight-binding: an approximate DFT method. *J. Braz. Chem. Soc.*, 20(7):1193–1205, 2009.

[226] Format of the v1.0 slater-koster files. website. online available: `https://www.dftb.org/fileadmin/DFTB/public/misc/slakoformat.pdf`; last time retrieved 2020-04-23.

[227] T. A. Niehaus. Approximate time-dependent density functional theory. *J. Mol. Struct. (Theochem)*, 914(1):38–49, 2009.

[228] R. A. Marcus. Electron transfer reactions in chemistry. Theory and experiment. *Rev. Mod. Phys.*, 65(3):599–610, 1993.

[229] R. Oshi, S. Abdalla, and M. Springborg. Study of the influence of functionalization on the reorganization energy of naphthalene using DFT. *Comput. Theor. Chem.*, 1099:209–215, 2017.

[230] D. F. Perepichka and M. R. Bryce. Molecules with Exceptionally Small HOMO-LUMO Gaps. *Angew. Chem. Int. Ed.*, 44(34):5370–5373, 2005.

[231] A. S. Khazaal, M. Springborg, C. Fan, and K. Huwig. Optimizing small conjugated molecules for solar-cell applications using an inverse-design method. *J. Mol. Graph. Model.*, 100:107654, 2020.

[232] A. S. Khazaal, M. Sprinborg, C. Fan, and K. Huwig. Application of an inverse-design method for designing new branched thiophene oligomers for bulk-heterojunction solar cells. *Comput. Condens. Matter*, 25:e00503, 2020.

[233] M. Bowker, E. Rowbotham, F. M. Leibsle, and S. Haq. The adsorption and decomposition of formic acid on Cu 110. *Surf. Sci.*, 349(2):97–110, 1996.

[234] K. A. Ali, A. Z. Abdullah, and A. R. Mohamed. Recent development in catalytic technologies for methanol synthesis from renewable sources: A critical review. *Renew. Sustain. Energy Rev.*, 44:508–518, 2015.

[235] S. Sui, X. Wang, X. Zhou, Y. Su, S. Riffat, and C. Liu. A comprehensive review of Pt electrocatalysts for the oxygen reduction reaction: Nanostructure, activity, mechanism and carbon support in PEM fuel cells. *J. Mater. Chem. A*, 5(5):1808–1825, 2017.

[236] S. Morisset, N. Rougeau, and D. Teillet-Billy. Hydrogenation reactions and adsorption: From CO to methanol on a graphene surface. *Mol. Astrophys.*, 14:1–9, 2019.

[237] F. Schedin, A. K. Geim, S. V. Morozov, E. W. Hill, P. Blake, M. I. Katsnelson, and K. S. Novoselov. Detection of individual gas molecules adsorbed on graphene. *Nat. Mater.*, 6(9):652–655, 2007.

[238] P. Shankar and J. B. B. Rayappan. Gas sensing mechanism of metal oxides: The role of ambient atmosphere, type of semiconductor and gases – A review. *Sci. Lett. J.*, 4:126, 2015.

[239] M. Sajjad, E. Montes, N. Singh, and U. Schwingenschlögl. Superior Gas Sensing Properties of Monolayer $PtSe_2$. *Adv. Mater. Interfaces*, 4(5):1600911, 2017.

[240] Z. Gao, W. Yang, X. Ding, G. Lv, and W. Yan. Support effects in single atom iron catalysts on adsorption characteristics of toxic gases (NO_2, NH_3, SO_3 and H_2S). *Appl. Surf. Sci.*, 436:585–595, 2018.

[241] A. T. Mathauser and A. V. Teplyakov. The effects of surface poisoning by HCl on cyclization processes on a $Cu_3Pt(111)$ surface. *Surf. Sci.*, 523(1):37–47, 2003.

[242] D. N. Goldstein and S. M. George. Surface poisoning in the nucleation and growth of palladium atomic layer deposition with Pd(hfac)$_2$ and formalin. *Thin Solid Films*, 519(16):5339–5347, 2011.

[243] C. R. Bernard Rodríguez and J. A. Santana. Adsorption and diffusion of sulfur on the (111), (100), (110), and (211) surfaces of FCC metals: Density functional theory calculations. *J. Chem. Phys.*, 149(20):204701, 2018.

[244] T. Schober. On the activation of FeTi for hydrogen storage. *J. Less-Common Met.*, 89(1):63–70, 1983.

[245] A. Pundt and R. Kirchheim. HYDROGEN IN METALS: Microstructural Aspects. *Annu. Rev. Mater. Res.*, 36(1):555–608, 2006.

[246] M. V. Lototsky, M. Williams, V. A. Yartys, Y. V. Klochko, and V. M. Linkov. Surface-modified advanced hydrogen storage alloys for hydrogen separation and purification. *J. Alloys Compd.*, 509:S555–S561, 2011.

[247] V. Tozzini and V. Pellegrini. Prospects for hydrogen storage in graphene. *Phys. Chem. Chem. Phys.*, 15(1):80–89, 2013.

[248] J. Nawrocki, M. Rigney, A. McCormick, and P. W. Carr. Chemistry of zirconia and its use in chromatography. *J. Chromatogr. A*, 657(2):229–282, 1993.

[249] Q.-C. Zhang, Y. Yin, and D. R. Mills. High efficiency Mo-Al$_2$O$_3$ cermet selective surfaces for high-temperature application. *Sol. Energy Mater. Sol. Cells*, 40(1):43–53, 1996.

[250] Y. Wang, S. Nakamura, M. Ue, and P. B. Balbuena. Theoretical Studies To Understand Surface Chemistry on Carbon Anodes for Lithium-Ion Batteries: Reduction Mechanisms of Ethylene Carbonate. *J. Am. Chem. Soc.*, 123(47):11708–11718, 2001.

[251] S. Rousset, V. Repain, G. Baudot, Y. Garreau, and J. Lecoeur. Self-ordering of Au(111) vicinal surfaces and application to nanostructure organized growth. *J. Phys.: Condens. Matter*, 15(47):S3363–S3392, 2003.

[252] C. M. Friend and X. Xu. Reactions on Transition Metal Surfaces. *Annu. Rev. Phys. Chem.*, 42(1):251–278, 1991.

[253] F. Zaera. The Surface Chemistry of Hydrocarbons on Transition Metal Surfaces: A Critical Review. *Isr. J. Chem.*, 38(4):293–311, 1998.

[254] K. P. Kuhl, T. Hatsukade, E. R. Cave, D. N. Abram, J. Kibsgaard, and T. F. Jaramillo. Electrocatalytic Conversion of Carbon Dioxide to Methane and Methanol on Transition Metal Surfaces. *J. Am. Chem. Soc.*, 136(40):14107–14113, 2014.

[255] A. G. Sault, R. J. Madix, and C. T. Campbell. Adsorption of oxygen and hydrogen on Au(110)-(1x2). *Surf. Sci.*, 169(2):347–356, 1986.

[256] W. Sesselmann, B. Woratschek, J. Küppers, G. Doyen, G. Ertl, H. Haberland, and H. Morgner. Evidence for paramagnetism of NO molecules chemisorbed on transition-metal surfaces. *Phys. Rev. Lett.*, 60(14):1434–1437, 1988.

[257] J. T. Stuckless, N. Al-Sarraf, C. Wartnaby, , and D. A. King. Calorimetric heats of adsorption for CO on nickel single crystal surfaces. *J. Chem. Phys.*, 99(3):2202–2212, 1993.

[258] J. Greeley, J. K. Nørskov, and M. Mavrikakis. Electronic structure and catalysis on metal surfaces. *Annu. Rev. Phys. Chem.*, 53(1):319–348, 2002.

[259] M. N. Huda and L. Kleinman. Density functional calculations of the influence of hydrogen adsorption on the surface relaxation of Ti(0001). *Phys. Rev. B*, 71(24):241406, 2005.

[260] X. Ding, V. Pagan, M. Peressi, and F. Ancilotto. Modeling adsorption of CO_2 on Ni(110) surface. *Mater. Sci. Eng. C*, 27(5):1355–1359, 2007.

[261] P. Ferrin, S. Kandoi, A. U. Nilekar, and M. Mavrikakis. Hydrogen adsorption, absorption and diffusion on and in transition metal surfaces: A DFT study. *Surf. Sci.*, 606(7):679–689, 2012.

[262] L. Xu, J. Lin, Y. Bai, and M. Mavrikakis. Atomic and Molecular Adsorption on Cu(111). *Top. Catal.*, 61(9):736–750, 2018.

[263] A. Mohsenzadeh, K. Bolton, and T. Richards. DFT study of the adsorption and dissociation of water on Ni(111), Ni(110) and Ni(100) surfaces. *Surf. Sci.*, 627:1–10, 2014.

[264] X. Hao, B. Wang, Q. Wang, R. Zhang, and D. Li. Insight into both coverage and surface structure dependent CO adsorption and activation on different Ni surfaces from DFT and atomistic thermodynamics. *Phys. Chem. Chem. Phys.*, 18(26):17606–17618, 2016.

[265] S. Liu, X. Tian, T. Wang, X. Wen, Y.-W. Li, J. Wang, and H. Jiao. Coverage dependent water dissociative adsorption on Fe(110) from DFT computation. *Phys. Chem. Chem. Phys.*, 17(14):8811–8821, 2015.

[266] R. Brosseau, M. R. Brustein, and T. H. Ellis. Water adsorption on Cu(100): The effect of defects. *Surf. Sci.*, 294(3):243–250, 1993.

[267] S. Vollmer, G. Witte, and C. Wöll. Determination of Site Specific Adsorption Energies of CO on Copper. *Catal. Letters*, 77(1):97–101, 2001.

[268] Y. Xu and M. Mavrikakis. Adsorption and Dissociation of O_2 on Gold Surfaces: Effect of Steps and Strain. *J. Phys. Chem. B*, 107(35):9298–9307, 2003.

[269] Y. Jiang, J. Li, G. Su, N. Ferri, W. Liu, and A. Tkatchenko. Tuning the work function of stepped metal surfaces by adsorption of organic molecules. *J. Phys.: Condens. Matter*, 29(20):204001, 2017.

[270] D. C. Sorescu and J. T. Yates. First Principles Calculations of the Adsorption Properties of CO and NO on the Defective TiO_2(110) Surface. *J. Phys. Chem. B*, 106(24):6184–6199, 2002.

[271] M. S. Mahabal, M. D. Deshpande, T. Hussain, and Rajeev Ahuja. Sensing Characteristics of Phosphorene Monolayers toward PH_3 and AsH_3 Gases upon the Introduction of Vacancy Defects. *J. Phys. Chem. C*, 120(36):20428–20436, 2016.

[272] N. Tit, K. Said, N. M. Mahmoud, S. Kouser, and Z. H. Yamani. *Ab-initio* investigation of adsorption of CO and CO_2 molecules on graphene: Role of intrinsic defects on gas sensing. *Appl. Surf. Sci.*, 394:219–230, 2017.

[273] K. Dolui, I. Rungger, C. Das Pemmaraju, and S. Sanvito. Possible doping strategies for MoS_2 monolayers: An *ab initio* study. *Phys. Rev. B*, 88(7):075420, 2013.

[274] L. Zhang, I. A. W. Filot, Y.-Q. Su, J.-X. Liu, and E. J. M. Hensen. Transition metal doping of Pd(111) for the NO + CO reaction. *J. Catal.*, 363:154–163, 2018.

[275] H. Gong, Y. He, J. Yin, S. Liu, M. Qing, Q. Peng, C.-F. Huo, H. Wang, Y. Yang, and X.-D. Wen. Electronic effects of transition metal dopants on Fe(100) and Fe_5C_2(100) surfaces for CO activation. *Catal. Sci. Technol.*, 10(7):2047–2056, 2020.

[276] G. F. Cabeza, N. J. Castellani, and P. Légaré. THEORETICAL STUDY OF CO ADSORPTION ON Ni(111), Pt(111) AND Pt/Ni(111) SURFACES. *Surf. Rev. Lett.*, 06(03&04):369–381, 1999.

[277] A. Eichler. CO adsorption on Ni(111)–a density functional theory study. *Surf. Sci.*, 526(3):332–340, 2003.

[278] K. M. Gameel, I. M. Sharafeldin, and N. K. Allam. First-principles descriptors of CO chemisorption on Ni and Cu surfaces. *Phys. Chem. Chem. Phys.*, 21(21):11476–11487, 2019.

[279] P. Cremaschi and J. L. Whitten. Chemisorption Theory: Dissociation of H_2 on Ti(0001). *Phys. Rev. Lett.*, 46(18):1242–1244, 1981.

[280] P. Cremaschi and J. L. Whitten. Chemisorption of hydrogen on titanium: Embedding theory and comparisons with small clusters. *Surf. Sci.*, 112(3):343–358, 1981.

[281] K. Nobuhara, H. Kasai, W. A. Diño, and H. Nakanishi. H_2 dissociative adsorption on Mg, Ti, Ni, Pd and La Surfaces. *Surf. Sci.*, 566–568:703–707, 2004.

[282] J. W. Wang and H. R. Gong. Adsorption and diffusion of hydrogen on Ti, Al, and TiAl surfaces. *Int. J. Hydrog. Energy*, 39(11):6068–6075, 2014.

[283] Y. Liu, Y. Huang, Z. Xiao, and X. Ren. Study of Adsorption of Hydrogen on Al, Cu, Mg, Ti Surfaces in Al Alloy Melt via First Principles Calculation. *Metals*, 7(1):21, 2017.

[284] F. Bloch. Über die Quantenmechanik der Elektronen in Kristallgittern. *Phys. Z.*, 52(7):555–600, 1929.

[285] L. Brillouin. Les électrons libres dans les métaux et le role des réflexions de Bragg. *J. Phys. Radium*, 1(11):377–400, 1930.

[286] A. N. Cleland. Two- and Three-Dimensional Lattices. In *Foundations of Nanomechanics: From Solid-State Theory to Device Applications*, pages 43–85. Springer Berlin Heidelberg, Berlin, Heidelberg, 2003.

[287] J. D. Pack and H. J. Monkhorst. "Special points for Brillouin-zone integrations"—a reply. *Phys. Rev. B*, 16(4):1748–1749, 1977.

[288] G. Blyholder. Molecular Orbital View of Chemisorbed Carbon Monoxide. *J. Phys. Chem.*, 68(10):2772–2777, 1964.

[289] G. Blyholder and M. C. Allen. Infrared spectra and molecular orbital model for carbon monoxide adsorbed on metals. *J. Am. Chem. Soc.*, 91(12):3158–3162, 1969.

[290] G. Blyholder. CNDO model of carbon monoxide chemisorbed on nickel. *J. Phys. Chem.*, 79(7):756–761, 1975.

[291] K. Christmann, O. Schober, and G. Ertl. Adsorption of CO on a Ni(111) surface. *J. Chem. Phys.*, 60(12):4719–4724, 1974.

[292] G. Teeter and J. L. Erskine. Surface relaxation of Ti(0001): Influence of hydrogen contamination. *Phys. Rev. B*, 61(20):13929–13935, 2000.

[293] J. Guo, L. Guan, S. Wang, Q. Zhao, Y. Wang, and B. Liu. Study of hydrogen adsorption on the Ti (0001)-(1x1) surface by density functional theory. *Appl. Surf. Sci.*, 255(5, Part 2):3164–3169, 2008.

[294] P. Giannozzi, S. Baroni, N. Bonini, M. Calandra, R. Car, C. Cavazzoni, D. Ceresoli, G. L. Chiarotti, M. Cococcioni, I. Dabo, A. Dal Corso, S. de Gironcoli, S. Fabris, G. Fratesi, R. Gebauer, U. Gerstmann, C. Gougoussis, A. Kokalj, M. Lazzeri, L. Martin-Samos, N. Marzari, F. Mauri, R. Mazzarello, S. Paolini, A. Pasquarello, L. Paulatto, C. Sbraccia, S. Scandolo, G. Sclauzero, A. P. Seitsonen, A. Smogunov, P. Umari, and R. M. Wentzcovitch. QUANTUM ESPRESSO: a modular and open-source software project for quantum simulations of materials. *J. Phys.: Condens. Matter*, 21(39):395502, 2009.

[295] P. Giannozzi, O. Andreussi, T. Brumme, O. Bunau, M. Buongiorno Nardelli, M. Calandra, R. Car, C. Cavazzoni, D. Ceresoli, M. Cococcioni, N. Colonna, I. Carnimeo, A. Dal Corso, S. de Gironcoli, P. Delugas, R. A. DiStasio, A. Ferretti, A. Floris, G. Fratesi, G. Fugallo, R. Gebauer, U. Gerstmann, F. Giustino, T. Gorni, J. Jia, M. Kawamura, H.-Y. Ko, A. Kokalj, E. Küçükbenli, M. Lazzeri, M. Marsili, N. Marzari, F. Mauri, N. L. Nguyen, H.-V. Nguyen, A. Otero de-la Roza, L. Paulatto, S. Poncé, D. Rocca, R. Sabatini, B. Santra, M. Schlipf, A. P. Seitsonen, A. Smogunov, I. Timrov, T. Thonhauser, P. Umari, N. Vast, X. Wu, and S. Baroni. Advanced capabilities for materials modelling with QUANTUM ESPRESSO. *J. Phys.: Condens. Matter*, 29(46):465901, 2017.

[296] J. M. Soler, E. Artacho, J. D. Gale, A. García, J. Junquera, P. Ordejón, and D. Sánchez-Portal. The SIESTA method for *ab initio* order-N materials simulation. *J. Phys.: Condens. Matter*, 14(11):2745–2779, 2002.

[297] G. Kresse and J. Furthmüller. Efficient iterative schemes for *ab initio* total-energy calculations using a plane-wave basis set. *Phys. Rev. B*, 54(16):11169–11186, 1996.

[298] B. Aradi, B. Hourahine, and Th. Frauenheim. DFTB+, a Sparse Matrix-Based Implementation of the DFTB Method. *J. Phys. Chem. A*, 111(26):5678–5684, 2007.

[299] M. Elstner. The SCC-DFTB method and its application to biological systems. *Theor. Chem. Acc.*, 116(1):316–325, 2006.

[300] R. G. Parr, Y. Weitao, and W. Yang. *Density-Functional Theory of Atoms and Molecules.* International Series of Monographs on Chemistry. Oxford University Press, Oxford, U.K., 1994.

[301] T. T. Rantala. *Ab initio* studies of compound semiconductor surfaces. In D. A. Jelski and T. F. George, editors, *Computational Studies of New Materials.* World Scientific, Singapore, 1999.

[302] D. M. Ceperley and B. J. Alder. Ground State of the Electron Gas by a Stochastic Method. *Phys. Rev. Lett.*, 45(7):566–569, 1980.

[303] J. P. Perdew and A. Zunger. Self-interaction correction to density-functional approximations for many-electron systems. *Phys. Rev. B*, 23(10):5048–5079, 1981.

[304] S. H. Vosko, L. Wilk, and M. Nusair. Accurate spin-dependent electron liquid correlation energies for local spin density calculations: a critical analysis. *Can. J. Phys.*, 58(8):1200–1211, 1980.

[305] J. P. Perdew and Y. Wang. Accurate and simple analytic representation of the electron-gas correlation energy. *Phys. Rev. B*, 45(23):13244–13249, 1992.

[306] J. Nocedal. Updating Quasi-Newton Matrices With Limited Storage. *Math. Comput.*, 35(151):773–782, 1980.

[307] D. C. Liu and J. Nocedal. On the limited memory BFGS method for large scale optimization. *Math. Program.*, 45(1):503–528, 1989.

[308] G. Zheng, H. A. Witek, P. Bobadova-Parvanova, S. Irle, D. G. Musaev, R. Prabhakar, K. Morokuma, M. Lundberg, M. Elstner, C. Köhler, and Th. Frauenheim. Parameter Calibration of Transition-Metal Elements for the Spin-Polarized Self-Consistent-Charge Density-Functional Tight-Binding (DFTB) Method: Sc, Ti, Fe, Co, and Ni. *J. Chem. Theory Comput.*, 3(4):1349–1367, 2007.

[309] M. Elstner, D. Porezag, G. Jungnickel, J. Elsner, M. Haugk, Th. Frauenheim, S. Suhai, and G. Seifert. Self-consistent-charge density-functional tight-binding method for simulations of complex materials properties. *Phys. Rev. B*, 58(11):7260–7268, 1998.

[310] L. Guo, C. Qi, X. Zheng, R. Zhang, X. Shen, and S. Kaya. Toward understanding the adsorption mechanism of large size organic corrosion inhibitors on an Fe(110) surface using the DFTB method. *RSC Adv.*, 7(46):29042–29050, 2017.

[311] L. Guo, M. Wu, S. Kaya, M. Chen, and L. H. Madkour. Influence of the alkyl chain length of alkyltriazoles on the corrosion inhibition of iron: A DFTB study. *AIP Conf. Proc.*, 1995(1):020015, 2018.

[312] G. Kresse and J. Hafner. First-principles study of the adsorption of atomic H on Ni (111), (100) and (110). *Surf. Sci.*, 459(3):287–302, 2000.

[313] F. Mittendorfer and J. Hafner. Hydrogenation of Benzene on Ni(111) - A DFT Study. *J. Phys. Chem. B*, 106(51):13299–13305, 2002.

[314] G. Kalibaeva, R. Vuilleumier, S. Meloni, A. Alavi, G. Ciccotti, and R. Rosei. *Ab Initio* Simulation of Carbon Clustering on an Ni(111) Surface: A Model of the Poisoning of Nickel-Based Catalysts. *J. Phys. Chem. B*, 110(8):3638–3646, 2006.

[315] A. B. Kamara, A. J. Ardell, and C. N. J. Wagner. Lattice misfits in four binary Ni-Base γ/γ' alloys at ambient and elevated temperatures. *Metall. Mater. Trans. A*, 27(10):2888–2896, 1996.

[316] S. Irle, A. J. Page, B. Saha, Y. Wang, K. R. S. Chandrakumar, Y. Nishimoto, H.-J. Qian, and K. Morokuma. Atomistic Mechanism of Carbon Nanostructure Self-Assembly as Predicted by Nonequilibrium QM/MD Simulations. In J. Leszczynski and M. K. Shukla, editors, *Practical Aspects of Computational Chemistry II.*, pages 103–172. Springer Netherlands, Dordrecht, Netherlands, 2012.

[317] H. Shi, P. Koskinen, and A. Ramasubramaniam. Self-Consistent Charge Density-Functional Tight-Binding Parametrization for Pt-Ru Alloys. *J. Phys. Chem. A*, 121(12):2497–2502, 2017.

[318] G. Dolgonos, B. Aradi, N. H. Moreira, and Th. Frauenheim. An Improved Self-Consistent-Charge Density-Functional Tight-Binding (SCC-DFTB) Set of Parameters for Simulation of Bulk and Molecular Systems Involving Titanium. *J. Chem. Theory Comput.*, 6(1):266–278, 2010.

[319] P. Cremaschi and J. L. Whitten. The effect of hydrogen chemisorption on titanium surface bonding. *Theor. Chim. Acta*, 72(5):485–496, 1987.